



# Ion energy loss at maximum stopping power in a laser-generated plasma

Witold Cayzac

## ► To cite this version:

Witold Cayzac. Ion energy loss at maximum stopping power in a laser-generated plasma. Physics [physics]. Université Sciences et Technologies - Bordeaux I; Technische Universität (Darmstadt, Allemagne), 2013. English. NNT : 2013BOR14920 . tel-00949958

**HAL Id: tel-00949958**

**<https://theses.hal.science/tel-00949958>**

Submitted on 20 Feb 2014

**HAL** is a multi-disciplinary open access archive for the deposit and dissemination of scientific research documents, whether they are published or not. The documents may come from teaching and research institutions in France or abroad, or from public or private research centers.

L'archive ouverte pluridisciplinaire **HAL**, est destinée au dépôt et à la diffusion de documents scientifiques de niveau recherche, publiés ou non, émanant des établissements d'enseignement et de recherche français ou étrangers, des laboratoires publics ou privés.

# Thesis presented at Université Bordeaux 1

Ecole Doctorale des Sciences Physiques et de l'Ingénieur

by **Witold CAYZAC**

to obtain the degree of

DOCTOR OF UNIVERSITÉ BORDEAUX 1

AND

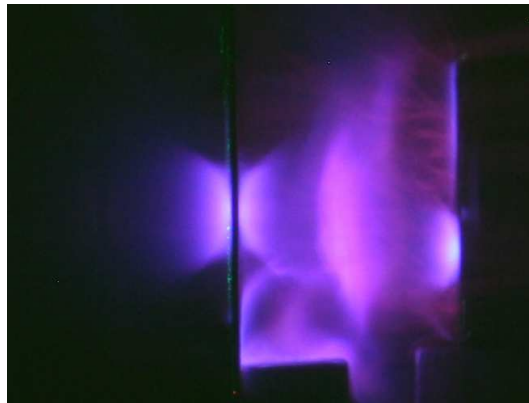
DOCTOR RER. NAT. OF TECHNISCHE UNIVERSITÄT  
DARMSTADT

SPECIALITÉ: ASTROPHYSIQUE, PLASMA, NUCLÉAIRE  
FACHBEREICH PHYSIK, INSTITUT FÜR KERNPHYSIK

---

## Ion energy loss at maximum stopping power in a laser-generated plasma

---



Defended on December, 2nd 2013 in front of the committee composed of

Gérard MALKA	Université de Bordeaux 1	Supervizor
Ludovic HALLO	CEA-CESTA	Supervizor
Gilles MAYNARD	Université de Paris 11	Referee
Markus ROTH	Technische Universität Darmstadt	Supervizor
Dieter HOFFMANN	Technische Universität Darmstadt	Referee
Gernot ALBER	Technische Universität Darmstadt	Professor
Vladimir TIKHONCHUK	Université de Bordeaux 1	Professor
Emmanuel ABRAHAM	Université de Bordeaux 1	Professor

Thesis prepared within a joint international PhD program between Université Bordeaux 1 and  
Technische Universität Darmstadt

N° d'ordre: 4920



# Acknowledgments

This thesis work would never have been possible and successful without the support of numerous people both in France and in Germany, and even beyond. I am indebted to so many people, be it for their support in the experiments, in the theory or other aspects of the work, or in the overall organization and coordination of this joint international thesis, that acknowledging them all properly is a difficult task. Should I omit some people or not explicitly mention them, which is more than likely to happen, I beg them to accept my apologies and I express them my high gratitude.

Foremost, I would like to express my sincere gratitude to my PhD supervisors, Gérard Malka, Ludovic Hallo and Markus Roth, for the continuous guidance and enthusiastic support they provided me and the trust they gave me along these three years, and for the possibility to carry out the thesis under the best conditions between CELIA, CEA/CESTA and TU-Darmstadt/GSI. In this place I would like to particularly thank Markus Roth who has actually followed me for the last five years, since I entered his office at TU Darmstadt in 2008 as a young master aspirant barely knowing what a plasma and what fusion were. He was also the instigator of this thesis work.

I am also deeply indebted to Vladimir Tikhonchuk who, responding to this instigation, made this thesis possible and welcomed me at CELIA, and who also provided me a regular mentoring throughout my work there. Likewise, I would like to acknowledge Theodor Schlegel for his mentoring guidance and support.

Furthermore, I want to thank Philippe Balcou, Dimitri Batani, Francis Hardouin and Thomas Stöhlker who welcomed me in CELIA, in the PETRUX group of CELIA, in CEA-CESTA and in GSI, respectively. I wish to express my gratefulness to Dieter Hoffmann and Gilles Maynard for being the referees of my work and for their useful remarks and comments. I also want to thank Gernot Alber and Emmanuel Abraham who kindly accepted to become part of the jury members even if they were asked very late.

I should give a particular Danke schön to the Z6 wizard Abel Blažević for his constant and friendly support in the experimental part of the work, from the organization of the campaigns to the development of the setup and the realization of the experiments. His precious and efficient guidance has highly contributed to the success of the experiments.

Furthermore, I shall thank the three 'Alex' who have been highly involved in this work and greatly participated to its success, namely:

I want to express a sehr besonderen Dank to Alexander Frank "Alf", who was my forerunner and my "big brother" in the field of the ion energy loss in plasma at GSI, and who played a key role in this work. My work is indeed based, to a large extent, on the achievements of his PhD thesis. Not only did I use the same plasma target in my experiments, but I also used his Monte-Carlo code, that he kindly provided me, for the calculation of the charge-state distribution of the projectile ions. His constant availability, support, advice, critics and enthusiasm along these three years have been a major ingredient of the success of my thesis, in the experiments as well as in

the theory and the simulations. Thank you for the numerous discussions and for answering my ten thousand Fragen !

I also wish to express un remerciement tout particulier to Alex Ortner, my energy-loss partner along these three years and the “Nhelix-Meister” of Z6, for the crucial role he played in the experimental part of the work and especially in the main campaign of November 2012. He guided me through the wonders and perils of the fantastic Z6 world, explained me everything there and was indispensable in the preparation, the adjustment and the realization of the experimental campaigns. Thank you for the countless constructive and stimulating discussions and exchanges, and also for reading and correcting my thesis manuscript.

I am also particularly grateful to Alexander Knetsch for his work and commitment on the development of the new large-area diamond detector, that decisively contributed to the success of the main experimental campaign.

Moreover I wish to acknowledge the friendly support of Gabriel Schaumann and of his team of the Target Laboratory of TU Darmstadt in the design, the fabrication and the adjustment of the targets for each experimental campaign.

I acknowledge Mikhail Basko and Anna Tauschwitz for providing the RALEF2D simulation data, that were indispensable for the theoretical part of the work and for comparing the experimental energy-loss data with the predictions of the stopping theories, as well as for answering my questions about the simulations. Furthermore, I thank Dirk Gericke and Jan Vorberger for providing the calculation data of the stopping power in the T-Matrix and RPA approaches and for enlightening theoretical discussions. I also want to thank Kévin Pépitone for providing me the GEANT4 simulation data, as well as Florian Grüner for support with the CTMC code even if this task proved to be too ambitious to fit in the time frame of the thesis.

I am also indebted to the members of the TU-Darmstadt / GSI plasma-physics group that I did not mention yet and who were also involved in the preparation and the realization of the experiments, sometimes beyond decent work hours. These are Dennis Schumacher, Stefan Bedacht, Oliver Deppert, Dominik Kraus and Florian Wagner. Thank you particularly Florian for the unforgettable sauna sessions with you and for teaching me beautiful German songs ;-). But please improve yourself in badminton, you don't want me to fall asleep on the court again, do you ? By the way, when are we going back to this chapel somewhere in the center of France ??

I express my deep gratitude to Bettina Lommel, Andreas Beusch and Birgit Kindler as well as to the whole team of the Target Laboratory of GSI for fabricating and providing the deceleration foils, plasma-target foils and gold-filter foils, and also for metalizing the diamond samples for the detector. They were given a lot of work with target requirements that were not easy to achieve, and it yet finally worked out. I also acknowledge all the other people of GSI who contributed to the development and to the construction of the diamond detector and of its screening system: Elèni Berdermann for advice and discussions on the detector, Michael Träger for the preparation, the bonding and the test of the diamond samples, Bernd Zumbach for the development of the detector masks, Markus Romig and his whole team of the Mechanical Workshop of GSI for the construction of all the required parts.

A special thank goes also to Vincent Bagnoud for his laser assistance in the preparation and the realization of the main campaign and for the numerous jogging sessions we had (even during the German winter because we are French, so we are tough guys !), as well as to the whole PHELIX team for their excellent technical support. Likewise I thank the UNILAC team for their expert

support during the experiments.

Furthermore I wish to thank all the other people who, though not directly involved in my work, either helped me in various aspects, or simply contributed to a pleasant and stimulating work environment. These are, in the Plasma Physics group of TU-Darmstadt/GSI: Anke Otten, Simon Busold, Gabriele Hoffmeister, Rober Jäger and Jan Helfrich. As for CELIA, there are also a lot of people to thank.

I especially thank Rémi Capdessus who shared my office in my CELIA periods during those three years, for the numerous and daily discussions we had, for the good time spent on summer schools together and for providing some snickers to his office mates (sometimes even without knowing it !), Michaël Touati for all the good time spent together at work and beyond work, for the traditional soup breaks (soupelette, Messire ?), for the uncountable enlightening discussions about physics as well as the multiple philosophical debates we had, the surfing sessions and much more, Dario Del Sorbo for the bunga-bunga parties with Berlusconi and an unforgettable biking ride around the Arcachon bay, Alexandra Vallet for the good times in Bordeaux and in Crete, Jessy Mallet for the good times at work and beyond even if he is only a mathematician, Barthélémy Delorme, Mokrane Hadj-Bachir, Anton Helm, Rémi Jugier and Elise Estibal who have been great office mates, as well as Marion Lafon, Céline Beaucourt, Xavier Vaisseau, Basil Deschaud, Yohann Maheut, Arnaud Colaitis, Benjamin Vauzour, Sébastien Guisset, Teddy Pichard, Gabriel Georges and others. I also want to thank Céline Oum, Emmanuelle Lesage and Sophie Heurtebise for their friendly support with administrative stuff, Loïc Baucher and Elodie Béziat for their support with computer issues, and all the other people of CELIA whom I did not explicitly mention.

Last but not least, I thank all my friends and relatives for the support and the motivation I got throughout these three years of thesis, and especially my parents, Hanna and Claude, for the constant support they provided me along my whole curriculum.

## Summary

In the frame of this thesis, a new experimental setup for the measurement of the energy loss of carbon ions at maximum stopping power in a hot laser-generated plasma has been developed and successfully tested. In this parameter range where the projectile velocity is of the same order of magnitude as the thermal velocity of the plasma free electrons, large uncertainties of up to 50 % are present in the stopping-power description. To date, no experimental data are available to perform a theory benchmarking. Testing the different stopping theories is yet essential for inertial confinement fusion and in particular for the understanding of the alpha-particle heating of the thermonuclear fuel.

Here, for the first time, precise measurements were carried out in a reproducible and entirely characterized beam-plasma configuration. It involved a nearly fully-stripped ion beam probing a homogeneous fully-ionized plasma. This plasma was generated by irradiating a thin carbon foil with two high-energy laser beams and features a maximum electron density of  $10^{21} \text{ cm}^{-3}$  and a maximum electron temperature of 200 eV. The plasma conditions were simulated with a two-dimensional radiative hydrodynamic code, while the ion-beam charge-state distribution was predicted by means of a Monte-Carlo code describing the charge-exchange processes of projectile ions in plasma.

To probe at maximum stopping power, high-frequency pulsed ion bunches were decelerated to an energy of 0.5 MeV per nucleon. The ion energy loss was determined by a time-of-flight measurement using a specifically developed chemical-vapor-deposition diamond detector that was screened against any plasma radiation.

A first experimental campaign was carried out using this newly developed platform, in which a precision of  $\leq 200 \text{ keV}$  on the energy loss was reached. This allowed, via the knowledge of the plasma and of the beam parameters, to reliably test several stopping theories, either based on perturbation theory or on a nonlinear T-Matrix formalism. A preliminary analysis suggests that the energy deposition at maximum stopping power is significantly smaller than predicted, particularly, by perturbation approaches.

**Key words:** Ion stopping power, energy loss, laser-generated plasma, charge-state distribution, time-of-flight measurement, CVD-diamond detector

## Résumé

Dans le cadre de cette thèse, un nouveau dispositif expérimental pour la mesure du dépôt d'énergie d'ions carbone au maximum du pouvoir d'arrêt dans un plasma généré par laser a été développé et testé avec succès. Dans ce domaine de paramètres où la vitesse du projectile est de l'ordre de grandeur de la vitesse thermique des électrons libres du plasma, l'incertitude théorique sur le pouvoir d'arrêt peut atteindre 50 %. Or à l'heure actuelle, aucune donnée expérimentale ne permet de vérifier et de tester les différentes prédictions. Une discrimination des théories existantes du pouvoir d'arrêt est cependant essentielle pour la Fusion par Confinement Inertiel et particulièrement pour comprendre le chauffage du combustible par les particules alpha dans la phase d'allumage.

Pour la première fois, des mesures précises du dépôt d'énergie des ions ont été effectuées dans une configuration expérimentale reproductible et entièrement caractérisée. Celle-ci consiste en un faisceau d'ions entièrement ionisé interagissant avec un plasma entièrement ionisé et homogène. Le plasma a été généré par l'irradiation d'une cible mince de carbone avec deux faisceaux laser à haute énergie, et présente une densité électronique maximale de  $10^{21} \text{ cm}^{-3}$  et une température électronique maximale of 200 eV. Les paramètres du plasma ont été simulés à l'aide d'un code hydrodynamique radiatif bi-dimensionnel, tandis que la distribution de charge du faisceau d'ions a été estimée avec un code Monte-Carlo qui décrit les processus d'échange de charge des ions dans le plasma.

Pour sonder le plasma au maximum du pouvoir d'arrêt, un faisceau d'ions pulsé à haute fréquence a été freiné à une énergie de 0.5 MeV par nucléon. Le dépôt d'énergie des ions a été déterminé via une mesure de temps de vol à l'aide d'un détecteur à base de diamant produit par dépôt chimique en phase vapeur, protégé contre les radiations émises par le plasma.

Une première campagne expérimentale a été conduite pour exploiter le nouveau dispositif, dans laquelle le dépôt d'énergie a été mesuré avec une précision inférieure à 200 keV. Cela a permis, grâce à la connaissance des paramètres du plasma et du faisceau d'ions, de tester différentes théories de pouvoir d'arrêt de manière fiable. Une analyse préliminaire des résultats montre que le dépôt d'énergie au maximum du pouvoir d'arrêt est plus faible qu'il n'a été prédit par la plupart des théories, et en particulier par les théories des perturbations.

**Mots clés:** Pouvoir d'arrêt des ions, dépôt d'énergie, plasma généré par laser, distribution de charge, mesure par temps de vol, détecteur diamant CVD



## Zusammenfassung

Im Rahmen dieser Arbeit wurde ein neuer experimenteller Aufbau für die Messung des Energieverlusts von Kohlenstoff-Ionen bei maximalem Bremsvermögen in einem lasererzeugtem Plasma entwickelt und getestet. In diesem Parameterbereich, wo die Projektilgeschwindigkeit nah der thermischen Geschwindigkeit der Plasmaelektronen liegt, weist die theoretische Beschreibung des Bremsvermögens erheblichen Unsicherheiten bis 50 % auf. Ausserdem sind bisher keine experimentellen Daten verfügbar, um die theoretischen Vorhersagen zu testen. Eine Bewertung der verschiedenen Theorien des Bremsvermögens ist jedoch von grosser Bedeutung für die Trägheitsfusion und insbesondere für das Verständnis der Heizung des Fusionsbrennstoffs mittels Alpha-Teilchen.

Zum ersten Mal wurden präzisen Messungen in einer reproduzierbaren und vollständig bekannten Strahl-Plasma Einstellung durchgeführt. Sie besteht in einem vollionisierten Ionenstrahl, der mit einem homogenen und vollionisierten Plasma wechselwirkt. Das Plasma wurde von der Bestrahlung einer dünnen Kohlenstoffolie mit zwei hochenergetischen Laserstrahlen erzeugt, und weist eine maximale Elektronendichte von  $10^{21} \text{ cm}^{-3}$  und eine maximale Elektronentemperatur von 200 eV auf. Die Plasmaparameter wurden mithilfe eines zweidimensionalen radiativen hydrodynamischen Codes simuliert, während die Ladungsverteilung des Ionenstrahls wurde mit einem Monte-Carlo Code berechnet, der die Umladungsprozesse von Projektilionen im Plasma beschreibt.

Um das Plasma bei maximalem Bremsvermögen zu untersuchen, wurde ein hoch-Frequenz gepulster Ionenstrahl zu einer Energie von 0.5 MeV pro Nukleon heruntergebremst. Der Ionenenergieverlust wurde mit der Flugzeitsmethode mit einem gegen Plasmastrahlung abgeschirmten CVD-Diamant-Detektor gemessen.

Eine erste experimentelle Kampagne wurde mit dem neuen Aufbau durchgeführt, in der eine Messungspräzision besser als 200 keV auf dem Energieverlust erreicht wurde. Dies ermöglichte, mit der Kenntnis der Plasma- und Strahlparameter, mehreren Bremsvermögen-Theorien zuverlässig zu testen und zu vergleichen. Eine vorläufige Datenanalyse zeigt, dass die Energiedeposition bei maximalem Bremsvermögen ist kleiner, als insbesondere von den störungstheoretischen Ansätzen vorhergesagt wurde.

**Stichwörter:** Bremsvermögen von Ionen, Energieverlust, lasererzeugte Plasma, Ladungsverteilung, Flugzeitsmessung, CVD-Diamant-Detektor

# Dépôt d'énergie des ions au maximum du pouvoir d'arrêt dans un plasma généré par laser

Dans le cadre de cette thèse, un nouveau dispositif expérimental pour la mesure du dépôt d'énergie des ions au maximum du pouvoir d'arrêt dans un plasma généré par laser a été développé et testé avec succès. Dans ce domaine de paramètres, la vitesse du projectile  $v_p$  est de l'ordre de grandeur de la vitesse thermique des électrons libres du plasma  $v_{th}$ . Le couplage coulombien entre les ions projectiles et les électrons du plasma, sur lesquels l'essentiel de l'énergie est déposée, est alors maximal et une description théorique complète du pouvoir d'arrêt des ions dans la plasma (énergie déposée par unité de longueur), n'a pas encore été établie. En particulier, le spectre complet en paramètre d'impact de collision entre les projectiles et les électrons du plasma doit être pris en compte, incluant aussi bien les collisions binaires rapprochées (diffusion coulombienne à grand angle) que les effets dynamiques du plasma comme l'excitation d'ondes de Langmuir. De plus, la description de l'état de charge des projectiles, quantité cruciale pour le pouvoir d'arrêt, est alors particulièrement complexe. Cet état de charge résulte de la compétition entre différents processus d'ionisation et de recombinaison (capture) des projectiles avec les électrons du plasma. Au maximum du pouvoir d'arrêt, les sections efficaces de tous ces processus d'échange de charge sont mal connues, d'autant plus que des processus de collisions multiples peuvent également survenir. De plus, l'état de charge se trouve alors généralement hors de l'état d'équilibre, ce qui nécessite pour l'évaluer l'utilisation de codes Monte-Carlo modélisant l'ensemble des processus.

Il résulte de ces difficultés que, pour  $\frac{v_p}{v_{th}} \approx 1$ , les écarts entre les prédictions des différentes théories du pouvoir d'arrêt sont importants. Ils peuvent atteindre 30-50 % entre les descriptions linéaires basées sur une approche diélectrique du plasma et les descriptions non-linéaires qui prennent en compte les corrélations ions-plasma. Jusqu'à présent, les rares données expérimentales disponibles dans ce domaine de paramètres n'ont pas permis de valider les différentes prédictions en raison d'incertitudes sur les paramètres du plasma ou sur l'état de charge des projectiles au cours de l'interaction dans les travaux antérieurs.

Dans cette étude, pour la première fois, des mesures précises ont été effectuées dans une configuration expérimentale complètement caractérisée. Ainsi, en exploitant les résultats de simulation du plasma et de l'état de charge des projectiles, un test des théories existantes du pouvoir d'arrêt a pu être réalisé. Il s'agit à notre connaissance du premier test de ce genre.

Valider les théories du pouvoir d'arrêt dans ce domaine de paramètres revêt une grande importance pour la fusion par confinement inertiel (FCI), où l'interaction ions-plasma joue un rôle central. Une connaissance plus précise des mécanismes du pouvoir d'arrêt est également essentielle pour la physique des hautes densités d'énergie, la physique des accélérateurs d'ions ainsi que l'astrophysique. En FCI, deux enjeux principaux sont de mise. Il s'agit, en premier lieu, d'une meilleure compréhension du freinage des particules alpha dans le combustible de deutérium-tritium en phase d'allumage et de combustion thermonucléaire, crucial pour le processus de fusion. En second lieu, il s'agit aussi d'une modélisation améliorée des schémas de FCI utilisant des faisceaux d'ions, tels que la fusion par ions lourds ou l'allumage rapide par faisceaux de protons ou d'ions carbone. L'étude du pouvoir d'arrêt dans un plasma généré par laser dans cette thèse permet justement de se rapprocher des conditions de température et de densité typiques de la FCI.

Le plasma utilisé dans cette étude est créé par l'irradiation en mode "single-shot" d'une cible plane de carbone d'une densité surfacique de  $100 \mu\text{g}/\text{cm}^2$  avec deux faisceaux laser simultanés venant de directions opposées et avec de petits angles d'incidence par rapport à l'axe ionique. Les faisceaux sont doublés en fréquence à des longueurs d'onde respectives de 532 et 527 nm et ont une énergie de 30 J, une durée de 7 ns (en largeur à mi-hauteur, FWHM) et un diamètre focal de 1 mm sur la cible, résultant d'un lissage spatial à l'aide de lames de phase aléatoires. Ces paramètres ont été choisis, sur la base de simulations hydrodynamiques réalisées avec le code RALEF2D, de sorte à obtenir un plasma suffisamment homogène spatialement et entièrement ionisé. Les résultats des simulations ont été validés via des mesures de profils de la densité des électrons libres du plasma à l'aide d'un diagnostic d'interférométrie laser multi-frame résolue en espace et en temps. Le plasma est ainsi entièrement caractérisé et présente une densité électronique maximale proche de  $10^{21} \text{ cm}^{-3}$  et une température électronique maximale de 180 eV. L'irradiation laser de la cible sur les deux faces avec des faisceaux doublés en fréquence permet notamment d'obtenir un transport radiatif efficace au sein du plasma, ce qui conduit à une uniformisation

rapide des gradients de densité et de température le long de l'axe ionique et en particulier à des paramètres plasma reproductibles de façon systématique. De plus, une ionisation complète du plasma est atteinte entre 7 et 13 ns après le début du chauffage laser, ce qui simplifie considérablement l'interaction ions-plasma. En outre, le lissage des faisceaux via les lames de phase aléatoires, d'autant plus efficace que les faisceaux sont doublés en fréquence, conduit à la formation d'un plasma homogène dans la direction normale à l'axe ionique sur un diamètre d'environ 800  $\mu\text{m}$ , et s'étendant de façon quasi-mono-dimensionnelle le long de l'axe ionique durant les 7 premières nanosecondes de l'interaction. De par ses propriétés d'homogénéité, de reproductibilité et d'ionisation, et étant de plus entièrement caractérisé, ce plasma constitue donc un cas d'étude idéal pour des mesures de dépôt d'énergie des ions.

Une énergie de projectile de 0.5 MeV/u est requise pour que l'interaction avec le plasma se déroule au maximum du pouvoir d'arrêt, pour  $\frac{v_p}{v_{th}} \approx 1$ . Des ions carbone sont employés en tant que projectiles, le carbone constituant un compromis entre la stabilité du faisceau d'ions et une ionisation complète de ce faisceau dans le plasma, qui est une condition essentielle pour l'interprétation des résultats expérimentaux du dépôt d'énergie des ions. L'ionisation du faisceau a été calculée avec un code Monte-Carlo qui décrit les processus d'échange de charge, ionisation et capture d'électrons, subis par des ions qui traversent un plasma à l'équilibre thermodynamique. Outre les processus d'échange de charge qui existent déjà dans la matière non-ionisée, à savoir l'ionisation/excitation des projectiles par collisions avec les ions du plasma ainsi que la capture radiative et non-radiative d'électrons (liés) de la cible, le code prend en compte les mécanismes additionnels qui apparaissent dans un plasma: ionisation/excitation des projectiles par les électrons libres, ainsi que la capture diélectronique et la recombinaison à trois corps. Selon les prédictions, plus de 90 % des ions carbone deviennent rapidement entièrement ionisés après leur entrée dans le plasma tant que celui-ci conserve un haut degré d'ionisation. La raison essentielle en est la disparition du processus de capture d'électrons liés par les projectiles dans le plasma fortement ionisé, qui est le mécanisme de capture de loin le plus efficace tant que la matière est non complètement ionisée. En conclusion, la configuration expérimentale considérée met en jeu un faisceau d'ions complètement ionisé interagissant avec un plasma entièrement ionisé, et tous les paramètres sont connus. Une interprétation fiable et précise des résultats expérimentaux de dépôt d'énergie est donc rendue possible dans ce schéma simplifié. L'interaction du faisceau de  $\text{C}^{6+}$  à une énergie de 0.5 MeV/u avec le plasma est caractérisée par un important couplage coulombien, étant donné que le paramètre de Coulomb  $\eta > 1$ . Par conséquent, elle ne peut a priori pas être décrite dans le cadre d'une première approximation de Born du pouvoir d'arrêt. Diverses approches théoriques du pouvoir d'arrêt ont été comparées pour cette configuration ions-plasma. D'une part, plusieurs descriptions standard reposant sur une première approximation de Born de l'interaction (couplage linéaire entre le faisceau et le plasma) ont été utilisées: (i) la formule asymptotique de Bethe pour les vitesses très élevées, (ii) la formule de Bethe-Bloch pour les vitesses intermédiaires qui rajoute l'effet des collisions rapprochées, (iii) le modèle standard du pouvoir d'arrêt qui repose sur une formule de Bethe avec l'ajout, outre du terme de Bloch, du terme correctif de Barkas pour la polarisation locale (du second ordre) du plasma et du facteur de Chandrasekhar (couplage thermique avec une distribution maxwellienne des électrons libres du plasma) pour le domaine de vitesses  $\frac{v_p}{v_{th}} \leq 1$ , (iv) le pouvoir d'arrêt dans la théorie diélectrique issue de l'équation cinétique de Vlasov qui décrit le pouvoir d'arrêt sur la base d'une polarisation du plasma résultant d'une perturbation électrostatique et (v) le modèle de Li et Petrasso qui permet de décrire tout le spectre en paramètre d'impact de collision depuis les collisions binaires rapprochées jusqu'aux oscillations collectives du plasma, couramment utilisé dans le cadre des calculs en FCI. D'autre part, ces approches perturbatives ont été comparées à un schéma théorique non-perturbatif dit de la "Matrice T". Celui-ci, utilisant une équation cinétique de Boltzmann, décrit le pouvoir d'arrêt résultant de collisions binaires et incorpore approximativement les effets collectifs en utilisant une longueur d'écrantage du projectile qui dépend de sa vitesse. Ce schéma de la matrice T est en outre en bon accord avec les simulations numériques (Particle-in-Cell PIC et Molecular Dynamics MD) dans le cas d'une interaction à fort couplage, d'après la littérature. Il s'avère que, tandis que les théories perturbatives prévoient toutes des valeurs très proches du pouvoir d'arrêt, un écart significatif, de l'ordre de 30 %, est attendu entre les prédictions perturbatives et les résultats obtenus à l'aide de la théorie non perturbative de la matrice T.

Ces calculs théoriques du pouvoir d'arrêt ont ensuite été appliqués au calcul du dépôt d'énergie des ions carbone dans la configuration expérimentale considérée. Pour cela, les profils de densité et de température du plasma ont été directement extraits des simulations hydrodynamiques, tandis que les distributions de charge correspondantes du plasma ont été calculées en résolvant l'équation de Saha via un algorithme itératif. Quant aux distributions de charge du faisceau d'ions, elle ont été calculées sur la base des profils de densité, de température et d'ionisation du plasma avec le code Monte-Carlo. Puis à l'aide de tous les

paramètres de l'interaction, les profils du pouvoir d'arrêt des projectiles dans le plasma ont été obtenus. Ces calculs ont été effectués avec un pas de temps de 0.5 ns donné par les simulations hydrodynamiques, entre 0 et 16 ns après le début du chauffage de la cible par les lasers. Finalement, l'intégration des pouvoirs d'arrêt le long des profils de densité surfacique de la cible a permis de déterminer les valeurs de l'énergie déposée à chaque pas de temps.

Il est à noter que dans ce calcul, toute corrélation entre les ions du faisceau a été négligée en raison d'un nombre d'ions relativement faible (quelques milliers tout au plus). En outre, du fait d'une vitesse du projectile près de 100 fois supérieure à la vitesse thermique des ions du plasma, le pouvoir d'arrêt sur les ions ainsi que les effets de perte d'énergie transverse ont aussi été complètement négligés. Par ailleurs, le calcul prend deux effets expérimentaux en compte. L'un est le fait que la vitesse des projectiles diminue au fur et à mesure de leur propagation dans le plasma, ce qui résulte en un écart de 10-20 % en sortie du plasma. Cela modifie en conséquence leur pouvoir d'arrêt de quelques pourcents le long de leur trajectoire. Le second est la durée d'un bunch d'ions dans l'expérience, qui est de 3 ns (FWHM). Celle-ci implique que tous les ions d'un bunch n'interagissent pas avec les mêmes paramètres du plasma et que le dépôt d'énergie doit être moyenné sur la durée du bunch.

Les simulations prévoient une augmentation du dépôt d'énergie dans le plasma, avec un maximum de l'ordre de 200-300 % de sa valeur dans la cible froide selon les différentes théories. Ce maximum est atteint à la fin de la durée de l'impulsion laser, soit vers  $t = 7$  ns, ce qui correspond en outre au moment où la température du plasma est proche de son maximum, et donc où le pouvoir d'arrêt des ions est maximal. A partir de  $t = 7$  ns, la densité surfacique du plasma commence à chuter, ce qui fait donc progressivement diminuer le dépôt d'énergie. A l'image des courbes de pouvoir d'arrêt, les diverses courbes théoriques de dépôt d'énergie présentent des écarts dépassant 30 %. Ces courbes permettent par ailleurs d'estimer la résolution en énergie nécessaire dans l'expérience pour pouvoir distinguer entre les différentes théories, soit environ 100 keV.

Le travail expérimental a été mené au GSI Helmholtzzentrum für Schwerionenforschung à Darmstadt en Allemagne, où un faisceau d'ions carbone pulsé à une fréquence de 36 MHz issu de l'accélérateur UNILAC a interagi avec des plasmas générés par les deux systèmes laser de haute énergie PHELIX et *nhelix*. La perte d'énergie des ions dans le plasma a alors été mesurée via une méthode de temps de vol (TDV).

Afin de sonder le plasma à l'énergie de projectile de 0.5 MeV/u, le faisceau, doté d'une énergie initiale de 3.6 MeV/u, a été freiné à travers une feuille de carbone d'une épaisseur de 45  $\mu\text{m}$ . Ceci a eu pour effet secondaire une dispersion du faisceau, en énergie (de l'ordre de 19 %) et en angle (près de  $\pm 3^\circ$ ), selon des simulations Monte-Carlo du processus de freinage réalisées à l'aide des programmes TRIM et GEANT4. Pour faire en sorte que la majorité des ions interagisse avec la partie transversalement homogène du plasma malgré la divergence angulaire du faisceau, la feuille de freinage a été positionnée à une distance de seulement 10 mm avant la cible plasma. L'imprécision sur le TDV des ions résultant du profil transversal de densité surfacique du plasma n'est alors que de 150 ps en moyenne et reste en-deçà de la résolution temporelle du détecteur. Une distance plus petite introduirait le risque d'irradier la feuille de freinage avec le faisceau laser de *nhelix*. En outre, une distance de TDV des ions de 50 cm a été choisie en tant qu'optimum pour la résolution des mesures. Ainsi, les effets de recouvrement des signaux d'ions sur le détecteur causés par la dispersion en énergie du faisceau sont évités, tandis que la résolution en énergie est de l'ordre de 60 keV avec un détecteur d'ions à base de diamant CVD (Chemical Vapor Deposition). Cette résolution autorise des mesures très précises du dépôt d'énergie, permettant de tester quantitativement les théories du pouvoir d'arrêt.

Un détecteur semi-conducteur à base de diamant CVD est utilisé car ce matériau possède les propriétés idéales pour la détection de faisceaux d'ions à haut flux. Le diamant CVD présente en effet, de par ses propriétés structurelles, une très bonne résistance aux radiations ainsi qu'une excellente résolution temporelle. De plus, sa constante de temps peut atteindre des valeurs suffisamment petites pour obtenir des signaux d'une durée de quelques nanosecondes, bien plus brefs que la période des bunches d'ions de 27.6 ns. Cela est notamment possible grâce à l'utilisation d'amplificateurs DBA (Diamond Broadband Amplifier) à large bande et avec une impédance de 50  $\Omega$ .

L'élargissement transversal du faisceau d'ions dû à sa divergence angulaire conduit à un diamètre de faisceau de près de 10 cm sur le détecteur, ce qui a imposé la conception d'un nouveau dispositif à base de diamant CVD doté d'une grande surface de détection. Cela a permis de détecter un nombre d'ions conséquent, garantissant ainsi des amplitudes de signaux suffisantes pour le dépouillement des dépôts d'énergie. Le détecteur est composé de 10 diamants individuels d'une épaisseur de 13  $\mu\text{m}$  et avec une constante de temps de 3 ns, juxtaposés de façon à détecter environ 20 % des ions du faisceau. La distance

de 50 cm entre le détecteur et le plasma impose par ailleurs de positionner le détecteur directement dans la chambre d'expériences. Cela a nécessité le développement d'un système d'écrantage pour protéger le détecteur des signaux électromagnétiques émis dans la chambre d'expérience, à savoir les rayons X émis par le plasma et le pulse électromagnétique (EMP) qui résulte de la désexcitation des éléments conducteurs irradiés à l'intérieur de la chambre. Afin de réduire la durée de saturation du détecteur en-deçà du TDV des ions, en l'occurrence 50 ns, et d'obtenir ainsi des signaux exploitables, deux méthodes d'écrantage ont été mises en place. D'une part, un filtre à rayons X constitué d'une feuille de densité surfacique d'environ  $2 \text{ mg/cm}^2$  a été positionné directement devant le détecteur. Et d'autre part, ce dernier, en même temps que la ligne de transmission des signaux, a été confiné dans une cage de Faraday, ce qui l'a ainsi isolé électriquement de la chambre.

Une première campagne expérimentale a été conduite avec succès dans le cadre de la thèse. Après calibration et optimisation du dispositif, la durée de saturation du détecteur a pu être réduite à 20 ns, au prix toutefois d'une réduction de l'amplitude des signaux d'ions. Même si la plupart des tirs n'ont pas été exploitables en raison d'une saturation due aux rayons X, 5 tirs ont pu être dépouillés et de premières données de dépôt d'énergie ont été obtenues.

Le dépôt d'énergie des ions dans le plasma a été déduit du décalage temporel subi par les bunches lors de leur traversée du plasma. Pour cela, les centres de gravité en temps des signaux ont été calculés et comparés à leur valeur de référence dans le vide. L'erreur expérimentale, qui résulte essentiellement des faibles amplitudes des signaux, est comprise entre 10 % et 25 %, ce qui correspond à une résolution en énergie effective de près de 200 keV. Cette dernière est donc supérieure aux 100 keV souhaités mais toujours suffisante pour pouvoir différencier la plupart des prédictions théoriques.

Les données révèlent une augmentation maximale du dépôt d'énergie dans le plasma de 153 % par rapport à sa valeur dans la cible froide. Les valeurs mesurées du dépôt d'énergie aux instants où le plasma est hautement ionisé et par conséquent où la température du plasma et donc le pouvoir d'arrêt des ions sont proches de leur maxima, diffèrent significativement des valeurs théoriques. Elles se situent en effet 30 % en-deçà des prédictions de la matrice T et près de 60 % en-deçà des prédictions des théories perturbatives du pouvoir d'arrêt. En outre, afin d'évaluer le pouvoir d'arrêt dans l'expérience, le point de mesure à l'instant 10.5 ns a été considéré, où l'erreur expérimentale est la plus petite. Alors il apparaît que le pouvoir d'arrêt dans l'expérience est près de 16 % plus petit que celui, prédit par la matrice T, associé aux valeurs moyennes des profils de densité, de température ainsi que d'ionisation du plasma et des projectiles. Etant donné que le calcul de la matrice T a été effectué à l'aide d'une formule de fit issue de la littérature dont la précision est de 25 % selon son auteur, le dépôt d'énergie dans l'expérience est donc compatible avec cet intervalle d'erreur. Il serait donc souhaitable de réaliser un calcul exact de la matrice T se basant sur les sections efficaces de collisions pour le comparer également aux valeurs expérimentales. Ces résultats suggèrent donc que le dépôt d'énergie au maximum du pouvoir d'arrêt est surévalué par la plupart des théories. Cependant, il s'agit encore de résultats préliminaires et d'autres études, tant sur le plan expérimental que théorique, sont encore nécessaires pour pouvoir précisément interpréter ces données. D'une part, de nouvelles campagnes de mesure doivent être conduites afin de mesurer le dépôt d'énergie de façon plus systématique et de rassembler ainsi davantage de données, avec une précision expérimentale accrue. Pour cela, les filtres et les feuilles de freinage utilisés dans le dispositif seront essentiellement optimisés. D'autre part, plusieurs questions d'ordre théorique surgissent concernant l'interprétation exacte des données. Un point notable à approfondir est l'influence du transfert de charge non perturbatif sur la distribution de charge du faisceau d'ions. En effet, les sections efficaces des processus d'échange de charge ont été déterminées par des méthodes essentiellement perturbatives avec le code Monte-Carlo, alors que le couplage coulombien est important. Toutefois, étant donné que la dynamique d'échange de charge est dominée par la disparition du processus de capture d'électrons liés, les effets non perturbatifs n'ont pas nécessairement une influence notable. En outre, la question de l'extrapolation des résultats aux particules alpha dans la FCI se pose, et invite à étendre l'étude à d'autres paramètres plasma et notamment à des densités plus élevées.

## List of symbols

Constants	
$c$	light velocity in vacuum
$e$	elementary electric charge
$h$	Planck constant
$\hbar$	reduced Planck constant
$k_B$	Boltzmann constant
$a_0$	Bohr radius
$v_0$	Bohr velocity
Symbols	
$t$	time
$r, x, y, z$	radius, Cartesian coordinates
$\theta, \vec{\Omega}$	angle, solid angle
$v, E, p$	velocity, energy, momentum
$\nu, k$	frequency, wave number
$v_p, E_p, k_p$	projectile velocity, projectile energy, projectile wave number
$\lambda_L$	laser wavelength
$\omega_L, \omega_p$	laser circular frequency, plasma frequency
$m_e, m_i, \mu$	electron mass, ion mass, reduced mass
$\rho, n_e, n_i$	target mass density, electron number density, ion number density
$n_c$	critical plasma density
$T_e, T_i$	electron temperature, ion temperature
$v_{th}, v_r$	thermal electron velocity, relative velocity
$T_F, E_F, v_F$	Fermi temperature, energy and velocity
$Z, Z_p, Z_T$	atomic number, projectile charge state, target ionization degree
$Z_{eff}$	effective projectile charge state
$a$	Wigner-Seitz radius
$r_0$	Landau length
$b, b_{min}, b_{max}$	impact parameter, minimum and maximum impact parameter
$b_0$	minimum classical collision radius
$\lambda, \lambda_D, \kappa$	screening length, Debye screening length, inverse screening length
$\lambda_e, \lambda_r$	electron thermal wavelength, De Broglie wavelength of mutual interaction
$\vec{E}, \vec{B}$	electric field, magnetic field
$\Gamma, \gamma$	nonideality parameter, nonlinearity parameter
$\eta$	Coulomb or Bohr parameter
$\Theta$	degeneracy parameter
$\nu_{ei}$	electron-ion collision frequency
$\ln\Lambda$	Coulomb logarithm
$\sigma$	Standard deviation of a Gaussian distribution



# Contents

<b>1</b>	<b>Introduction</b>	<b>3</b>
1.1	Applications of ion stopping in plasma . . . . .	3
1.2	Description of the physical case . . . . .	5
1.3	Context of the work . . . . .	7
<b>2</b>	<b>Theoretical basis</b>	<b>11</b>
2.1	Laser-plasma interaction . . . . .	11
2.1.1	Plasma physics fundamentals . . . . .	11
2.1.2	Absorption of laser light in plasma . . . . .	19
2.2	Ion-plasma interaction . . . . .	26
2.2.1	General features of ion stopping . . . . .	26
2.2.2	Simple model of ion stopping in plasma . . . . .	32
2.2.3	Beam-plasma interaction . . . . .	38
2.2.4	Approaches to ion stopping power . . . . .	41
2.2.5	Unified stopping description in plasma . . . . .	44
2.2.6	Summary on ion stopping in plasma . . . . .	47
<b>3</b>	<b>Theoretical modeling</b>	<b>51</b>
3.1	Suited beam-plasma configuration . . . . .	51
3.1.1	Previous experiments at stopping maximum in plasma . . . . .	52
3.1.2	Plasma target . . . . .	53
3.1.3	Projectile ions . . . . .	59
3.2	Theoretical predictions . . . . .	63
3.2.1	Parameters of the interaction . . . . .	65
3.2.2	Stopping power . . . . .	66
3.2.3	Range in plasma . . . . .	69
3.2.4	Energy loss . . . . .	70
3.3	Relevance to Inertial Confinement Fusion . . . . .	76
3.3.1	Characteristics of alpha-particle stopping in ICF . . . . .	76
3.3.2	Stopping-power estimations for alpha particles in ICF . . . . .	77
<b>4</b>	<b>Experimental setup</b>	<b>79</b>
4.1	Existing setup at the Z6 experimental area . . . . .	79
4.1.1	The UNILAC accelerator . . . . .	79
4.1.2	The PHELIX and <i>nhelix</i> laser systems . . . . .	81
4.1.3	TOF measurements with CVD-diamond detectors . . . . .	88
4.1.4	Ion-stopping experiments at Z6 . . . . .	90
4.2	Setup for measurements at stopping maximum . . . . .	92
4.2.1	Target design . . . . .	93
4.2.2	Detector design . . . . .	103
4.2.3	Detector screening . . . . .	112



4.2.4	Summary . . . . .	116
<b>5</b>	<b>Experimental results</b>	<b>121</b>
5.1	First experimental campaign . . . . .	121
5.1.1	Adjustment of the experiment . . . . .	121
5.1.2	Calibration of the experiment . . . . .	122
5.2	Experimental results . . . . .	124
5.2.1	Principle of the measurements . . . . .	124
5.2.2	Data analysis . . . . .	127
5.2.3	Energy-loss results . . . . .	133
5.3	Comparison with theory . . . . .	136
<b>6</b>	<b>Conclusions and perspectives</b>	<b>139</b>
6.1	Conclusions of the work . . . . .	139
6.1.1	Thesis results . . . . .	139
6.1.2	Setup optimization for further experiments . . . . .	140
6.1.3	Questioning the projectile charge state . . . . .	141
6.2	Outlook: nonlinear regime of ion stopping . . . . .	142
6.2.1	Aiming for the nonlinear regime of ion stopping . . . . .	143
6.2.2	Preliminary work . . . . .	144
	<b>Bibliography</b>	<b>157</b>
	<b>List of publications and communications</b>	<b>158</b>

# List of Figures

1.1	Principle of indirect heavy-ion fusion . . . . .	4
1.2	Principle of proton fast ignition . . . . .	4
1.3	Stopping maximum and Bragg peak . . . . .	6
2.1	Characteristic regions of the laser-plasma interaction . . . . .	21
2.2	Principle of the resonant plasma absorption mechanism . . . . .	23
2.3	Velocity regimes of ion stopping in matter . . . . .	28
2.4	Charge-exchange processes of a projectile ion interacting with cold matter . . . . .	29
2.5	Chandrasekhar temperature coupling parameter $G$ as a function of $\frac{v_p}{v_{th}}$ . . . . .	35
2.6	Additional charge-exchange processes of a projectile ion interacting with plasma . . . . .	36
2.7	Schematic representation of the Coulomb interaction between a projectile ion and a plasma electron . . . . .	39
2.8	Regimes of the projectile-plasma interaction . . . . .	41
2.9	Impact-parameter domains of the various stopping theories . . . . .	45
2.10	Domains of applicability of the various stopping theories . . . . .	47
2.11	Comparison of existing stopping theories with numerical simulations by D. Gericke . . . . .	48
3.1	Comparison of RALEF2D plasma-density profiles with interferometric measurements at different times . . . . .	54
3.2	Comparison of RALEF2D plasma-density profiles with different interferometric measurements at a given time . . . . .	54
3.3	Plasma conditions obtained at times of 3, 7 and 13 ns after beginning of laser irradiation according to the RALEF2D code . . . . .	57
3.4	Plasma charge-state distribution for electron densities of $10^{20} \text{ cm}^{-3}$ and $10^{21} \text{ cm}^{-3}$ , as a function of the plasma temperature . . . . .	58
3.5	Charge-state distributions of carbon projectile ions at an energy of 0.5 MeV/u entering a plasma of electron density $10^{20} \text{ cm}^{-3}$ and $10^{21} \text{ cm}^{-3}$ , as a function of the plasma temperature . . . . .	62
3.6	Charge-state distributions of carbon projectile ions at an energy of 0.5 MeV/u entering the plasma at $t = 3, 7$ and $13$ ns after beginning of laser irradiation . . . . .	64
3.7	Comparison of various theoretical stopping-power predictions for $C^{6+}$ projectile ions interacting with a $10^{21} \text{ cm}^{-3}$ density and 200 eV temperature plasma as a function of the projectile energy . . . . .	68
3.8	Comparison of the ranges of $C^{6+}$ projectile ions penetrating a plasma at $10^{21} \text{ cm}^{-3}$ electron density and 200 eV electron temperature, according to various stopping theories . . . . .	70
3.9	Principle of the theoretical energy-loss calculations . . . . .	71
3.10	Stopping-power profiles as a function of the target areal density at $t = 3, 7$ and $13$ ns after beginning of laser irradiation . . . . .	74
3.11	Comparison of theoretical energy losses for the experimental case . . . . .	75

3.12	Comparison of various theoretical stopping-power predictions for alpha particles in the igniting ICF fuel as a function of the projectile velocity . . . . .	77
4.1	Scheme of the UNILAC accelerator of GSI . . . . .	80
4.2	Temporal bunch structure of the UNILAC accelerator of GSI . . . . .	81
4.3	Scheme of the PHELIX laser system . . . . .	83
4.4	Scheme of the <i>nhelix</i> laser system . . . . .	85
4.5	Scheme of the multi-frame interferometry setup . . . . .	87
4.6	Scheme of the time shift of ion micro-bunches due to an increase of the ion energy loss in plasma. . . . .	88
4.7	Working principle of a CVD-diamond charged-particle detector . . . . .	89
4.8	Setup of previous energy-loss experiments with two-sided laser irradiation at Z6 .	91
4.9	Comparison of the stopping power of carbon ions in solid carbon according to the TRIM and GEANT4 codes . . . . .	94
4.10	Mean energy of projectile ions exiting the decelerating foil as a function of the foil thickness . . . . .	95
4.11	Distributions of energy for a mean projectile energy of 0.5 MeV/u exiting the decelerating foil, as estimated with the TRIM and GEANT4 codes . . . . .	96
4.12	Distributions of angle for a mean projectile energy of 0.5 MeV/u exiting the decelerating foil, as estimated with the TRIM and GEANT4 codes . . . . .	97
4.13	Transversal profile of the areal density of the plasma as a function of time . . . .	99
4.14	Test experiment to determine the minimum distance between the decelerating target and the plasma target . . . . .	101
4.15	Transversal plasma and ion-bunch profile at plasma position in the experiment .	102
4.16	Photograph of the target setup with a scheme of the incoming ion and laser beams	104
4.17	Scheme of the effect of the angular ion-beam divergence on the ion time-of-flight	105
4.18	Overlapping of the ion signals on the detector for different TOF distances, for a 108 MHz and for a 36 MHz bunch frequency respectively . . . . .	106
4.19	Penetration range of projectile ions at various initial energies in the diamond detector	108
4.20	Ion-beam profile at detector position . . . . .	109
4.21	Scheme of the metalized diamond-detector plate . . . . .	110
4.22	Transversal profile of TOF differences of the projectile ions in plasma due to the plasma areal-density profile . . . . .	111
4.23	Photographs of the complete detector design . . . . .	112
4.24	Graph showing the influence of electromagnetic radiation resulting from the laser-plasma interaction on the detector signals . . . . .	114
4.25	Simulated plasma-emission spectrum and transmission of the filter foil . . . . .	115
4.26	Photograph of the isolating vacuum flange developed for the electric screening of the detector . . . . .	116
4.27	Representation of the detector and screening system . . . . .	117
4.28	Experimental setup for the ion-stopping measurements at stopping maximum in plasma . . . . .	118
5.1	Photograph of the new design of decelerating target implemented in the calibration process . . . . .	122
5.2	Photograph of the plasma taken with a digital camera . . . . .	123
5.3	Photograph of the focus-spot profile of the PHELIX laser beam . . . . .	123
5.4	Example of measured detector signals in the experiment . . . . .	125
5.5	Illustration of the data-analysis method on measured detector signals . . . . .	128
5.6	Temporal evolution of the ion energy loss in both targets over the duration of a macro-bunch . . . . .	129

5.7	Examples of measured detector signals featuring additional uncertainties in the energy-loss determination . . . . .	130
5.8	Detector signal of the X-ray pulse coming from the plasma emission . . . . .	131
5.9	Principle of the determination of the experimental time resolution . . . . .	133
5.10	Measured ion time shifts caused by the energy loss in the plasma target . . . . .	134
5.11	Measured ion energy loss in MeV . . . . .	135
5.12	Measured energy loss normalized to its value in the solid state . . . . .	135
5.13	Comparison of the measured energy loss with theoretical predictions . . . . .	136
5.14	Comparison of the theoretical stopping powers to the experimental data for the point at $t = 10.5$ ns . . . . .	138



# Chapter 1

## Introduction

The interaction of ions with matter has been investigated for one century, since this subject was addressed for the first time in the pioneering work of Bohr on the deceleration of alpha particles in matter in 1913 [Boh13]. Since then, numerous theoretical, experimental and numerical investigations have been carried out worldwide in order to understand and precisely quantify the energy deposition of charged particles in matter. While ion stopping in cold matter is now relatively well-known and has been characterized with the help of numerous experimental data [Pau], a lot of interrogations remain when it comes to ion stopping in ionized matter, i.e in a plasma. There, a complete theoretical description remains particularly challenging and only few experimental data have been gathered so far. Ion interaction with a plasma is however a topic of major importance for several fields of modern physics. It plays a central role in plasma physics and in particular in the realization of the Inertial Confinement Fusion (ICF) concept.

### 1.1 Applications of ion stopping in plasma

#### Ion stopping in Inertial Confinement Fusion

In ICF, a small pellet of an equimolar mixture of cryogenic deuterium and tritium (DT) fuel is heated, directly or indirectly, by several driver beams. The latter are typically high-energy laser beams, enabling to reach a huge target temperature and density in the resulting hydrogen plasma. In the frame of ICF, two main points motivate the study of the ion-plasma interaction. A first motivation is the use of ion beams as an alternative driver to the laser beams. The ion energy-deposition profile in matter is indeed advantageous due to its typical peaked energy deposition at the end of the ion range (the so-called *Bragg peak*, see Fig. 1.3). This enables an important and localized energy deposition, which is also highly valued e.g for tumor therapy.

- **Heavy-ion fusion**

Ion beams can play the role of a primary driver either in the direct heavy-ion fusion scheme [LPB08] or in the more extensively studied indirect heavy-ion fusion scheme [HHT95, CT99]. In the first case, intense ion beams directly impinge on the DT target in order to compress and heat it to reach the ignition. In the second case, the ion beams interact with a converter target (hohlraum), generating intense X-rays that heat the DT target homogeneously, as shown in Fig. 1.1.

- **Ion-driven fast ignition**

In addition, ion beams can be used as a secondary driver in ICF, in the so-called Fast-Ignition (FI) scheme. There, the compression phase and the heating phase of the target are decoupled from each other and carried out in two distinct successive steps. First, the pellet is compressed by using multi-hundred kiloJoule energy and nanosecond duration

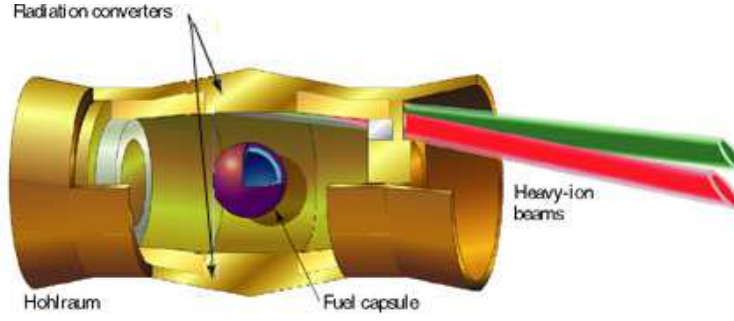


Figure 1.1: Principle of heavy-ion fusion in its indirect scheme (from [Tab]).

laser beams. Subsequently, when the DT has reached its maximum compression (stagnation state), a secondary much shorter laser beam, with picosecond duration, is employed to trigger an intense and ultrashort ion beam that in turn heats the dense target and potentially brings it to ignition. The most popular variant for ion FI is proton FI, where an intense proton beam is accelerated by using the secondary laser beam, either in the DT pellet itself (in-situ) [TSR<sup>+</sup>10] or from an external target located in the vicinity of the DT pellet [RCK<sup>+</sup>01, Tem06] as shown in Fig. 1.2. Alternatively, carbon ion beams [FHA<sup>+</sup>09, HFT<sup>+</sup>10], or even heavier ion projectiles [DPM11], can be used. Ion-driven FI offers a promising alternative to the previously developed and still highly challenging FI scheme using fast electrons [THG<sup>+</sup>94].

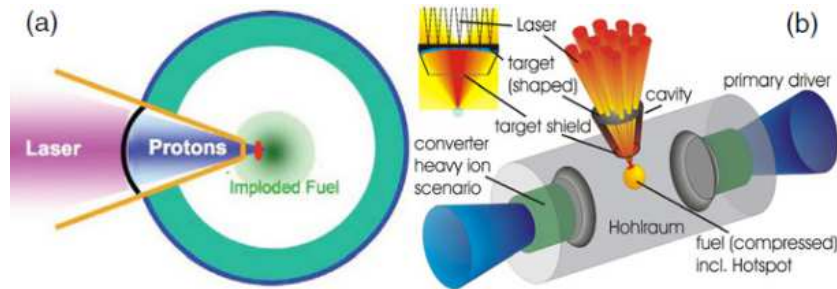
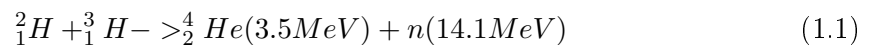


Figure 1.2: Principle of ion-driven fast ignition by using a proton beam from an external target (from [FHA<sup>+</sup>09]), with a direct (a)) or indirect (b)) fuel heating by the primary beams.

### • Alpha-particle heating

The second main motivation, which is even more important, because it is inherent to any fusion scheme, is the alpha-particle heating of the ICF fuel. When thermonuclear fusion reactions are triggered in the hot dense DT fuel, alpha particles  ${}^4_2\text{He}$  are created, in the reaction:



These alpha particles play a key role as they heat in turn the surrounding colder and denser plasma medium, enabling the fusion burning wave to propagate and self-sustain. The efficiency of the alpha-particle heating therefore determines the yield of the fusion process to a large extent [DLTB95, OAM96, HLS<sup>+</sup>00].

Be it for ion-driven fusion and ion-driven fast ignition or for fuel heating by alpha particles

in the burning fusion plasma, the precise understanding of the energy-deposition mechanisms of ions in plasma is of paramount importance for the modeling and the control of the whole fusion process.

### **Ion stopping in high-energy-density physics**

Furthermore, besides fusion, ion stopping in plasma plays an important role in high-energy-density physics in general. One application concerns electron-cooling systems [Pot90, WBB<sup>+</sup>97], where very cold electron plasmas are employed as a stopping medium to reduce the emittance of heavy-ion beams in storage rings.

Another application lies in the target response to intense heavy-ion beams used in modern accelerator infrastructures like the LHC or the future FAIR facility [TSS<sup>+</sup>12]. There, the dimensioning of efficient beam dumps for the ion beams requires, in particular, a good knowledge of the ion-stopping process. Still in the frame of accelerator physics, plasmas can also serve as ion strippers or ion focusing lenses, which as well requires a fine understanding of the ion-plasma interaction. The knowledge of the ion-stopping mechanisms is also crucial for the precise dimensioning and the interpretation of experiments investigating the equation of state of dense matter [HBF<sup>+</sup>00, THK<sup>+</sup>01], in particular involving the generation and the diagnostic of the warm-dense-matter state. Ion stopping also plays a major role in the proton or ion radiography of dense plasmas [WSS<sup>+</sup>97, GBF<sup>+</sup>98]. Similarly, it can be used for the diagnostic of the areal density, the implosion symmetry and the yield of a fusion plasma [HLS<sup>+</sup>00, LP95].

Finally, ion stopping is highly relevant for astrophysical phenomena, where plasma is the basic state of matter. For example, the transport and interaction of cosmic-ray particles [Fer98], the stellar transport or the famous r-process in nucleosynthesis require a precise understanding of the ion-stopping mechanisms in plasma.

## **1.2 Description of the physical case**

### **Physical case of ion stopping in plasma**

Meanwhile, the understanding of ion stopping in plasma still remains challenging. Even in cold matter, no full theoretical description is available and some uncertainties are still present. Such a description indeed needs to be developed on the microscopic level and to take all the relevant atomic-physics processes into account, which has not been achieved until now. Therefore most calculations have to be based on approximate data tables or semi-empirical approaches. In plasma, the interaction of projectile ions is even more complex as it involves numerous different parameters and phenomena, particularly due to the additional presence of free electrons. Very different and quickly varying plasma density, temperature and ionization conditions can arise within the projectile-plasma interaction, leading to very different ion stopping behaviors. Notably, both short-range plasma interactions (collisions) and long-range interactions (collective effects) have to be treated to obtain a complete physical picture. A particularly significant quantity, whose precise correlation with the stopping power is still not well established, is the charge-state value of the projectile in the plasma, which in turn is closely linked to the atomic cross sections of the charge-transfer processes and thus depends closely on the plasma parameters. Depending on the projectile and plasma characteristics, and especially on the ion-plasma coupling and the relative amount of collisional and collective phenomena involved, different theoretical descriptions of the ion stopping power exist. Therefore, to date, a unified picture of the ion-stopping process in plasma remains a very difficult task.

The interaction between ions and plasma is now pretty well understood for a high projectile ion velocity  $v_p$ . This velocity is most adequately measured in units of the thermal velocity of the free plasma electrons  $v_{th}$ . Hence, for  $\frac{v_p}{v_{th}} \gg 1$ , the energy deposition of the ions in plasma can be described by a simple Bethe formula, relating to another pioneering work conducted by Bethe



in the early thirties [Bet30, Bet32]. But when reducing the projectile velocity, effects like close collisions and plasma polarization start gaining importance in the stopping process, and adapted correction terms are needed. However, when the projectile ion velocity reaches the parameter region  $\frac{v_p}{v_{th}} \approx 1$ , the theoretical description of the ion stopping power becomes very difficult because of the various phenomena involved. This is the region of maximum stopping power, sometimes improperly referred to in the literature as "Bragg peak" or featuring a "Bragg-peak velocity". As the term "Bragg peak" usually designates the peak of energy deposition as a function of the ion range in matter, the parameter region of interest in this work is simply called "stopping maximum" (see Fig. 1.3).

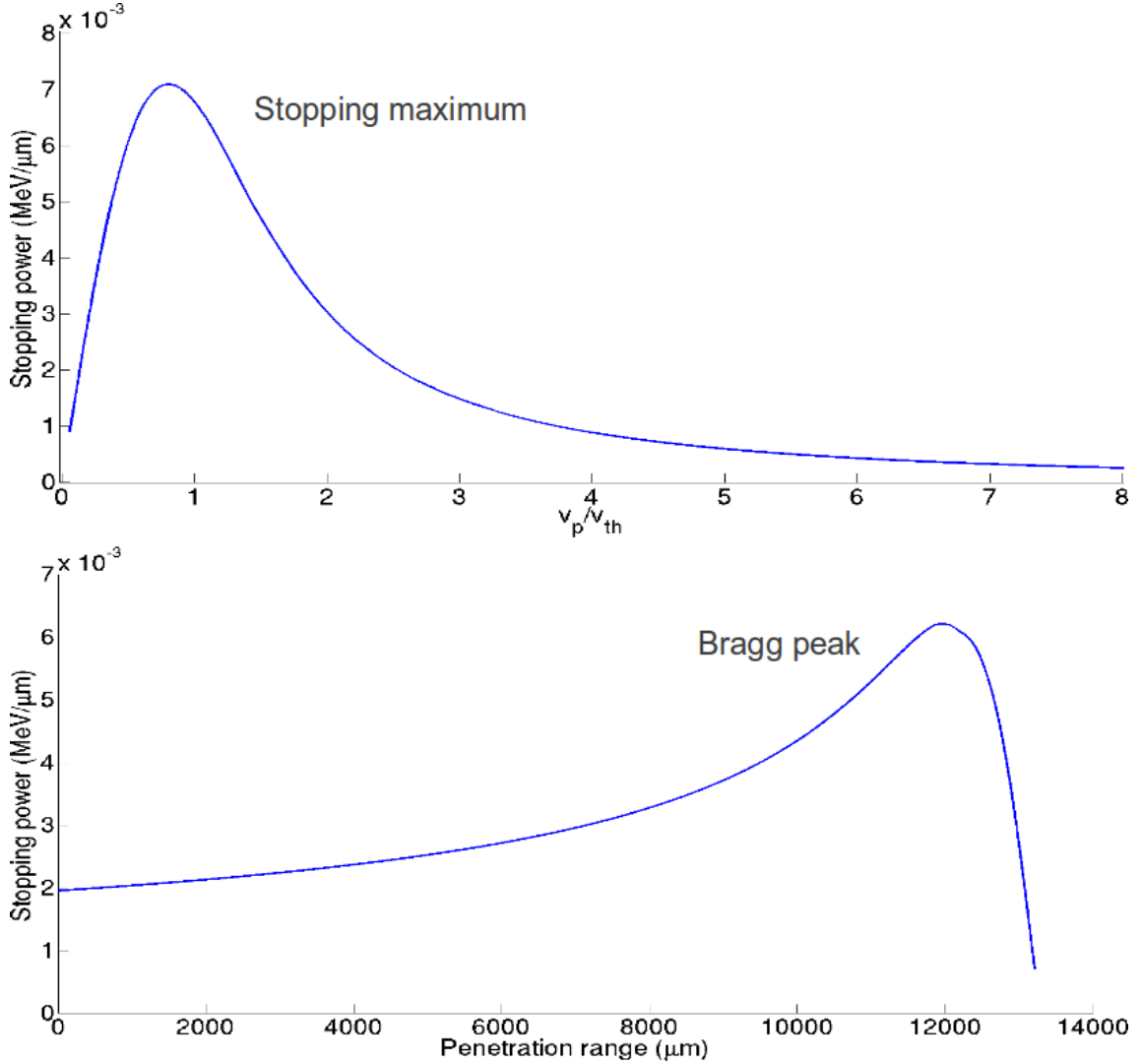


Figure 1.3: Top: curve of the ion stopping power in plasma as a function of the projectile velocity, featuring a maximum at  $\frac{v_p}{v_{th}} \approx 1$  designated as *stopping maximum* that is the object of this thesis. Bottom: curve of stopping power as a function of the ion penetration range in matter, featuring a maximum resulting from the existence of the stopping maximum and called *Bragg peak*.

Close to this stopping maximum, the projectile ions thus have a velocity of the same order of magnitude as the thermal velocity of the free plasma electrons. In that velocity regime, both close particle collisions and collective plasma oscillations are expected to significantly contribute to the stopping power, and the projectile charge state is likely to feature an important nonequilibrium behavior [PM91b]. Moreover, the Coulomb coupling between the projectile and the plasma

electrons is maximal [HLS<sup>+</sup>00], hence the interaction cannot necessarily be described in the frame of perturbation theory.

While in the high-velocity regime all the different theoretical descriptions agree pretty well with each other, in the velocity regime of stopping maximum important discrepancies arise between the available theoretical and numerical approaches [GS99, GS03]. Moreover, up to now, because of a difficult experimental access, very few measurements have ever been carried out at  $\frac{v_p}{v_{th}} \approx 1$  in a hot dense laser-generated plasma to our knowledge ([HLS<sup>+</sup>00]). While the general shape of the stopping curve and especially the presence of the maximum has been verified, the precision of the previous measurements did not allow to test the stopping theories individually. Yet the recently developed theories and numerical simulations strongly need experimental verification and benchmarking.

### Special importance of the maximum of the stopping curve

A reliable description of ion stopping at stopping maximum is highly needed as this part of the stopping curve has a major influence on the stopping process and on the final range of the projectile ions in the plasma target. This problematic is also highly relevant in cold matter, where the stopping-power maximum is reached for a projectile velocity close to the velocity of the bound target electrons, i.e approximately the Bohr velocity  $v_0$ . There as well, a precise and complete understanding of the stopping-power maximum is still missing, depending on the projectile and target species. Yet it has a major importance e.g for the control of the Bragg peak in ion radiotherapy applications.

In the plasma case, the maximum of the stopping curve is of key importance for ICF, where the alpha particles are generated at an initial energy of 0.875 MeV/u by the DT fusion reactions. Therefore, the velocity of the alpha particles lies around or below the stopping maximum over a large part of their trajectory in the dense plasma, depending on the plasma temperature. A slight difference in the stopping power at stopping maximum for the alpha particles can thus lead to significant modifications in their final range in the burning fuel, and consequently on the yield of the fusion reaction.

A precise description of this stopping region is also particularly important in ion-driven FI, notably because of the phenomenon of *range lengthening* of the intense laser-accelerated proton or carbon beams in plasma [HFT<sup>+</sup>09]. Due to the very high beam intensities involved, the plasma can be significantly heated by the ion energy deposition, which influences the subsequent energy deposition, modifying the range of the ions in the plasma. This mechanism is expected to play a major role around the region of stopping maximum, when the thermal electron velocity of the heated plasma matches the velocity of the projectile ions. For all these reasons, an experimental characterization of the stopping process around the stopping-power maximum is of considerable interest.

Particularly challenging is the understanding of ion stopping at stopping maximum in a dense nonideal plasma. There, strong coupling effects play an important role in the interaction and complicate even more the physical picture [Zwi99]. Strong coupling is present, at least at the initial times of the interaction, in all of the applications mentioned above. Then, the correlations between the ion beam and the plasma are particularly important and the interaction is expected to feature nonlinear effects, and notably a modified charge dependence of the stopping power. The discrepancies between the theoretical predictions then become even more dramatic.

## 1.3 Context of the work

The main purpose of the present work is to obtain the first precise experimental energy-loss data at stopping-power maximum in a hot laser-generated plasma. In this way, the existing theories and numerical codes can be tested and benchmarked. This contributes in developing a more

precise modeling of the ion energy-deposition process, which is particularly useful for improving ICF simulation codes.

The theoretical and computational part of the work was carried out at Centre Lasers Intenses et Applications (CELIA) at Université Bordeaux 1 under the aegis of Commissariat à l'Energie Atomique. The present work is indeed relevant to the upcoming ICF-related activities in the next years at the Laser Mégajoule facility.

The experimental part of the work was conducted at the only scientific infrastructure worldwide enabling combined experiments using swift pulsed ion beams and high-energy laser beams: the GSI Helmholtzzentrum für Schwerionenforschung GmbH in Darmstadt, Germany. At the experimental area Z6 of GSI, a hot dense plasma can be generated by the single-shot laser irradiation of a thin solid target foil, while being probed by a high-frequency pulsed ion beam from a heavy-ion accelerator. The time-of-flight (TOF) method is applied for determining the energy loss of the projectile ions in the plasma, by using fast time-resolved charged-particle detectors. This makes the experimental area Z6 unique for ion energy-loss experiments in plasma. In fact, an important part of the experimental history of ion stopping in plasma has been written there in the last 25 years. The group "Laser and plasma physics" of Technische Universität Darmstadt (TUD), for which energy-loss experiments have always been a central research topic, is now a world leader in the field. Yet before the present study in the regime  $\frac{v_p}{v_{th}} \approx 1$  in a hot laser-generated plasma could be considered, a long history of successive experimental improvements was necessary.

## Historical perspective

### • Discharge plasma

In the early 90s at GSI, cold hydrogen plasma was generated either by electric discharge or by pinched gas discharge. This enabled to access to relatively low electron densities of up to  $10^{17} \text{ cm}^{-3}$  and  $10^{19} \text{ cm}^{-3}$  respectively, while electron temperatures of a few eV were reached. A significant increase of the energy loss of ions in plasma was observed [HWW<sup>+</sup>90, DHB<sup>+</sup>92].

First experiments investigating the stopping maximum in plasma were carried out for heavy ions interacting with a fully ionized hydrogen plasma [JHL<sup>+</sup>95, JBF<sup>+</sup>96], where the energy-loss enhancement appeared to be dramatic. Along with previous ion-stopping experiments, the corresponding energy-loss data could be interpreted in the frame of a simple stopping model based on an extension of the Bethe formalism for ion stopping in cold matter: the standard stopping model (SSM). Yet, uncertainties about the projectile charge-state value did not make it possible to test different theoretical predictions.

### • Laser plasma

To access regimes of higher temperature and higher density that are relevant to ICF, experiments using laser-generated plasmas had to be carried out. This was first achieved in [CDN<sup>+</sup>94] by using a laser-ablated plasma expanding orthogonally to the ion beam. Yet this plasma remained limited to electron-density values below  $10^{19} \text{ cm}^{-3}$  and electron temperatures of a few tens eV.

In order to obtain a denser and hotter plasma, the high-energy laser system *nhelix* was commissioned at GSI in the late 90s for ion-stopping experiments with a plasma expansion along the ion-beam axis. By using *nhelix* at parameters of up to 100 J energy, 15 ns pulse length and 1-2 mm focus spot size, plasmas with electron densities of  $10^{20-21} \text{ cm}^{-3}$  and temperatures of 60-100 eV were generated [Rot97, RSS<sup>+</sup>00]. However, the plasma was quite inhomogeneous and partially ionized, making the interpretation of the results difficult. In particular, a time-resolved charge-state measurement was missing, leaving an uncertainty on the ion charge state in plasma. New experimental capabilities and theoretical modeling tools, beyond the SSM, were therefore needed in order to progress in the understanding of the stopping process.

Meanwhile, first experiments at stopping maximum in a laser-generated plasma were carried out at the OMEGA laser facility [HLS<sup>+</sup>00] by measuring the energy loss of fusion products in a hot dense plasma by means of a spectroscopic method. For the first time, the presence of the maximum was confirmed experimentally, and the measurements were in qualitative agreement with the various stopping theories. However, the energy resolution did not allow to quantitatively test the stopping models and to determine which one is most precise.

- **Laser plasma with upgraded tools**

At GSI, stopping experiments with the *nhelix* laser were continued at the end of the years 2000 [FBG<sup>+</sup>10]. They benefited from upgraded laser parameters and thus higher electron temperatures and densities, as well as from newly developed time-resolved CVD-diamond detectors and from the backup of more advanced theoretical tools based on a microscopic interaction model. But still, the plasma was inhomogeneous because of the one-sided laser irradiation and its parameters were not perfectly controlled. A better understanding of the interaction was nevertheless reached. In 2011, the newly built high-energy laser system PHELIX became available with the  $2\omega$  option at Z6. This has allowed, combining the *nhelix* and PHELIX laser systems, with direct two-sided laser heating using the frequency-doubling option, at 30 J beam energy, 7 ns pulse length and 1 mm focus spot diameter, to generate hot plasmas with an electron density of up to  $10^{21} \text{ cm}^{-3}$  and an electron temperature of up to 200 eV. In conjunction with this upgraded laser-heating scheme, new advanced hydrodynamic plasma simulations [TBF<sup>+</sup>13] as well as new time-resolved plasma diagnostics [BFF<sup>+</sup>12] were developed, and a new time-resolved TOF charge-state spectrometer [CFS<sup>+</sup>13] for ion detection was implemented. Following these upgrades, a fully-ionized homogeneous plasma can now be generated in a systematic way and completely characterized. The improved setup enabled highly precise stopping measurements, while the new numerical capabilities combined with an advanced microscopic theoretical modeling allowed a complete interpretation of the results. In this way, significant improvements in the understanding of the ion energy loss in a hot laser-generated plasma have been reached [FBB<sup>+</sup>13].

The plasma used in this latter work appears to be well-suited as a test bed for precise ion-stopping measurements as it can be systematically generated and is homogeneous and completely characterized. Hence, energy-loss experiments can now be carried out by keeping the same plasma parameters and modifying the ion parameters. Until now, all the measurements at Z6 had been carried out with ions at high or intermediate energies ( $\geq 4 \text{ MeV/u}$ ). Following the progress achieved in the past years, the beam parameters can now be adapted, within a new specific setup, to investigate the velocity regime of maximum stopping power in a laser-generated plasma.

And for the first time, the combination of (i) advanced stopping theories, (ii) advanced plasma simulations, (iii) precise experimental plasma and ion diagnostics, implemented in a suited beam-plasma configuration, makes it possible to *test* the various theoretical models. In this work, this new setup is developed and tested, and the obtained energy-loss data are analyzed and compared with theory.

## Structure of the thesis

The goal of the thesis is to provide experimental energy-loss data at maximum stopping power and to compare it with different theoretical predictions. Comparing different stopping-power theories requires a precise understanding of the mechanisms involved in the stopping process, in order to estimate the physical relevance and the domain of applicability of each of them. For this purpose, a quite detailed and complete description of the ion-plasma interaction is necessary, as well as of the underlying fundamental plasma-physics phenomena and parameters.

Therefore, chapter 2 is devoted to a detailed description of the theoretical basis required for this

work. It first deals with general plasma physics and laser-plasma interaction, and then addresses the interaction of ions with plasma. The important features of ion stopping are described and a summarized state-of-the-art of the modern stopping-power theories and models is presented.

After this general theoretical chapter, chapter 3 presents the specific modeling of an experiment by using the concepts and the theories described previously. A beam-plasma configuration for ion-stopping experiments at maximum stopping power is first defined, and the corresponding plasma, projectile and stopping properties are simulated.

In chapter 4, the experimental setup for the described configuration is presented. It starts with the existing scientific infrastructure at the Z6 experimental area of GSI, including the accelerator system, the high-energy laser systems and the usual laser and ion diagnostics. Then, the new setup for measurements of ion stopping at stopping maximum is addressed. The used target configuration and the new CVD-diamond TOF detector as well as its screening system are presented.

Subsequently, in chapter 5, the experimental results obtained in the first campaign are described and compared with the existing stopping theories. Finally, in chapter 6, a general conclusion of the thesis is drawn, and an outlook is proposed with future work perspectives.

# Chapter 2

## Theoretical basis

In this chapter, the important physical notions that are necessary in this work are presented. Its goal is to provide a detailed theoretical understanding of the ion-plasma interaction, which is required for the simulations conducted in chapter 3 and for the comparisons of experimental data with theory in chapter 5.

Before coming to the ion-plasma interaction that is the topic of this thesis, the plasma itself as well as its important parameters and properties have to be described. Therefore, in a first part an introduction to plasma physics is presented, where the important plasma properties and characteristics are highlighted. On this basis, the key processes and features of a laser-generated plasma are explained. In a second part, the interaction of ions with a plasma is addressed in details and an overview of the theory of ion stopping in plasma is presented.

### 2.1 Laser-plasma interaction

In this work, a hot and dense laser-induced plasma is used for energy-loss measurements, with a nearly  $10^{21} \text{ cm}^{-3}$  electron density and 200 eV electron temperature. This is motivated by applications in ICF where lasers are the main drivers. Compared to ICF where the electron density reaches  $10^{23}$ - $10^{27} \text{ cm}^{-3}$ , the considered plasma is significantly less dense. However, its temperature is typical of the compressed ICF fuel and it is thus relevant for HIF, FI and alpha-particle stopping, the latter point being discussed in details in 3.3. Moreover, as is shown in next chapter, it is possible to create a laser-induced plasma with nearly uniform conditions for a sufficient time span, that is well-suited for ion-stopping experiments and for a test of the theories.

Now, the theory of a laser-generated plasma is presented. The main plasma parameters and properties are estimated for two distinct cases: for the plasma of this work with  $n_e = 10^{21} \text{ cm}^{-3}$  and  $T_e = 200 \text{ eV}$ , and for a plasma relevant to alpha-particle stopping in ICF with  $n_e = 10^{26} \text{ cm}^{-3}$  and  $T_e = 200 \text{ eV}$ .

#### 2.1.1 Plasma physics fundamentals

The goal of this section is essentially to introduce and to explain the role of the plasma parameters that will be useful in this work. All physical quantities in the theoretical part of this work are expressed in the cgs unit system (centimeter, gram, second), while numerical values are given in SI base units.

A plasma is defined as a gas in which at least a part of the atoms have been ionized. It is thus constituted of a mixture of positively charged ions, negatively charged free electrons and eventually neutral species. In a plasma, the motion of the charged particles is mostly caused by the local electric and magnetic fields. Yet, the latter fields themselves are generated by the motion of the charged particles. This coupled process makes the description of the plasma dynamics

particularly complex.

From a global point of view, a plasma can be seen as electrically neutral because of the mutual screening of the electric potential of the ions and of the free electrons. However, locally, the existing electric fields between the species can lead to spatially limited charge fluctuations. Therefore, locally, a plasma cannot be considered as neutral, the term of *quasi-neutrality* is employed instead. In the following, assimilating the plasma to a two-component fluid, composed of free electrons of mass  $m_e$  and ions of mass  $m_i$ , the mean parameters electron density  $n_e$  and ionic density  $n_i$ , electron temperature  $T_e$  and ion temperature  $T_i$  as well as mean ionization degree  $Z_T$  can be defined.

### Plasma statistics

The plasma electrons can be assumed to follow a Maxwell-Boltzmann energy distribution function as long as their temperature  $T_e \gg T_F$ , where  $T_F$  is the Fermi temperature, or equivalently if their kinetic energy  $E_k \gg E_F$  with  $E_F$  the Fermi energy. For a given electron system, the Fermi energy depends only on the electron density and can be expressed as:

$$E_F = \frac{1}{2}m_e v_F^2 = \frac{\hbar^2}{2m_e}(3\pi^2 n_e)^{\frac{2}{3}} \quad (2.1)$$

with  $v_F$  the associated Fermi velocity. When  $T_e \approx T_F$ , degeneracy effects start becoming significant (see also below) and the Maxwell-Boltzmann statistics cannot be applied for the plasma electrons anymore. A Fermi-Dirac statistics is needed instead. This is important in ICF where  $T_F \approx 800$  eV and  $T_e$  spans over a wide 50 eV-5 keV range. In contrast, for an electron density  $n_e = 10^{21} \text{ cm}^{-3}$  as considered in this work,  $T_F \approx 0.4$  eV, therefore in view of the plasma temperature of 200 eV, the Fermi term can be neglected and the Maxwell-Boltzmann statistics is valid. In this case, the mean kinetic energy of the nondegenerate free electrons can be written as

$$E_k = k_B T_e = m_e v_{th}^2 \quad (2.2)$$

with the electron thermal velocity

$$v_{th} = \sqrt{\frac{k_B T_e}{m_e}} \quad (2.3)$$

Strictly speaking,  $v_{th} = \sqrt{\frac{3k_B T_e}{m_e}}$  when considering the three-dimensional Maxwellian speed distribution of the electrons, and the expression 2.3 corresponds to the standard deviation of this distribution. Yet the simplified formula 2.3 is usually employed in the literature for stopping-power calculations, hence also in this thesis, unless otherwise indicated.

For a plasma in which the energy distribution function of the electrons follows a Maxwell-Boltzmann statistics and with the assumption of local thermal equilibrium (LTE), the charge-state distribution of the plasma ions can be described with the help of the Saha ionization law:

$$\frac{n_{Z+1}}{n_Z} = \frac{1}{4\pi^{\frac{3}{2}}} \frac{Q_{Z+1}(T_e)}{Q_Z(T_e)} \left( \frac{k_B T_e}{I_H} \right)^{\frac{3}{2}} \frac{1}{n_e a_0^3} \exp \left( -\frac{I_Z}{k_B T_e} \right) \quad (2.4)$$

There,  $n_Z$  represents the density of plasma ions carrying the charge state  $Z$ ,  $Q_Z$  is the statistical partition function of the ions in the charge state  $Z$ ,  $I_H$  is the ionization energy of hydrogen,  $I_Z$  is the ionization energy associated with the charge state  $Z$ , and  $a_0$  is the Bohr radius, i.e the most probable distance between the proton and the electron in a hydrogen atom within the Bohr atomic model, given by:

$$a_0 = \frac{\hbar^2}{m_e e^2} \quad (2.5)$$

### Plasma characteristic lengths

A few characteristic lengths can be defined in a plasma, that play an important role in the characterization of plasma interactions or of the interaction between an external beam and a plasma. Indeed, due to the nature of the plasma and especially because of the property of quasi-neutrality, different types of particle interactions can take place depending on the considered length scale.

Locally, particle collisions (Coulomb scattering) are the relevant process, while on a larger spatial scale, collective plasma effects can arise. The hierarchy of the characteristic lengths also makes it possible, in addition of describing the collisional and collective aspects of the plasma interactions, to estimate the strength of the interaction between two particles in the plasma.

- **Wigner-Seitz radius**

The mean distance  $a$  between two plasma electrons is called Wigner-Seitz radius and depends on the electron density:

$$a = \left( \frac{4\pi n_e}{3} \right)^{-\frac{1}{3}} \quad (2.6)$$

A similar distance can also be defined for plasma ions. For ICF plasmas  $a \approx 10^{-11}$  m, while it reaches  $6.2 \times 10^{-10}$  m in this work.

- **Landau length**

The Landau length  $r_0$  is the classical distance of minimum approach between two plasma electrons. It corresponds to the point where the electron kinetic and potential energies are equal:

$$m_e v_{th}^2 = k_B T_e = \frac{e^2}{r_0} \quad (2.7)$$

The Landau length can therefore be written as

$$r_0 = \frac{e^2}{m_e v_{th}^2} \quad (2.8)$$

Similarly, a generalized "Landau length" for the interaction of two particles  $\alpha$  and  $\beta$  in plasma with respective charges  $Z_\alpha$  and  $Z_\beta$  can be defined. If  $v_r = |v_\alpha - v_\beta|$  is the relative velocity of the considered particles and  $\mu = m_\alpha m_\beta / (m_\alpha + m_\beta)$  is the reduced mass of the interacting system of the two particles, the "Landau length"  $r_{\alpha\beta}$  is given by

$$r_{\alpha\beta} = \frac{Z_\alpha Z_\beta}{\mu v_r^2} \quad (2.9)$$

For  $T_e = 200$  eV,  $r_0$  can be estimated to  $7.2 \times 10^{-12}$  m.

- **De Broglie wavelength**

The De Broglie wavelength  $\lambda_r$  is the distance under which quantum diffraction effects start appearing in the interaction of two plasma particles  $\alpha$  and  $\beta$  and can be written as:

$$\lambda_r = \frac{\hbar}{\mu v_r} \quad (2.10)$$



A De Broglie wavelength can in particular be defined for the plasma electrons, called thermal plasma wavelength and expressed by:

$$\lambda_e = \frac{\hbar}{m_e v_{th}} \quad (2.11)$$

For a 200 eV plasma temperature,  $\lambda_e \approx 6 \times 10^{-12}$  m.

### • Screening length

A specificity of plasma that makes its theoretical description particularly difficult is the presence of collective effects. They arise due to the property of quasi-neutrality of the plasma: locally quite important electric fields can appear but globally the plasma stays electrically neutral. It means that if a local perturbation of the electric field occurs, e.g. by the interaction of an external projectile ion, the surrounding charged particles are re-distributed in a way that neutralizes the generated electric potential. Ions are screened by the electrons and conversely.

This fundamental plasma property is called screening, or shielding of the electric potential of a charged particle in plasma. It means that while the electric potential of a test charge in plasma can have a strong local influence, its influence range stays limited to a plasma region defined by the screening sphere. The radius of this sphere, called screening length  $\lambda$ , characterizes the range of an electric potential in plasma before it is screened by the surrounding particles. A typically used screening length is the *Debye length*, defined as

$$\lambda_D = \sqrt{\frac{k_B T_e}{4\pi e^2 n_e}} \quad (2.12)$$

The Debye length is the screening length of an ion carrying a charge  $Z_p$  with an electric potential  $\Phi(r) = \frac{Z_p e}{r} \exp(-\frac{r}{\lambda_D})$  (screened Coulomb potential). It corresponds to the simple case of a static (independent of the velocity of the screened particle) and linear screening. The latter condition means that the potential energy of the interaction between the considered plasma particles is small compared to their kinetic energy. The concept of Debye screening is thus only valid as long as the number of electrons in the Debye sphere  $N_D = \frac{4}{3}\pi n_e \lambda_D^3$  (sometimes called plasma parameter in the literature) is sufficiently large, i.e.  $N_D \gg 1$ . As is shown later in this section, this case corresponds to an ideal plasma. For example, in the plasma of this work,  $N_D \approx 800$ , hence  $\lambda_D$  is relatively large  $\approx 6$  nm. For a nonideal plasma, where  $N_D$  is small, no Debye length can be defined as the screening becomes nonlinear. This may be the case of an ICF plasma where  $\lambda_D \approx 2 \times 10^{-11}$  m and  $N_D \approx 2$ .

For an external particle interacting at a sufficiently high velocity  $v_p$  in the plasma, a dynamic screening length  $\lambda = \lambda(v_p)$  has to be considered.

### Characterizing the plasma interactions

By using the previously defined length scales, the interactions within the plasma can be quantified and characterized. For this purpose, several parameters are now defined. These are the plasma coupling parameter, the degeneracy parameter and the Coulomb logarithm, as well as the electron-ion collision frequency and the characteristic plasma frequency.

Plasma interaction processes that occur on a length scale larger than the screening length  $\lambda$  are collective effects, such as the excitation of plasmons or dynamic screening (see 2.2.2 or 2.2.4 for more details). Yet in the case of a strongly nonideal plasma where the screening length is very small (the electric potential of a particle is almost immediately screened), with  $\lambda < a$ , collective effects are defined for interaction distances larger than  $a$ . This in particular the case for dense

ICF plasmas. In contrast, interaction processes occurring over distances below the screening length are direct particle interactions, i.e particle collisions or Coulomb scattering.

The distance between two interacting particles, that determines which kind of effect is dominant, is the *impact parameter*  $b$  of the interaction.

- **Plasma coupling parameter**

The plasma coupling or nonideality parameter, measuring the strength of electron-electron correlations or of the electron-electron coupling in plasma, is given by

$$\Gamma = \frac{e^2}{ak_B T_e} = \frac{1}{3} \left( \frac{a}{\lambda} \right)^2 \quad (2.13)$$

Hence  $\Gamma$ , quotient of the potential interaction energy of the electrons  $\frac{e^2}{a}$  over their thermal, kinetic energy  $k_B T_e = m_e v_{th}^2$ , is also directly related to the quotient of two fundamental plasma length scales: the Wigner-Seitz radius  $a$  and the screening length  $\lambda$ .

For  $\Gamma \ll 1$ , the kinetic energy of the electrons dominates over their potential energy, which means that the plasma is ideal, collisionless and dominated by long-range collective plasma effects. Then,  $N_D \gg 1$  and the Debye length is well-defined and relatively large. This is the case for the plasma of this work, where  $\Gamma \approx 0.01$ . In contrast, from  $\Gamma > 0.1$ , the plasma is said to be moderately nonideal, i.e the effect of inner plasma collisions cannot be neglected, and for  $\Gamma > 1$ , the plasma is nonideal, dominated by collisions between the electrons. For a strongly nonideal plasma,  $N_D$  becomes small and the concept of Debye screening becomes ill-defined; plasma collisions are preponderant over collective effects. In the dense ICF plasma taken as example,  $\Gamma \approx 0.5$ , indicating nonideality.

A similar coupling parameter can be defined to characterize the strength of the correlations between electrons and ions in the plasma and is noted  $\Gamma_{ei}$ , while the notation  $\Gamma$  designates strictly speaking  $\Gamma_{ee}$ . The expression given for  $\Gamma$  is however only valid as long as the considered plasma is nondegenerate. The concept of degeneracy, already mentioned at the head of this chapter, is now explained.

- **Plasma degeneracy**

The plasma degeneracy degree measures the influence of the Pauli exclusion rule on the target electrons and is quantified by the parameter  $\Theta$ :

$$\Theta = \frac{k_B T_e}{E_F} = 2\alpha^2 \left( \frac{a}{\lambda_e} \right)^2 \quad (2.14)$$

where  $E_F$  is the Fermi energy and  $\alpha = (\frac{4}{9\pi})^{\frac{1}{3}}$ .  $\Theta$  is the ratio between the kinetic energy of the plasma electrons and their Fermi energy and can alternatively be viewed as the ratio between the Wigner-Seitz radius  $a$  and the thermal wavelength  $\lambda_e$ . For  $\Theta \gg 1$ , the kinetic energy of the electrons dominates over their Fermi energy and the plasma is said to be nondegenerate, obeying a classical Maxwell-Boltzmann statistics. For  $\Theta \leq 1$ , the effect of Pauli exclusion cannot be ignored and the plasma is degenerate, obeying a Fermi-Dirac statistics. The electron kinetic energy is then expressed as  $E_k = k_B T_e + E_F = m_e v_{th}^2 + \frac{1}{2} m_e v_F^2$ , where  $v_F$  is the Fermi velocity. As an illustration, the dense ICF plasma is partially degenerate because  $\Theta \approx 0.25$ , while the plasma of this work is nondegenerate as  $\Theta \approx 550$ .

- **Coulomb logarithm**

While  $\Gamma$  characterizes the plasma in respect to the collective or collisional aspect, another parameter is necessary to quantify the importance of small-angle collisions over large-angle

collisions, i.e between "soft" (distant) and "hard" (close) collisions.

Collisions are defined as encounters with impact parameter  $b < \lambda$ , or for a strongly coupled plasma  $b < a$ . The minimum  $b$  value  $b_{min}$  is either the Landau length  $r_{\alpha\beta}$  of the two colliding particles, equal to the classical distance of minimum approach  $b_0$  that corresponds to a  $90^\circ$  angle deflection, or, if quantum effects are important, the De Broglie wavelength of the two-particle interaction. Soft collisions or small-angle scattering thus correspond to  $b \approx b_{max}$ , while close collisions or large-angle scattering, on the opposite, are collisions where  $b \approx b_{min}$ . The ratio quantifying the relative importance of small-angle to large-angle scattering is the *Coulomb logarithm*  $\ln \Lambda$ :

$$\ln \Lambda = \ln \left( \frac{b_{max}}{b_{min}} \right) = \max \left( \ln \left( \frac{\max(\lambda, a)}{\max(b_0, \lambda_r)} \right), 2 \right) \quad (2.15)$$

It gives an estimation of the dominant collision phenomena in plasma. Its minimum value is often taken as 2 in the literature in order to ensure its positivity. Its lowest values (between 2 and 4) are reached for a strongly nonideal plasma where close collisions are important, as in a dense ICF plasma. In contrast, the ideal collisionless plasma of this work features values between 6 and 8. The Coulomb logarithm is strongly dependent on the choice of  $b_{min}$  and  $b_{max}$ . Yet no consensus exists on the ad hoc values that should be used in this place.

The Coulomb logarithm also enables to define a further plasma parameter: the electron-ion collision frequency.

- **Electron-ion collision frequency**

When a plasma is generated, it is usually out of thermal equilibrium. It therefore subsequently undergoes an equilibration, or relaxation process until the equilibrium is reached. This is achieved through collisional energy exchange between the plasma particles. First, electrons equilibrate among themselves to an equilibrium temperature  $T_e$ , then ions follow the same process to a temperature  $T_i$ , and finally the electron-ion relaxation process can start, by means of electron-ion collisions until  $T_e = T_i$ . The electron-ion temperature equilibration is characterized by a collision frequency  $\nu_{ei}$ , that can be written, for a classical plasma governed by weak collisions ( $\Gamma_{ei} \ll 1$ ), as:

$$\nu_{ei} = \frac{4\sqrt{2\pi}Z^2e^4n_i \ln \Lambda}{3\sqrt{m_e}(k_B T_e)^{\frac{3}{2}}} \propto \frac{n_i}{T_e^{\frac{3}{2}}} \quad (2.16)$$

directly depending on the Coulomb logarithm defined previously. This formula constitutes the Landau-Spitzer model [Lan36, Spi56] of the electron-ion temperature equilibration process. Similarly, the electron-electron collision frequency  $\nu_{ee}$  can be defined. For the plasma of this work,  $\nu_{ei} = 4.6 \times 10^{13} \text{ s}^{-1}$ . This description is suited for weak coupling and breaks down when  $\Gamma_{ei}$  is not small anymore. This is the case in the dense ICF plasma, where  $\Gamma_{ei} \approx 3$ .

Furthermore, the collision frequency can be used for defining the distance that a particle can travel in the plasma between two successive collisions. This distance is called the *mean free path* of the particle and it can be expressed as follows for an ion undergoing electron collisions in the plasma:

$$l_{ei} = \frac{v_{th}}{\nu_{ei}} \quad (2.17)$$

For the plasma of this work,  $l_{ei} = 0.22 \text{ } \mu\text{m}$ .

While  $\nu_{ei}$  describes the collision dynamics, collective plasma effects are characterized by the plasma frequency  $\omega_p$ .

- **Plasma frequency**

When free plasma electrons are repelled by an electric field, the resulting positive space charge generates a restoring force. This effect leads to oscillations of the free electrons similarly to a harmonic oscillator, with a characteristic frequency  $\omega_p$  that depends only on the density of the free electrons  $n_e$ :

$$\omega_p = \sqrt{\frac{4\pi n_e e^2}{m_e}} \quad (2.18)$$

The rapid oscillations of the plasma density characterized by  $\omega_p$  are called Langmuir waves and correspond to the propagation of plasmons. The complete expression also includes an ion contribution but the latter is usually neglected because  $m_i \gg m_e$ . The plasma frequency can also be expressed as a function of the Debye length  $\lambda_D$  and of the thermal velocity  $v_{th}$  of the plasma electrons,  $\omega_p = \frac{v_{th}}{\lambda_D}$ . The plasma frequency thus enables to describe collective plasma oscillations. In the plasma of this work,  $\omega_p = 1.8 \times 10^{15} \text{ rad.s}^{-1}$ , hence by a factor 40 larger than the electron-ion collision frequency. Meanwhile, it is  $5.6 \times 10^{17} \text{ rad.s}^{-1}$  in the dense ICF plasma.

## Plasma description

Three different approaches exist to describe the evolution of a plasma, depending on the spatial and temporal scales that are considered. These are a hydrodynamic, a kinetic and a particle-oriented approach. All of them are present in this work.

- **Hydrodynamic approach**

While the kinetic approach allows a very detailed plasma description in a 6-dimensional space (both in the real space and in the velocity space), it is complex to implement and time-consuming. A calculation can thus be reasonably carried out only over a reduced amount of dimensions. This is why a simplified hydrodynamic description is often preferred for describing the plasma evolution over a relatively long time scale of several nanoseconds, considering slow-varying average quantities. It is valid if the particle-energy distribution functions can be considered as Maxwellian, i.e if the plasma is at LTE, which means that collision processes are dominant over excitation and de-excitation processes caused by plasma radiation. LTE is always assumed for the description of the plasma in this work. This is justified by the fact that (i) the collision frequency  $\nu_{ei} \gg \frac{1}{\tau_H}$  where  $\tau_H$  is the characteristic time of the hydrodynamic motion (on ns-scale) and (ii) the mean particle free path in plasma  $l_{ei} \ll L_H$  where  $L_H$  is a characteristic hydrodynamic length (the plasma expands quickly over mm-scales).

In the hydrodynamic model, the plasma is considered as neutral, made of two different fluids, namely the electrons and the ions. Each fluid can be described by the so-called four hydrodynamic variables: the mass density  $\rho$ , the average velocity  $\vec{u}$ , the average energy  $\epsilon$  (or alternatively the temperature  $T$ ), and the pressure  $P$ . They correspond to the physical quantities that can be accessed by means of plasma diagnostics, unlike the particle distribution functions. The hydrodynamic point of view has been assumed from the beginning of this theoretical part, as it is the most convenient way of introducing the plasma parameters.

For both the electron and the ion fluid, the equations of conservation of mass, momentum and energy respectively can be written as

$$\frac{\partial \rho_{e,i}}{\partial t} + \nabla \cdot \rho \vec{u}_{e,i} = 0 \quad (2.19)$$

$$\rho \frac{\partial \vec{u}_{e,i}}{\partial t} + \rho (\vec{u}_{e,i} \cdot \nabla) \vec{u}_{e,i} + \nabla P = \vec{F}_{ext} \quad (2.20)$$

$$\frac{\partial}{\partial t} \left[ \rho \left( \epsilon + \frac{1}{2} u_{e,i}^2 \right) \right] + \vec{\nabla} \cdot \left[ \rho \vec{u}_{e,i} \left( \epsilon + \frac{1}{2} u_{e,i}^2 \right) + P \vec{u}_{e,i} \right] = w_V + w_S + q_H + q_{ext} + q_{exch} + q_{rad} \quad (2.21)$$

with  $\rho_{e,i}$  the electron respectively ion density,  $\vec{u}_{e,i}$  the mean electron respectively ion velocity,  $P$  the pressure,  $\vec{F}_{ext}$  the external forces,  $\epsilon$  the internal energy,  $w_V$  the volumetric work,  $w_S$  the surface work,  $q_H$  the heat transport,  $q_{ext}$  the external heat,  $q_{exch}$  the heat exchanged between the two fluids and  $q_{rad}$  the radiative contribution. The resulting system of three hydrodynamic equations features four unknowns:  $\rho_{e,i}$ ,  $\vec{u}_{e,i}$ ,  $\epsilon_{e,i}$  and  $P$ . A fourth equation is therefore necessary to solve the system, by giving an additional relation between the hydrodynamic variables. This is the so-called *equation of state* (EOS) of the species  $\epsilon = \epsilon(P, \rho)$ . The system resolution by means of the EOS requires the LTE condition. For a complete resolution, the heat transport coefficients of the system also have to be determined, and furthermore the hydrodynamic equations have to be coupled to the Maxwell equations, as the external force  $\vec{F}_{ext}$  and the pressure  $P$  may depend on the electromagnetic fields. More details on the hydrodynamic description can be found in e.g [Eli02]. The hydrodynamic equations coupled to the Maxwell equations are solved in the plasma hydrodynamic codes, which are usually employed to predict the evolution of the plasma conditions over space and time.

### • Kinetic approach

However the hydrodynamic model remains a simplified approach, only valid under the LTE condition. In particular, it cannot take transient, rapid plasma phenomena into account. The most precise and complete method for plasma description, which does not require LTE, is a kinetic approach. For the description of a macroscopic plasma system with a large number of particles, a statistical method is necessary. Therefore, each plasma species is described by an average distribution function  $f(r, v, t)$ , and the temporal evolution of this distribution function is ruled by a kinetic equation for this species. The resulting set of kinetic equations for the distribution functions of the plasma species is then combined with the Maxwell equations, or alternatively with the Poisson equation if the magnetic fields are neglected, constituting the Vlasov-Poisson equation system. Two kinds of numerical simulations are possible to solve this system. Either a full Vlasov-Poisson simulation (VP) is carried out to determine the distribution function itself, or an approximate method, called Particle-in-Cell simulation (PIC), can be applied by considering the plasma as composed of macro-particles. The PIC approach is computationally less expensive but generates more noise, and is able to describe the plasma dynamics but without accessing the distribution function.

A crucial point in the kinetic description is the level of approximation of the plasma interactions. If only the mean electromagnetic fields are considered, thus assuming the plasma to be collisionless, a Vlasov kinetic equation describes the temporal evolution of the distribution function of the given species:

$$\frac{\partial f}{\partial t} + v \cdot \frac{\partial f}{\partial r} + \frac{q}{m} (\vec{E} + \vec{v} \times \vec{B}) \frac{\partial f}{\partial v} = 0 \quad (2.22)$$

where  $q$  is the particle charge and  $\vec{E}$  and  $\vec{B}$  are the electric and the magnetic field respectively. In order to introduce the collisions in the Vlasov description, a term has to be added on the right hand side of the equation, called the collision integral  $(\frac{\partial f}{\partial t})_c$ . Depending on

the considered impact-parameter domain (small-angle or large-angle Coulomb scattering),  $(\frac{\partial f}{\partial t})_c$  is derived by using a suited approximation. For soft to moderate collisions, a Landau or Lenard-Balescu collision integral is employed, whereas a Boltzmann collision integral treats the case of moderate to close collisions. The level of approximation chosen for the interaction is particularly crucial for the description of the stopping power of charged particles and for the temperature relaxation process of species in the plasma. A more detailed discussion is given in sections 2.2.4 and 2.2.5 in the kinetic description of the ion stopping power.

- **Particle approach**

Finally, a particle-oriented approach is possible. In this frame, the equations of motion for the individual plasma particles are solved by means of simulation codes. Strictly speaking, PIC simulations belong to this kind of approach. PIC simulations enable to numerically solve the Vlasov-Maxwell or Vlasov-Poisson equation system, constitute a mean-field treatment, relevant for the description of collective plasma phenomena, but are unable to describe collisions.

In contrast, classical MD calculations base on the equations of motion for each particle  $j$ :

$$\frac{d\vec{r}_j}{dt} = \vec{v}_j \quad (2.23)$$

$$\frac{d\vec{v}_j}{dt} = \frac{q_j}{m_j} \left( \vec{E} + \frac{\vec{v}_j \times \vec{B}}{c} \right) \quad (2.24)$$

where  $r_j$  and  $v_j$  are the position and the velocity of the considered particles respectively, while  $q$  is the charge and  $\vec{E}$  and  $\vec{B}$  are the electric and the magnetic field respectively. These simple equations of motion are combined with the Maxwell equations, and integrated by means of standard numerical algorithms. MD simulations, contrarily to PIC computations, allow to describe the whole many-body dynamics of the system with all correlations and collisions as well as collective effects. However, because of computational limits, they are restricted to dense coupled plasmas, and are inefficient for  $\Gamma \ll 1$ .

In this work, for evaluating the plasma dynamics, whose evolution occurs on a ns time scale, the hydrodynamic description is required. It is implemented in the hydrodynamic code RALEF2D for the simulation of the considered laser-induced carbon plasma. In contrast, the stopping powers, that depend in particular on fast transient collective plasma phenomena, are described in a kinetic or, if PIC and MD codes are considered, in a particle-oriented frame.

While the previous paragraphs have been dealing with general plasma properties and characteristics, the next section explains the specific case of a laser-generated plasma. This part, by presenting the absorption and transport mechanisms of such a plasma, notably enables to understand the properties of the plasma simulated in next chapter, and justifies the experimental setup described in chapter 4.

### 2.1.2 Absorption of laser light in plasma

This section is devoted to the description of the interaction between high-energy laser beams and the plasma that is created by the interaction of these beams with solid matter. Present high-energy laser systems make it possible to generate pulses in a very wide range of intensity, from  $10^9$  to  $10^{21-22}$  W/cm<sup>2</sup>. From about  $10^9$  W/cm<sup>2</sup>, the intensity is sufficient to ionize the surface of a solid target and to lead to the creation of a plasma. The intensities considered in this thesis for the direct irradiation of laser beams on solid targets by using the PHELIX and *nhelix* laser systems are in the range  $10^{11} - 10^{12}$  W/cm<sup>2</sup>. This irradiation therefore leads to the creation

of a hot, dense and fast expanding plasma. For a detailed description of the various processes of plasma generation by means of intense laser pulses, the reader is referred to e.g [Eli02].

When a sufficiently intense laser beam irradiates the surface of a solid target, a snowballing ionization process is triggered. First, the photons of the laser beam interact with the free electrons that are always present on the surface of a solid due to thermal energy, or the presence of defects or impurities in the crystal structure. These electrons are accelerated by the electric field of the laser and can therefore ionize atoms on the target surface, whose freed electrons can in turn be accelerated and cause further ionization processes. Finally, a thin layer of ionized matter is created on the target surface, that is further heated by the laser light over the whole duration of the laser pulse.

Yet the laser light cannot penetrate arbitrarily far into the generated plasma. Indeed, as soon as the incoming laser radiation reaches a density for which the plasma frequency  $\omega_p$  is equal to the (circular) frequency of the laser light  $\omega_L$ , the latter cannot propagate further and is reflected. The corresponding density, called critical density  $n_c$ , is established at a time of about 100 ps after the beginning of the irradiation. It is given, in  $\text{cm}^{-3}$ , by the following expression, where  $\lambda_L$  is the laser wavelength expressed in  $\mu\text{m}$ :

$$n_c = 1.1 \times 10^{21} \left( \frac{1\mu\text{m}}{\lambda_L} \right)^2 \quad (2.25)$$

Consequently, as long as  $\omega_L > \omega_p$  in the plasma, the laser light can propagate to higher densities. However, as soon as it reaches the plasma region with density  $n_c$ , where  $\omega_L = \omega_p$ , it is blocked and reflected. No laser light can propagate in dense plasma parts for which  $\omega_L < \omega_p$ . In these regions, the heat has to be transported by other mechanisms than direct laser radiation. The PHELIX and *nhelix* laser systems that are employed in this work have a fundamental wavelength of 1053 nm and 1064 nm respectively, which corresponds to critical densities in the plasma of  $9.92 \times 10^{20} \text{ cm}^{-3}$  and  $9.71 \times 10^{20} \text{ cm}^{-3}$  respectively. As the value of  $n_c$  scales with  $\frac{1}{\lambda_L^2}$ , a frequency doubling and a frequency tripling of the beam lead to a fourfold and ninefold increase in  $n_c$  respectively. This plays an important role in the experimental setup of this work, as explained in 4.1.

The plasma generated by the irradiation of a target with an intense laser beam can be divided into three main interaction zones, as shown in figure 2.1. Three characteristic regions of the laser-plasma interaction are thus defined depending on the plasma density and temperature. The main heating and transport processes present in each of these three zones are explained in the following.

### Zone of laser absorption - corona

The zone ranging from outwards up to the critical layer (surface corresponding to the critical density  $n_c$ ) is called *corona*. It can be shown that electromagnetic waves obey the following dispersion relation in the plasma corona, where  $k_p$  is the propagation wave number and  $\omega_L$  is the frequency of the incident laser light:

$$k_p^2 c^2 = \omega_L^2 - \omega_p^2 \quad (2.26)$$

From this relation it can clearly be seen that for  $\omega_L < \omega_p$ ,  $k_p$  is purely imaginary, hence electromagnetic radiation at a frequency lower than  $\omega_p$  cannot propagate beyond the critical surface.

The corona is a hot, dilute and extended plasma region that is almost completely ionized. It also expands quickly and its ablation velocity can be estimated as the plasma sound velocity  $c_s$ :

$$c_s = \sqrt{\frac{Z_T k_B T_e}{m_i}} \quad (2.27)$$

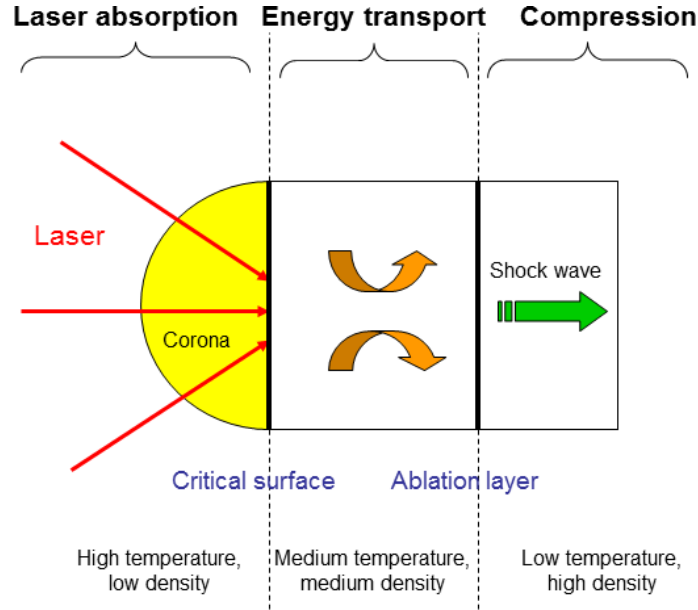


Figure 2.1: Characteristic regions of the laser-plasma interaction: corona, transport zone and compression zone.

with  $Z_T$  the plasma ionization degree,  $T_e$  the plasma temperature and  $m_i$  the ion mass. For a 200 eV fully ionized Carbon plasma as in this work, an expansion velocity close to  $100 \mu\text{m/ns}$  is thus estimated.

As the laser field is stopped at the critical surface, the laser energy is deposited only in the corona, which is the zone of actual laser absorption. Several absorption mechanisms are present.

- **Collisional absorption**

The most important laser absorption process taking place for the considered intensities of  $10^{11}$ - $10^{12} \text{ W/cm}^2$  is the *collisional absorption*, in which a photon is absorbed by an electron while being scattered on a plasma ion. It is also designated as *inverse bremsstrahlung*, since it is the opposite process of the electron bremsstrahlung emission. The absorption coefficient of this mechanism can be estimated as follows.

The equation of motion of a free electron submitted to the electric field of the laser can be written as:

$$\frac{d\vec{v}}{dt} = -\frac{e\vec{E}}{m_e} - \frac{\vec{v}}{\nu_{ei}} \quad (2.28)$$

where  $\nu_{ei}$  is the Spitzer electron-ion collision frequency presented in section 2.1.1. The Spitzer expression can be applied because the plasma corona is a hot region corresponding to an ideal plasma. From the dispersion relation for transversal waves in plasma, obtained by combining the equation of motion and the Maxwell equations for a free charge in vacuum, the spatial damping rate of the laser beam by inverse bremsstrahlung  $K_{iB}$ , can be derived as:

$$K_{iB} = \left(\frac{\nu_{ei}}{c}\right) \left(\frac{\omega_p^2}{\omega_L^2}\right) \left(1 - \frac{\omega_p^2}{\omega_L^2}\right)^{-\frac{1}{2}} \propto \frac{Z_T n_e^2}{T_e^{\frac{3}{2}}} \left(1 - \frac{n_e}{n_c}\right)^{-\frac{1}{2}} \quad (2.29)$$



The total absorption coefficient in the corona  $A_L$  can be inferred by the integration of  $K_{iB}$  over the corona. The factor 2 in the integral comes from the fact that the laser light traverses the corona twice, before and after reflection at the critical surface:

$$A_L = 1 - \exp\left(-2 \int_{-\infty}^0 K_{iB}(x) dx\right) \quad (2.30)$$

It can be noted that the importance of collisional absorption decreases when the plasma density increases, and is significantly enhanced when the critical density is increased. It means that for a frequency-doubled laser pulse, the laser heating of the plasma is much more efficient. It can be shown [AMtV04] that the fraction of absorbed laser radiation in the corona  $A_L$  decreases with the ratio  $\frac{I_L}{I_L^*}$  where  $I_L^*$  is a critical laser intensity that scales with  $\frac{1}{\lambda_L^4}$ ,  $\lambda_L$  being the laser wavelength. Hence, the frequency doubling of the laser pulse leads to an increase in  $I_L^*$  by a factor 16, which almost doubles the value of the absorption coefficient, reaching nearly 90 % instead of 50 % for the considered hot C plasma heated at 532 nm wavelength.

### • Resonant absorption

Beyond the dominant collisional inverse bremsstrahlung, further absorption processes are present in the corona, especially in the vicinity of the critical surface. Collective mechanisms also arise, consisting in the excitation of waves in plasma. The most important collective absorption process, taking place at the critical surface, is the resonant absorption, in which Langmuir waves (plasmons) are resonantly excited by the laser pulse.

For this mechanism to take place, two conditions have to be fulfilled. First, the laser light has not to be normally incident on the critical surface, but have an oblique incidence with an angle  $\theta_0$ . In that case, the laser beam cannot reach the critical surface because of the resulting refraction and is stopped short before it. Assuming that the density gradient before the critical surface is linear and extending from  $-d$  to 0, the distance of minimum approach  $z_{min}$  of the laser light to the critical surface can be written as:

$$z_{min} = -d \sin^2(\theta_0) \quad (2.31)$$

Second, the laser light must be p-polarized, which implies that the electric field of the laser has a part that is parallel to the density gradient at the critical surface. Then, a part of the laser photons can reach the critical surface by tunneling. Matching the condition  $\omega_L = \omega_p$  and being polarized in the direction of the density gradient, i.e the direction of the plasmon oscillations at the critical surface, the photons can thus transmit their energy to the plasma waves. The s-polarized light instead cannot be coupled along the density gradient and is therefore unable to excite plasma waves. The mechanism of resonant absorption is represented in Fig. 2.2.

The corresponding absorption efficiency depends only on the parameter  $q$  as derived in e.g [Kru88]:

$$q = (kL)^{\frac{2}{3}} \sin^2(\theta_0) \quad (2.32)$$

By using this relation, it can be shown that the absorption reaches a maximum of 49 % when  $q = 0.5$ . It sinks to 0 when  $q = 0$  (normal incidence) or  $q \gg 1$  (then  $z_{min}$  is too large for an efficient energy coupling). A characteristic feature of resonant absorption is that, in contrast to collisional absorption that heats all the plasma electrons, it heats only a minority of them, thus generating a population of hot electrons.

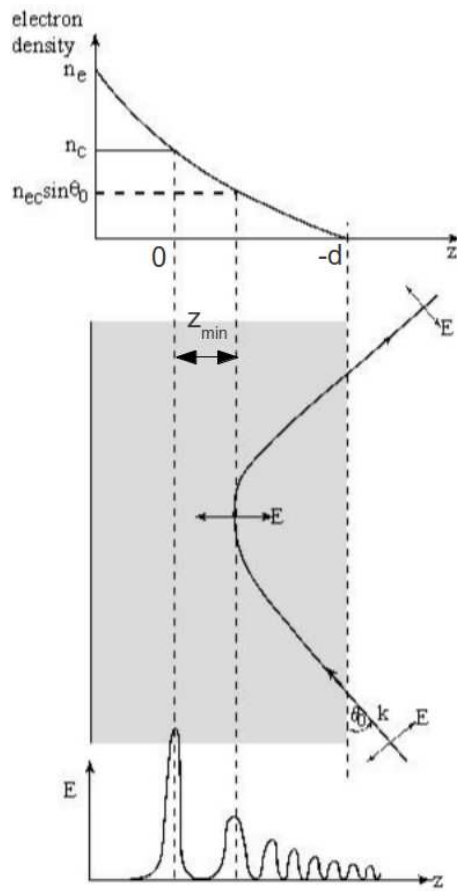


Figure 2.2: Mechanism of the resonant plasma absorption, from [Eli02].

- **Other absorption mechanisms**

Apart from inverse bremsstrahlung and resonant absorption, other absorption mechanisms exist. They arise through parametric instabilities and consist in the coupling of the laser light with various plasma waves. Unlike the resonant absorption, they can also take place in a homogeneous plasma, i.e without density gradient. These are (i) the stimulated Raman scattering (SRS), in which the laser beam couples with a Langmuir wave, (ii) the stimulated Brillouin scattering (SBS), in which it couples with an ion acoustic wave, (iii) the parametric decay where a laser photon is converted into a plasmon and an ion acoustic wave, and finally (iv) the two-plasmon-decay for which a photon decays into two Langmuir waves.

Yet all these wave-coupling phenomena are nonlinear and become significant only from a laser intensity of the order of magnitude of  $10^{15}$  W/cm<sup>2</sup>. In conclusion, only collisional and, to a smaller extent, resonant absorption play a role at the considered intensities of  $10^{11} - 10^{12}$  W/cm<sup>2</sup>.

The energy that has been deposited in the corona by the previously explained mechanisms is then transported further into the plasma by other processes.

### Zone of energy transport

In the energy transport region, two main mechanisms ensure the transmission of the energy deposited in the corona into deeper plasma parts. These are thermal conduction and radiation transport.

- **Thermal conduction**

The thermal conduction process is characterized by the energy density  $q_H$ , that is determined as follows as a function of the plasma temperature gradient  $\nabla T$ :

$$q_H = -\nabla \kappa \nabla T \quad (2.33)$$

$\kappa$  is the heat transport coefficient, whose form depends on the level of approximation of the plasma interactions. For a hot ideal plasma, the Spitzer form [SH53] can be applied:

$$\kappa = \zeta \frac{k_B^{\frac{7}{2}}}{\sqrt{m_e} Z_i e^4 \ln \Lambda} T_e^{\frac{5}{2}} \quad (2.34)$$

As in the Spitzer electron-ion collision frequency formula (equation 2.16), a dependence on the Coulomb logarithm appears, but the temperature dependence is now stronger. The factor  $\zeta$  adds the influence of electron-electron correlations to the formula that otherwise considers only the major contribution of electron-ion collisions.

- **Radiation transport**

The radiation that is emitted and absorbed in plasma also contributes to the energy transport. The radiation emitted in plasma is a superposition of X-rays from two distinct origins. On the one hand, line radiation is generated by atomic transitions (bound-bound or bound-free), and on the other hand a continuum radiation is produced by free-free transitions in the bremsstrahlung process of free electrons.

While the thermal conduction process is based on collisional energy exchange and is therefore relatively slow, depending on the electron-ion collision frequency, the radiation transport is a much more rapid mechanism. However, in most experimental cases, its contribution is small in comparison with thermal conduction. Because the microscopic cross sections for the transition processes creating the radiation increase significantly with the

plasma density, the radiation transport becomes all the more significant as the laser beam deposits its energy deeper into the plasma. In other words, the efficiency of radiative transport increases with the critical density.

Therefore, the frequency doubling of the beam leads to an enhancement of radiation transport. This plays a central role for the experiment of this work. Indeed, as radiation transport is fast in comparison with thermal conduction, this helps to obtain, in a time span of a few nanoseconds, a nearly homogeneous plasma slab (see 3.1.2 and 4.1.4).

If  $f(\nu, \vec{r}, \vec{\Omega}, t)$  is the photon distribution function of the emitted radiation, then the energy density  $U_\nu$  of the radiation at frequency  $\nu$  (spectral energy density) at position  $\vec{r}$  and time  $t$  in a volume element of the plasma can be obtained by integration of the distribution function  $f$  over all solid angles  $\vec{\Omega}$ :

$$U_\nu(\vec{r}, t) = h\nu \int 4\pi f(\nu, \vec{r}, \vec{\Omega}, t) d\vec{\Omega} \quad (2.35)$$

Similarly, the radiative energy flux  $S_\nu$  in a volume element at position  $\vec{r}$  through a surface with a normal vector  $\vec{n}$  can be written as:

$$S_\nu(\vec{r}, t, \vec{n}) = h\nu \int 4\pi f \vec{\Omega} d\vec{\Omega} \quad (2.36)$$

Finally, writing the energy balance in the previously considered volume element leads to the equation of radiative transport:

$$\frac{\partial U_\nu}{\partial t} + \nabla \cdot \vec{S}_\nu = c\kappa_\nu(U_{\nu,p} - U_\nu) \quad (2.37)$$

The coefficient  $\kappa_\nu$  is called opacity of the given material at the radiation frequency  $\nu$  and  $U_{\nu,p}$  is a reference spectral energy density corresponding to a Planckian emission. In the RALEF2D and ESTHER hydrodynamic codes employed in the frame of this thesis, the radiative transport contribution is considered because it plays a potentially important role in the plasma heating process. The codes must therefore solve the above written equation of radiative transport in addition of treating the thermal conductivity mechanism. The opacity values are crucial in the resolution of the equation of radiative transport. Depending on the plasma conditions, they can be taken from existing opacity tables or must be calculated by using ab-initio methods (see 6.2).

In comparison with the corona, the energy transport zone features a higher plasma density and a lower plasma temperature. It spreads from the critical surface until the so-called *ablation front*. The ablation front, defining the external boundary of the shock wave that the laser has induced in the target, is the surface from which the plasma starts to expand outwards.

### Zone of compression

The zone of high density and low temperature located within the ablation front is called the compression zone. It indeed undergoes a compression by a shock wave coming from the ablation front, leading to increasingly high densities in the target center. The compression zone is yet only significantly extended if the target is sufficiently thick. In the experiment carried out in this work, carbon targets of only 500 nm thickness are employed. Consequently, the compression region is very limited in space and time. According to the RALEF2D simulations, even the most dense plasma regions are dominated by heating through radiative transport after less than one nanosecond after the beginning of the laser irradiation.

This section has been dealing with the target physics in the beam-target interaction, presenting all important plasma parameters and phenomena that are relevant for this work. These concepts are now applied, in the coming section, in the description of the ion-plasma interaction.

## 2.2 Ion-plasma interaction

The purpose of this section is to present the different stopping theories that will be compared in the simulations and with the experimental data. Before entering the details of these theories, a phenomenological overview of ion stopping is first given in 2.2.1. The general features of the ion-target interaction as well as the involved processes are described. A basic stopping-power formalism is also introduced for the case of cold matter. Then, in 2.2.2, the stopping-power modifications in the plasma case are explained, and a basic ion-stopping model in plasma is described.

Yet for the stopping-power description at stopping maximum, more advanced theoretical considerations are required. A description as a function of the different perturbation regimes of the ion-plasma interaction and the different regimes of impact parameter, that require different theoretical treatments, is thus necessary. For this purpose, in 2.2.3 a characterization of the beam-plasma interaction is carried out. On this basis, in 2.2.4 the different theoretical approaches to the ion stopping power in plasma are presented, basing on the dielectric theory, the binary-collision theory or the kinetic plasma theory. Approaches aiming at a unified stopping description are then presented in section 2.2.5. Finally, a brief summary and state-of-the-art on ion stopping in plasma is provided in 2.2.6. The domain of applicability of each theory is particularly highlighted. Stopping predictions basing on the described theories are made for the experiment of this work in chapter 3.

### 2.2.1 General features of ion stopping

Ion stopping in a medium is a complex process that encompasses numerous physical phenomena and depends on both the projectile and the target properties. When a projectile ion with velocity  $v_p$  and charge  $Z_p$  interacts with a portion of matter, two phenomena are observed. On the one hand, the ion loses a part of its energy in the matter, and on the other hand charge-exchange processes occur, leading to a variation of the charge-state value. This charge-state value, which also depends on the projectile energy, has in turn an important influence on the energy deposition. In plasma, because of the specific properties of this medium, both the energy loss and the charge-state are substantially modified in relation to cold matter, and a different treatment is required. The energy loss and the charge-state evolution of a projectile ion in matter are based on the interaction cross sections of the underlying microscopic Coulomb processes. These can be viewed as collision cross sections, or scattering cross sections in the frame of Coulomb scattering theory.

#### Overview of stopping processes in matter

First, the distinction between the stopping power and the energy loss of a charged particle interacting with matter has to be made clear. The *stopping power*  $S(E)$  of an ion in a medium is defined as its differential energy loss, i.e the amount of energy  $\partial E$  lost by the ion per length element  $\partial x$ . It has the dimension of a force (typically expressed in MeV/ $\mu\text{m}$ ) and is positive:

$$S(E) = -\frac{\partial E}{\partial x} \quad (2.38)$$

The *energy loss*  $\Delta E$  of an ion is the integral of its stopping power over the ion trajectory in the stopping medium.

$$\Delta E = -\int \frac{\partial E}{\partial x} dx = -\int \frac{\partial E}{\partial \rho x} \rho dx \quad (2.39)$$

with  $\rho$  the mass density of the target medium. The right hand side of equation 2.39, by introducing  $\rho$  in the energy-loss expression, shows that the latter can equivalently be seen as the integral of the stopping power per unit of areal density  $\rho x$  over the target areal density. The expression with the areal density is more relevant for the description of the experimental case, because the important quantity for the energy loss is not the length of the medium, but the amount of matter present on the ion path. While the stopping power is a theoretical local microscopic quantity, the energy loss  $\Delta E$  is the observable quantity that can be determined experimentally. In this theoretical part, only the stopping power is thus addressed.

Projectile ions traversing a portion of matter can lose their energy in different ways depending essentially on their incident energy. As described in [Sig05], the following phenomena can contribute to the stopping:

1. Excitation and ionization of the target electrons
2. Excitation and ionization of the projectile
3. Capture of the target electrons
4. Nuclear energy loss
5. Electromagnetic radiation

On the one hand, the projectile ions can lose energy by inelastic collisions with the target electrons, as well as by elastic collisions with the plasma ions. This corresponds to the electronic and to the nuclear energy loss respectively. While the excitation and ionization of target electrons is the dominant energy-loss process over a wide velocity range, the nuclear energy loss only becomes significant for low projectile velocities below 0.1 MeV/u.

On the other hand, the projectile itself can be excited and ionized, and it can also capture target electrons. These two energy-loss processes are important only for projectile velocities typically below 1 MeV/u. In contrast, for very high velocities, an electromagnetic energy loss must also be taken into consideration, essentially in the form of bremsstrahlung or Cherenkov radiation. In this work, an intermediate projectile energy of 0.5 MeV/u is considered. The interaction is therefore nonrelativistic, and the electromagnetic energy loss can be neglected. Likewise, the nuclear energy loss can be neglected. As a consequence, the stopping-power quantity that is considered in the following is always an *electronic* stopping power, unless otherwise indicated.

Traditionally, as shown in Fig. 2.3, the energy (or velocity) spectrum of the ion stopping power in matter can be divided into three main regimes, within a non-relativistic frame. For each of these regimes, a different description of the stopping power is necessary.

It must be noted that the example of Fig. 2.3 is just one specific case, in solid matter, to illustrate the concept of the different velocity regimes on the stopping power. The borderlines of these regimes may vary from case to case, notably in the plasma case.

In the high-velocity regime ( $> 10$  MeV/u), a simple description based on the asymptotic Bethe formula [Bet30, Bet32] can be applied. The Bethe formula will be explained more in details later in this section. In the low-velocity regime ( $< 0.1$  MeV/u), a simple model is also available, where the stopping power is proportional to the velocity  $v_p$  of the projectile, similarly to a friction force [LS61].

The physical picture is more complicated in the intermediate-velocity regime, where excitation and ionization of the target electrons and of the projectile as well as electron capture are expected to be important. Moreover, strong Coulomb coupling and complex charge-transfer processes are potentially present. These multiple mechanisms lead to the existence of a maximum in the intermediate-velocity part of the stopping curve, where the theoretical stopping description is particularly involved. The projectile velocity for which the maximum is reached is the characteristic velocity of the target electrons. In the case of cold matter it is the velocity of the

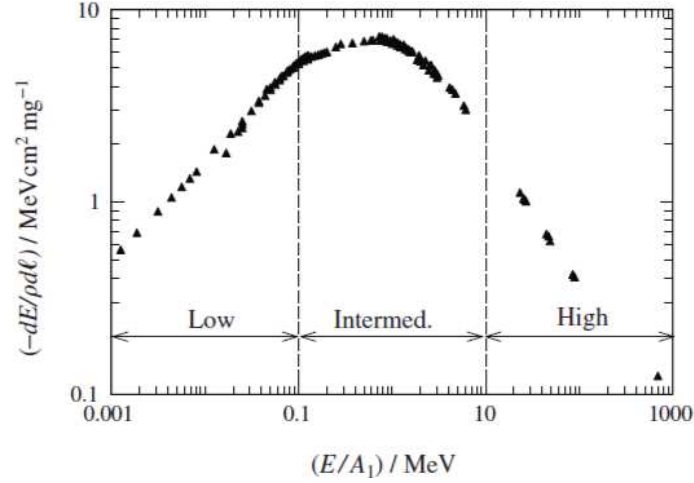


Figure 2.3: The three velocity regimes of ion stopping in matter, exemplified in the case of experimental data of oxygen ion stopping in (cold) aluminum [Sig05]. The data were compiled by H. Paul ([Pau]).

bound target electrons which is close to the Bohr velocity  $v_0$ , while in plasma it is the thermal velocity of the free electrons  $v_{th}$ . To describe the intermediate-velocity region in cold matter, modified Bethe formulas with the adding of several corrections (Bloch [Blo33], Barkas [BDH63] and shell [SS06] corrections) can provide an estimation in some cases. The shell correction takes the motion of the individual target electrons into account and is only of relevance for a projectile velocity below the Thomas-Fermi velocity of the electrons [Sig05]. This corresponds to projectile energies below 0.3 MeV/u and this correction can thus be neglected in the present case where the projectile energy is 0.5 MeV/u. A good overview of these corrections in cold matter can be found in [Zie99] or in [SS02]. The Bloch and Barkas corrections will be addressed more in details in the plasma case in section 2.2.2. Attempts of scalings between the high- and the low-velocity regime have also been proposed [Sug81] but a complete self-consistent description is still missing. Several advanced theories have been developed recently but none can provide a complete stopping-power description over the whole velocity spectrum. Among them, the binary theory by P. Sigmund [SS02] bases on an extended classical approach with numerous corrections. In particular, the stopping model in the GEANT4 code is based on the results of this model (see 4.2.1). Another approach is the convergent kinetic theory (CKT) by G. Maynard and co-workers ([MDD<sup>+</sup>02]). It constitutes an extension of the standard Bohr-Bethe-Bloch ansatz that also contains various corrections and whose main focus is the description of ion stopping in plasma (see also 2.2.5). Finally, the Unitary Convolution Approximation (UCA) by P.L. Grande and G. Schiwietz ([GS02]) is cited. It is an impact-parameter-dependent Bloch theory that has led to the development of the CasP code (Convolution Approximation for Swift Particles), that is mentioned later in this work.

Even if a perfect description of ion stopping in cold matter (solids and gases) has not been achieved yet, especially around the stopping-power maximum, a relatively good understanding has been reached, and numerous experimental measurements have been conducted, enabling to scale the existing models and to establish quite reliable data tables [Pau06]. A detailed overview can be found in [Sig05], while a compilation of the existing stopping-power data is carried out in [Pau].

### Projectile charge state

The charge state of the projectile ion, or the charge-state distribution of the ion beam, is a very important parameter for the stopping power. As will be shown in the following, the stopping power indeed depends quadratically on the charge-state value, at least according to the linear descriptions like the Bethe formula and assuming a point charge. Although this dependence appears to be possibly weaker depending on the beam-plasma configuration [Zwi99], the charge-state value always plays a major role in the stopping process.

In cold matter, a projectile experiences three major charge-exchange processes. They are also present in a plasma and are depicted in Fig. 2.4.

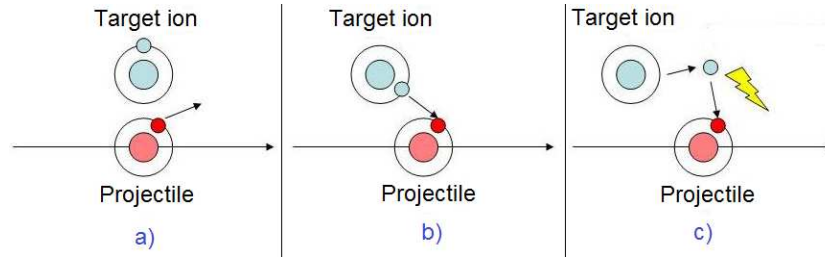


Figure 2.4: Charge-exchange processes for a projectile ion in cold matter: a) ionization by Coulomb collisions with the target ions, b) non-radiative electron capture (NREC), c) Radiative electron capture (REC).

The main ionization process is projectile ionization by Coulomb collisions with the target ions. It can cause either the excitation of a projectile electron to an upper energy level or the direct ionization of the projectile.

The dominant recombination mechanism in not fully ionized matter is recombination by capture of bound target electrons, due to its relatively high cross section. It is based on the presence of the corresponding target atom as a third collision partner for momentum transfer. In this way, the momentum conservation is guaranteed. This is not the case for collisions with free electrons, where there is no third partner available.

Another recombination process that mainly plays a role in ionized matter is recombination by radiative electron capture. In this mechanism, a free electron is generated by ionization of a target atom and is subsequently captured by the projectile. In order to ensure the conservation of energy and momentum, a photon is emitted, hence the designation "radiative electron capture". This mechanism can be viewed as the inverse process of photo-ionization. In "cold matter", it is only significant if the projectile energy is sufficiently high (several MeV/u) in order to ionize target atoms and thus to create free electrons that can then be captured by the projectile. It becomes dominant in a fully ionized plasma but only at low densities and moderate temperatures. In the following, the capture of bound electrons is designated as NREC (non-radiative electron capture), in opposition to REC (radiative electron capture).

The charge-exchange mechanisms are statistical processes whose cross sections depend on the plasma parameters as well as on the projectile velocity. Ionization and recombination are in permanent competition for determining the charge state distribution of an ion beam. If a beam with a sufficient number of projectile ions interacts with a homogeneous target over a sufficient interaction time and a sufficient distance, a statistical average equilibrium charge-state value is reached in the beam, resulting from a large number of ionization and recombination processes. This dynamic equilibrium charge-state value  $Q_{eq}$ , when reached, is equal to the average charge-state value and is described with the help of equation 2.40, where  $q_i$  are the different charge states and  $f_i$  are the corresponding statistical proportions.



$$Q_{eq} = \sum_i f_i q_i \quad (2.40)$$

$Q_{eq}$  usually reaches higher values in solids than in gases. This so-called *density effect* [MCG00] can be explained as follows. As a solid features a higher density than a gas, more collisions occur between each projectile ion and the atoms of the medium in a given time. Therefore the projectile electrons, after having been excited and having reached a higher energy level after a collision, have less time to de-excite before the next collision. Consequently, the ionization of a projectile ion in a solid is more probable than in a gas.

As the complete microscopic description of the charge-transfer cross sections is a difficult task, the equilibrium mean charge-state value is usually estimated by using semi-empirical scaling laws. One of the simplest and most frequently used ones, that has been verified experimentally in a wide range of beam-target configurations, is the Betz formula [Bet83]:

$$Q_{eq} = Z \left( 1 - a \exp \left( -\frac{v_p}{v_0 Z^f} \right) \right) \quad (2.41)$$

where  $Z$  is the atomic number of the projectile,  $v_0$  is the Bohr velocity, and  $a$  and  $f$  are fit parameters whose values are close to 1 and  $2/3$  respectively. The Betz formula only takes the projectile parameters into account and ignores medium properties.

More advanced fit formulas for the equilibrium mean charge state are given by the Ziegler-Biersack-Littmark model [ZBL85] used notably in the SRIM [sri] code and the Schiwietz-Grande model [SG01], which in addition include the target dependence. The Schiwietz-Grande semi-empirical formula for a solid target is given by:

$$Q_{eq} = Z_p \frac{12x + x^4}{\frac{0.07}{x} + 6 + 0.3 \cdot x^{0.5} + 10.37 \cdot x + x^4} \quad (2.42)$$

with

$$x = \left( \frac{v_p}{v_0} \cdot Z_p^{-0.52} Z_T^{-0.019 Z_p^{-0.52} \frac{v_p}{v_0}} \frac{1}{1.68} \right)^{1 + \frac{1.8}{Z_p}}. \quad (2.43)$$

where  $v_0 = 2.19 \times 10^6$  m/s is the Bohr velocity. Specifically for formulas 2.42 to 2.45,  $Z_p$  and  $Z_T$  designate the projectile and the target atomic number respectively. For gases there is a similar expression:

$$Q_{eq} = Z_p \frac{376x + x^4}{1428 + 1206x^{0.5} + 690x + x^6} \quad (2.44)$$

with

$$x = \left( \frac{v_p}{v_0} \cdot Z_p^{-0.52} Z_T^{0.03 - 0.019 Z_p^{-0.52} \frac{v_p}{v_0}} \right)^{1 + \frac{0.4}{Z_p}}. \quad (2.45)$$

At an ion energy of 0.5 MeV/u, as in the experiment carried out in this work, for carbon projectile ions ( $Z_p = 6$ ) in a carbon medium ( $Z_T = 6$ ), an equilibrium mean charge state  $Q_{eq} = 4.38$  is obtained for the solid state and  $Q_{eq} = 3.98$  for the cold gaseous state.

If it is assumed that the projectile is a point charge with charge-state value  $Z_p$ , the stopping power depends quadratically on  $Z_p$ , at least at high projectile velocity, where the projectile-plasma coupling is linear (see section 2.2.3). However, in reality, as the projectile is not punctual and possibly carries bound electrons, the screening of the projectile by these bound electrons tends to reduce the charge value felt by the target electrons. At high velocity, as can be seen with the help of the Betz or the Schiwietz-Grande formulas, the projectile is expected to be

fully stripped and thus no bound projectile electrons screen its potential. Yet at lower velocity, bound electrons are mostly present and have to be taken into account. This has led, for a long time, to the utilization of the concept of an *effective charge*  $Z_{eff}$ , aimed at including the Coulomb screening by bound electrons in the stopping-power expression. This concept has been introduced by Bohr [Boh41] and one of the most used forms has been developed by Northcliffe [Nor63]. However, the use of an effective charge state is physically improper and can be avoided, as recently pinpointed in [Fra11, FBB<sup>+</sup>13]. For a correct description of the stopping process, a full microscopic description including an impact-parameter dependence of the stopping cross sections is needed in order to account for the presence of bound electrons around the projectile. Such an impact-parameter description is for example possible with the CasP code [cas]. By the self-consistent combination of this approach with a Monte-Carlo calculation of the charge-state distribution of the projectile, the need of an artificial effective charge state description can thus be eliminated [FBB<sup>+</sup>13].

The exact relation between the charge state and the stopping power of a projectile ion generally remains a complex task, and in most stopping theories, the charge state is considered as an external input parameter. Hence, no self-consistent theory is available for both the stopping power and the charge state to date, and only a microscopic description relying on simulation codes can provide a complete description.

Now, analytic stopping-power formulas in cold matter are presented for the simple case of a high projectile velocity. Basing on the introduced formalism, equivalent stopping formulas will be derived later for plasmas. Therewith, the standard ion-stopping model in plasma, which relies on an extension of the stopping-power formulation in cold matter, will be derived.

Theoretical descriptions that are more adapted to the physical case of interest in this work than the basic standard model, are presented in sections 2.2.4 and 2.2.5.

### Fast ion stopping in cold matter: the Bohr and Bethe formulas

Ion stopping in matter has first been described by Bohr [Boh13] by using a classical approach, and then by Bethe [Bet30, Bet32] with the help of a quantum-mechanical approach. The Bohr and Bethe formulas are asymptotic formulas, valid for high projectile-ion velocities. The Bohr formula in a solid can be obtained by considering a series of binary collisions undergone by a fast projectile ion with the bound electrons of the medium, whose density is  $n_T$  in  $\text{cm}^{-3}$ . The energy transfer from the projectile to a target particle can be written as  $\Delta E = (\Delta p)^2/2m$ , where  $m$  is the particle mass and  $p$  the exchanged momentum. The interaction of a projectile ion of mass  $m_i$ , charge number  $Z_p$  and velocity  $v_p$  with an impact parameter  $b$  is considered in the vicinity of a target electron. Because  $m_i \gg m_e$ , the ionic stopping-power contribution is neglected. The transferred momentum from the projectile to the electron is:

$$\Delta p(b) = Z_p e^2 \int \frac{b}{((v_p t)^2 + b^2)^{\frac{3}{2}}} = 2 \frac{Z_p e^2}{b v_p} \quad (2.46)$$

where only the component normal to the projectile trajectory has been considered, as the longitudinal component is averaged out over the interaction time. Consequently, the exchanged amount of energy can be written as:

$$\Delta E(b) = \frac{(\Delta p)^2}{2m_e} = 2 \frac{Z_p^2 e^4}{b^2 v_p^2} \quad (2.47)$$

If the projectile propagates over a distance  $\partial x$  in the medium, it interacts with  $2\pi b db n_T \partial x$  electrons at impact parameter  $b$ , which leads to the stopping-power expression:

$$\frac{\partial E}{\partial x} = - \frac{4\pi Z_p^2 e^4 n_T}{m_e v_p^2} \int \frac{db}{b} \quad (2.48)$$

As the integral in  $b$  is divergent both at 0 and at  $+\infty$ , two cutoffs have to be set up for the integration, namely the minimum and maximum impact parameter ( $b_{min}$  and  $b_{max}$ ) that contribute to the stopping power.

$b_{min}$  is usually taken as the classical length of minimal approach and thus of maximum energy transfer, i.e the Landau length:  $b_{min} = r_0 = \frac{Z_p e^2}{m_e v_p^2}$ . Here equ. 2.9 has been applied with  $\mu = m_e$  because  $m_i \gg m_e$  and  $v_r = v_p$  because  $v_p \gg v_0$ . Furthermore, the energy transfer can occur as long as the collision duration  $\Delta t \approx \frac{b}{v_p}$  stays smaller than the frequency  $\omega$  associated to the oscillations of the bound electron. It means that  $b$  has to be smaller than  $b_{max} = \frac{v_p}{\omega}$ . Finally, by calculating the integral, the Bohr classical stopping-power expression 2.49 is obtained. The logarithmic term coming from the integration over  $b$  is the Coulomb logarithm describing the strength of the interaction between the projectile and the target electrons.

$$\left(\frac{\partial E}{\partial x}\right)_{bound} = -\frac{4\pi Z_p^2 e^4 n_T}{m_e v_p^2} \ln \left( \frac{m_e v_p^3}{Z_p e^2 \omega} \right) \quad (2.49)$$

This classical approach is adapted for relatively small impact parameters and it tends to overestimate the stopping power otherwise.

For large impact parameters, a perturbative quantum-mechanical calculation as conducted by Bethe is appropriate, leading to the well-known Bethe formula:

$$\left(\frac{\partial E}{\partial x}\right)_{bound} = -\frac{4\pi Z_p^2 e^4 n_T}{m_e v_p^2} \ln \left( \frac{2m_e v_p^2}{I} \right) \quad (2.50)$$

where  $I$  is the excitation energy of the bound target electrons. As can be seen from the Bohr and Bethe expressions, two key parameters other than the projectile velocity strongly influence the stopping power. These are the projectile charge state  $Z_p$  with its quadratic dependence, and the Coulomb logarithm describing the nature of the projectile-target interaction. These two parameters are modified in ionized matter, which induces important changes and notably a substantial increase of the stopping power in plasma.

### 2.2.2 Simple model of ion stopping in plasma

In ionized matter, due to the simultaneous presence of bound and free electrons, the cross sections of the stopping power as well as of the charge-transfer processes are modified. Indeed, excited free electrons, that oscillate collectively in plasma at frequency  $\omega_p$ , also participate to the stopping process. These plasmon excitations have to be included in addition of Coulomb collisions in the description of the stopping power. Two main effects appear for ion stopping in plasma, both leading to an enhancement of the stopping power in relation to cold matter: the increase in the Coulomb logarithm due to different excitation energies of the electrons, and the increase in the projectile charge state due to different cross sections of the charge-transfer processes.

- **Modifications in the Coulomb logarithm**

The excitation energy of target electrons in the case of cold matter (and bound plasma electrons) is given, for the atomic transition  $j$ , by:

$$I_j = \hbar \omega_j \quad (2.51)$$

There,  $\omega_j$  is the corresponding oscillation frequency, assuming that each electronic transition in a target atom can be modeled as an oscillator system. Yet, for practical calculations, the mean value  $I$  of all the oscillator energies of an electron in an atom is considered, defined as:

$$\ln I = \sum_j f_j \ln(\hbar\omega_j) \quad (2.52)$$

Here the coefficients  $f_j$  are the rates of the corresponding electronic transitions. For the excitation energy of free plasma electrons, the oscillator frequencies  $\omega_j$  have to be replaced by the frequency of the collective plasma response to a perturbation, i.e the plasma frequency  $\omega_p$ . Consequently, the corresponding excitation energy is the energy of a plasmon  $\hbar\omega_p$ . Expression 2.53 can thus be applied for the Bethe stopping power by free electrons. If the plasma is partially ionized, the Coulomb logarithm has to be split into two terms, where the one for bound electrons is similar to the solid case (2.50).

$$\left(\frac{\partial E}{\partial x}\right)_{free} = -\frac{Z_p^2 e^2 \omega_p^2}{v_p^2} \ln\left(\frac{2m_e v_p^2}{\hbar\omega_p}\right) \quad (2.53)$$

Similarly, the Bohr formula in plasma can be expressed as:

$$\left(\frac{\partial E}{\partial x}\right)_{free} = -\frac{Z_p^2 e^2 \omega_p^2}{v_p^2} \ln\left(\frac{m_e v_p^3}{Z_p e^2 \omega_p}\right) \quad (2.54)$$

where the upper cutoff is now  $b_{max} = \frac{v_p}{\omega_p}$ , which is the dynamic screening length  $\lambda$  of a projectile ion in the plasma.

Both descriptions are complementary and their domain of validity is limited to relatively high projectile velocities. While the Bethe formula describes collisions with a relatively large impact parameter in a quantum perturbative manner, including the domain  $b > \lambda$  for collective plasma oscillations, the Bohr formula describes collisions for  $b_0 < b < \lambda$  in a classical and nonperturbative way.

The replacement of the oscillation frequency of bound atomic states by the plasma frequency causes an important modification of the stopping power. For example, in a plasma at electron density  $n_e = 10^{21} \text{ cm}^{-3}$ , the mean excitation energy in the Bethe formula for bound electrons is 86 eV for carbon atoms [Sig05], while the plasmon excitation energy  $\hbar\omega_p \approx 1 \text{ eV}$ . Due to the considerably lower excitation energy of the free electrons in comparison with bound atomic electrons, the Coulomb logarithm of the projectile-plasma interaction is increased in comparison with the interaction in cold matter. For the same example, the Bethe Coulomb logarithm is increased by about 50 % at a projectile energy of 4 MeV/u. For lower projectile energies as 0.5 MeV/u, the Bethe formula is inappropriate and over-evaluates the stopping power, as is shown in 3.2.

Even if the Bethe formula consists in a high-velocity approximation, it has served as a basis for the description of numerous ion energy-loss experiments in plasma. Indeed, most experiments were carried out at high projectile velocities. The Bethe description can also be, to a certain extent, applied to intermediate projectile velocities if adequate correction factors are added, as already mentioned for cold matter.

#### – Bloch correction

One usual correction to the Bethe formula to extend the considered impact-parameter domain is the Bloch term. It adds closer collisions that are present in the Bohr description. It was introduced by Bloch in 1933 [Blo33] and is extensively described in e.g [LS96]. It "bridges the gap" between the quantum-mechanical description at large impact parameters (for which the projectile is only a small perturbation on the target electrons) and the classical description at smaller impact parameters, where

the perturbation is not necessarily small. When the Bohr parameter  $\eta = Z_p v_0 / v_p$  becomes larger than 1, small impact parameter events must be taken into account, which is notably the case at intermediate projectile velocity. In that case, to include these close collisions, the Bloch correction term has to be added to the Bethe Coulomb logarithm, enabling to recover the Bohr result. The corrective Bloch term is:

$$L_{Bloch} = \psi(1) - \text{Re}[\psi(1 + i\eta)] = \sum_{k=1}^{\infty} \frac{1}{k} \frac{\eta^2}{k^2 + \eta^2} \quad (2.55)$$

where  $\psi(1) = -\gamma = -0.57721$ ,  $\gamma$  is the Euler-Mascheroni constant and  $\psi$  designates the Digamma function, i.e the logarithmic derivative of the Gamma function.

By extending the Bethe regime to closer collisions and lower velocities, the Bloch term enables to access a quantum stopping-power description beyond the basic perturbation theory. It can be noted that, similarly, the Bohr regime can be extended with the help of an inverse Bloch correction in order to recover the Bethe regime for large impact parameters, as is done e.g in the binary stopping theory [SS00, SS02].

#### – Barkas correction

Furthermore, a second correction term can be considered that makes it possible to go beyond perturbation theory. It is the Barkas correction, which takes the local plasma polarization by the projectile into account. This effect, discovered by Barkas and Andersen in 1963 [BDH63], is responsible for different stopping-power values between charged particles and their anti-particles. Indeed, a positively charged projectile ion tends to attract plasma electrons; this polarization effect leads to an enhanced free-electron density in the vicinity of the projectile and thus to a slightly enhanced stopping power. Conversely, a negatively charged ion repels electrons from its trajectory, which results in a weaker stopping power. The Barkas effect becomes significant for projectile energies below 1 MeV/u. More details on the Barkas term can be found in [SS03]. An expression of the Barkas correction in a fully-ionized plasma is given by [PREZ93]:

$$L_{Barkas} = \frac{3\pi e^2 \omega_p}{2m_e v_p^3} \ln \left( \frac{2m_e v_p^2}{\hbar \omega_p} \right) \quad (2.56)$$

#### – Thermal correction

A further correction has to be added when considering ion velocities near or below  $v_{th}$ , which actually enables to describe the maximum in the stopping formula at  $\frac{v_p}{v_{th}} \approx 1$ . Indeed, while the stopping-power model basing on the Bethe formalism as described until now diverges towards  $+\infty$  for low velocities, the introduction of the Chandrasekhar thermal correction factor (or temperature coupling parameter)  $G(\frac{v_p}{v_{th}})$  [Cha43, Cha60] in the general formula, makes the stopping power approach zero when  $v_p$  approaches zero. Consequently, the stopping curve reaches a maximum at  $\frac{v_p}{v_{th}} \approx 1$ . The  $G$  function can be viewed as a measure of the strength of the Coulomb interaction between the projectile and the plasma. It is present in several stopping theories (see 2.2.4 and 2.2.5) and is expressed by:

$$G(x) = \text{erf}(\sqrt{x}) - 2\sqrt{\frac{x}{\pi}} \exp(-x) \quad (2.57)$$

where  $\text{erf}$  is the error function. The evolution of  $G(\frac{v_p}{v_{th}})$  is plotted in Fig. 2.5. It can be seen that for  $v_p \gg v_{th}$ ,  $G \approx 1$  and does not have any influence on the stopping power. Coming to the region of lower velocities,  $G$  becomes smaller and reaches zero at zero velocity, correcting the asymptotic Bethe formula at low projectile velocity

and thus accounting for the stopping maximum at  $\frac{v_p}{v_{th}} \approx 1$  (here at  $\approx 1.6$  because  $v_{th} = \sqrt{\frac{k_B T_e}{m_e}}$ ).

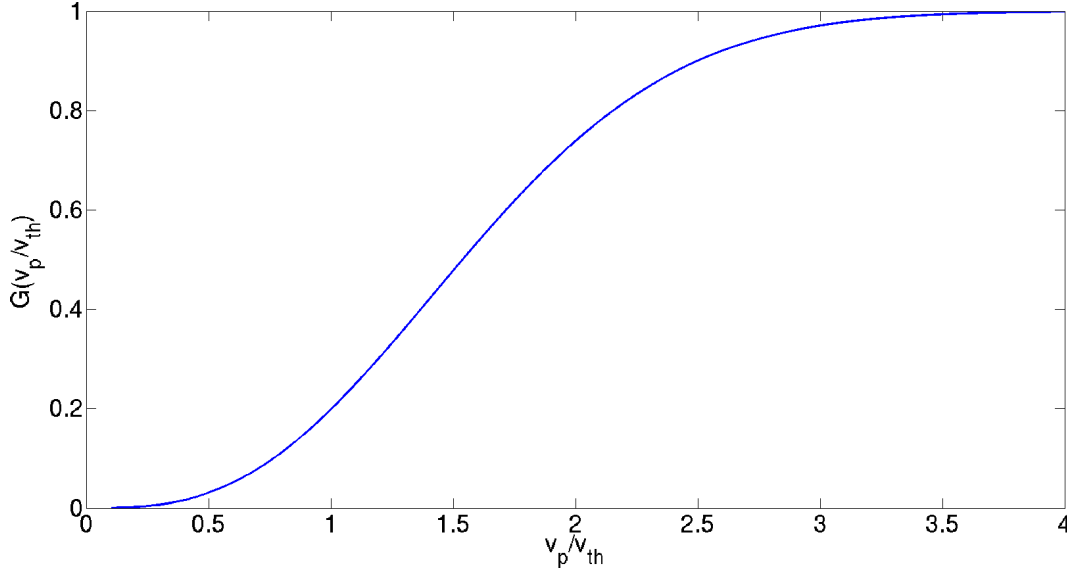


Figure 2.5:  $G(\frac{v_p}{v_{th}})$  for  $\frac{v_p}{v_{th}}$  varying from 0 to 4. When  $\frac{v_p}{v_{th}} = 4$ ,  $G \approx 1$  and has no influence. For lower ion velocities,  $G$  decreases significantly, enabling to describe the stopping maximum if combined with a Bethe-like ansatz.

#### – Standard stopping model in plasma

The corrected Bethe formula can be applied to the whole velocity spectrum, where  $Z_p$  is usually taken as the effective charge  $Z_{eff}$ . The complete expression of the stopping power in a fully ionized plasma is thus obtained by adding the Bloch and Barkas contributions to the Bethe Coulomb logarithm, and multiplying the expression with the factor  $G(\frac{v_p}{v_{th}})$ . This expression constitutes the *Standard Stopping Model* (SSM) and has been used for many practical cases in the interpretation of experiments [CDN<sup>+</sup>94, JHL<sup>+</sup>95, RSS<sup>+</sup>00, DMC<sup>+</sup>]. For experiments at high ion energies,  $G \approx 1$  and can thus be neglected.

$$\left(\frac{\partial E}{\partial x}\right)_{SSM} = -\frac{Z_p^2 e^2 \omega_p^2}{v_p^2} G\left(\frac{v_p}{v_{th}}\right) \left[ \ln\left(\frac{2m_e v_p^2}{\hbar \omega_p}\right) + L_{Bloch} + Z_p L_{Barkas} \right] \quad (2.58)$$

The Barkas contribution scales with the projectile charge as  $Z_p^3$ , whereas the Bloch term depends on  $Z_p^4$ . Both corrections quickly become negligible at high projectile velocities.

While the SSM makes it possible to extend the domain of validity of the Bethe formula, it remains limited to intermediate velocity regimes where the perturbation induced by the projectile on the plasma electrons is still moderate. The SSM is indeed an extension of the high-velocity stopping formulation in cold matter, with ad-hoc corrections for the plasma case. It remains hence an approximate phenomenological model, quite accurate at high projectile velocity but likely to be inappropriate around the stopping maximum.

#### • Modifications of the projectile charge state

The presence of free electrons in addition of bound electrons also induces important changes in the diverse charge-transfer processes and thus on the resulting charge-state distribution

of an ion beam interacting with the plasma. Not only are the cross sections of the previously described charge-transfer processes modified, but also new ionization and recombination processes of the projectile appear, as depicted in Fig. 2.6.

Ionization by Coulomb collisions with target ions remains the dominant ionization mechanism. As the electric potential of the target ions is now less screened because of the ionization of the target, the cross section for this process is enhanced in plasma.

NREC remains the main recombination mechanism as long as the plasma has not reached a high ionization degree. Indeed, the main contribution to NREC comes from recombination with target electrons from the most inner shells of the target atoms, particularly the K-shell. As soon as the electrons from the K-shell of the target ions start becoming free due to the increasing ionization degree, the cross-section of NREC is strongly reduced. In a fully-ionized plasma, NREC thus disappears.

Concerning REC, its cross section in plasma increases due to the presence of more numerous free electrons that can be captured.

Moreover, a new projectile ionization process appears in plasma, namely ionization by free plasma electrons. For this mechanism to take place, the energy of the projectile and/or of the free electrons has to be sufficiently high. The higher the plasma temperature, the higher the thermal energy of the plasma electrons and the more probable is a ionization by means of free plasma electrons.

Furthermore, two additional recombination mechanisms are present in plasma: dielectronic recombination and three-body recombination.

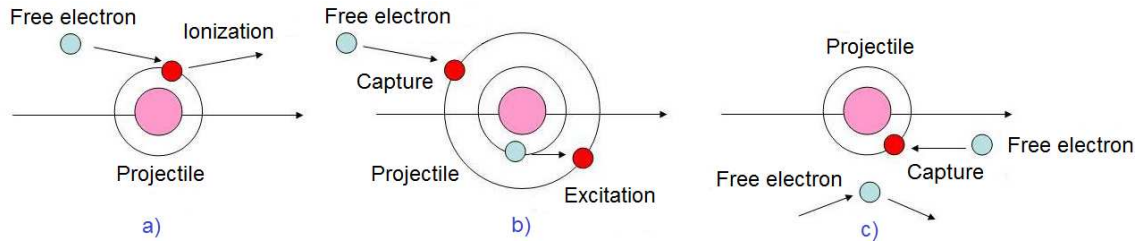


Figure 2.6: Additional charge-exchange processes arising for a projectile ion in plasma: a) ionization by free plasma electrons, b) dielectronic recombination and c) three-body recombination.

Dielectronic recombination consists in the excitation of a bound projectile electron during the capture process of a free electron by the projectile. The energy gained by the capture process is not directly converted into radiation to ensure energy and momentum conservation like in REC, but this energy is transferred to a bound electron of the projectile. This process is only possible if a precise resonance condition is fulfilled. Indeed, the sum of the kinetic energy  $E_k$  of the free electron and of the binding energy  $E_b$  of the bound electron has to equal the excitation energy  $E_i - E_j$  of the bound electron between the energy levels  $i$  and  $j$ :

$$E_k + E_b = E_i - E_j \quad (2.59)$$

Consequently, a doubly excited state is created, whose decay can occur in two different ways. Either a photon is emitted from the excited bound electron, or a secondary electron is ejected from the atom in an Auger process. Hence, in this second case, there is actually no recombination taking place. Dielectronic recombination is the dominant recombination process in a hot highly ionized plasma [PM91b]. As the resonance condition requires a high plasma temperature, REC dominates instead if the plasma is highly ionized but of

moderate temperature.

Three-body recombination is only significant for dense plasmas. Indeed, in a low-density plasma, the ionization and recombination processes always occur as binary collisions. As mentioned in section 2.2.1, the recombination of the projectile with a free plasma electron in these conditions is improbable, as a third partner is usually missing to guarantee momentum and energy conservation. However, when the plasma density is higher, the probability that another free electron is available in the vicinity of the interaction is increased. This electron can play the role of the third collision partner. Three-body recombination only has an important contribution in a very dense plasma. Even then, the cross section of this process remains significantly smaller than that of REC or NREC.

Mainly due to the reduced cross section of the NREC process in plasma (and even its complete suppression in a highly ionized plasma) and to the increased cross section of ionization by Coulomb collisions with the target ions, the equilibrium charge state  $Q_{eq}$  of the projectile is enhanced in plasma in relation to cold matter. This was predicted theoretically in [NZ82] and demonstrated experimentally in e.g [DHB<sup>+</sup>92].

- **Plasma effect**

In conjunction with the increase in the Coulomb logarithm, this leads, because of the quadratic (or a bit weaker) charge dependence of the stopping expression, to a substantial increase of the ion stopping-power in plasma in relation to cold matter. This *plasma effect*, which is all the stronger when the plasma ionization grade increases, has been regularly observed and characterized experimentally. For example, in [DHW<sup>+</sup>90] and [HWW<sup>+</sup>90], experiments at GSI with highly ionized hydrogen plasma and  $v_p \gg v_{th}$  demonstrated an enhancement of a factor 2-3 depending on the projectile ions. A few years later, similar experiments with much slower ions, close to the stopping maximum in plasma, revealed an extreme stopping enhancement in this parameter region, reaching a factor of up to 35-40 [JHL<sup>+</sup>95, JBF<sup>+</sup>96] in the considered beam-plasma configuration.

- **Nonequilibrium charge state**

Here it is also important to note that, while  $Q_{eq}$  is higher in a plasma than in cold matter, this equilibrium value is not necessarily reached in the interaction. In cold matter, the characteristic time scale of the charge-transfer processes lies significantly below the time scale of the stopping process. Therefore, except for a very thin target, a projectile ion always reaches its equilibrium charge-state value, that only depends on its velocity. In a highly ionized plasma, the situation is quite different. Mainly due to the vanishing of the NREC mechanism, the characteristic time of charge transfer is increased, and lies on the same level as the time scale of the stopping process. In a highly ionized plasma, the projectile thus does not systematically reach its equilibrium charge-state value. Hence, nonequilibrium charge states are likely to arise, especially around and below the stopping-power maximum. This can lead to a further increase of the charge-state value and thus of the stopping power [PM91b].

This fact points out the need for a self-consistent charge-state description by solving the rate equations for the charge-state distribution simultaneously to the stopping-power calculation. This is the purpose of the Monte-Carlo code that is presented in section 3.1.3.

A basic description of the ion stopping power in plasma has been presented, basing on an extension of the Bethe formalism for cold matter to ionized matter. The resulting expression, constituting the standard stopping model (SSM) is able to explain most of experiments on ion stopping to date. However, the SSM remains an approximation that has been constructed for the case of relatively high projectile velocities. It may lead to erroneous results in the region



of the stopping-power maximum, where close collisions and important collective effects may be present simultaneously and where the projectile-plasma coupling can be strong (see 2.2.3 and 3.2.1). The SSM may thus be inappropriate in this velocity regime.

Therefore, more advanced theoretical approaches are required to properly describe the ion stopping power in the region of stopping maximum. Both the projectile-plasma coupling and the nature of the interactions have to be taken into account. This is the purpose of the next sections, where a rigorous theoretical description of the stopping power is addressed depending on the plasma and beam-plasma parameters. On this basis, a state-of-the-art of ion-stopping theories in plasma is finally presented.

### 2.2.3 Characterization of the beam-plasma interaction

The various theoretical descriptions essentially depend on two parameter scales. First, they depend on the regime of ion-plasma interaction, that is defined by the strength of the beam-plasma correlations. These are the so-called *linear*, *semi-linear* and *nonlinear* regime of the beam-plasma interaction, where *linear* is a synonym for *perturbative*. Second, the different theoretical descriptions depend on the considered impact-parameter domain, i.e whether short-range collisions (elastic or inelastic Coulomb scattering) or long-range collective effects (plasmon excitation, plasma polarization, dynamic screening) are concerned.

To be comprehensive, a description of the stopping power has therefore to take both perturbative and non-perturbative effects into account, and to consider both short-range and long-range projectile-electron encounters. As is explained in 2.2.5, this has not been achieved yet and each parameter region has its dedicated modeling. The unification of all these parameter ranges within one theory remains very challenging.

In this section, the parameters characterizing the beam-plasma interaction are introduced. On this basis, the strength of the perturbation induced by the projectile ions on the plasma medium, i.e the linearity of the interaction, is estimated. Hence, three interaction regimes, from weak to strong coupling between the projectile and the target, are correspondingly established. In this way, perturbative and nonperturbative stopping-power descriptions can then be defined.

#### Beam-plasma parameters

Let us consider a homogeneous plasma slab at electron density  $n_e$ , electron temperature  $T_e$  and ionization degree  $Z_T$ , that is probed by projectile ions at velocity  $v_p$ , energy  $E_p$  and charge-state  $Z_p$ . This plasma has a thermal electron velocity  $v_{th}$  and  $v_r = |v_p - v_{th}|$  is the relative velocity between the projectile and the nondegenerate plasma electrons.  $\lambda_r = \frac{\hbar}{m_e v_r}$  is the quantum De Broglie wavelength associated to the interaction, where  $m_e$  is taken instead of the reduced mass  $\mu$  because  $m_i \gg m_e$ . This De Broglie wavelength is the distance in plasma under which quantum effects play a dominant role in the projectile-electron interaction. Besides, the projectile ion is screened in plasma according to the screening length  $\lambda(v_r)$  which describes the collective plasma motion. The impact parameter in the projectile-ion Coulomb scattering interaction is noted  $b$ . An important parameter in the following discussion is the impact parameter corresponding to a Coulomb deflection of  $90^\circ$  between the projectile and the electron (the equivalent of the Landau length for the target electrons) and representing the classical distance of minimal approach between the projectile and a target electron. It is noted  $b_0$ , and is expressed as:

$$b_0 = \frac{Z_p e^2}{m_e v_r^2} \quad (2.60)$$

where the electron mass  $m_e$  is again written instead of the reduced mass  $\mu$  of the projectile-electron system. The quantities  $v_r$ ,  $\lambda_r$  and  $b_0$  are averages over the plasma electron distribution in order to account for the projectile-plasma interaction. The projectile-electron interaction is

depicted in Fig. 2.7.

From the characteristic lengths of the projectile-plasma interaction  $\lambda_r$  and  $b_0$ , a non-dimensional parameter  $\eta$  can be defined, called Coulomb parameter:

$$\eta = \frac{b_0}{\lambda_r} = \frac{Z_p e^2}{\hbar v_r} \quad (2.61)$$

$\eta$  describes the transition between the classical and the quantum-mechanical regime. If  $\eta \ll 1$  (low charge and high projectile velocity), the interaction has to be treated quantically, whereas if  $\eta > 1$  (for lower projectile velocities or higher charges), the interaction can be described in a classical way [Zwi99].

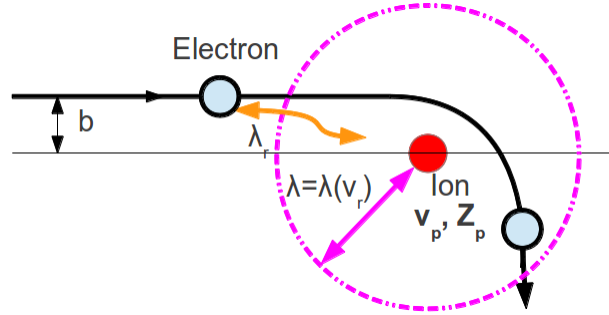


Figure 2.7: Scheme of the projectile-plasma interaction. A projectile ion with velocity  $v_p$  and charge state  $Z_p$  interacts, at impact parameter  $b$ , with a plasma electron at thermal velocity  $v_{th}$ . The relative ion-electron velocity is  $v_r$  and the electron is scattered on the projectile ion. The local interaction can be characterized by using the De Broglie wavelength of the interaction  $\lambda_r$ , while the interaction with the whole plasma zone surrounding the electron can be measured with the help of the screening length  $\lambda$  of the plasma.

### Projectile-plasma coupling

The coupling strength of the interaction can be defined in two respects. It has to be distinguished between the correlation strength among plasma electrons (plasma nonideality) and the correlation between the projectile and the plasma electrons (nonlinearity of the interaction). The electron-electron coupling depends exclusively on the plasma properties ( $n_e$ ,  $T_e$ ), while the projectile-plasma coupling depends on the parameters of the projectile (chiefly), and of the plasma target. In particular, it also depends on the electron-electron coupling of the plasma target if the perturbation is strong. Depending on the projectile-plasma parameters, the interaction can be either linear, weakly nonlinear or nonlinear and taking place in an either ideal or nonideal plasma.

Similarly to the definition of the nonideality parameter  $\Gamma$ , quantifying the strength of the target electron interactions as the ratio between the potential and the kinetic energy of the electrons, a parameter is defined for the strength of the projectile-electron interaction in plasma as the ratio between the potential and the kinetic energy of the projectile-electron system. The associated kinetic energy is

$$E_k = m_e v_r^2 \quad (2.62)$$

and the maximal potential energy (corresponding to the maximal perturbation) is the Coulomb potential between the projectile and the electron at a distance of  $\lambda_r$ :

$$V_{ie} = \frac{Z_p e^2}{\lambda_r} \quad (2.63)$$

It can be seen that the ratio  $V_{ie}/E_k$  is equal to the Coulomb parameter  $\eta$ . Therefore, not only does  $\eta$  give the limit of applicability between a quantum-mechanical and a classical approach, but it also measures the strength of the perturbation of the projectile on the plasma electrons, i.e the projectile-plasma coupling.

For  $\eta \ll 1$ , the induced perturbation is small and the interaction can be treated with the help of perturbative quantum mechanics. This defines the linear regime of the ion-plasma interaction. But for  $\eta \geq 1$ , where a classical approach is relevant, the perturbation induced on the medium becomes significant and a perturbative approach is therefore inadequate. Hence, the interaction is not linear anymore.

Here it can be noted that the Coulomb parameter actually corresponds to the Bohr parameter introduced in 2.2.1. Therefore the linear regime can be identified with the Bethe regime, while the Bohr regime corresponds to a stronger perturbation beyond the linear regime. It can also be noted that the Coulomb or Bohr parameter depends only on the relative velocity between the projectile and the electron and on the charge state of the projectile. So it features a dependence on the plasma electron temperature, but not on its density, thus not on  $\Gamma$ . The Coulomb parameter indeed represents a local criterion, estimating the perturbation on one plasma electron, which is adequate as long as the perturbation remains localized.

If the perturbation is more significant, it does not remain limited within one projectile-electron system but it influences an extended spatial zone around the projectile. Then, in order to describe the transition between a moderate perturbation ( $\eta > 1$  but localized) and a strong perturbation ( $\eta > 1$  and extended to a plasma region), a slightly different criterion has to be used. An estimation of the characteristic length of the perturbation is then the plasma screening length  $\lambda$ . Hence, in the expression 2.63 of the potential energy, the local De Broglie wavelength has to be replaced by the larger characteristic length  $\lambda$ . Here it is assumed that  $\lambda > \lambda_r$ , which is always the case in most applications [Zwi99]. The ratio  $\gamma$  of the potential and kinetic energy of the projectile-plasma system is:

$$\gamma = \frac{b_0}{\lambda} = \frac{\sqrt{3} Z_p \Gamma^{\frac{3}{2}}}{\left(1 + \left(\frac{v_p}{v_{th}}\right)^2\right)^{\frac{3}{2}}} \quad (2.64)$$

Due to the introduction of  $\lambda$  in the expression, a dependence on the plasma density and thus on  $\Gamma$  has now appeared.  $\gamma$  is called the nonlinearity parameter of the interaction and defines the borderline between the so-called semi-linear regime and the truly nonlinear regime. In the semi-linear regime ( $\gamma \ll 1$ ), the perturbation can be strong (if  $\eta > 1$ ) but stays restricted to a space region smaller than one screening length, in the vicinity of one plasma electron. In all other plasma regions, the perturbation remains small and the linear regime is valid. In the nonlinear regime, for  $\gamma > 1$ , the plasma is perturbed in a spatial region larger than the screening length.

To summarize, the problem can be understood in terms of characteristic lengths. The minimal classical collision radius  $b_0$  is associated to a strong perturbation, as a deflection of  $90^\circ$  then takes place in the Coulomb scattering process. In order to characterize the perturbation strength, this "distance of strong perturbation"  $b_0$  is compared to the two key plasma characteristic lengths: the distance under which quantum diffraction effects are important:  $\lambda_r$  and the distance over which the collective behavior of the plasma has to be considered:  $\lambda$ . The three interaction regimes are represented in Fig. 2.8. If  $b_0 \ll \lambda_r$ , the perturbation is small and the interaction is linear. If  $\lambda_r < b_0 < \lambda$ , the perturbation is small except in the vicinity of the interacting electron: the regime is semi-linear. Finally, for  $b_0 > \lambda$ , the perturbation is strong and the regime is nonlinear.

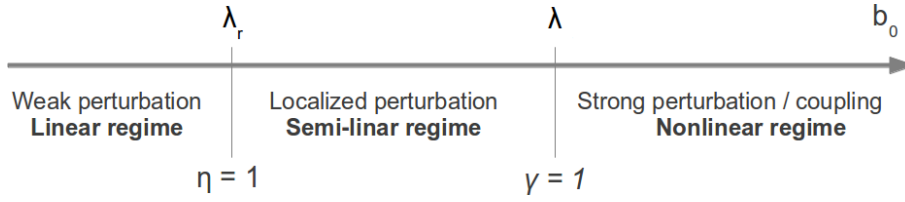


Figure 2.8: Characteristic regimes of the projectile-plasma interaction.

The linear regime, corresponding to a weak perturbation, is identified with the first Born approximation in scattering theory. The first Born approximation stipulates that the electric potential exerted on the scatterer (the perturbation) can be approximated by the incident potential of the projectile. The scattered field (the target response) is thus neglected. This situation precisely corresponds to a small perturbation of the target by the projectile.

Hence, if  $\eta \ll 1$ , a perturbative analysis relying on a first Born approximation in the quantum-mechanical theoretical frame can be applied. This is where the Bethe stopping formula is relevant. However, when  $\eta \approx 1$ , the first Born approximation starts losing its validity. Corrections can then be added like in the SSM as an attempt to extend the application range of the linear description. For  $\eta \geq 1$ , in the weakly nonlinear regime, perturbative approaches, corrected or not, are likely to fail. There, more advanced theories beyond the first Born approximation are necessary. The modeling is even more complicated in the nonlinear regime, in which strong coupling effects have additionally to be considered. The regime of interaction resulting from the beam-plasma configuration has therefore important consequences on the stopping-power description.

Each of these regimes of interaction can now be considered for various impact-parameter regions. Even if the impact parameter is statistically larger in an ideal plasma than in a nonideal plasma, all impact parameters are likely to contribute to the stopping process. Particularly at stopping-power maximum, both close collisions and collective effects have to be considered in the ion-plasma interaction.

Depending on the fact whether the plasma and more importantly the ion-plasma interaction are rather governed by close binary collisions or by long-range collective plasma motion, the theoretical approach to the ion stopping power is very different.

#### 2.2.4 Approaches to ion stopping power

Now, the different impact-parameter domains involved in the ion-stopping process are addressed and the corresponding theoretical frameworks are presented.

##### Stopping-power formalisms

Two general complementary formalisms for the description of ion stopping in plasma can be implemented, depending on the type of interaction considered between the projectile and the target electrons. At low projectile velocity, i.e at a relatively strong beam-plasma coupling, binary collisions are predominant, while at high projectile velocity, in a lower-coupled regime, collective effects are important. At intermediate projectile velocities and in particular around the stopping maximum, both close collisions and collective effects have to be taken into account. The linear-response approach can describe intermediate- to long-range interactions including collective plasma effects, while the binary-collision approach is able to describe close- to intermediate-range interactions. These two formalisms can then be generalized and combined in the frame of kinetic plasma theory.

- **Stopping power by long-range interactions: linear-response approach**

This formalism bases on a continuous medium description by using a dielectric function. It relies on the electrodynamics of polarizable media, within the linear response approach to many-body systems. The projectile ion is seen as generating an electrostatic perturbation polarizing the target medium in its wake. The polarized plasma responds by generating an electric potential on the ion, corresponding to the stopping force on the projectile. The designation *linear response* comes from the fact that the electric field exerted by the plasma on the projectile is simply proportional to the perturbing field of the projectile. In the frame of the linear response, the stopping power is therefore proportional to  $Z_p^2$ .

The dynamic target response is characterized by the dielectric function or equivalently by the density-density response function of the medium. The energy loss is then expressed with the help of the imaginary part of the inverse expression of the dielectric function. The dielectric formalism in particular contains all the many-body physics that describes collective plasma effects.

What is understood under *collective effects* encompasses plasmon excitation, dynamic screening and plasma polarization. Dynamic screening corresponds to a modification of the screening of the projectile charge by the surrounding plasma electrons that depends on the projectile velocity. This effect notably leads to a lowering of the ionization energy of the projectile that is inversely proportional to the projectile velocity [NMH09]. This influences the dynamics of ionization and recombination of the projectile and therefore its charge state and its stopping power. Plasma polarization corresponds to a local modification of the electron density in the vicinity of the projectile ion. It is a collective effect beyond the first Born approximation, described by the Barkas term, which is the second term in the perturbation series of the solution of the Lippmann-Schwinger equation in quantum scattering theory.

This dielectric formalism applies to any target material as long as the dielectric function is available and the projectile potential can be treated as a small perturbation. It is not able to describe strong perturbations and/or close collisions. Therefore nonlinear collective effects are analytically out of range within this approach. An attempt to include close collisions can be made by modifying the dielectric function of the medium [Bar10].

- **Stopping power by short-range interactions: binary-collision approach**

Alternatively, a binary-collision approach, that is particle-oriented instead of medium-oriented, can be applied. In that frame, the stopping power results from the accumulation of energy transfers (momentum change per time unit) from independent binary ion-electron collisions, averaged over all possible scattering events and ion-electron relative velocities. In contrast to the linear-response approach, the binary-collision picture is able to account for close collisions. However, as it is a two-body approach, collective effects are not described and have to be included artificially, typically by the choice of an appropriate ion-electron effective interaction potential.

- **Stopping power in kinetic plasma theory**

The most suited theoretical frame to derive the stopping-power expressions corresponding to collective interactions on the one hand and to binary collisions on the other hand, is the frame of kinetic plasma theory, because it is the only one that allows a generalization. In this formalism, the transport of projectile ions in plasma is described by a plasma kinetic equation that contains, in its right-hand side, a collision integral corresponding to the nature of the considered projectile-plasma interaction (see 2.1.1).

If  $f(p, t)$  is the distribution function of the beam particles, then for a homogeneous plasma without external fields, the kinetic transport equation of the ion beam in the plasma can

be written in the generic form:

$$\frac{\partial f}{\partial t} = \sum_c I_c \quad (2.65)$$

where the collision terms  $I_c$  (collision integrals) describe the interaction between the projectile ions of the beam and the species  $c$  of the plasma target. In the treated case, this encompasses only the interaction of the ions with the plasma electrons. In this frame, the ion stopping power is given by:

$$\frac{\partial E}{\partial x} = \frac{1}{n_e} \int \frac{dp}{(2\pi\hbar)^3} \frac{\vec{p} \cdot \vec{v}}{v} \frac{\partial f}{\partial t} \quad (2.66)$$

where  $\vec{v}$  is the beam velocity and  $\vec{p}$  the beam momentum.

Now, the various approximations for the collision integrals are described, and the corresponding theoretical descriptions of the stopping power, for arbitrary projectile velocities, are presented.

### Long-range interactions: the Lenard-Balescu stopping power

By applying the Random Phase Approximation (RPA) [Lin54b] in the general expression of the collision integral, the quantum Lenard-Balescu collision integral can be derived [Len60, Bal60]. It describes long-range plasma fluctuations due to density oscillations with the help of the RPA dielectric function [Lin54a, AB84], in an ideal plasma. The resulting RPA stopping-power expression thus includes the effects of all the collective plasma phenomena as well as of soft to moderate collisions in the stopping description.

As the nonlinear description of the interaction is very difficult and cannot be explicitly derived [GS03], the Lenard-Balescu stopping power is always calculated in the first Born approximation, being thus limited to the linear regime of the beam-plasma interaction. The first-Born Lenard-Balescu stopping power in the frame of quantum scattering theory, or Born-RPA stopping power [MD85], also called  $V^S$  approximation to the stopping power by some authors, is given by:

$$\frac{\partial E}{\partial x} = -\frac{2Z_p^2 e^2}{\pi v_p^2} \int_0^{+\infty} \frac{dk}{k} \int_{\frac{\hbar k^2}{2m_e} - kv}^{\frac{\hbar k^2}{2m_e} + kv} d\omega \left( \omega - \frac{\hbar k^2}{2m_e} \right) \text{Im} \left( \frac{1}{\epsilon_{RPA}}(k, \omega) \right) n_B(\omega) \quad (2.67)$$

$k$  and  $\omega$  are the wave number and the circular frequency of the scattered wave of the projectile ion respectively, while  $\epsilon_{RPA}$  is the RPA dielectric plasma function and  $n_B$  is the Bose distribution function of the plasmons. This Born-RPA description, valid for a linear ion-plasma interaction in an ideal plasma, is the standard weak-coupling approach that has been used in the last decades to interpret experimental investigations. It is nearly equivalent to the SSM, which encompasses higher-order corrections but remains less rigorous and rather suited for high velocities.

A special simplified case of the Lenard-Balescu equation is given by the Vlasov kinetic equation, where plasma collisions are neglected. The Vlasov stopping power (or dielectric stopping power in its simplest expression) can be estimated by using the approximation formula 2.68, as derived from the analytic expression of [PM91a]. There  $G$  is again the Chandrasekhar factor, and  $H$  is another analytic function (see [PM91a] or [AMtV04]). This stopping power can be derived either from a simplification of the Lenard-Balescu expression, or by solving analytically the linear Vlasov-Poisson equation system.

$$\frac{\partial E}{\partial x} = -\frac{Z_p^2 e^2 \omega_p^2}{v_p^2} G \left( \frac{v_p}{v_{th}} \right) \ln \left( \frac{\lambda_D}{b_0} \right) + H \left( \frac{v_p}{v_{th}} \right) \ln \left( \frac{v_p}{v_{th}} \right) \quad (2.68)$$

When the projectile velocity is very high, both the Lenard-Balescu and the Vlasov stopping power can be further simplified, leading to the Bethe-formula (equ. 2.53). In this high-velocity regime, collective effects and especially the excitation of plasma waves play an important role in the interaction.

### Short-range interactions: the T-Matrix stopping power

For the description of short-range interactions between the projectile and the plasma electrons, including strong collisions, a Boltzmann collision integral is the relevant ansatz. As only two-body effects are considered, this equation is derived by applying a binary-collision approximation in the general kinetic equation [KSB85]. This scheme can be implemented in the framework of a T-Matrix approach, leading to a so-called T-Matrix model of the stopping power. The scattering cross sections of the Coulomb interaction are calculated by using a T-Matrix scheme in the Lippmann-Schwinger equation. The analytic expression of the stopping power in the T-Matrix approximation, [GS99, MR96] is:

$$\frac{\partial E}{\partial x} = -\frac{m_e^2}{\mu^3} \frac{n_e \lambda_e^3}{(2\pi)^2 \hbar^3} \frac{k_B T_e}{v_p} \int_0^{+\infty} dp p^3 Q_{bc}^T(p) \cdot \left[ p_- \exp\left(-\frac{m_e v_-^2}{2k_B T_e}\right) - p_+ \exp\left(-\frac{m_e v_+^2}{2k_B T_e}\right) \right] \quad (2.69)$$

with  $p_{\pm} = 1 \pm \frac{\mu k_B T_e}{m_e p v_p}$  and  $v_{\pm} = \frac{p}{\mu} \pm v_p$ , where  $p$  is the projectile momentum. The essential quantity in equation 2.69 is the transport cross section  $Q_{bc}^T(p)$  of the scattering process of the projectile ions on the target electrons. For a nondegenerate plasma,  $Q_{bc}^T(p)$  can be determined by employing the scattering phase shift method, where the scattering phase shifts are numerically obtained by solving the radial Schrödinger equation [GS99]. The T-Matrix calculation is restricted to a screened projectile Coulomb potential with spherical symmetry, i.e to the static screening case. Hence, the collective plasma motion is ignored. Yet, contrarily to the Lenard-Balescu stopping-power, the T-Matrix expression constitutes a nonlinear description, without restriction on the coupling strength.

If only the first Born approximation of the transport cross section  $Q_{bc}^T(p)$  is considered, a perturbative stopping-power formula dealing with binary collisions in the static screening case can be derived [GS99, MR96]. It corresponds to the Landau collision integral. Its domain of applicability yet remains limited to intermediate impact parameters. Indeed, it cannot deal with collective effects, and being perturbative, it cannot deal with the strong collisions, which are nonlinear. The Landau equation and the Lenard-Balescu equation are the most used kinetic equations for the description of interactions in plasma. Both are perturbative as they are not able to describe strong collisions and/or strong collective effects. The one features static screening and includes moderate to weak binary collisions but no long-range effects, whereas the second one features dynamic screening and includes long-range effects (weak collisions). It can be noted that both the Lenard-Balescu (RPA) and the Landau kinetic equations correspond to a Fokker-Planck kinetic framework, suited for small-angle-scattering particle interactions. The validity domains of the RPA, T-Matrix and Landau approaches in terms of impact parameter are shown in Fig. 2.9.

### 2.2.5 Unified stopping description in plasma

In order to reach a complete stopping-power description, which is particularly needed at maximum stopping power, the contributions of both short-range and long-range effects to the stopping power have to be considered. Several combined approaches have been proposed.

- **Li-Petrasso stopping model**

One idea comes from Li and Petrasso [LP93a], who, starting from an expression in the frame of a Fokker-Planck kinetic equation on the level of the Landau approximation, add

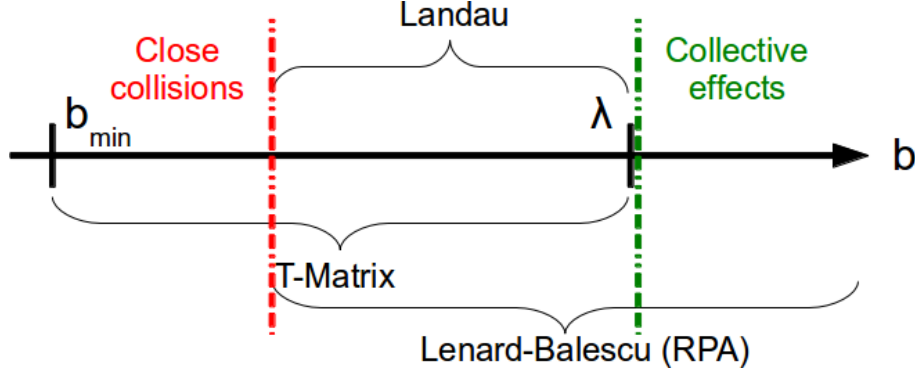


Figure 2.9: Impact-parameter diagram showing the realms of the T-Matrix, Landau and RPA stopping-power descriptions. The T-Matrix describes all collisions but no collective effects, the RPA approach describes all long-range interactions including collective effects but ignores close collisions, and the Landau expression includes neither close collisions nor collective effects.

both a close collision term and a collective term to extend the description over the whole energy spectrum:

$$\frac{\partial E}{\partial x} = -\frac{Z_p^2 e^2 \omega_p^2}{v_p^2} G \left( \left( \frac{v_p}{v_{th}} \right)^2 \right) \ln \left( \frac{\lambda_D}{b_{min}} \right) + \Theta \left( \left( \frac{v_p}{v_{th}} \right)^2 \right) \ln \left( 1.123 \frac{v_p}{v_{th}} \right) \quad (2.70)$$

$G$  is similar to the Chandrasekhar thermal correction factor with additional higher-order terms to treat close collisions (large-angle scattering) [LP93b]. Collective effects are modeled by a logarithmic term added with the help of a step function  $\Theta$ . The thermal velocity is taken as the most probable velocity value of the Maxwellian electron velocity distribution,  $v_{th} = \sqrt{\frac{2k_B T_e}{m_e}}$  and  $b_{min}$  is determined by a quadratic interpolation between  $b_0$  and  $\lambda_r$ . The model of Li and Petrasso, valid for a fully-ionized plasma, has been widely used in ICF calculations as e.g in [HL01], where it has become a standard ion energy deposition model. However, it is only valid for a small perturbation, thus in the linear regime of ion-plasma coupling.

- **T-Matrix with  $\lambda(v)$**

Another possibility is to "artificially" include dynamic screening and thus collective plasma excitations in the frame of a T-Matrix approach. This can be achieved by the choice of an appropriate ion-electron effective interaction potential [Zwi99]. A parametrization using Yukawa functions can for example be applied. Alternatively, a velocity-dependent screening length can be introduced to model dynamic screening, as proposed in [Zwi99] and implemented in [GSB02, GS03]. In this example, the inverse screening length  $\kappa$  is taken as shown in equation 2.71, where  $\kappa_D$  is the inverse Debye length.

$$\kappa = \kappa_D \left( 1 + \left( \frac{v_p}{v_{th}} \right)^2 \right)^{-\frac{1}{2}} \quad (2.71)$$

In [GSB02], the author combines this screening ansatz with the static T-Matrix model. The transport cross section in equation 2.69 then becomes  $Q_{bc}^T(p, \lambda(v_p))$ . A fit formula for the resulting stopping power is provided and the results are notably compared with those of the combined scheme.



- **Combined scheme**

In the frame of kinetic theory, a so-called *combined scheme* [GS99, MR96, MZDK01] can be used to include both short-range and long-range effects, by properly combining the corresponding collision integrals. This idea has first been developed by Gould and DeWitt [GD67], hence also the name "Gould-DeWitt scheme". It results in the stopping-power expression:

$$\frac{\partial E}{\partial x} = \left( \frac{\partial E}{\partial x} \right)^{T-Matrix} + \left( \frac{\partial E}{\partial x} \right)^{RPA}_{BornI} - \left( \frac{\partial E}{\partial x} \right)^{T-Matrix}_{BornI} \quad (2.72)$$

The first term describes binary interactions by the T-Matrix theory, for  $b \lesssim \lambda$ . The second term corresponds to long-range interactions in the Born-RPA approximation for  $b \gtrsim b_0$ . In order to avoid double counting, the stopping power for  $b_0 \leq b \leq \lambda$  is subtracted, i.e the Landau stopping power. This can be well-understood with the help of the impact-parameter domains of Fig. 2.9. In this way, all stopping effects, except collective processes beyond the first Born approximation, are included. The Lenard-Balescu stopping power and the T-Matrix stopping power can both be obtained as special cases of this scheme. At large projectile velocities, the first Born approximation becomes valid in the T-Matrix description, hence the full T-Matrix term and the Landau term compensate each other and only the dielectric RPA stopping power remains. In contrast, at small projectile velocities, the collective plasma behavior becomes negligible, hence the RPA and the Landau stopping power compensate each other in the expression, leaving the full static T-Matrix result. The most complicated case occurs when neither the RPA result nor the T-Matrix result dominates, i.e at intermediate velocities and in particular around the stopping-power maximum.

- **BPS stopping theory**

Another recent theory uses a combination of the Lenard-Balescu and Boltzmann equations, based on the method of dimensional continuation. This so-called BPS approach (Brown, Preston, Singleton) provides exact perturbative stopping results in highly ionized plasmas. It is valid for all projectile velocities and charge-state values, as long as the plasma is ideal. It notably makes it possible to eliminate some shortcomings present in other models. The derivation method as well as the results are explained in details in [BPS05, Sin08].

- **Numerical simulations**

In some cases of strong perturbation and/or of strong plasma coupling, the available theories may be inefficient in making correct predictions. Then, numerical simulations of the ion stopping power can be carried out to access parameter regions out of reach of the existing theories or to give a complementary approach.

To evaluate the nonlinear stopping power in the realm of the long-range interactions corresponding to the Lenard-Balescu description, as long as the plasma is ideal, PIC/VP simulations can be conducted. As the Lenard-Balescu stopping power beyond the first Born approximation is not within analytic reach, PIC simulations are actually the only tool that can access this part of the stopping spectrum. Nonlinear plasma polarization and nonlinear projectile screening are the main corresponding effects. Strictly speaking, PIC simulations can simulate only collective effects on the level of the Vlasov equation as they consist in a mean-field treatment, but if collision modules are added, the effects of (moderate-range) collisions can be included, and the calculation can potentially cover the whole range of the Lenard-Balescu equation (as in the PICLS code used at CELIA [SK08]). VP calculations [Boi96] as well as PIC simulations [DHL98] have been carried out in the past two decades for the determination of the nonlinear ion stopping power in plasma and

are in good agreement with each other [DHL98].

While PIC and VP simulations work in the case of an ideal plasma, only MD computations can access the regime of strong collisions, i.e. of a nonideal plasma. So both methods can describe nonlinearity properly, but only MD simulations can treat nonideality by including all particle correlations.

Now, a summary on the different theoretical stopping-power approaches is presented.

### 2.2.6 Summary on ion stopping in plasma

The different theoretical approaches to the stopping power are schematically summarized in Fig. 2.10 as a function of the ion-plasma coupling as well as of the impact-parameter regime of the interaction. In this way, the domains of applicability of the different theories are highlighted.

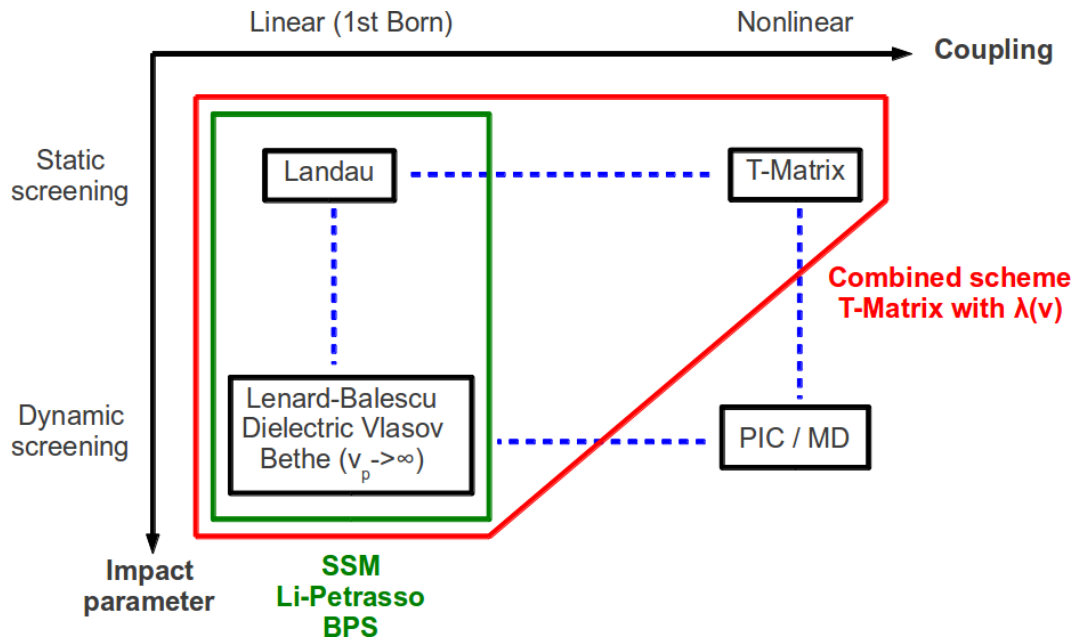


Figure 2.10: Overview of the modern stopping theories. While some approaches such as the Lenard-Balescu stopping power correctly describe the collective interaction (dynamic level) though only in the linear frame, other approaches like the T-Matrix allow the description at any perturbation strength but only for a statically screened projectile potential, thus neglecting all collective phenomena. A unified description must include both close collisions and dynamic screening, within a nonlinear description. Only the combined scheme and the T-Matrix with  $\lambda(v)$  take all these effects into account, if nonlinear collective phenomena are disregarded.

Furthermore, to assess the validity of the different stopping theories, extensive numerical simulations using VP and MD methods have been carried out in [Zwi99, Zwi02], and have then been compared to various theoretical approaches for different beam-plasma configurations [GS99, GS03]. The associated stopping-power results are shown in Fig. 2.11.

First, it can be seen that the various theories are in good agreement at high projectile velocity but show quite important discrepancies between each other at lower velocity, reaching 30 – 50 % around the stopping maximum. These discrepancies tend to increase with the plasma coupling, as can be recognized by comparing Fig. 2.11.a) and Fig. 2.11.b).

Second, the numerical simulations predict significantly lower stopping-power values than most theories at stopping maximum. The Bethe, RPA (Lenard-Balescu) and Fokker-Planck (Li and Petrasso) formulas, which are all perturbative approaches, over-evaluate the stopping power.

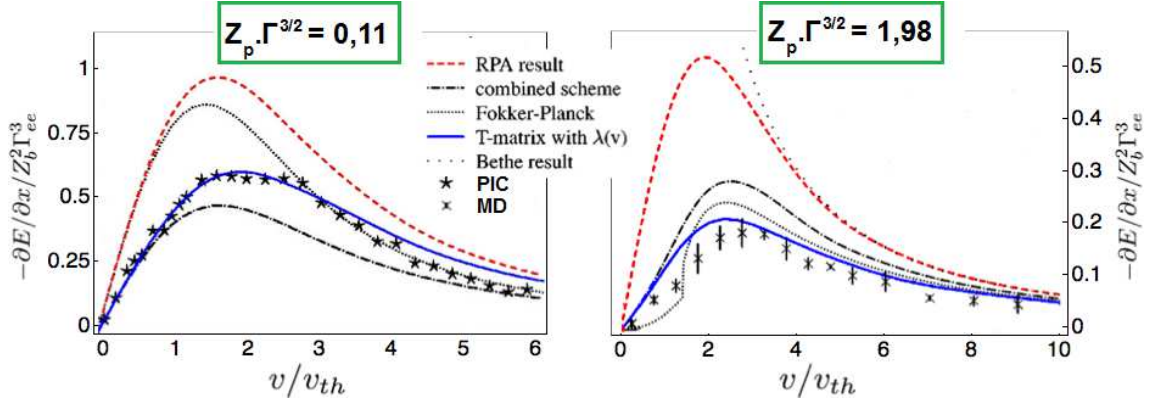


Figure 2.11: Comparison of various stopping theories: Bethe, Fokker-Planck (Li-Petrasso), RPA, combined scheme using static T-Matrix, T-Matrix with  $\lambda(v)$ , with PIC and MD simulations. The graphs come from [GS99, GS03] and correspond to two different strongly-coupled projectile-plasma configurations. The discrepancies between the theories tend to increase with a growing coupling strength  $Z_p \Gamma^{3/2}$  (maximum  $\gamma$  value, for zero velocity, when disregarding the factor  $\sqrt{3}$ ). In the left case,  $\gamma$  extends from 0.2 to  $8 \cdot 10^{-4}$  and in the right case from 3.43 to  $3 \cdot 10^{-3}$ . The T-Matrix ansatz with  $\lambda(v)$  is in good agreement with the numerical results.

These results are compared with the combined scheme and the T-matrix approach with  $\lambda(v)$ , which as described previously attempt to provide a unified stopping description. It appears that at the maximum, the combined scheme predicts stopping values different by 20-25 % from these of the T-Matrix ansatz with  $\lambda(v)$ . The T-Matrix with  $\lambda(v)$ , alone, is in quite good agreement with the numerical simulations.

To our knowledge, no experimental data exist for the test and the benchmarking of the theories in that projectile-velocity range. Yet, in view of the considerable discrepancies between the various predictions, experimental data are strongly needed for theory discrimination.

It has to be noted that the predictions of Fig. 2.11 have been calculated for a quite strongly coupled plasma, where the theoretical uncertainties are particularly large. Yet, to date, ion-stopping experiments at maximum stopping power at strong beam-plasma coupling are still out of reach (see also 6.2). Nevertheless, discrepancies of the same order of magnitude are expected around the stopping maximum in a hot ideal plasma, as is calculated in section 3.2. Also at stopping-power maximum in a hot ideal plasma, the ion-plasma interaction is likely to feature strong Coulomb coupling, a nonequilibrium charge-state behavior and both strong collisions and important collective excitations. Hence, even in an ideal plasma the description of the stopping maximum remains challenging, and the theoretical as well as the computational approaches also need to be benchmarked by experimental data in this simpler case.

The experimental access to ion stopping at maximum stopping power is now possible in a laser-generated plasma at GSI following recent progress in ion energy-loss experiments.

As mentioned at the beginning of this chapter, laser-induced plasmas have two major advantages. On the one hand, they are able to provide ICF-relevant plasma conditions, where the stopping theories feature uncertainties and need experimental benchmarking. On the other hand, if a convenient setup is used, this plasma can stay at quasi-uniform hot and dense conditions for a time of several nanoseconds, allowing reliable stopping measurements. Such a laser-generated plasma is thus well-suited for testing the different stopping-power theories, which motivates its use in the present work. The purpose of the following parts of this work is thus to define, simulate and carry out an experiment at maximum stopping power in a laser-generated plasma, whose

energy-loss results can be compared with the theories described previously.

Next chapter is devoted to simulations aiming at defining and characterizing a suited experiment. The plasma and beam-plasma parameters as well as the stopping theories and processes of this chapter are therefore now applied to the modeling of this practical case.



## Chapter 3

# Definition and theoretical modeling of an experiment

The purpose of this chapter is to define a projectile-plasma configuration that allows to carry out reliable energy-loss measurements for theory benchmarking, and to fully simulate the corresponding beam-plasma interaction.

In the past, a key difficulty for theory benchmarking came from uncertainties on the plasma and the projectile parameters throughout the interaction, notably on the plasma ionization degree and on the projectile charge-state value. To avoid this limitation, a setup involving a fully-stripped ion beam in a fully-ionized plasma is desirable, that has to be implemented in combination with a high-resolution detector for sufficiently precise energy-loss measurements. These requirements have been difficult to fulfill until now, preventing a precise quantitative stopping-power investigation.

At GSI, due to recent upgrades in ion energy-loss experiments with laser-induced plasmas, all the favorable conditions for such an investigation have now been reached.

The chapter is structured as follows. In section 3.1, a convenient experiment is defined and characterized basing on hydrodynamic plasma simulations and on Monte-Carlo simulations of the charge-state of projectile ion beams in plasma. Then, in section 3.2, theoretical stopping predictions are presented for the defined beam-plasma configuration, by using the various notions and theories introduced in the previous chapter. The ion energy loss in the simulated experiment is calculated, and can subsequently be used for comparison with the experimental data in chapter 5. Finally, section 3.3 is devoted to a close-up on ion stopping at stopping maximum in relation to alpha-particle stopping in ICF. The relevant parameters and the corresponding theoretical predictions concerning the ion stopping power are estimated and discussed, and the significance of this work in this respect is stressed.

### 3.1 Suited beam-plasma configuration

This section is devoted to the choice of an appropriate plasma target and of a suited projectile-ion properties for relevant energy-loss measurements enabling to reliably test the stopping theories. First, the few previous experiments carried out in the velocity regime of stopping maximum are focused on, and their main results and limitations are explained. Then, a new setup is proposed for more precise and reliable measurements. It combines a fully-stripped projectile-ion beam interacting with a fully-ionized plasma, a precise time-resolved TOF detector system for energy-loss measurements, as well as advanced plasma-diagnostic and -simulation capabilities.

### 3.1.1 Previous experiments at stopping maximum in plasma

To our knowledge, *two* energy-loss experiments have been reported in the region of stopping maximum in plasma. The first one, by Jacoby et al., has been conducted in a cold dilute plasma induced by electric discharge [JHL<sup>+</sup>95, JBF<sup>+</sup>96], and the second one, by Hicks et al., has been carried out in a hot dense laser-generated fusion plasma [HLS<sup>+</sup>00].

- **Discharge plasma**

In the work of Jacoby et al., a fully ionized hydrogen plasma was generated with an electron density below  $10^{17} \text{ cm}^{-3}$  and an electron temperature of a few eV. Projectile-ion velocities of 45 keV/u were employed, corresponding to the stopping maximum in this cold plasma. As the main interest of this research was focused on the generation of dense matter conditions, heavy projectile ions (krypton) were used.

This experiment, the first ever conducted in the region of stopping maximum in plasma, revealed an increase of the ion energy loss in plasma in relation to cold matter of up to a factor 35-40, due to the fact that the stopping maximum in this cold plasma is reached at significantly lower velocity than the stopping maximum in cold matter. The results globally fitted within the SSM description using an effective charge-state value  $Z_{eff}$ , and confirm the presence of the maximum of the stopping power around the energy region of thermal electron velocity in plasma.

Yet a large uncertainty remained on  $Z_{eff}$ , despite its evaluation by means of a Monte-Carlo code. The reason is that krypton ( $Z = 36$ ), which is a heavy ion species, features a complex charge-state distribution containing potentially numerous electrons. The charge-state distribution of krypton is thus very sensitive to the plasma conditions, and even a few-percent change in the plasma ionization degree can lead to an important change in the charge-state value. Because of this uncertainty, no theoretical interpretation in terms of stopping power can be carried out for that experiment. The use of lighter projectile ions, that would be fully stripped in the fully ionized plasma, would enable to eliminate this uncertainty.

- **Laser-induced plasma**

Lighter ions were indeed employed as projectiles in the experiment by Hicks et al., and also in a fully-ionized hydrogen and helium plasma. No uncertainty due to the charge state of either the plasma or the projectile was thus present. The experimental setup, at the OMEGA laser Facility, enabled to irradiate targets made of deuterium and helium with high-energy lasers, generating a dense and hot, fully ionized plasma ( $n_e \approx 10^{22} \text{ cm}^{-3}$  and  $T_e \approx 3 \text{ keV}$ ), in which thermonuclear fusion reactions occurred.

The projectile ions were the light ion species that were generated in the fusion reactions and lost energy in the dense surrounding plasma medium. Their energy loss was accessed by monitoring the energy shifts of these ion species by means of adapted spectrometers. Different projectile species (protons, tritons, alpha particles) generated by various fusion reactions interacted simultaneously with the plasma, at various initial velocities. In this way, measurements above, at and below the velocity of stopping maximum in plasma could be obtained simultaneously.

The results were the first of their kind at stopping maximum in a hot and dense laser-generated plasma, and they thus confirmed experimentally for the first time the existence of the maximum in such a plasma. Yet the experimental method led to quite important error bars in the measurements. Therefore, here again, even if a general qualitative agreement was found with the existing stopping theories and models, no precise comparison could be carried out and no theory discrimination could be conducted.

In order to eliminate the uncertainties that were present in these previous experiments, a complete control of the interaction parameters is now looked for. This can now be obtained at the Z6 area

of GSI due to the recent progress in ion energy-loss experiments achieved there. For a description of the experimental facilities offered by GSI and an overview of the previous experiments, the reader is referred to section 4.1.

In the following section, the used plasma target, identical to the laser-generated plasma generated and characterized in [Fra11, FBB<sup>+</sup>13], is presented and described.

### 3.1.2 Plasma target

In [FBB<sup>+</sup>13], a laser-generated plasma for energy-loss experiments was fully characterized, by using both simulation and experimental methods. The laser and target parameters were tailored to obtain a quite homogeneous, fully-ionized and reproducible plasma, following several setup upgrades accomplished in the few past years (see 4.1.4).

The plasma characterization was achieved thanks to the combined use of the multi-frame interferometry diagnostic [BFF<sup>+</sup>12] described in section 4.1 and of the 2D radiative hydrodynamic code RALEF2D [BMT09, Bas, BSM<sup>+</sup>12, TBF<sup>+</sup>13] for the simulation of the plasma conditions.

#### The RALEF2D hydrodynamic code

The RALEF2D (Radiation Arbitrary Lagrangian-Eulerian Fluid dynamics) code was mainly developed to model the dynamics and evolution of the hot plasmas generated by means of the PHELIX and *nhelix* lasers at GSI, in particular for ion energy-loss experiments. RALEF2D uses an arbitrary Lagrangian-Eulerian method for the mesh evolution and a second-order Godunov scheme for the numerical resolution of the fluid equations (see 2.1.1), either in Cartesian or in axi-symmetric coordinates. It is based on a one-fluid and one-temperature hydrodynamic model and considers heat conduction as well as radiative transport in its description of a laser-generated plasma. For this purpose, the 2D hydrodynamic code was coupled with the solution of the equation of frequency-dependent radiative transport (2.37) in its quasi-static approximation. The precise description of radiative transport is necessary as the dynamics of hot laser-generated plasmas is strongly influenced by radiative phenomena. This feature differentiates RALEF2D from most other hydrodynamic codes, which describe radiative transport in the frame of a diffusion approximation in a multi-group spectral approach. The successful more complete implementation of radiative transport thus makes RALEF2D one of the most advanced hydrodynamic codes worldwide in this respect.

#### Benchmarking of the plasma conditions

Parallel to the development of the RALEF2D code, the interferometry diagnostic that existed at Z6 was upgraded to a multi-frame version. In this way, four successive measurements of the plasma free-electron density can be carried out with a 2 ns interval and with a time resolution of 0.5 ns. This increased the reliability of the diagnostic, by minimizing the influence of fluctuations in single measurements.

A comparison of the plasma-density profiles calculated in the RALEF2D code with interferometric measurements [Fra11, BFF<sup>+</sup>12, FBB<sup>+</sup>13] is shown in Fig. 3.1 and Fig. 3.2.

In Fig. 3.1, free-electron density profiles calculated with RALEF2D (dotted curves) are compared with the experimental values (plain curves) obtained from the interferometric measurements, for four different times of the plasma evolution. The agreement between the measured and the simulated values is excellent, the maximum discrepancies reaching about 20 % in the highest-density part.

In Fig. 3.2, the reproducibility of the plasma evolution characteristics is demonstrated. The density profiles from three independent measurements, carried out with different interferometers of the multi-frame setup, are compared with the RALEF2D results for a time between 9 and 10 ns after the beginning of the laser irradiation of the plasma target.

On the one hand, the various measurements are in very good agreement with each other. It



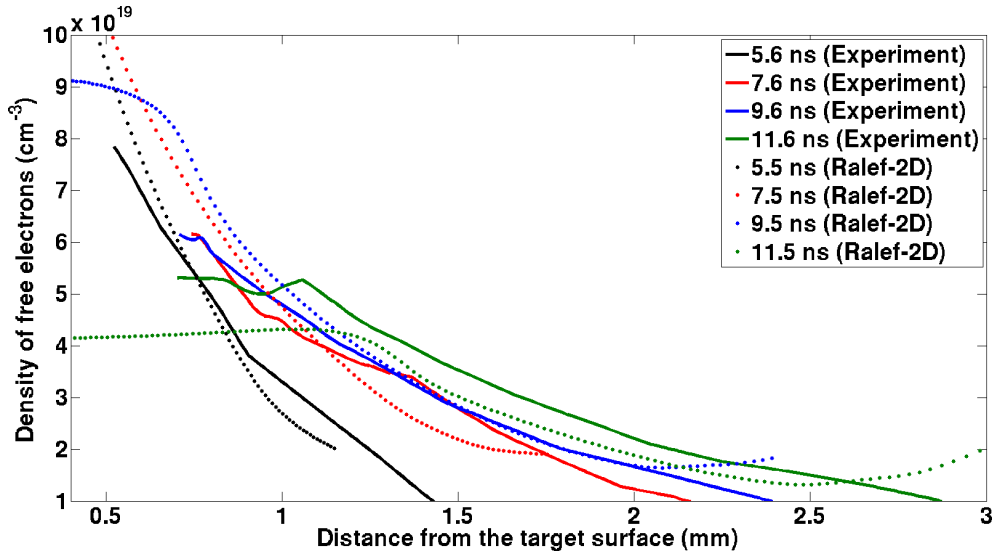


Figure 3.1: Comparison, at four different times of the plasma evolution, of the free-electron density profiles simulated by the RALEF2D code (dotted lines) and of the profiles resulting from multi-frame interferometry measurements (plain lines). An agreement better than 20 % is found, thus validating the hydrodynamic simulations.

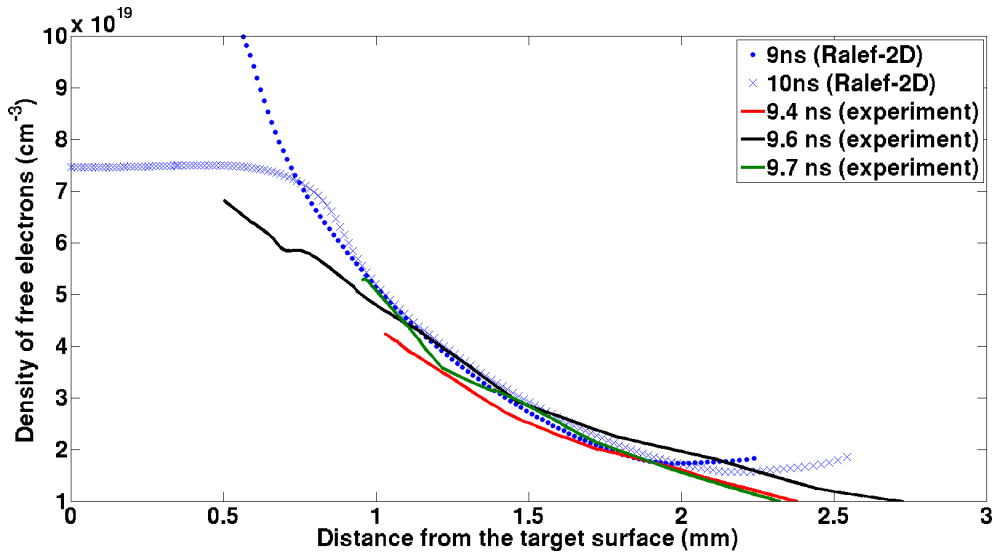


Figure 3.2: Comparison, at a given time of the plasma evolution, of three independent free-electron density measurements carried out with different arms of the multi-frame interferometric setup, with results of RALEF2D simulations. In addition of validating the code again, this graph shows that the plasma conditions are generated in a very reliable and reproducible way.

shows that the plasma conditions resulting from the laser irradiation of the target are very reproducible, hence the laser-heating process and the plasma characteristics are very stable from shot to shot. This was made possible by the implementation of a laser-heating scheme using a two-sided target irradiation with frequency-doubled beams (see 4.1.4).

On the other hand, the measurements are in excellent agreement with the RALEF2D results, showing again that the code is able to correctly reproduce the experimental plasma conditions. These comparisons allowed to validate the code, proving that it can precisely model the plasma generation and evolution. The other plasma parameters - electron temperature and ionization degree, can thus be determined by the code. Yet according to the code developers, there still might be some improvements to be added in the determination of the ionization degree, hence they recommend using the Saha law instead.

Furthermore, the code can take the spatial inhomogeneity of the incident laser focus profile into account, by simply modeling it by means of a sine function.

Consequently, the RALEF2D code constitutes a powerful tool for the modeling and the description of laser-induced plasmas. It gives access to the complete knowledge of the plasma parameters as a function of space and time. In this way, it also enables the calculation of the projectile charge state as a function of space and time via the coupling of the hydrodynamic results with the Monte-Carlo code described in 3.1.3. Hence, it allows the calculation of the theoretical energy losses according to various ion stopping-power models described in 2.2.2, 2.2.4 and 2.2.5, as is presented in 3.2. The comparison of the energy losses then allows to test the stopping predictions.

### Plasma characteristics

A required condition for high-quality energy-loss measurements, apart from the reproducibility of the plasma conditions, is to obtain a homogeneous plasma layer. This plasma must also remain homogeneous for a sufficient time of at least a few nanoseconds, as the ion bunches used for probing the plasma have a temporal width of several nanoseconds at Full Width Half Maximum (FWHM), and for probing reliably different interaction times. The homogeneity is viewed in two respects.

On the one hand, a *transversal* homogeneity to the ion axis and to the beam-irradiation direction is looked for. This condition is important to ensure that all the ions of the beam interact at the same plasma conditions. If this is not the case, TOF differences arise among the beam ions and lead to a lowered resolution of the setup. On the other hand, a longitudinal uniformity is also looked for in order to ensure, notably, a constant ionization degree along the propagation path of the projectile ions in the target. These conditions are not easy to fulfill due to the inhomogeneous nature of laser-plasma heating and to the usual strong fluctuations in the intensity profiles of the laser focus spots.

A lot of efforts were dedicated in upgrading the experimental setup in order to finally be able to obtain homogeneous laser-induced plasmas in a systematic way. The RALEF2D code has played a major role in these improvements, by simulating the plasma conditions for different laser parameters. In this way, an optimal set of laser and target parameters has been found that enables to obtain a homogeneous plasma layer over a sufficient time span. A detailed discussion about the simulation of the homogeneous plasma layer and about its dependence on the laser parameters is presented in [TBF<sup>+</sup>13].

By means of the RALEF2D code, it was predicted that a two-sided laser irradiation of a 100  $\mu\text{g}/\text{cm}^2$  planar graphite foil by frequency-doubled beams (532 / 527 nm) with a 30 J pulse energy and a 7 ns pulse length at FWHM, leads to the generation of a hot fully ionized and sufficiently homogeneous carbon plasma at the end of the 7 ns laser irradiation. These laser parameters were therefore applied for the plasma generation in [FBB<sup>+</sup>13]. The main reason for obtaining the nearly homogeneous plasma layer is the important role played by radiation transport due

to the 532 nm laser wavelength that allows laser-energy deposition in dense plasma regions (see 2.1.2).

Plasma simulations are available for the first 16 ns of the interaction. The plasma conditions along the longitudinal target areal-density profile are illustrated in Fig. 3.3 for three characteristic times of the plasma evolution. These times correspond to (1) an early phase of the laser-plasma heating at 3 ns, (2) the time point at the end of the laser heating at 7 ns, where the maximum plasma temperature and ionization degree are reached, and (3) the time point where the plasma is not fully ionized anymore.

At  $t = 3$  ns after beginning of the laser heating of the target, the plasma is still partially ionized and features a non-uniform longitudinal profile. On the target edges, that have first been heated by the laser beams, the plasma is fully ionized and the temperature is maximal at values close to 130 eV, while the electron density is in the order of magnitude of  $10^{20} \text{ cm}^{-3}$ . Meanwhile, in the target center, the ionization degree reaches 3-4 as the temperature is only 20 eV, and the free electron density is of the order of magnitude of  $10^{21} \text{ cm}^{-3}$ .

At a time of 7 ns, the plasma is uniformly fully ionized and the free electron density reaches values of  $3 \times 10^{20} \text{ cm}^{-3}$ . The temperature profile is quite uniform, with values between 140 and 175 eV, the latter being close to the maximum plasma temperature reached during the interaction.

Finally, at  $t = 13$  ns, the plasma ionization degree is still very high, around 5.95, and starts decreasing. The electron temperature and density are now significantly lower, at values between 65 and 115 eV and around  $2\text{-}3 \times 10^{19} \text{ cm}^{-3}$  respectively. It can also be seen that the target areal density has strongly decreased at the time of 13 ns because of the three-dimensional plasma expansion. Its maximum value is indeed now around  $50 \mu\text{g}/\text{cm}^2$ , instead of its original value of  $100 \mu\text{g}/\text{cm}^2$ . This decrease in the areal density is also illustrated in Fig. 4.13 and Fig. 3.11.

As a conclusion here, even if density and temperature gradients are always present, the plasma features a quasi-uniform maximum ionization degree along its whole profile in the time window from 7 to 13 ns. This full plasma ionization is of great advantage for ion-stopping measurements as explained below, and in addition these favorable conditions can be probed over a large time window of 6 ns.

As for the plasma transversal homogeneity, it is shown in Fig. 4.13 by means of the transversal areal-density profile. First, it can be seen that the areal density in the target center remains nearly constant over the first 7 ns of the interaction, showing that the plasma expansion occurs in a one-dimensional way in this time span. Second, discrepancies of 20 – 30 % yet appear between the areal-density values on the ion axis and the values in the external parts of the transversal plasma profile. While their role can be neglected in [FBB<sup>+</sup>13] due to a relatively small ion-beam diameter, they might have a noticeable influence on the energy deposition in the present work because the ion beam is spatially more extended. More details on this issue can be found in 4.2.1 and 4.2.2.

### Plasma ionization

The fact that the plasma target reaches full ionization is an important point. First, it greatly simplifies the stopping-power expressions, as only the free electron contribution needs to be taken into account, at least for a significant time span of the interaction. Second, in a fully-ionized plasma, the NREC process, which is the main projectile recombination process in not fully ionized matter, is completely suppressed. This leads to a simplification of the charge-state distribution of the projectile, which is shifted towards higher ionization degrees. A light-ion projectile species is then expected to be fully stripped in the fully ionized plasma. The influence of the charge-state value in the stopping expressions is thus suppressed and the influence of the stopping Coulomb logarithm can directly be studied.

From the analysis of the RALEF2D results and of those of the Saha equation, it can be seen that

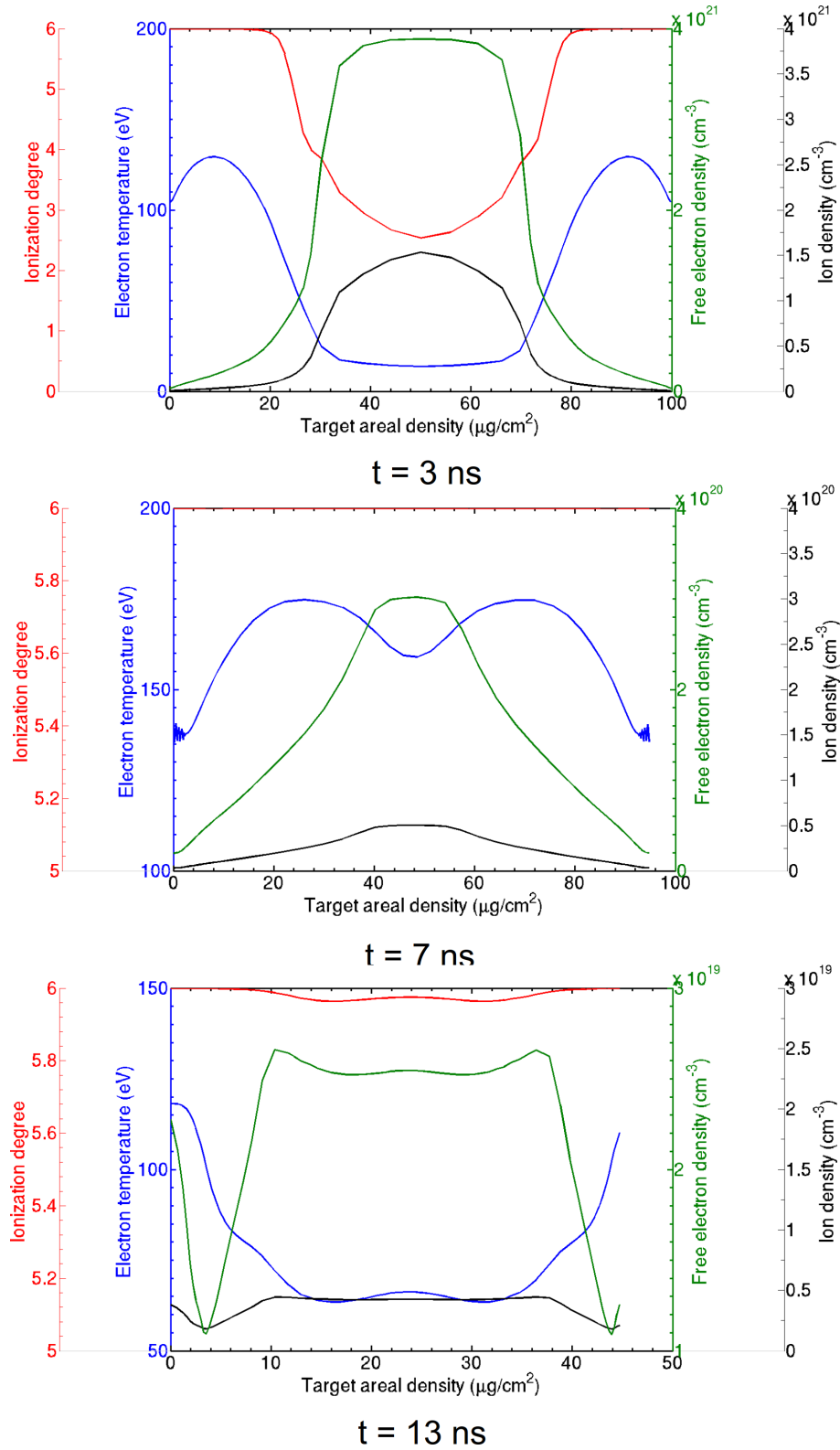


Figure 3.3: Profiles of ion density, free-electron density, electron temperature and ionization degree as a function of the target areal density in  $\mu\text{g}/\text{cm}^2$ , on the ion axis and at times of 3, 7 and 13 ns after beginning of laser irradiation, according to the RALEF2D code.

the plasma becomes fully ionized at  $t = 6-7$  ns after the beginning of laser irradiation, and that it stays fully ionized until approximately  $t = 13$  ns. In Fig. 3.4, the charge-state distribution of the carbon plasma ions is plotted as a function of the plasma temperature for two fixed electron densities of  $10^{20} \text{ cm}^{-3}$  and  $10^{21} \text{ cm}^{-3}$  respectively, as calculated by using the Saha law on the basis of [ZBD00]. The graphs show that for a typical density of  $10^{20} \text{ cm}^{-3}$  reached in the carbon plasma,  $C^{6+}$  constitutes more than 90 % of the distribution for  $T_e > 100$  eV and close to 100 % for  $T_e > 130$  eV. For the maximum density of  $10^{21} \text{ cm}^{-3}$ , the proportions of  $C^{6+}$  are slightly smaller, namely of 80 % at 100 eV and 95 % at 130 eV. Therefore  $C^{6+}$  is strongly dominant as long as  $T_e \geq 100$  eV, guaranteeing that the plasma is highly ionized.

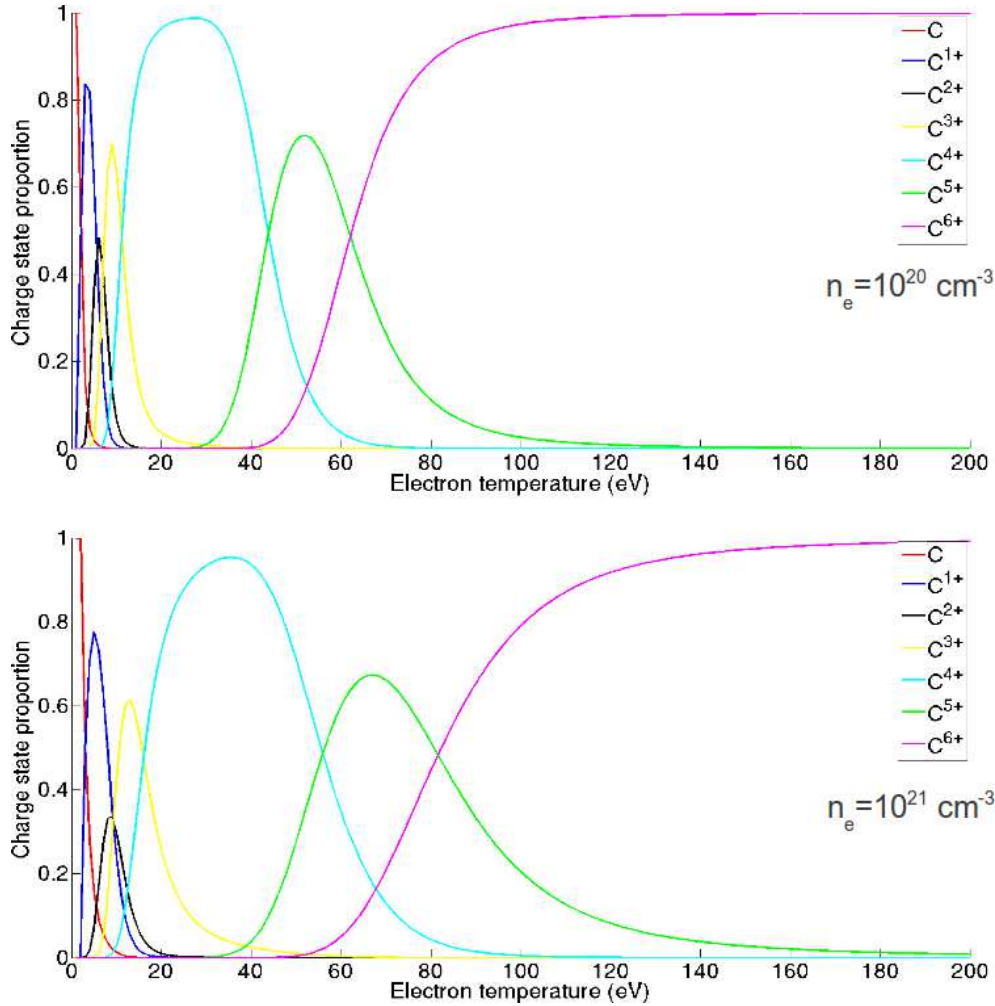


Figure 3.4: Proportions of the charge states, from neutral to 6+, of the carbon plasma ions, according to the Saha ionization law, as a function of  $T_e$  for fixed electron densities  $n_e = 10^{20} \text{ cm}^{-3}$  and  $n_e = 10^{21} \text{ cm}^{-3}$  respectively.

### An ideal test bed for ion-stopping studies

The described carbon plasma is therefore well characterized and can be generated in a reproducible way. It is quite homogeneous in space because of the two-sided irradiation with frequency-doubled laser pulses, for which radiative transport is significantly enhanced in comparison with the irradiation with the fundamental laser frequencies. The target is thus heated rapidly and it is uniformly fully ionized in a time span ranging from approximately 7 to 13 ns after the beginning of the laser irradiation. Therefore, the setup potentially enables to investigate the energy loss

of fully ionized projectile ions in fully ionized plasma if a convenient projectile ion species is chosen. Furthermore, the recent development of CVD-diamond time-of-flight detectors, enabling high-resolution energy measurements (see section 4.1.3), makes it possible to determine the ion energy loss with a high precision.

In conclusion, the plasma setup of [FBB<sup>+</sup>13] offers a suited frame for precise ion energy-loss measurements. An identical plasma setup is thus be implemented for the present work, and the projectile parameters are chosen in order to reach the energy region of maximum stopping power. As the plasma is hot (up to 200 eV), the thermal velocity of the plasma electrons is relatively high, which also simplifies the experimental access to the region of stopping maximum, as the ion beam has to be decelerated (see also section 4.1.4). For a plasma temperature of 200 eV, a projectile ion energy of 0.5 MeV/u is required to match the condition  $v_p/v_{th} \approx 1$ .

The next section is devoted to the choice of the projectile properties that are most relevant for an energy-loss measurement at stopping maximum.

### 3.1.3 Projectile ions

#### Motivations for carbon as projectile

Two main reasons motivate the choice of carbon as projectile ion species.

First, it is of great interest for ICF to better understand the energy deposition and the range of alpha particles in a hot dense plasma. In principle, helium ion beams ( $Z = 2$ ) can be generated by the GSI accelerator facility, but due to the large projectile charge-to-mass ratio, they are likely to be unstable and difficult to handle with the guiding magnets. Carbon ( $Z = 6$ ) is a good alternative instead, being also a light-ion species but more simple to handle and more stable. The choice of carbon is also relevant for ion-driven Fast Ignition, where it is one of the most promising candidate ion species [FHA<sup>+</sup>09]. Hence, the measurement of the energy loss of C ions is also meaningful for ion-driven FI schemes. The choice of carbon as projectile is thus relevant to several aspects of ICF.

Second, a light ion species is desirable for the interpretation of the energy-loss measurements. Indeed, the lighter the ion species, the less involved is its charge-state distribution in plasma, as already mentioned in 3.1.2, simplifying in this way the theoretical description of the stopping power and the interpretation of the measurements.

Around the stopping maximum, due to the potential nonequilibrium features of the charge-state value [PM91b], and of possible multiple charge-exchange phenomena due to strong Coulomb coupling [WM08], the description of the charge-state distribution is particularly complex.

Therefore, in order to suppress the uncertainties on the charge-state value (as was the case in [JHL<sup>+</sup>95, JBF<sup>+</sup>96] or in [RSS<sup>+</sup>00]) that prevent a precise interpretation of the energy-loss measurements, a projectile ion species expected to be fully ionized in the hot plasma has to be used. A light ion like carbon is therefore a suited choice, as demonstrated in the following.

#### Monte-Carlo code for projectile charge-state calculation

The charge-state distribution of a beam of C projectile ions in the hot carbon plasma was determined with the help of a Monte-Carlo code describing the charge-transfer processes of the projectile ions in plasma. The Monte-Carlo code together and the implementation of the corresponding charge-exchange processes are described in details in [Fra11] and more concisely in [FBG<sup>+</sup>10]. As no charge-state distribution measurement is possible in the setup developed in this work (see 4.2.2), the code is the only access to the charge-state value of the projectile. And even though the measurement was possible, it would only determine the charge-state distribution *exiting* the plasma. Therefore it would not give any information about the charge phenomena occurring during the interaction with the plasma. Yet the Monte-Carlo code permits to describe

the charge-state dynamics within the plasma target.

Now, the main features of the code, as well as the results obtained for the charge state of C ions in the plasma of interest are presented.

The present code is based on a previous Monte-Carlo code developed in [BBv02] for the calculation of the charge-exchange processes in cold matter. The latter code uses the cross sections of ionization and recombination processes determined by solving the corresponding rate equations in the ETACHA code [RVS96]. This is carried out for each atomic shell of the projectile and of the target, where the Slater atomic model [Sla30] is used. The code for cold matter has then been extended to the plasma case by adapting the existing charge-transfer processes and by adding the new mechanisms that arise in plasma.

ETACHA was developed for application at high projectile energies, and it was tested successfully in the range of 10-80 MeV/u. For its use at lower projectile energy, corrective scalings are applied by using experimental cross-section data. This scaling of the cross sections was e.g. conducted in the case of argon projectile ions in [FBB<sup>+</sup>13] basing on cross-section data from [BRH06]. The corrections in the case of argon proved to be small for ionization cross sections, whereas they led to an increase of recombination cross sections by a factor 2-3. For a carbon projectile ion, no experimental cross-section measurements are available to scale the cross sections calculated by ETACHA, the results are thus kept as they are. Consequently, the cross sections for recombination of the carbon projectile ions in this work are likely to be under-evaluated.

The charge-exchange processes considered in the code are the following.

- **Ionization by Coulomb collisions with the target ions**

Projectile ionization and excitation by Coulomb collisions on the target ions is the main ionization mechanism in plasma. It is enhanced because the target ions are less screened in plasma than the target atoms in cold matter. The screening lengths of the projectile ion as well as of the plasma ions have thus mainly to be modified. The screening length of the projectile ion is taken as the Debye length in the frame of a Yukawa description of the electric potential. The screening lengths of the plasma ions featuring various ionization degrees from 1+ to 6+ are determined with the help of a Hartree-Fock method. As for the plasma ionization degree, it is calculated with the help of the Saha equation.

- **Non-radiative electron capture**

The NREC process is the main recombination mechanism as long as the plasma is not fully ionized. The main modification in relation to the cold-matter case is the adaptation of the target screening as a function of the plasma ionization degree.

It can be seen from Fig. 3.4 that at the typically considered plasma densities, electrons from the K-shell of the plasma ions become free for  $T_e \geq 80$ -100 eV. As soon as such a temperature is reached, NREC is thus expected to be strongly reduced.

- **Radiative electron capture**

The cross sections for REC in cold matter are determined with the help of the Bethe-Salpeter formula describing the bound states of a two-body quantum-mechanical system. As this formula assumes that the captured electrons are free, no change must be carried out in plasma.

- **Ionization by free electrons**

Ionization by free plasma electrons is included by using fit parameters given in [SK06], where recommended cross sections are proposed in the form of analytic functions. As no comprehensive theoretical description is available for electron impact ionization, various approaches are considered depending on the collision energy and on the atomic transition of interest. Only the ionization cross sections have been included, while the excitation cross

sections have been neglected. The cross sections of ionization by free electrons remain small compared with the ones of the dominant ionization process by collision with target ions.

- **Dielectronic recombination**

For the description of the cross sections of dielectronic recombination, the model developed in [PAM86, PM91b] has been applied. In this process, the formed doubly-excited atomic state can decay either by emitting a photon (fluorescence or radiative decay) or by emitting a secondary electron (self-ionization or Auger-effect). The probability of the fluorescence and of the Auger processes are calculated in the ETACHA package basing on [Kra79] and can be directly employed for solving the rate equation of dielectronic recombination. Dielectronic recombination is the dominant recombination mechanism in the fully ionized plasma considered in this work, as NREC is strongly reduced or even suppressed due to the high ionization degree.

- **Three-body recombination**

The corresponding cross sections are calculated on the basis of [Pet85]. Yet they stay negligible for the relatively low plasma densities that are considered, and do not play any role in the frame of this work.

The total cross sections of the charge-transfer processes in plasma are calculated by summing the cross-sections of the cold-matter processes obtained by the modified version of the ETACHA code (adapted to plasma), and the cross-sections of the specific plasma processes. The cross sections are calculated via a Monte-Carlo method, by using the plasma conditions obtained with the RALEF2D code.

The initial charge-state value of each ion when entering the plasma is taken as the closest value to the result of the Schiwietz-Grande formula for the charge-state equilibrium in solid matter (equ. 2.42), i.e 4+. Before entering the plasma, the ions indeed interact with a solid carbon foil in order to be decelerated down to the desired energy (see 4.2.1), where they reach their equilibrium charge-state value.

A grid in areal density is defined along the path of the projectile ions in the plasma, and the probabilities for each charge-transfer process are determined in each cell of areal density. It was shown that for carbon ions at a projectile energy of 0.5 MeV/u, the cell size has very little influence on the resulting charge-state distribution. Calculations employing grid cells of  $5 \mu\text{g}/\text{cm}^2$  and  $20 \mu\text{g}/\text{cm}^2$  have indeed been carried out and compared, and delivered very similar results. A step size of  $10 \mu\text{g}/\text{cm}^2$  has thus been employed. The charge-state distribution of the projectile ions is determined at each time step of the RALEF2D simulations, i.e at each 0.5 ns. Each calculation uses 100000 successive projectile ions.

### Charge-state results for carbon projectile ions in plasma

The charge-state distributions of the 0.5 MeV/u carbon ion beam obtained with the code for a fixed electron density of  $10^{20} \text{ cm}^{-3}$  and  $10^{21} \text{ cm}^{-3}$  respectively, are shown in Fig. 3.5 as a function of the plasma temperature. It appears that for high plasma temperatures, the charge state 6+ is clearly dominant, this dominance being more pronounced for a higher plasma density of  $10^{21} \text{ cm}^{-3}$ . Then, for  $T_e > 120 \text{ eV}$ ,  $C^{6+}$  constitutes more than 80 % of the distribution, and for  $T_e > 150 \text{ eV}$  this proportion exceeds 90 %. Yet for a lower density of  $10^{20} \text{ cm}^{-3}$ , the preponderance of the charge state  $C^{6+}$  in the projectile ion beam becomes less pronounced, thus a significant part of the beam ions is not fully-stripped.

In Fig. 3.6, the charge-state distribution of the carbon ion beam in the studied plasma, as determined with the help of the plasma profiles obtained with the RALEF2D code, is plotted as a function of the target areal density, at times of 3, 7 and 13 ns after beginning of laser irradiation. These charge distributions thus correspond to the plasma parameters represented in Fig. 3.3.



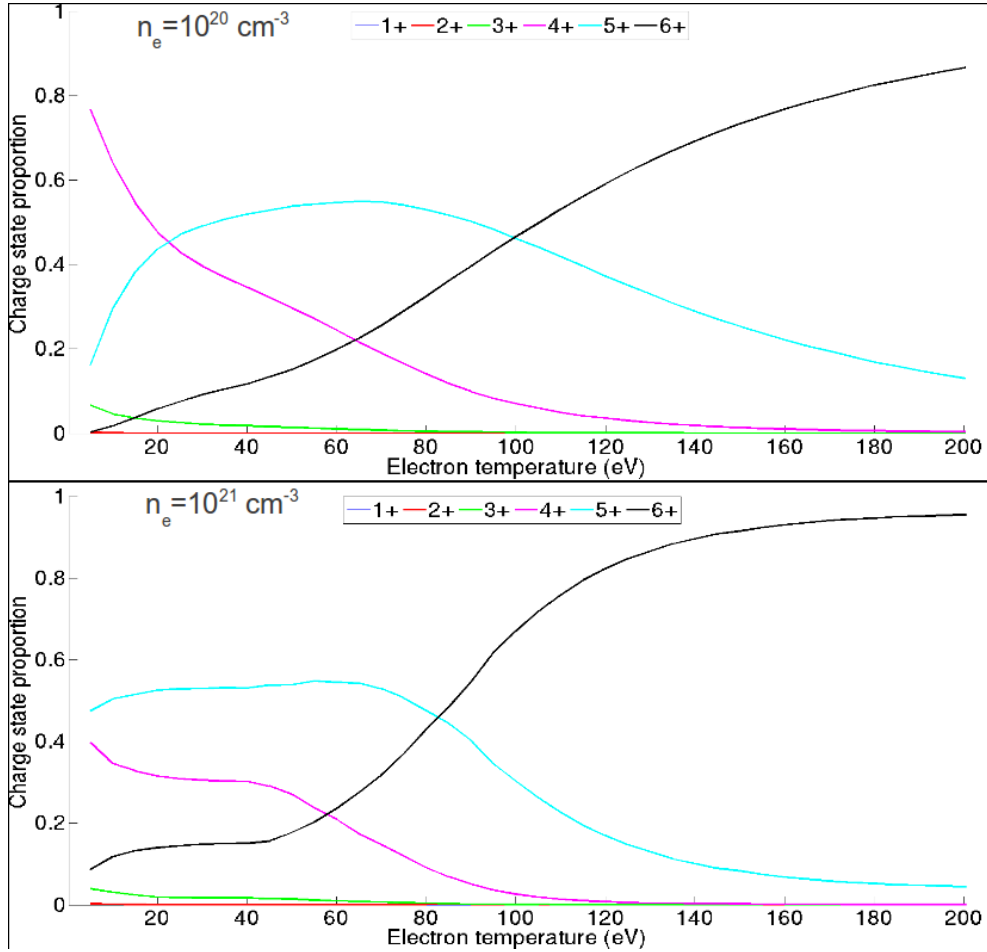


Figure 3.5: Charge-state distributions of carbon projectile ions at an energy of 0.5 MeV/u entering a plasma of electron density  $10^{20} \text{ cm}^{-3}$  and  $10^{21} \text{ cm}^{-3}$  respectively, as a function of the plasma temperature, as determined with the Monte-Carlo code simulating projectile charge-transfer processes in plasma.

The initial charge-state value of the projectile ions is  $4+$  and the latter penetrate the plasma from the left side. As can be seen, as soon as the projectile ions penetrate the plasma target, important charge-exchange processes occur.

In any case, due to the increased ionization and the reduced recombination in the hot plasma, the charge state  $4+$  quickly disappears and the higher charge states  $5+$  and  $6+$  are strongly enhanced. The main feature is the strong reduction of the NREC process because of the ionization of the K-shell electrons of the plasma carbon ions. After propagation through  $5 \mu\text{g}/\text{cm}^2$  in the plasma target, the charge state  $5+$  reaches a maximum proportion of 0.6 and then quickly disappears in turn, being converted into  $6+$ . After  $20 \mu\text{g}/\text{cm}^2$ , the charge state  $6+$  almost exclusively remains present, while all other charge states have disappeared.

While this tendency can be observed at all interaction times, small differences appear depending on the plasma conditions. At  $t = 3 \text{ ns}$ , when the projectile ions pass through the colder and partially ionized zone of the plasma target, NREC becomes important again and leads to a decrease of the projectile mean charge state in this part of the target. In the subsequent hot and highly ionized plasma part, the mean charge state increases again but it does not reach the value of  $6+$  when exiting the target, hence final equilibrium is not achieved. In contrast, for  $t = 7 \text{ ns}$ , due to the uniform fully ionized plasma conditions, NREC is absent and the projectile ions reach a stable equilibrium maximum value of  $6+$ . Later, at  $t = 13 \text{ ns}$ , due to the reduced plasma temperature, the plasma is not fully ionized anymore. Therefore, NREC is present again and recombination occurs. As a consequence, the charge state  $6+$  represents close to 90 % of the final distribution and the beam is not fully stripped.

Therefore, according to the code, the charge state  $6+$  becomes strongly dominant for all interaction times. In the time window where the plasma is fully ionized (7-13 ns), a stable full ion-beam ionization is reached, while other charge states than  $6+$  also play a role when  $Z_T \leq 6$ . In particular, at all interaction times, the beam needs to propagate across at least  $20 \mu\text{g}/\text{cm}^2$  of the target in order to reach a nearly equilibrium value. Depending on the time, this can correspond to more than 50 % of the target areal density profile.

These results thus show that even if the other charge states also have to be considered, a large majority of the beam ions is fully-stripped in the hot fully-ionized plasma. This nearly fully-ionized behavior in the fully-ionized plasma justifies the choice of carbon as projectile ion species for the experiment.

The charge-state distribution of the projectile can thus be evaluated by using the code at each time step of the hydrodynamic simulations for determining the stopping power and thus the energy loss. In conclusion, carbon projectile ions at an energy of  $0.5 \text{ MeV/u}$  appear as the optimal variant for the investigation of interest. Still, it has to be noted that all cross sections in the code are calculated by means of perturbative methods, as is explained in details in [Fra11]. Nonperturbative effects as multiple-electron ionization or capture are thus ignored. That might play a role in the interpretation of the experimental results as explained in 6.1.

With the knowledge of the plasma as well as of the projectile parameters by means of the RALEF2D code and of the Monte-Carlo code, the beam-plasma configuration is completely determined. Now, theoretical calculations can be carried out for characterizing the stopping power and the energy loss in the experiment, and for predicting the effects to be observed. In particular, these calculations make it possible to estimate the needed energy resolution in the experiment.

## 3.2 Theoretical predictions

The defined beam-plasma configuration is now characterized with the help of the plasma and beam-plasma parameters defined in chapter 2. First, in 3.2.1, the interaction features such as the beam-plasma coupling and the relative importance of collisional and collective effects in the

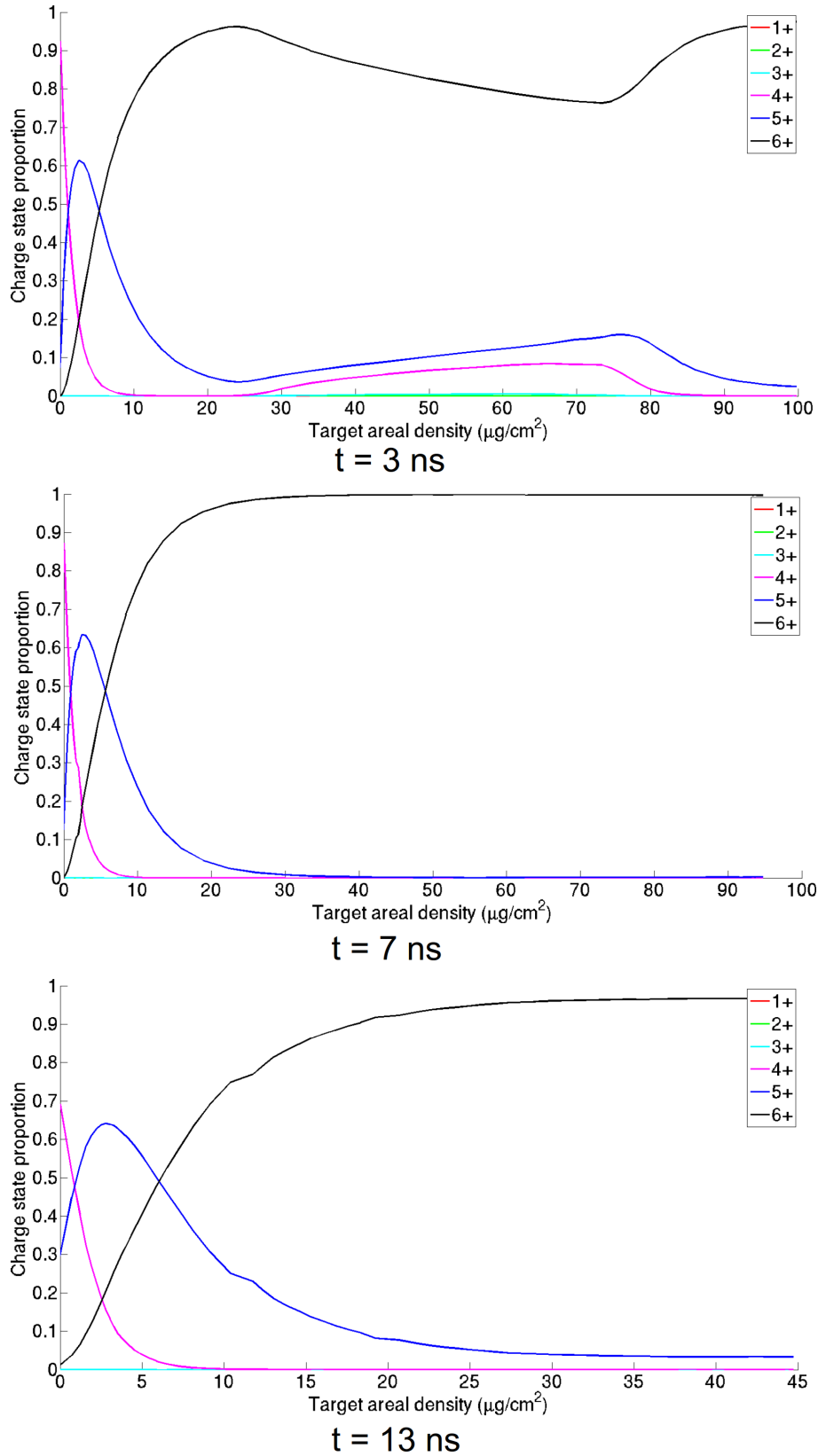


Figure 3.6: Charge-state distributions of carbon projectile ions at an energy of 0.5 MeV/u entering the plasma as  $t = 3, 7$  and  $13$  ns after beginning of laser irradiation, as determined with the help of the Monte-Carlo code and of the RALEF2D code, as a function of the plasma areal density.

stopping process is evaluated. In this way, the relevance of the diverse stopping-power theories and models presented in 2 is discussed. The next sections are devoted to stopping calculations for the chosen projectile and plasma conditions. In 3.2.2 the stopping powers obtained by different approaches are compared and discussed. Subsequently, in 3.2.3, the implications of the various stopping models on the range of projectile ions in plasma is analyzed. Finally, in 3.2.4, the energy loss according to various theoretical approaches is derived for the precise beam-plasma configuration of the experiment, mainly by using the results of the RALEF2D code and of the Monte-Carlo code for charge-transfer processes. Similar estimations for an ICF plasma are carried out in section 3.3.

### 3.2.1 Parameters of the interaction

In this section, the important quantities characterizing the beam-plasma interaction are estimated. The plasma interactions, the projectile-plasma coupling as well as the importance of collisions and of collective oscillations in the stopping process are successively addressed. In this way, the relevance of the various stopping models for the correct description of this parameter region is evaluated.

For these calculations, the plasma is assumed to be fully ionized, featuring an electron density of  $10^{21} \text{ cm}^{-3}$  and an electron temperature of 200 eV. The projectile is fully stripped ( $C^{6+}$ ) and has an energy of 0.5 MeV/u corresponding to a velocity of  $9.8 \times 10^6 \text{ m/s}$ .

- **Plasma parameters**

The hot carbon plasma is clearly non-degenerate ( $\Theta > 500$ ), thus a Maxwell-Boltzmann statistics can be applied for the plasma particles. Moreover, the plasma is ideal as  $\Gamma \approx 0.01$ , with about 800 electrons contained in a Debye sphere. The plasma is thus dominated by long-range, collective effects, and particle collisions within the plasma are scarce. As a consequence, no effects of plasma degeneracy or of plasma coupling have to be considered.

- **Beam-plasma coupling**

The velocity ratio  $\frac{v_p}{v_{th}} \approx 1.6$  in this configuration ( $\approx 1$  if  $v_{th} = \sqrt{\frac{3k_B T_e}{m_e}}$ ) and the Coulomb parameter  $\eta = \frac{Z_p e^2}{\hbar v_r} \approx 1.1$ , while the nonlinearity parameter is very small:  $\gamma \approx 0.002$ . Therefore the perturbation strength exerted by the projectile ions on the plasma electrons is significant but the interaction is far from being nonlinear. The interaction thus belongs to the semi-linear regime defined in 2.2.3.

For this reason, the first Born approximation may be inappropriate to describe the problem. All approaches basing on a first-Born approximation (Lenard-Balescu, Vlasov, Bethe, Li-Petrasso) are therefore likely to determine the ion stopping power incorrectly. A first-Born approach including higher-Born corrections (like the SSM) is likely to account for a part of the nonperturbative effects, but it remains essentially valid at high projectile velocity and may be ill-adapted at stopping maximum.

Hence, nonperturbative approaches as basing on the T-Matrix theory are a priori more relevant, provided both collisions and collective effects are properly described. It can be noted that  $\eta > 1$  also means that the interaction can be treated in the classical way and that quantum-mechanical effects can be neglected.

- **Collisions**

Even if the plasma is ideal and collisionless, collisions can occur between the projectile and the plasma electrons, potentially bringing a significant contribution to the stopping process. The Coulomb logarithm of the projectile-electron interaction  $\ln \Lambda_{pe} \approx 6.6$ , which means that small-angle collisions are dominant over large-angle collisions. As far as the impact-parameter domain is concerned, an approach in the frame of a Fokker-Planck equation or

physically equivalent (Lenard-Balescu, Li-Petrasso, SSM) should therefore be appropriate. But these approaches are linear and thus ignore the beam-plasma coupling.

The amount of collisions undergone by the projectile when probing the plasma can be estimated by calculating its mean free path. This mean free path  $l_{ep}$  can be expressed, similarly as in equ. 2.17, as:

$$l_{ep} = \frac{v_r}{\nu_{ei}} \quad (3.1)$$

where  $v_r$  is the mean relative velocity between the projectile and the plasma electrons. In the given projectile-plasma configuration, this mean free path has a value of  $0.3 \mu\text{m}$ . Hence, the projectile experiences approximately three collisions per micrometer of the plasma. A significant number of collisions is thus expected.

- **Collective effects**

The contribution of collective plasma effects in the stopping power at  $\frac{v_p}{v_{th}} \approx 1$  is estimated to 9 % by using the Li-Petrasso stopping formula. Even if the collective term there is a priori adapted for  $\frac{v_p}{v_{th}} \gg 1$ , a calculation using a more precise expression for  $\frac{v_p}{v_{th}} \approx 1$  as given in [Li93] provides a very similar result. Therefore, collective plasma effects are expected to contribute moderately to the stopping process, while the stopping power by collisions is the dominant mechanism.

### 3.2.2 Stopping power

The theoretical stopping powers are now calculated for the projectile-plasma configuration defined in the previous section. The following approaches to the ion stopping power are employed and compared.

#### Stopping-power theories and models

- **Bethe formula**

The Bethe stopping power constitutes the high-velocity limit of the perturbative Lenard-Balescu stopping power. It is determined analytically by using formula 2.53. The improved Bethe-Bloch formula for intermediate projectile velocities is obtained by adding the term of equation 2.55 in the expression. Both formulas are valid at high projectile velocity, and are not able to describe the maximum of the ion-stopping curve. They are thus not expected to evaluate the stopping power correctly, but they are used in this section for comparison purposes.

- **Standard stopping model**

The stopping power in the SSM frame is determined with the help of formula 2.58.  $G = 0.5$  for  $\frac{v_p}{v_{th}} \approx 1$ , reducing the stopping power considerably in relation to the Bethe formula. The Bloch correction represents an important part of 30 % of the stopping value, and the Barkas term accounts for close to 10 % of it, which is not negligible. Yet the SSM remains approximate and essentially perturbative. It is thus not expected to predict correct stopping results in that velocity region.

- **Vlasov dielectric stopping theory**

The stopping power in the dielectric formalism originating from the Vlasov equation is a simplified version of the Lenard-Balescu stopping power for which no plasma collisions are considered. It is calculated by means of the approximate analytic formula 2.68 derived by T. Peter and J. Meyer-ter-Vehn. It is expected to provide very similar results to the Born-RPA approach because the plasma is collisionless.

- **Li-Petrasso stopping model**

The Li-Petrasso stopping power is in principle able to describe the whole spectrum of projectile-electron impact parameters but it remains perturbative. It is calculated analytically by using equation 2.70 and the parameter expressions of [LP93a]. It differentiates from other linear approaches in the fact that it in addition considers close collisions in the stopping description. If close collisions are not significant, the Li-Petrasso model is thus expected to predict results comparable to the RPA stopping power or to the SSM.

- **Lenard-Balescu stopping theory**

The Lenard-Balescu or RPA approach, describing the stopping power by collective plasma oscillations as well as by moderate collisions, is calculated by using equation 2.67 with the help of the Max-Planck-Institute for the Physics of complex systems in Dresden. On the physical level, it is expected to be close to the SSM, while being more rigorous. Because it is perturbative, it is likely to predict the stopping power incorrectly at maximum stopping power.

- **T-Matrix stopping theory**

The T-Matrix approach enables to express the stopping power by binary collisions in a nondegenerate electron gas. The calculation was carried out with the help of the Max-Planck-Institute for the Physics of complex systems in Dresden. The cross sections are determined for the full T-Matrix calculation and for its first Born approximation (Landau expression) simultaneously. Then the corresponding cross sections are integrated by using equation 2.69 and the stopping power is obtained. The T-Matrix approach is nonperturbative but considers exclusively binary collisions. As the stopping power contribution due to collective plasma oscillations is estimated as only 9 %, the T-Matrix approach is thus likely to be quite accurate.

- **Combined model**

For the calculation of the stopping power in the combined model approach, the expressions of the Lenard-Balescu stopping power, full T-Matrix stopping power and Landau stopping power are simply combined following equation 2.72. The combined model is nonperturbative by including the T-Matrix expression and it also describes collective effects. If nonlinear collective effects are disregarded, it is thus a priori able to provide a precise stopping-power description.

- **T-Matrix theory with  $\lambda(v)$**

The T-Matrix theory with  $\lambda(v)$  is calculated by means of an approximate fit formula described in [Ger02a, Ger02b]. As stated there, the fit precision is of 25 % for plasma temperatures below 400 eV. As the combined scheme, this theory, being nonperturbative and describing the whole spectrum of impact parameters, is expected to be well-suited for the considered physical case. Moreover, it proved to better agree with numerical simulations than the combined scheme (see 2.2.6).

All these approaches only describe the stopping power by free plasma electrons. They are therefore able to calculate the stopping power properly as long as the plasma is highly ionized. In the experiment, this corresponds to a time window of several nanoseconds after the end of the laser irradiation of the target. Yet for early interaction phases (from 0 to 7 ns) or for later times (after 13 ns), the plasma is not fully ionized and the number of bound electrons may be important. Even if the stopping power by the excitation of free electrons is significantly higher than the stopping power on bound target electrons, the bound-electron contribution may be not negligible and it must thus be taken into account.

As the bound-electron contribution remains small in comparison to the free-electron term, it is

roughly calculated by using the Bethe formula (equation 2.50), by summing the contributions of each single ion charge state of the plasma that contains bound electrons, i.e from 1+ to 5+.

### Stopping-power predictions

In Fig. 3.7, the stopping power of  $C^{6+}$  projectile ions is plotted for typical expected plasma conditions of  $n_e = 10^{21} \text{ cm}^{-3}$  electron density and  $T_e = 200 \text{ eV}$  electron temperature, assuming a fully ionized plasma, as a function of the projectile energy in the range 0-3.6 MeV/u, according to different theoretical predictions. The stopping power is expressed in units of energy per element of areal density, which makes it possible to compare it with its value in cold matter, represented in dashed lines. This calculation does not necessarily correspond to a precise parameter set of the experiment. Yet, the qualitative behavior of the stopping curves remains very similar when  $T_e$  and  $n_e$  are slightly varied. This case therefore enables to evaluate the order of magnitude of the discrepancies between the stopping models in a large parameter span of the experiment, as long as the plasma is hot and highly ionized. Only the stopping power by free plasma electrons is considered in this calculation.

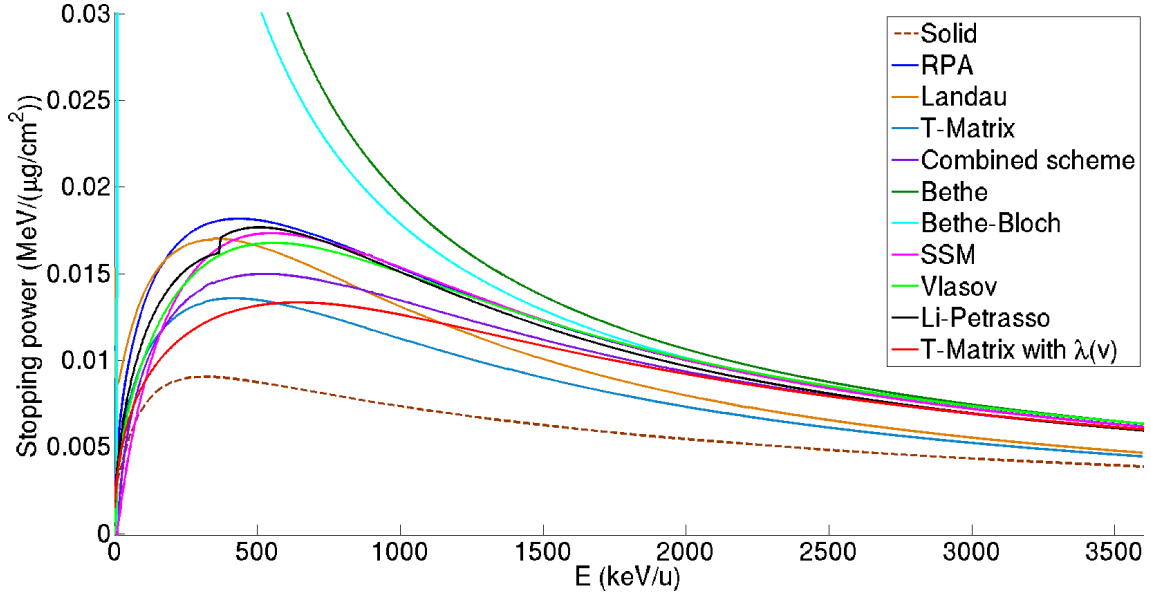


Figure 3.7: Comparison of various theoretical stopping-power predictions for  $C^{6+}$  projectile ions interacting with a  $10^{21} \text{ cm}^{-3}$  density and 200 eV temperature plasma, as a function of the projectile energy in the range 0-3600 keV/u.

On this graph, it clearly appears that most theories and models in plasma are in good agreement for a high projectile velocity. They all reach the Bethe limit, with the exception of the T-Matrix theory as well as its first-Born approximation (Landau stopping power). This is because these approaches consider a purely static projectile screening and ignore all collective effects, that are important at high projectile velocity. Their limit at high velocity lies therefore below the Bethe limit. In contrast, all the other approaches include collective plasma oscillations and thus identify to the Bethe asymptotic formula for  $v_p \gg v_{th}$ . Hence at relatively high energy, the first-Born approximation is valid, provided dynamic screening is described. That high-energy range, or Bethe regime, corresponds to most stopping experiments carried out in the past.

However, below a projectile energy of 2 MeV/u, discrepancies start to arise between the different curves. The discrepancies grow as the energy decreases, and culminate in the region of stopping maximum at 0.5 MeV/u energy. In the vicinity of the stopping maximum, the Bethe and Bethe-Bloch formulas clearly over-evaluate the stopping power, even if the Bloch correction tends to

reduce the stopping-power value. The four approaches basing on the first-Born approximation and accounting for the stopping maximum (Vlasov, RPA, SSM, Li-Petrasso) feature quite similar stopping curves, with differences of only a few  $\text{keV}/(\mu\text{g}/\text{cm}^2)$  at maximum stopping power. The step in the Li-Petrasso curve comes from the step function adding the collective contribution in the stopping formula 2.70.

The comparison between the RPA and the Landau result, showing a difference close to 2  $\text{keV}/(\mu\text{g}/\text{cm}^2)$ , i.e 11 %, gives an estimation for the importance of dynamic screening for the stopping power at stopping maximum, within the first Born approximation. The comparison of the Landau result with the T-Matrix result shows the effect of close collisions, beyond first Born approximation, on the stopping power. That effect appears to be significant, leading to an approximately 20 % decrease in stopping power in respect to the Landau result. Hence, a discrepancy close to 30 % can be noted between the RPA and the T-Matrix results.

Finally, the combined scheme and the T-Matrix with  $\lambda(v)$ , which are the most complete considered theories, feature significantly lower values than the standard perturbative models around the stopping maximum, lying about 20 % and 30 % below the Born-RPA result, respectively.

The combined scheme, and even more the T-Matrix with  $\lambda(v)$ , which has proved to best agree with particle simulations (see 2.2.6), thus predict an important reduction of the stopping power in the region of stopping maximum in relation to the standard theories. This occurs even if the plasma is ideal, with  $\Gamma \approx 0.01$ . As only the combined scheme and the T-Matrix with  $\lambda(v)$  are able to take nonperturbative effects into account as well as collective effects at the same time, these results suggest that these significant discrepancies in relation to the standard approaches indeed come from nonperturbative effects. The latter thus seem to play an important role in the region of stopping maximum, where the Coulomb coupling between the projectile and the plasma is maximal.

Next section illustrates the effect of the uncertainties on the stopping power on the ion range in plasma.

### 3.2.3 Range in plasma

The ion range is a quantity depending on the stopping power, that has a key importance for the related applications, as for example in the case of the alpha-particle heating of a burning fusion fuel.

In Fig. 3.8, the ranges of  $C^{6+}$  projectile ions with an initial energy of 3.6 MeV/u penetrating a plasma with  $n_e = 10^{21} \text{ cm}^{-3}$  and  $T_e = 200 \text{ eV}$  are exemplified by using the stopping powers of the previous section. As the projectile propagates in the plasma, it progressively loses energy. For the first 5 mm of its path, the ion energy is still relatively high and the stopping power curve (Fig. 3.7) is nearly linear, hence the energy deposition curve is also nearly linear. Beyond 5 mm, this behavior changes as the ion energy further decreases, and discrepancies in the energy deposition curves appear as they also appear in the stopping power curves. The energy deposition curves reach a maximum when the projectile reaches the stopping maximum, which is the Bragg peak of energy deposition. After the Bragg peak where most of its energy is deposited, the projectile is rapidly stopped.

As shown on the graph, significant range differences arise due to different stopping behaviors especially around the stopping maximum. The Bethe and Bethe-Bloch formulas predict a very sharp Bragg peak due to their incapacity in describing the maximum of the stopping curve and a range close to 11 mm. In contrast, the other approaches basing on the first-Born approximation and describing the collective effects show a less peaked energy deposition, and similar ranges around 13 mm. Finally, the nonperturbative T-Matrix with  $\lambda(v)$  and the combined scheme feature a range between 14 and 15 mm. The range according to the T-Matrix and Landau approaches is over-evaluated because their stopping power is largely under-evaluated at higher velocities, due to the absence of collective plasma effects.

Hence, a range difference close to 2 mm appears between the perturbative first-Born results



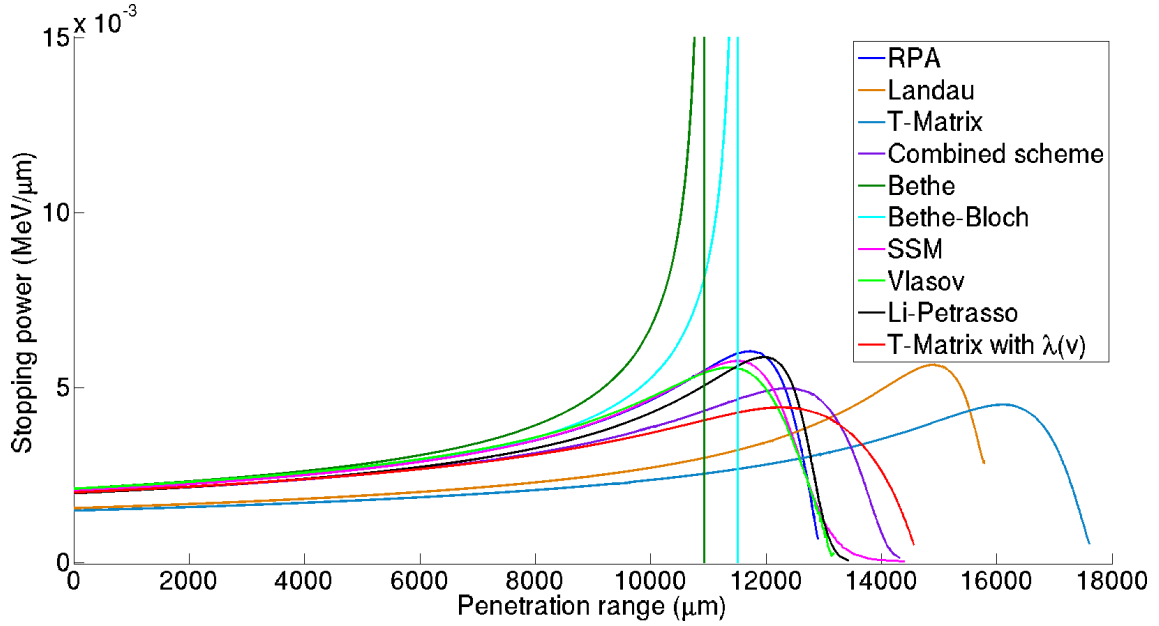


Figure 3.8: Comparison of the energy deposition curves of  $C^{6+}$  projectile ions at an initial energy of 3.6 MeV/u in a plasma with  $10^{21} \text{ cm}^{-3}$  electron density and 200 eV electron temperature according to various stopping theories.

and the nonperturbative results, due to the lower stopping power of the latter in the region of stopping maximum. With a corresponding ion mass density of  $3.3 \times 10^3 \mu\text{g}/\text{cm}^3$ , this results in a difference in areal density of  $660 \mu\text{g}/\text{cm}^2$ . The nonperturbative approaches thus predict a 15 % range increase in that case. That value of course depends on the initial ion energy. At an initial projectile energy of 0.5 MeV/u as for the projected beam-plasma setup, the range according to the RPA result is about  $430 \mu\text{g}/\text{cm}^2$  and it reaches  $630 \mu\text{g}/\text{cm}^2$  for the T-Matrix ansatz with  $\lambda(v)$ . This corresponds to a range discrepancy of  $200 \mu\text{g}/\text{cm}^2$ , therefore the T-Matrix with  $\lambda(v)$  approach predicts a range increase of almost 50 % at maximum stopping power in the hot laser-induced plasma. In the frame of alpha-particle stopping in ICF, a significantly enhanced ion range implies that the areal density  $\rho R$  of the fuel that is required to stop the alpha particles is larger, which makes ignition more difficult to achieve.

### 3.2.4 Energy loss

The theoretical energy loss in the experiment of this work is now evaluated, for 0.5 MeV/u carbon projectile ions interacting with a hot plasma generated by two-sided laser irradiation of an originally  $100 \mu\text{g}/\text{cm}^2$  carbon foil.

#### Principle of the calculation

The energy loss is determined by integration of the stopping power along the projectile path in the target, following equation 2.39. Therefore, if the stopping power is expressed in units of energy per element of areal density ( $\text{MeV}/(\mu\text{g}/\text{cm}^2)$ ), it has to be integrated over the target areal density along the projectile trajectory ( $\mu\text{g}/\text{cm}^2$ ). The calculation requires the complete knowledge of the parameters of the plasma and of the projectile, resolved in space and time. Because the RALEF2D plasma simulations have been carried out with a 0.5 ns time step, the stopping-power profiles can be determined at most for every 0.5 ns time interval. As the simulations are two-dimensional, the results are available along the longitudinal target profile with a  $2 \mu\text{m}$  step in the direction transversal to the ion beam.

The following procedure is applied to determine the energy losses.

In a first step, the plasma density and temperature profiles from the RALEF2D simulations, available for every 0.5 ns, are extracted as a function of the target areal density  $\rho x$ . These profiles are then used as input in solving the Saha equation [ZBD00], providing thus the plasma ionization profile as a function of the plasma areal density. The obtained ionization profiles, together with the RALEF2D density and temperature profiles, are subsequently used as input data for the Monte-Carlo code describing the projectile charge-exchange processes in plasma. As previously, the computation is carried out for 100000 ions featuring an initial charge state 4+, and the step in areal density is taken as  $10 \mu\text{g}/\text{cm}^2$ . In this way, the proportions of each charge state of the projectile ion beam, from  $\text{C}^{1+}$  to  $\text{C}^{6+}$ , are determined, still as a function of the target areal density. Next, as all the parameters of the beam-plasma configuration are known, the stopping-power profiles are calculated over the target areal density. Finally, by integration of the stopping powers following equ. 2.39, the energy losses are determined as a function of time. The calculation steps are summarized in Fig. 3.9.

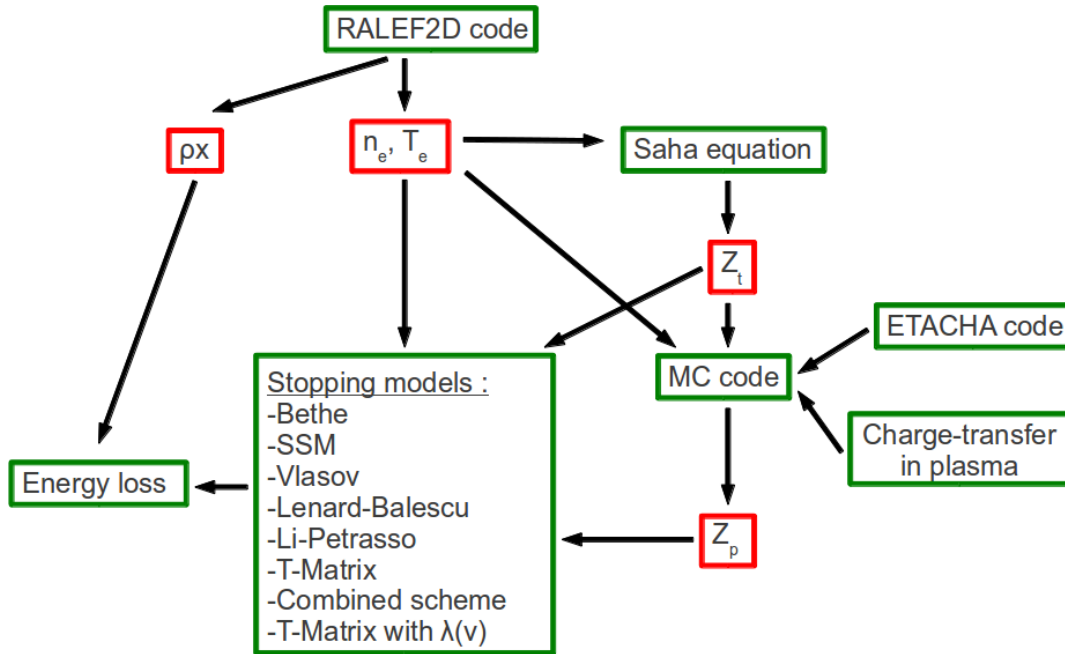


Figure 3.9: Functional scheme of the theoretical energy-loss calculation. The plasma-temperature and -density profiles are determined by the RALEF2D code. The plasma ionization degree is calculated by solving the Saha equation on the basis of the latter profiles. The density, temperature and ionization profiles serve then as input for the Monte-Carlo code for charge-transfer processes. Finally, the obtained charge-state distribution of the projectile enables, together with the ionization, density and temperature profiles, to calculate the stopping-power profiles and to infer the theoretical energy losses in the plasma target, as a function of time.

### Additional ion-beam effects

Two additional effects may have a noticeable influence and have thus to be taken into account when calculating the energy losses.

First, when a projectile ion with an initial energy of 0.5 MeV/u interacts with a  $100 \mu\text{g}/\text{cm}^2$  target foil, it loses a substantial part of its energy in the target. This fraction is 11 % in the cold target (see 4.2.4) and it is increased in plasma by a factor depending on the considered theory.

As a consequence, the projectile velocity cannot be assumed as constant during the interaction. The influence of the projectile energy loss has thus to be considered for inferring the actual value of the projectile velocity along its propagation path. As the initial velocity corresponds to the region of maximum stopping power in plasma, a reduction in the velocity leads to a reduction in the stopping power. To implement this energy-loss influence on the subsequent stopping power, a simple Runge-Kutta scheme of first order (Euler method) was implemented to determine the new projectile energy  $E_{x+dx}$  after a step  $dx$  in the plasma:

$$E_{x+dx} = E_x - dx \frac{\partial E}{\partial x} \quad (3.2)$$

The step  $dx$  was based on the step in areal density obtained from the RALEF2D data. The stopping-power reduction between the projectile entering the plasma and leaving the plasma reaches 3 – 4 %, and the corresponding effect on the total energy loss in plasma is thus of a few percent at most.

Second, the temporal extension of the ion beam has to be taken into account in the calculation. Indeed, the ion beam has a temporal width of 3 ns at FWHM when entering the plasma (see 4.1.1), and it contains at least several hundred ions. Each single ion of the beam travels very quickly through the plasma due to its energy of 0.5 MeV/u, thus probing *fixed* plasma conditions. However, due to the quick expansion dynamics of the laser-generated plasma (on the nanosecond scale), the various ions of the beam experience various plasma parameter values. This effect is included by simulating an ion beam containing 1000 ions and featuring a temporal width of 3 ns at FWHM. The time of the maximum of the Gaussian-distributed ion beam corresponds to its time of incidence on the plasma,  $t = t_0$  ns after beginning of the plasma generation. The ions at  $t = t_0$  ns in the bunch thus interact with the plasma parameters of the time  $t_0$  of the RALEF2D simulation. Then, the ions positioned at a time  $t_0 + t_1$  in the beam are associated with the plasma parameters of the time  $t_0 - t_1$  of the simulation because they interacted with the plasma  $t_1$  ns earlier than the ions at the center of the beam. Similarly, the ions positioned at a time  $t_0 - t_1$  in the beam are associated with the plasma parameters of the time  $t_0 + t_1$  of the simulation. As this procedure uses plasma conditions on a time span of 3 ns, it is not applicable on the whole time range of 16 ns provided by the RALEF2D simulations but only until 14.5 ns. Taking this effect into account leads to an energy-loss decrease of up to 10 % around the energy-loss maximum (see Fig. 3.11).

### Important remarks

Moreover, two important features are assumed in the subsequent calculation.

First, the so-called *reduction principle* [DMC<sup>+</sup>] is applied. Because of the small number density of projectile ions in the ion beam (a few thousand ions at most per micro-bunch), all correlation effects between the ions within the beam are neglected. Moreover, the low energy density of the ion beam does not lead to any change in the plasma parameters due to the stopping process. In contrast, laser-accelerated ion beams can strongly influence the plasma properties as in the phenomenon of range-lengthening [HFT<sup>+</sup>09].

It can furthermore be noted that in this calculation, effects of (i) plasma ions and of (ii) transverse velocity spreading of the projectile on its stopping power have been neglected. Such effects only become significant when the projectile velocity matches the thermal velocity of plasma ions  $v_{thi} = \sqrt{\frac{k_B T_e}{m_i}}$ . In this expression it is assumed that the electron-ion temperature equilibration has been achieved, i.e  $T_i = T_e$ . For the plasma of interest,  $v_{thi} = 4 \times 10^4$  m/s and is indeed  $\ll v_p = 9.8 \times 10^6$  m/s.

### Energy-loss predictions

The stopping-power calculation is illustrated in Fig. 3.10, at times of  $t = 3, 7$  and  $13$  ns after beginning of laser heating. There, by using the plasma profiles of Fig. 3.3 and the projectile charge-state distribution of Fig. 3.6, the stopping powers according to various theories are calculated along the areal-density profile of the plasma target. The reduction of the projectile velocity in plasma has been taken into account.

At  $t = 3$  ns, where strong plasma non-uniformities are present along its longitudinal areal-density profile, important discrepancies appear between the different stopping-power theories in the hot and highly ionized plasma regions. It is because in these parts,  $v_p/v_{th} \approx 1$ . In contrast, in the central lower-temperature region,  $v_p/v_{th} \approx 2-3$ , and as expected the discrepancies are smaller.

For  $t = 7$  ns, where the plasma temperature profile is nearly uniform,  $v_p/v_{th}$  has a stable value around unity, which explains that the different predictions correspondingly feature large discrepancies, and quite stable values along the projectile path in the plasma target. As in the previous case, the Bethe and Bethe-Bloch stopping powers increase at the end of the projectile propagation in the target because of the reduction of the projectile velocity, and of their incapacity in describing correctly the maximum of the stopping curve.

Finally for  $t = 13$  ns, the general behavior of the stopping curves is similar to the previous case. Yet, as the plasma temperature has decreased, the ratio  $v_p/v_{th}$  is approximately 2 and the interaction is not at stopping maximum anymore, hence the differences between the curves are slightly reduced. Furthermore, the curves are closer to each other in the target center where the temperature is lower, as for the case at 3 ns. The stopping-power maximum is reached around  $t = 7$  ns where the plasma reaches its maximum temperature, and the probed velocity domain is then progressively shifted towards larger  $v_p/v_{th}$  ratios.

Now, the presented stopping-power profiles are integrated over the target areal density at each time step to infer the total energy loss.

In Fig. 3.11, the energy loss is plotted as a function of time over the first 16 ns after the beginning of plasma creation, according to the diverse stopping-power models mentioned in 3.2.2 and using the results of the Monte-Carlo code for the calculation of the charge-state distribution of the ion beam. The effect of the projectile energy loss on the subsequent projectile energy as well as the duration of the ion bunches have been taken into account. The effect of the variation of the projectile velocity during the propagation in the plasma on the projectile charge-state value was estimated with the Monte-Carlo code. It turns out to be very small and it is thus neglected in the calculation. The energy-loss calculations according to the RPA and T-Matrix stopping theories as well as in the combined scheme could not be finished in the frame of this work and they are thus not included here.

The projectile energy loss in the solid target was calculated with the TRIM code for a  $0.5$  MeV/u carbon projectile interacting with a  $100 \mu\text{g}/\text{cm}^2$  graphite foil. Its value is  $0.66$  MeV and it is also plotted for comparison purposes. Moreover, the temporal evolution of the target areal density is also represented, normalized to the level of the areal density in the solid target, in order to show the evolution of the amount of matter on the projectile trajectory.

At  $t = 0$  ns, the laser beams start irradiating the target and the plasma is created. Along with the progressive ionization of the target, the density of free plasma electrons increases and the recombination processes of the projectile are increasingly less important. Therefore, as explained in 2.2.2, the ion stopping power and therefore the energy loss are enhanced due to the simultaneous increase in the stopping Coulomb logarithm and in the mean charge state of the ion beam. The increase in energy loss is present for all the theories and a maximum is reached at a time of  $6-7$  ns, where the plasma becomes fully ionized. It corresponds to the time where the plasma reaches its maximum temperature of  $200$  eV and thus of actual interaction at maximum stopping power. Subsequently, due to the progressive decrease of the plasma areal density caused by the three-dimensional expansion of the plasma in vacuum, the energy loss decreases and reaches

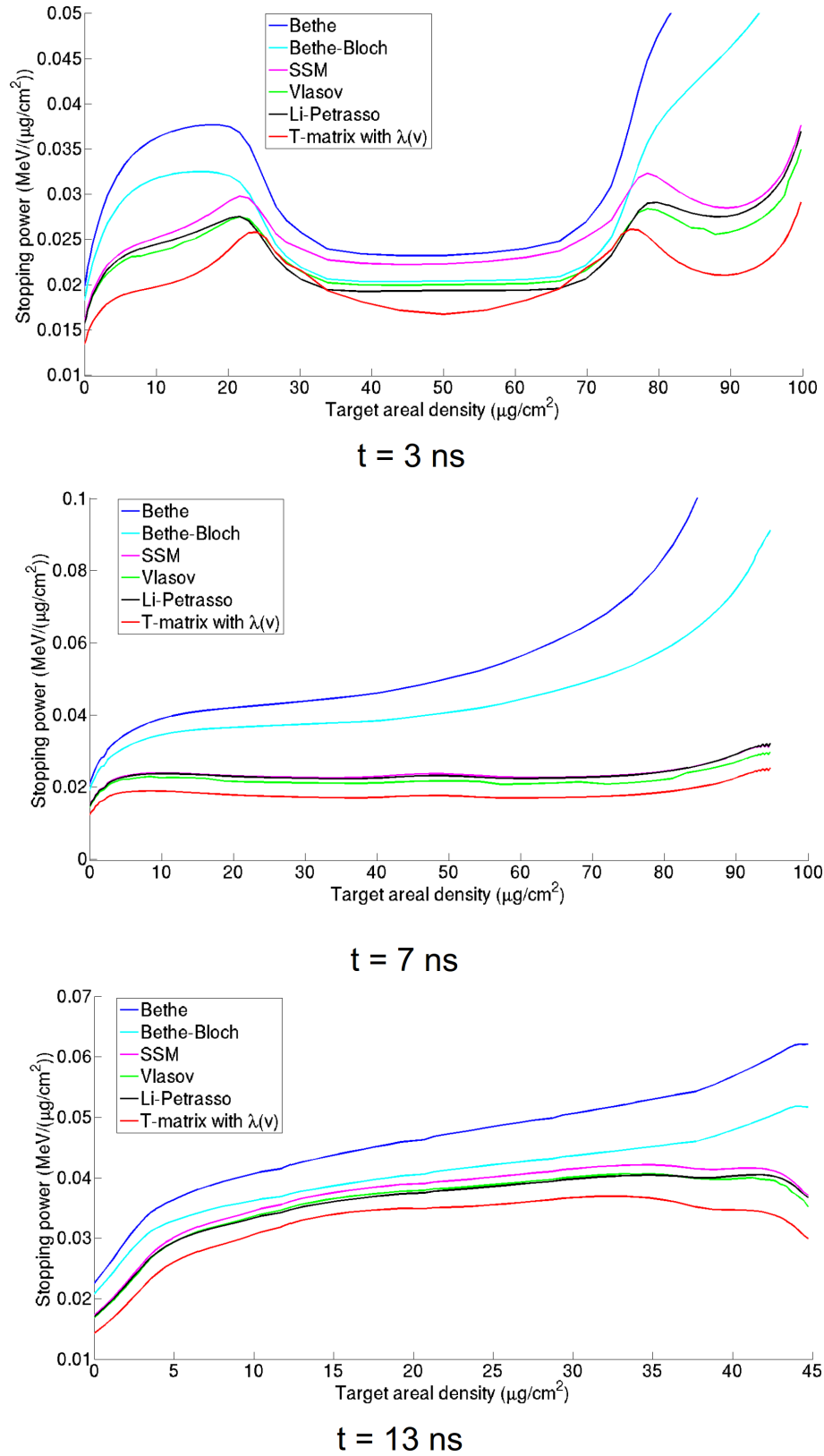


Figure 3.10: Stopping-power profiles in the plasma target as a function of the target areal density, at times of 3, 7 and 13 ns.

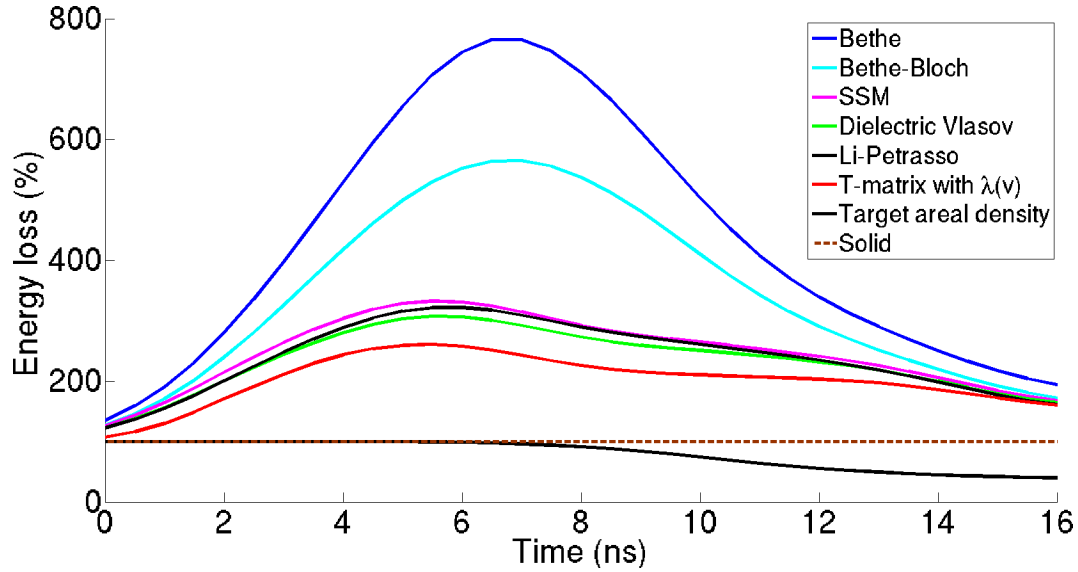


Figure 3.11: Comparison of theoretical energy losses in the experiment using the charge state obtained with the Monte-Carlo code.

again its level in cold matter at  $t = 15$  ns. Yet, if considering the evolution of the target areal density, which represents the actual reference to the cold-matter target, it can be seen that the energy loss still lies above its value in cold matter.

Depending on the considered stopping theory, various energy-loss enhancements in relation to cold matter are predicted for the experimental configuration. The Bethe and Bethe-Bloch theories predict a maximal enhancement of approximately 650 % and 500 %, the theories basing on the first-Born approximation predict values between 250 % and 300 %, and the result of the T-Matrix ansatz with  $\lambda(v)$  lies between 200 % and 250 %.

As can be seen, energy-loss differences of several hundred keV appear between the various theoretical approaches. These discrepancies appear essentially in the region of maximum energy loss, because in that region the plasma temperature is maximal and the quotient  $v_p/v_{th}$  is close to unity, therefore the stopping power is maximal. Around this energy loss maximum, the discrepancies between the stopping theories are therefore similar to the discrepancies exposed in Fig. 3.7 for a plasma temperature of 200 eV and an electron density of  $10^{21} \text{ cm}^{-3}$ . Only measurements around the maximum energy loss can thus potentially enable to distinguish between the results of the different theories and to benchmark them.

From these results, the needed energy resolution in the experiment can be estimated. A resolution better than 100 keV would make it possible to distinguish between all the presented stopping theories, provided the measurements are carried out in a time span between 7 and 9 ns after beginning of laser irradiation. This would indeed allow to distinguish differences smaller than 10 % between the theoretical predictions. The experimental error bars also should have values smaller than  $\pm 100$  keV in order for the benchmarking to be always possible. Meanwhile, a significantly worse resolution of 300-400 keV would still allow to distinguish the result of the T-Matrix with  $\lambda(v)$  from the other theories. For the experimental setup, the resolution that is aimed for is 100 keV, in order to be able to differentiate between all the theoretical predictions, provided the time span of maximum energy loss and stopping power is probed by the ion beam.

In the following section, the problematic of alpha particle stopping in the frame of ICF plasmas is discussed with the help of the theoretical notions of this chapter. The previous stopping-power approaches are applied to the corresponding projectile-target configuration. In this way, the

importance of the present study on ion stopping power at stopping maximum for ICF studies is highlighted.

### 3.3 Relevance to Inertial Confinement Fusion

As mentioned in the introduction of this work, the investigation of ion stopping at stopping maximum in a hot plasma is of high relevance for ICF, and especially for the understanding of the fuel heating mechanisms by the alpha particles resulting from thermonuclear reactions. In this section, the stopping power of alpha particles in ICF conditions is examined with the help of the theoretical notions exposed in chapter 2. An estimation of the relevant parameters of the beam-plasma interaction as well as predictions and comparisons of the alpha-particle stopping powers in the ICF fuel are provided. In this way, the importance of a fine understanding of the stopping mechanisms, in particular around the stopping maximum, is underlined.

#### 3.3.1 Characteristics of alpha-particle stopping in ICF

The energy deposition of the alpha particles is the key driver of the propagating thermonuclear burn wave in the DT fuel, and therefore one of the essential mechanisms determining the success of the ICF ignition process. Depending on the range of the alpha particles in the medium, a different plasma areal density  $\rho R$  is required to stop them completely, and hence different dimensions and/or plasma parameters of the DT pellet are necessary. The precise dimensioning of a fusion pellet is therefore directly related to the alpha-particle stopping mechanisms. The alpha particles mainly deposit their energy to the plasma electrons, though the ionic contribution is not to be neglected for the very hot plasmas involved, and then the temperature-equilibration process between the electrons and the ions occurs to actually heat the medium. For an efficient propagation of the burning wave, this equilibration process, which is based on the same physics as the stopping power (see e.g [BPS05] for details), must be achieved in a sufficiently short time scale. A better understanding of the stopping-power mechanisms enables therefore a better knowledge of the electron-ion temperature equilibration as well.

Beyond the Coulomb coupling related to the stopping maximum, a very important parameter for the stopping power of alpha particles is the plasma degeneracy [LEMP01]. The latter can be neglected in the hot carbon plasma of this work, but it plays a major role in a cold dense ICF plasma, in the early phase of alpha-particle heating. The role of degeneracy is yet beyond the scope of this work and will not be further addressed. In the following, mainly the Coulomb coupling effects are thus discussed.

A few studies can be cited to emphasize the importance of a precise understanding of the alpha-particle energy-deposition mechanisms. In [LP93a], the effects of large-angle scattering as well as of collective effects are estimated, and the role of the energy deposition to the plasma ions is underlined, showing to lead to considerable differences in the range of the alpha particles in comparison with pure electronic stopping. In [DLTB95], the role of dynamic projectile screening and thus of collective plasma effects in the stopping process is discussed, and discrepancies of up to 20% appear in the needed areal density  $\rho R$  of the DT pellet depending on how the collective effects are treated. In [OAM96], PIC simulations of collisional kinetic equations predict a significantly lower burn yield than other models. In [Sin08], the range of the alpha particles calculated within the BPS stopping-power approach appears to be 20 – 30% higher than is predicted by most of other stopping models. This increases the required  $\rho R$  of the fuel to achieve ignition. In particular, important discrepancies are demonstrated between the BPS results and the widely used Li-Petrasso model. These examples show that the stopping behavior of alpha particles in ICF plasmas and the corresponding range are far from being fully understood.

### 3.3.2 Stopping-power estimations for alpha particles in ICF

In the following, estimations of the stopping power of alpha particles in a ICF plasma are carried out basing on the previous theories and models. It is shown how the investigation of the present work can bring insights into the problem of alpha-particle stopping.

From the triggering of the first thermonuclear reactions in the DT fuel to the propagation of the thermonuclear burn wave through the whole fusion pellet, the plasma conditions that the alpha particles interact with are very different. When the first alpha particles are created, with an initial energy of 0.875 MeV/u, the surrounding plasma medium is very dense and relatively cold, featuring typical electron densities of  $10^{26-27} \text{ cm}^{-3}$  and plasma temperatures of 50-100 eV. For this beam-plasma configuration, the velocity quotient is  $v_p/v_{th} \approx 4$ , thus well above the stopping maximum. Subsequently, in the hot burning fuel, the electron density is about one order of magnitude lower (about  $10^{25-26} \text{ cm}^{-3}$ ) and the electron temperature reaches 5 keV. Then, the velocity quotient is  $v_p/v_{th} \ll 1$ , significantly below the stopping maximum. Therefore, while the plasma density roughly stays around the value of  $10^{26} \text{ cm}^{-3}$ , the temperature is enhanced by a factor 100, from 50 to 5000 eV. Hence, the alpha particles evolve over a wide interval of  $v_p/v_{th}$ , and a large part of their stopping power spectrum as a function of velocity is involved. The maximum of stopping power for the alpha particles at 0.875 MeV/u energy is reached for temperatures around 200 eV as in this work at their initial energy value. It can be noted that in the 5 keV burning plasma, the thermal velocity of the plasma ions is not negligible anymore and the contribution of the plasma ions to the projectile stopping power must be taken into account. However, here only the electronic stopping is treated, as the stopping models and the discrepancies appearing between them are similar for the electronic and the ionic stopping power.

On the thermodynamic path experienced by the alpha particles, typical plasma parameters corresponding to maximum stopping power are thus an electron density of  $10^{26} \text{ cm}^{-3}$  and an electron temperature of 200 eV. The corresponding stopping-power predictions are shown in Fig. 3.12 with the same theories as in Fig. 3.7.

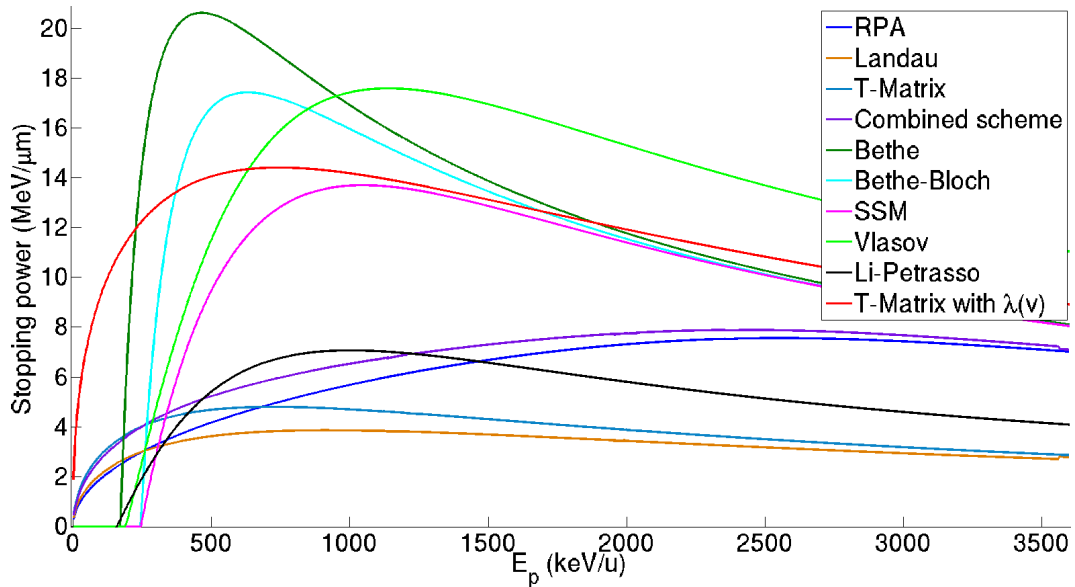


Figure 3.12: Comparison of various theoretical stopping-power predictions for alpha particles in ICF fuel as a function of the projectile energy, at  $n_e = 10^{26} \text{ cm}^{-3}$  and  $T_e = 200 \text{ eV}$ . The initial energy of the alpha particles is 0.875 MeV/u. The interpretation of the stopping values is particularly involved because of the presence of degeneracy and strong coupling effects.

Here, the beam-plasma interaction is significantly more complex because of the high density of the



ICF plasma. The degeneracy coefficient  $\Theta \approx 0.1$ , hence the corresponding effects on the stopping power may be important, and they are not taken into account by most of the stopping theories. Moreover,  $\Gamma \approx 0.5$  and  $\gamma \approx 0.1$ , meaning that the plasma is nonideal and that the interaction is slightly nonlinear. Important plasma correlations as well as beam-plasma correlations, in addition of the degeneracy, are therefore likely to strongly influence the ion-stopping process. This is why the discrepancies in the stopping powers calculated by the different theories are particularly pronounced in that case, and they reach factors of 5-6 around the region of maximum stopping power. An alpha particle generated in the considered plasma conditions, at an initial energy of 0.875 MeV/u close to the stopping maximum, therefore experiences a very different stopping force depending on the considered stopping-power approach. This might have a considerable influence on the whole alpha-particle stopping process and range. The predictions show that as the plasma temperature increases, the coupling strength of the interaction is reduced and that at the same time the ratio  $v_p/v_{th}$  is shifted to the region below the stopping-power maximum, where most theories agree again with each other. As soon as the burning plasma reaches temperatures of a few keV, the stopping-power description is thus relatively simple. But in the colder fuel, and particularly at temperatures around 200 eV which correspond to the stopping-power maximum of the generated alpha particles, the description is problematic. Testing the validity of the stopping theories at stopping maximum at a temperature of 200 eV in an ideal plasma constitutes a first step towards the understanding of the stopping mechanisms of alpha particles, even if for that purpose strong coupling effects and degeneracy have in addition to be considered.

# Chapter 4

## Experimental setup

In this chapter, the experimental setup and methods for the measurement of the energy loss of carbon ions at stopping maximum in a hot laser-generated plasma are presented.

In a first section 4.1, the existing scientific infrastructure used in the frame of this work is described and the diagnostics for ion energy-loss experiments are presented. The setup of the latest energy-loss experiments carried out by using this infrastructure, already introduced in section 3.1, is described in details, as it constitutes a basis for the experimental work of this thesis.

The second section 4.2 is devoted to the modifications of this setup for the special case of energy-loss measurements at maximum stopping power. It starts with the specific target design, continues with the design and construction of an adapted CVD-diamond detector, and ends with the development of a detector-screening system for mitigation of the influence of plasma radiation on the measurements.

### 4.1 Existing setup at the Z6 experimental area

This paragraph gives an overview of the main components of the scientific infrastructure at the experimental area Z6 [Z6] of GSI, where the experiment has been carried out. The Z6 area benefits from the simultaneous presence of a beamline of the UNILAC (UNiversal Linear ACcelerator) for ion-beam generation, of the high-energy laser system *nhelix* (NanosekundenHochEnergieLasersystem für IonenstrahleXperimente) and of the  $10^\circ$  beamline of the high-energy laser system PHELIX (Petawatt HochEnergie Laser für SchwerIoneneXperimente). In this worldwide unique combination, the two laser beams can be used to generate a hot plasma by heating a solid foil target inside the target chamber, while the plasma is probed by high-frequency pulsed ion beams. This setup therefore offers opportunities for unique experiments on ion energy loss in a hot dense plasma.

#### 4.1.1 The UNILAC accelerator

##### Accelerator facility

The accelerator infrastructure of GSI can be divided into a low-energy area and a high-energy area. The low-energy part is constituted by the UNILAC, which is a 120 m long high-frequency linear accelerator for ions of all elements from hydrogen to uranium in an energy range of 3.6-20 MeV/u, corresponding to velocities of up to 20 % of light velocity. The UNILAC can either be employed for experiments in that intermediate ion energy range where it can deliver ion beams into several beamlines including the Z6 experimental area, or it can serve as an injector for the higher-energy part, which consists of the SIS 18 synchrotron (SchwerIonenSynchrotron) and the ESR storage ring (ExperimentierSpeicherRing). In the SIS 18, the ions can be further accelerated in order to reach velocities of up to 90 % of light velocity, corresponding to energies higher than

2 GeV/u. Subsequently, the ions can be further injected and stored into the ESR.

In this work, only the lower-energy UNILAC part of the facility is used, where the Z6 experimental area is attached. A scheme of the UNILAC is presented in Fig. 4.1. While detailed information about the UNILAC facility can be found in [Uni], a brief description is given in the following .

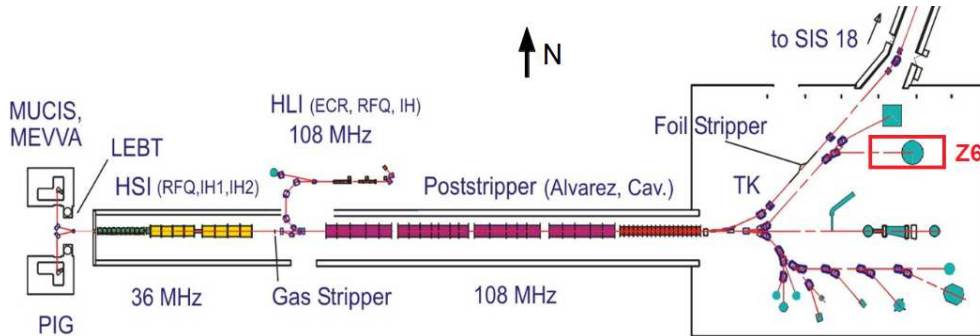


Figure 4.1: Scheme of the UNILAC accelerator facility [Uni]. The interaction between ion beams and plasmas is investigated at the Z6 experimental area, which is marked in the picture.

### **Ion-beam generation**

The UNILAC offers three different ion injectors, basing on various ion sources and delivering different ion characteristics.

On the one hand, at the west-end of UNILAC are located the two high-current injectors (Hoch-StromInjektor, HSI): the so-called Terminal North-Injektor and Terminal South-Injektor. Terminal North uses various volume-type or vacuum-arc sources (MeVVA, MUCIS, CHORDIS), enabling to generate ion beams of a wide range of elements at beam intensities of up to 300 mA, depending on the element, and at low duty cycle (up to 10 Hz). Terminal South instead uses a Penning source (PIG) to produce ions with relatively low energy and small charge-state value ( $< 10+$ ) at a beam current of up to several hundred  $\mu\text{A}$  and at high duty cycle. The ions from North- and South-Terminal are transported into a so-called *Low-Energy Beam Transport* line (LEBT). There, they pass through Radio Frequency Quadrupoles (RFQ), inter-digitated H-type accelerators (IH) and are then charged in a gas-stripper. Through the RFQ, the ion beam is given a temporal micro-bunch structure at 36.136 MHz frequency (corresponding to a bunch period of 27.673 ns) in addition of its macro-bunch structure given by the 50 Hz line frequency. On the other hand, the High Charge Injector (HochLadungsInjektor, HLI), situated North of the UNILAC, produces highly charged and pre-accelerated pulsed ion beams by using an electron-cyclotron-resonance (ECR) source. These ions then traverse an RFQ structure at 108.404 MHz frequency and an IH.

Subsequently, the generated ion beams from the three injectors are directed into the post-stripper, made of four Alvarez accelerating cavities. These Alvarez tanks are operated at a frequency of 108.404 MHz, and make it possible to progressively increase the ion energy into the range 3.6-11.6 MeV/u. Ions from the HLI are thus able to fill every Alvarez period, whereas ions from the HSI only fill every third period. After the Alvarez cavities, other single resonators enable to continuously increase the ion energy to up to 20 MeV/u, and the beam can be distributed to the different experimental areas with the help of dipole and quadrupole magnets. The ion beam can be diagnosed in position by using gratings and in intensity by using either Faraday-cups or transformers.

To summarize, the ion beam generated by the UNILAC is pulsed with a macro-bunch frequency of 50 Hz, which corresponds to a 20 ms period, and a micro-bunch frequency of either 36.136

MHz (HSI) or 108.404 MHz (HLI), corresponding to a micro-bunch period of respectively 27.673 ns and 9.224 ns. The temporal width of the micro-bunches is determined by the oscillation period of the electric field in the Alvarez accelerating cavities. As the duty cycle in these cavities is approximately 60/360, an initial bunch width of  $60/360 \cdot T$ , where  $T$  is the Alvarez period, of about 1.54 ns is obtained. The value at Z6 experimental area is in fact higher (2-3 ns at FWHM), on the one hand because of the intrinsic energy imprecision, and on the other hand because of the drift distance between the last resonators and the Z6 target chamber. The temporal profile of the micro-bunches can be approximated by a Gaussian shape. The macro-bunches are usually 1-5 ms long but at Z6 their duration can be reduced down to 40  $\mu$ s by using a chopper. The temporal structure of the UNILAC ion beam is depicted in Fig. 4.2.

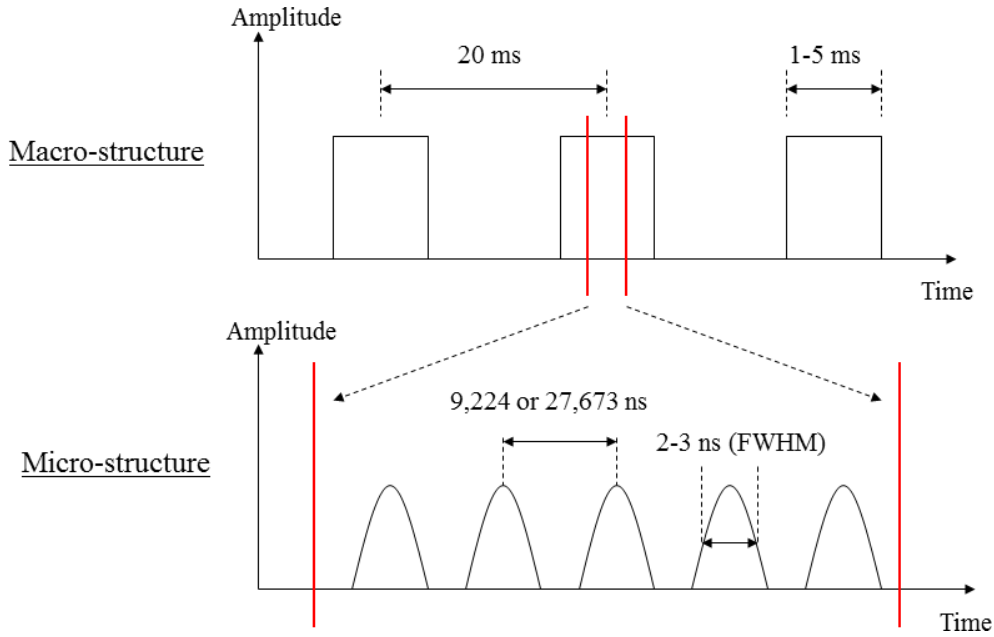


Figure 4.2: Macro-bunch and micro-bunch temporal structure of the UNILAC ion beam. At Z6, the macro-bunch period is increased to 200 ms.

At Z6, the experiments are actually carried out with a 5 Hz frequency (one macro-bunch every 200 ms), as this is needed for synchronization with the laser systems employed in the ion energy-loss experiments. Hence the experiments described in this work are designated as "parasitic" in relation to the main UNILAC experiments, because they only need 10 % of the UNILAC ion bunches.

It has to be noted that due to the operation mode of the Alvarez accelerating cavities, the ion energy has a minimum value of 3.6 MeV/u. In order to obtain a lower energy, the projectile ions therefore have to be decelerated, as described in details in paragraph 4.2.1 for the experiment of this work.

#### 4.1.2 The PHELIX and *nhelix* laser systems

At the Z6 experimental area, two high-energy laser systems can be employed in conjunction in order to heat targets to the plasma state, in a single-shot mode. In this way, hot dense plasmas can be generated with electron densities reaching one hundredth of solid density and electron temperatures of up to a few hundred eV. The obtained plasma conditions are therefore relevant to ICF. The plasma typically stays hot and dense for a few tens ns, before being diluted by its own rapid hydrodynamic expansion. As mentioned in 3.1.2, the requirements on the plasma for the experiment are the following.

First, the plasma must be transversally homogeneous to the ion axis for high-quality energy-loss measurements. Second, the plasma parameters must be systematically reproducible. Third, a plasma temperature of 200 eV is required for reaching full ionization of the carbon target. Fourthly, the plasma must stay highly ionized and homogeneous for a sufficient time window of at least a few nanoseconds so that stopping measurements can be conducted at different times, probing different plasma conditions.

For these purposes, the laser beams have to be highly energetic, spatially homogeneous and sufficiently extended, and they must feature a sufficiently long pulse duration as well as a preferably rectangular temporal form. The PHELIX and *nhelix* laser systems are able to fulfill these requirements and can be synchronized with the UNILAC ion beam to probe the wished plasma conditions.

This section describes the two laser systems as well as the plasma interferometry diagnostic that is implemented with the *nhelix* laser system, and of the synchronization system between the laser and ion beams.

## PHELIX

The PHELIX laser system is based on a Master Oscillator Power Amplifier (MOPA) model, that enables a separation of the oscillator and of the amplification system. PHELIX can provide for either short or long pulses, depending on the frontend, and can be used at Z6 via several beamlines. The one frontend, consisting of a Ti:sapphire oscillator, can produce short pulses with a duration down to 100 fs (high-power mode). It is subsequently amplified by using the CPA (Chirped-Pulse Amplification) technique [SM85, MSB<sup>+</sup>88]. The other frontend, relying on an optical-fiber system, generates longer pulses in the range 700 ps-20 ns, whose form can be adjusted with a pulse generator. In all cases, the fundamental wavelength of the beam is 1053 nm. Detailed information about the PHELIX facility can be found in [?, BAB<sup>+</sup>10].

- **Long-pulse frontend**

The long-pulse frontend generates a continuous beam with the optical-fiber system<sup>1</sup>, that is subsequently sampled to pulses of 100 ns duration at 10 Hz frequency at a maximal energy of 10 nJ with the help of an acousto-optical modulator. Then, the pulses are amplified a first time in a double-pass amplifier and temporally modulated in a chopper. In order to compensate for the losses in the system, the beam is conducted through another fiber amplifier for improving its contrast. Then the beam pulse length is adjusted in the range 1-20 ns with the help of an electro-optical modulator, and the pulses subsequently enter a Nd:glass ring amplifier, after which they feature a typical energy of 20 mJ and a frequency of 0.5 Hz. Finally, the beam is coupled into the pre-amplifier and then into the main amplifier.

- **Short-pulse frontend**

In the short-pulse frontend, a pulse of short duration and thus of large spectral bandwidth is used to reach a high beam power. This is why Ti-sapphire amplifiers, featuring a high amplification bandwidth, are employed. First, a pulse of 100 fs duration and 4 nJ energy is generated in a laser oscillator<sup>2</sup>. This pulse then crosses a stretcher where its peak intensity is reduced in view of the subsequent CPA process in the main amplifier (see below). The stretcher is followed by two regenerative Ti-sapphire amplifiers, respectively linear and annular, enabling the beam to reach a 30 mJ energy with a 1.2 ns pulse length before the pre-amplifier.

- **Pre-amplifier**

---

<sup>1</sup>Commercially available *Koheras Basik*

<sup>2</sup>Commercially available *Coherent Mira*

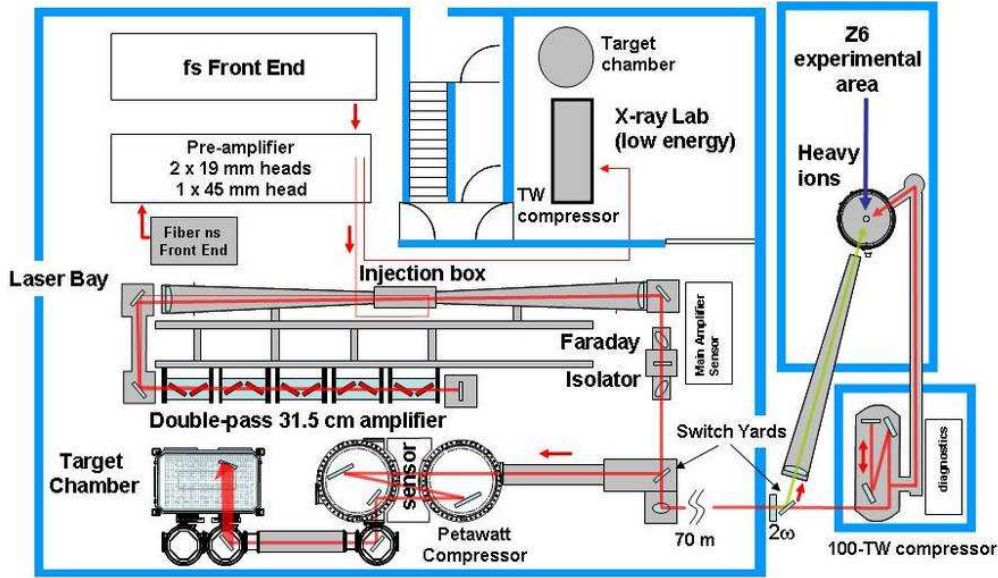


Figure 4.3: Scheme of the PHELIX laser system (from [?]).

The pre-amplifier is composed of three Nd:glass rod amplifiers pumped with flash-lamps, which are able to convert the 30 mJ energy from the short-pulse frontend to a 5 J energy and the 50 mJ energy from the long-pulse frontend to a 10 J energy. In order to obtain circular or elliptic pulse profiles, the Gaussian beam profile is turned into a Gaussian profile of higher order by using a serrated aperture. This aperture behaves like a low-pass room-frequency filter, steeping the edges of the profile and creating a flat profile, named *Top-Hat* profile. However this pulse profile is more sensitive to beam modulations and especially to self-focusing. This is the reason why four telescopes, serving as room-frequency filters, are placed in the pre-amplifier system for preventing these beam-modulation phenomena. The weak thermal conductivity of the glass rods of the amplifiers is the reason why laser shots using the pre-amplifier cannot be carried out more frequently than every 3 minutes.

- **Main amplifier**

The main amplifier consists of Nd:glass disk amplifiers, which make it possible to amplify the beam by a factor 100. In this way, it is possible, when using the long-pulse frontend, to obtain 0.7-20 ns long pulses with an energy up to several hundred J, and, by using the short-pulse frontend, to obtain 0.4-20 ps long pulses with a 120 J energy. In the short-pulse mode, the CPA technique is applied. In this process, as mentioned before, the pulse is first stretched through a dispersive element before being introduced into the pre-amplifier and amplifier chain. In this way, strongly intensity-dependent undesirable nonlinear effects are avoided as well as possible damage to the system. After traversing the whole amplifier chain and before being conducted to the experimental area, the beam is chirped again in a grid-compressor, which is an element of negative dispersion. A maximal beam intensity of  $10^{16}$  W/cm<sup>2</sup> for the long-pulse mode and of  $10^{21}$  W/cm<sup>2</sup> for the short-pulse mode can thus be reached.

- **Target area**

The PHELIX beam is then transported by a series of mirrors to the target area at Z6. Presently, two PHELIX beamlines lead to Z6. The so-called 10° beamline can be used for long and short pulses, whereas the 100 TW beamline is used for short pulses in relation to experiments on laser-ion acceleration. A 90° beamline is also in project to make it

possible to irradiate the target perpendicularly to the ion-beam axis. Before arriving in the target chamber through the  $10^\circ$  beamline, the laser beam passes through a DKDP crystal (Deuterated Potassium Dihydrogen Phosphate), where it is frequency-doubled, reaching a wavelength of 527 nm. Short before the interaction region, the beam is focused by means of a 527 nm-matched lens and its spatial focus profile is smoothed through a Random Phase Plate (RPP). Then the beam enters the target chamber from the opposite direction to the one of the ion beam, with a strictly speaking  $9^\circ$  vertical angle in relation to the ion axis. This configuration results in a 1 mm focus spot diameter on the target.

### *nhelix*

The *nhelix* laser system makes it possible, with its various beamlines, to simultaneously generate a hot dense plasma by irradiating a solid target and to diagnose it. A detailed description of the system can be found in [Azi04, SSR<sup>+</sup>05, Sch07] and a scheme of the infrastructure is shown in Fig. 4.4. The *nhelix* laser system is based on two different oscillators, namely the *Powerlite*<sup>3</sup> (OS1) and the *Geola*<sup>4</sup> (OS2). Both are Nd:YAG (Neodymium-doped yttrium-aluminum-garnet) oscillators, that generate a fundamental wavelength of 1064 nm. The beams from both oscillators can be amplified through six Nd:glass rods (RA on the scheme) to reach their final output energies. While the Powerlite oscillator provides the beam for the target irradiation, the Geola oscillator is used for diagnostic purposes, namely to perform the multi-frame interferometry diagnostic.

#### • Target heating beam

The Powerlite is based on an active Q-switch and generates long Gaussian-profiled pulses with a temporal width of 15 ns (FWHM) and an energy of 200 mJ. The corresponding beam is represented in red on the scheme. After leaving the oscillator frontend, the beam goes through a Faraday rotator (FI1), whose role is to protect the oscillator from beam back-reflections. In order to obtain a rectangular temporal pulse profile, the pulse edges are cut with the help of an external Pockels cell (PC), resulting in a pulse width of 6-7 ns FWHM. This is the minimum pulse duration that can be obtained, as the opening and closing time of the cell lead to a rising and falling edge duration of 3 ns each. These steep edges make it possible to approach the wished rectangular time profile of the beam. The final beam output energy can be increased to up to 70 J by using the successive Nd:glass rod amplifiers. Before each amplifier, the beam passes through a telescope. The latter contains a room-frequency filter to progressively broaden the beam spatially, protecting in this way the optical components from too high peak intensities. Five successive amplifiers are available with respective diameters of 16, 25, 32, 45 and 64 mm.

Leaving the laser room, the final beam, approximately 60 mm broad, is transported to the target chamber room via several mirrors. For this purpose, the beam can follow two different paths. The red way on the scheme is employed for the beam at the original wavelength of 1064 nm, while the yellow one is employed when the laser beam is to be frequency-doubled. The latter case is used for the present work, as a frequency-doubled beam makes it possible to obtain a more homogeneous plasma. The beam is thus converted to a wavelength of 532 nm through a KDP-crystal (Potassium-Dihydrogen-Phosphate) before the target chamber, with a conversion efficiency close to 55 %. After entering the target chamber, the Powerlite beam focus profile is spatially homogenized through a RPP [PDB<sup>+</sup>93] and focused, by means of a frequency-matched lens, on the target situated in the center of the target chamber. Due to the RPP, a focus spot diameter of 1 mm (when at best focus) is reached on the target.

<sup>3</sup>Model *Powerlite Precision 8000* by the *Continuum* company

<sup>4</sup>Model *G-Mini-B100-GSI* by the *Geola Technologies* company

Therefore, all the beamline parameters are tuned so that the incoming PHELIX and *nhelix* beams have the same characteristics.

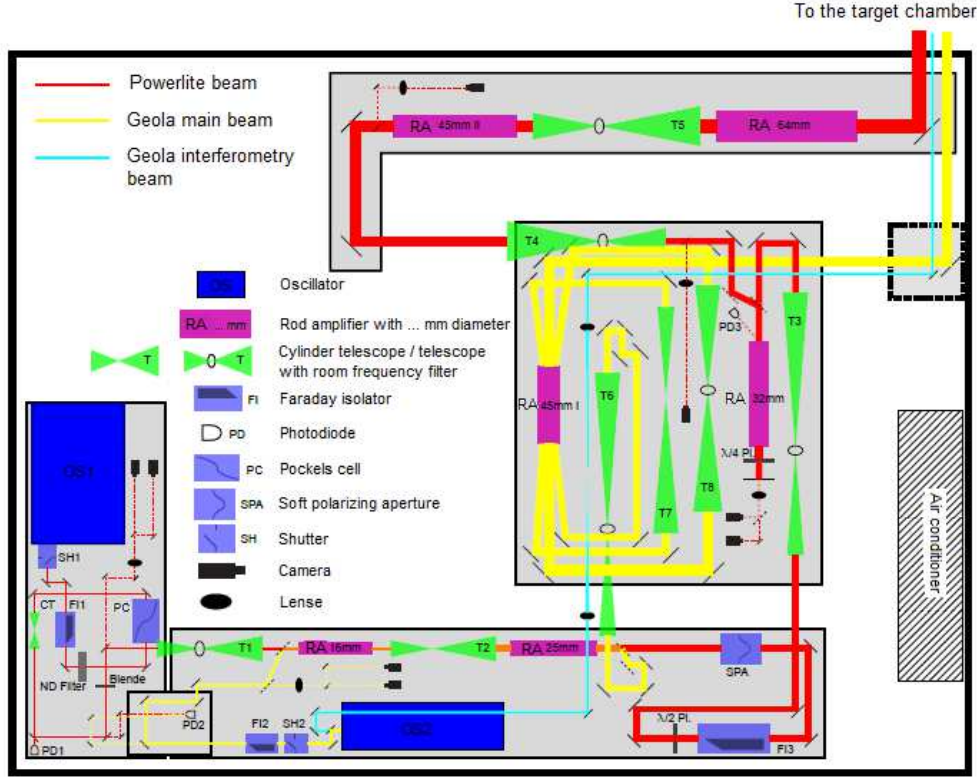


Figure 4.4: Scheme of the *nhelix* laser system (from [Sch07]).

#### • Interferometric beam

The Geola oscillator is also based on active Q-switching and enables to generate 5 ns long pulses. These are additionally shortened to 0.5 ns by using a SBS-cell (Stimulated Brillouin Scattering), with an output energy of 120 mJ. In principle, the Geola oscillator can deliver beams into two different beamlines. The one, represented in yellow on the scheme, is dedicated to optical Thomson scattering but it was not in service at the time of the work, only serving in its final part to conduct the Powerlite beam to the target chamber through the KDP-crystal. The other available beamline, represented in blue on the scheme, is used for the multi-frame interferometry plasma diagnostic. It uses about 1 % of the Geola beam intensity, as selected via a beam splitter, and is not amplified. From the oscillator room, the interferometry beam is led into the target chamber room via other mirrors, where it is frequency-tripled by using two successive BBO-crystals (Beta-Barium-Borate). The frequency tripling makes it possible to obtain a beam wavelength of 355 nm. As a consequence, the critical density of the plasma for the Geola beam is increased by a factor 9 in comparison with the one of the initial beam, reaching a value  $\approx 9 \times 10^{21} \text{ cm}^{-3}$  (see 2.1.2). In this way, the interferometric beam can probe plasma regions of higher density.

In the following paragraph, the experimental diagnostics giving access to the plasma conditions are presented, namely the laser diagnostics and the interferometric diagnostic.



### Diagnosing the plasma conditions

As is discussed in details in 3.1.2, the full knowledge of the plasma conditions over space and time is necessary to interpret the experimental ion-stopping data and to compare them with the theoretical predictions. The needed precision for the characterization of the plasma conditions in time is of about 1 ns, as the plasma dynamics evolves over a ns-scale.

The multi-frame interferometry diagnostic enables to determine the temporal evolution of the plasma free-electron density. By comparing the measured electron-density profiles to the results of the RALEF2D simulations, the hydrodynamic code can be benchmarked. In this way, the other plasma parameters: electron temperature and ionization degree, can be accessed by simulations.

Yet the dense plasma parts beyond the critical surface cannot be probed by interferometry. This is why the code benchmarking is carried out in the sub-critical region, which then enables to determine the parameters of all plasma parts.

A very important point for assessing the precision of the hydrodynamic simulations is to diagnose the laser parameters in the experiment. The pulse length and energy must be determined in order to know if the simulation results, obtained for a pulse energy of 30 J and a pulse length of 7 ns at FWHM, indeed correspond to the experimental plasma conditions. This is why for each experimental shot, the energy of the laser pulses is measured with the help of calorimeters shortly before the target area, while the corresponding laser-pulse lengths and shapes are registered by using photodiodes.

The working principle of the interferometric diagnostic for determining the plasma conditions is now exposed. A detailed description of the interferometric setup and of its properties can be found in [B10, BFF<sup>+</sup>12], and the main components of the interferometric setup are shown in Fig. 4.5.

The diagnostic is based on a Nomarski-type interferometer. In this scheme, the probe beam is split into two parts through a Wollaston crystal *after* its interaction with the plasma. Due to the birefringence properties of the prism, the beam is separated into an ordinary and an extraordinary beam. As these beams propagate at slightly different velocities in the crystal, the refraction behavior of the medium leads to different propagation angles when exiting the prism. After passing through a polarizer and an additional wavelength filter for improving the final contrast of the measurement, the two beams impinge on a CCD-camera, where the beam part that interacted with the plasma overlaps with the reference beam part. From the arising interference patterns, the density of the free plasma electrons can be determined when assuming a cylindrical symmetry of the plasma. Theoretically, the maximum plasma density that can be probed is the critical density, equal in the case of the 355 nm Geola beam to  $8.8 \times 10^{21} \text{ cm}^{-3}$ . However, due to the gradients of the plasma refractive index leading to beam deviations, the actual maximum density that can be measured with the setup lies around or slightly below  $10^{20} \text{ cm}^{-3}$ .

The diagnostic is said to be *multi-frame* because it uses four distinct beams that probe the plasma successively with a 2 ns time interval. The setup is thus composed of four parallel Nomarski interferometers. In this way, four successive density measurements are obtained for a given laser-plasma experiment. It therefore makes it possible to monitor the evolution of the free-electron density over a time range of 6 ns in intervals of 2 ns. The temporal resolution corresponds to the duration of the Geola pulse of 0.5 ns.

The key element of the setup, which generates the four successive pulses, is an optical ring positioned before the zone of interaction with the plasma. There, the combination of a thin film polarizer (TFP) and of a  $\lambda/2$  waveplate makes it possible to decouple a fraction of the beam energy at each passage through the ring. The latter is built so that each beam passage requires 2 ns, hence each pulse is decoupled 2 ns after the previous one. Moreover, the ring is purposely slightly mis-adjusted so that each exiting pulse features a small angle in relation to the pre-

vious one. In this way, after the interaction with the plasma, the four beams can be separately deviated by using micro-mirrors, and thus directed to their respective Nomarski interferometer setups. Only the first four pulses are used for the measurements, because they still feature a sufficient beam intensity.

After leaving the ring and before entering the plasma, the four beams are broadened by means of a telescope in order to reach a diameter of several millimeters. In this way, the entire plasma expansion region can be probed, while a part of the beam does not interact with plasma, serving as reference in the subsequent interferometry measurement.

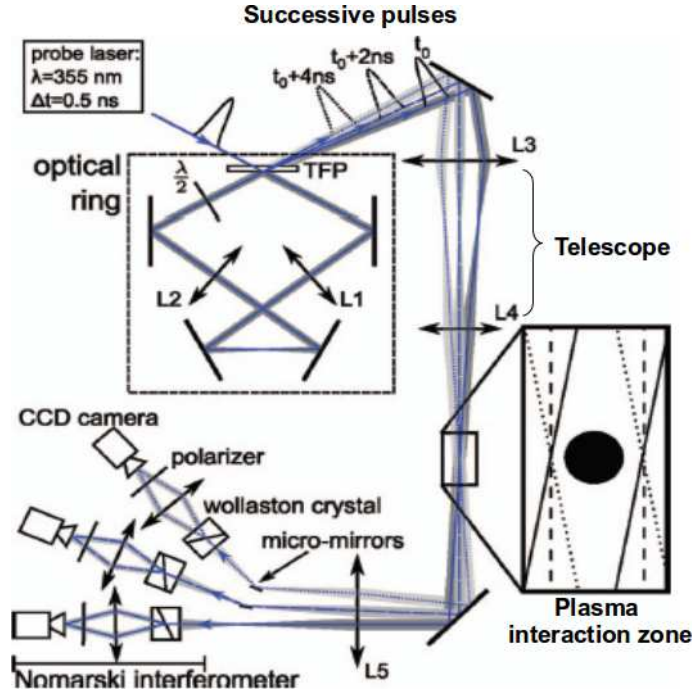


Figure 4.5: Working principle of the multi-frame interferometry setup. The Geola laser beam, featuring a 355 nm wavelength and a 0.5 ns duration, is split into four successive pulses with a 2 ns time interval and with slightly different propagation angles through an optical ring. The pulse diameters are subsequently increased via a telescope before interacting with the plasma. Finally, micro-mirrors guide the pulses into their respective Nomarski interferometers, where the interference patterns are detected by using CCD cameras.

The various beams employed in the setup: ion beam from the UNILAC, laser-heating beams from the PHELIX and *nhelix* systems, as well as interferometry-diagnostic beam from the *nhelix* system, have been presented. A last crucial point is the synchronization of these beams in order to probe the desired plasma conditions.

### Synchronization of the lasers with the UNILAC

For the energy-loss experiments, it is essential to properly synchronize the PHELIX and *nhelix* lasers, operated at frequencies of 0.5 Hz and 5 Hz respectively, with the micro-bunch frequency of the UNILAC accelerator. The ion macro-bunch and micro-bunch periodic signals, operated respectively at 5 Hz and either 36.136 MHz or 108.404 MHz frequencies, are converted to logical signals with the help of a level shifter and a discriminator respectively. After treatment in a coincidence unit, a 5 Hz signal is generated that is used to adjust the PHELIX delay in relation to the micro-bunches by means of a delay generator. By using another delay generator, the *nhelix* laser system is synchronized with PHELIX. Following this procedure, it is possible to adjust the

delay between the lasers and the ions in steps of 1 ns, and the synchronization precision  $\approx 1$  ns. In this way, the plasma can be probed by the ion beam at different times, and the temporal evolution of the ion energy loss in plasma can be determined.

### 4.1.3 TOF measurements with CVD-diamond detectors

#### TOF measurements

The time-of-flight (TOF) method enables to determine the energy loss of the projectile ions in plasma. In the middle of the Z6 target chamber, a thin free-standing solid target foil ([LHK<sup>+</sup>02]) is irradiated by laser beams from both laser systems, from opposite sides and simultaneously, generating a hot dense plasma whose lifetime is limited to several tens of nanoseconds. The ion beam from the UNILAC interacts with this plasma at a time determined by the synchronization process. After interaction, the ions are registered on a time-resolving semi-conductor chemical-vapor-deposition (CVD) diamond detector.

The principle of the TOF measurement is shown in Fig. 4.6, representing the ion micro-bunches as a function of time. Before the target is heated to the plasma state by the laser(s), the period of the micro-bunches is constant as the projectile ions probe the cold foil target. After the laser irradiation, assuming that the energy loss in plasma is enhanced in relation to the one in cold matter, the ion bunches (in blue) are shifted in comparison to the bunches that interacted with cold matter (in grey). This time shift corresponds to the energy-loss increase of the projectile ions in the plasma.

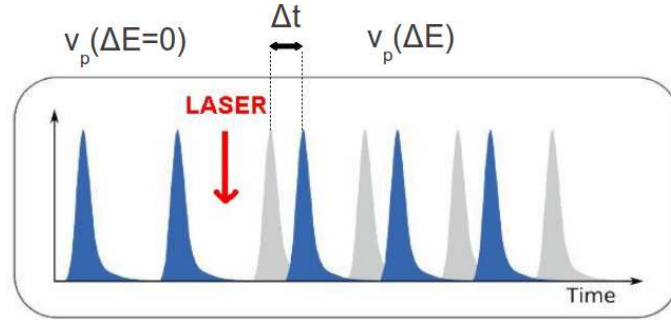


Figure 4.6: Scheme of the time shift of ion micro-bunches due to an increase of the energy loss in plasma. Blue: ion bunches undergoing an increased energy loss in plasma, after the laser impact. Grey: expected position of the bunches if the energy loss in plasma stays equal to the one in the cold target.

The energy loss can then be deduced by using equation 4.1, where  $v_p$  is the projectile ion velocity,  $L$  is the TOF-distance, and  $\Delta E$  is the energy loss of the ions. By determining the time shift  $\Delta t$  in the experiment with a time-resolved detector, and knowing the initial ion velocity  $v_p(\Delta E = 0)$ , the projectile velocity after the plasma and thus its energy loss in the plasma  $\Delta E$  can be inferred.

$$\Delta t = L \cdot \left( \frac{1}{v_p(\Delta E = 0)} - \frac{1}{v_p(\Delta E)} \right) \quad (4.1)$$

An important parameter in the experiment is the energy resolution of the TOF measurement. The relative energy resolution of the ion beam can be estimated with the help of equation 4.2, where  $\Delta t_{det}$  is the temporal resolution of the detector in the experiment.

$$\frac{\Delta E}{E} = 2 \cdot \frac{v_p}{L} \cdot \Delta t_{det} \quad (4.2)$$

$\frac{\Delta E}{E}$  depends on the TOF-detector resolution, as well as on the projectile energy and on the TOF-distance. As explained in paragraph 3.2, an energy resolution of 100 keV is needed in the experiment in order to be able to distinguish 10 % differences between the described stopping-power theories, making possible to discriminate them. If a CVD-diamond device, that features usual time-resolution values around 250 ps, is used as TOF detector, it implies that the TOF distance must be at least 30 cm large.

CVD-diamond detectors and their key properties are now presented.

### CVD-diamond TOF-detectors

CVD-diamond detectors are an ideal tool for the detection of intense high-frequency ion bunches and have hence been used in ion energy-loss experiments at Z6 for several years. The working principle of such a detector is shown in Fig. 4.7. When an ion traverses the diamond sample, it ionizes atoms on its track, generating pairs of electrons and holes. The sample is metalized on both sides in the scheme of a planar capacitor and an external electric field is applied between the electrodes. The generated charge carriers are thus attracted to the electrodes, where they generate an electric signal that is subsequently amplified in tension and registered on a digital oscilloscope.

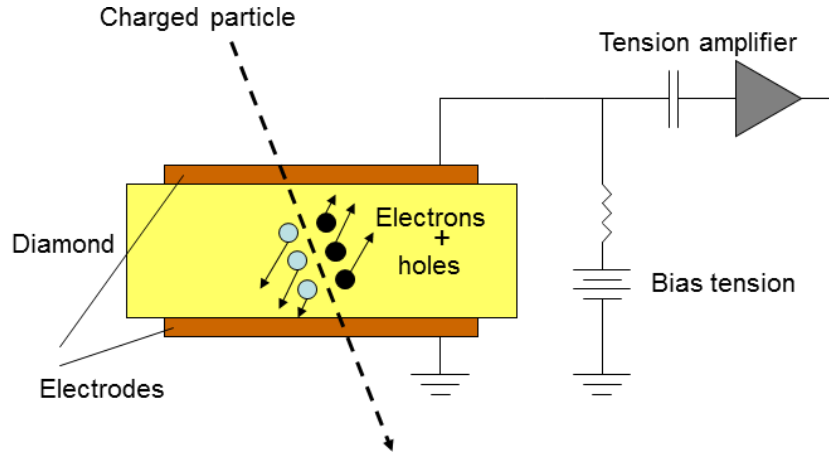


Figure 4.7: Working principle of a CVD-diamond charged-particle detector.

Details on the properties of CVD-diamond as well as on the design and the construction of CVD-diamond detectors, can be found in [Wam06, Cay09] and [CFS<sup>+</sup>13]. In the following, the most important diamond and detector features are summarized.

Due to its remarkable structural properties related to its sp<sup>3</sup>-hybride bonds, diamond features an excellent radiation hardness as well as very good temporal properties. Because it has the highest mechanical hardness and thermal conductivity among known materials, diamond is capable of withstanding very high ion fluxes, significantly higher than for example silicon. The temporal properties can be summarized in the following points.

First, the electron and hole mobilities have one of the highest values among semi-conductors. Second, the high electrical resistivity of diamond enables to apply high external electric fields of up to 2 V/ $\mu$ m. Combined with the first point, this leads to high drift velocities of the charge carriers in the material. Third, the dielectric constant  $\epsilon$  of diamond is twice lower than the one of silicon, which ensures a low capacitance value when a convenient electrode surface and sample thickness are chosen. The combination of these three aspects allows a very good intrinsic temporal resolution of down to several tens of picoseconds. Moreover, the low capacitance value ( $C$ ), when used in conjunction with a low-impedance ( $R$ ) broadband amplifier, leads to a low detector time constant  $\tau = RC$  of several nanoseconds, which results in short signals on the

nanosecond time scale.

A further important advantage of diamond is its high band-gap value of 5.45 eV, which has three consequences. First, no p-n junction is required in the sample as in other semi-conductors to create a charge-free zone, because the whole diamond is charge-free when not irradiated by charged particles. Second, the thermal noise is relatively low, making the operation of the detector possible at room temperature, and the signal-to-noise ratio is better than for silicon for example. Third, the sensitivity of diamond is slightly lower than the one of silicon. Therefore, while still enabling an efficient ion detection, even of single ions, diamond is less sensitive to plasma radiation. As is exposed in 4.2.3, the influence of plasma radiation on the detector is one of the key issues in the experimental part of this work.

Two crucial parameters for the design of a diamond detector are the surface area of the electrodes and the thickness of the diamond sample.

*A priori*, a large detector surface is desirable to detect as many ions as possible and thus to obtain signals featuring a sufficiently large amplitude to be exploitable. In addition, the detector thickness should be smaller than the range of the incident ions, so that the ions are not stopped inside the sample. In this way, a relatively homogeneous ionization density is generated along the ion track and in addition, damage in the sample is avoided.

However, the surface area and the thickness have to be chosen carefully because they also determine the capacitance value:

$$C = \frac{\epsilon S}{d} \quad (4.3)$$

where  $S$  is the surface of the electrodes,  $d$  is the thickness of the diamond sample, and  $\epsilon$  is the dielectric permittivity coefficient of diamond. The capacitance has to be small enough to keep the signals significantly shorter than the micro-bunch period of the ion bunches, i.e in the hardest case  $\tau = RC < 9.224$  ns, if  $R$  is the impedance of the transmission line. The surface area therefore cannot be arbitrarily large and a common process consists in dividing it into several sectors by segmenting the front electrode. Likewise, the thickness cannot be arbitrarily small and is usually chosen in the range 10-20  $\mu\text{m}$ , 20  $\mu\text{m}$  being the approximate range of projectile ions at the usual Z6 energies of 4-5 MeV/u, as estimated with the SRIM code [sri]. In addition, it can be noted that the CVD-diamond used for the TOF-detectors at Z6 is polycrystalline, i.e grown on a silicon wafer during the CVD-process. In this way, significantly larger and more cost-effective diamond samples can be produced than in the case of single-crystal-diamond. The latter is still in a development phase and not yet adapted to the kind of experiments as the one carried out in this work.

#### 4.1.4 Ion-stopping experiments at Z6

For the measurement of the ion energy loss at stopping maximum in a laser-generated plasma, a setup that is similar to previous energy-loss experiments at Z6 is employed. Indeed, as explained in 3.1.2, the present work partly bases on the setup and the results of [FBB<sup>+</sup>13] and can be seen as further extension of these experiments. Now, the recent experiments on ion stopping in a laser-generated plasma at Z6 are presented. The corresponding experimental setups are described and the obtained results are summarized. Hence the setup evolution leading to the present work is explained.

##### One-sided laser irradiation with fundamental frequency

First energy-loss experiments at Z6 using CVD-diamond detectors were carried out with a single-sided irradiation by the *nhelix* laser [FBG<sup>+</sup>10]. The newly developed detectors [Wam06] based on fourfold-segmented 8 mm×8 mm diamond samples, enabling more precise energy-loss measurements than with previously used multi-channel plates [RSS<sup>+</sup>00]. However, because of the

one-sided irradiation at fundamental laser wavelength of 1064 nm, the plasma parameters were not well reproducible and controlled. Due to the important spatial non-uniformities in the intensity distribution of the focus spot of the heating laser, the plasma was indeed generated in a non-homogeneous way and depending on the intensity distribution. Plasma transversal inhomogeneities in particular led to distorted measured energy-loss values in the first 10 ns of the interaction. Moreover, the plasma was only partially ionized because of the irradiation scheme. Hence, no reliable and systematic energy-loss measurements could be carried out for the whole interaction time span. A self-consistent theoretical description on the microscopic level combining a Monte-Carlo calculation of the charge-transfer processes and a modified version of the CasP code was developed and made it possible to reproduce the experimental results for times after 10 ns. For improved energy-loss measurements, a more systematic plasma creation with an enhanced homogeneity and with full ionization had to be obtained, therefore the setup had to be modified in several respects.

### Two-sided laser irradiation with frequency-doubled pulses

Subsequently, the laser-heating scheme was upgraded to a two-sided irradiation by using the PHELIX laser in addition of the *nhelix* laser, where both beams are in addition frequency-doubled. In this way, the obtained plasma is significantly more homogeneous, in spite of the still highly non-uniform intensity distribution in the laser focus-spot profiles. Though the two-sided irradiation contributed in this aspect, the decisive modification was the frequency doubling of the beams. Indeed, due to the fourfold higher critical density, not only is collisional absorption of the laser beams enhanced, but also and most importantly, radiative transport is strongly enhanced, as explained in 2.1.2. As radiative transport is a much quicker mechanism than thermal conduction, the plasma is then heated and homogenized more rapidly. In particular, full ionization of the plasma is reached at the end of the laser pulse irradiation. The non-uniformities coming from the laser-intensity distribution and their fluctuations from shot to shot are therefore smoothed out and the plasma evolution is more reproducible.

The modifications of the setup were theoretically backed up with the RALEF2D code, that predicted the optimum laser and target parameters to be used. A detailed discussion on this subject can be found in [TBF<sup>+</sup>13]. The resulting plasma was employed in [FBB<sup>+</sup>13] and this time, the theoretical description mentioned above made it possible to fully interpret the experimental measurements.

The created plasma thus matches the conditions that were stated in 3.1.2 for high-quality energy-loss measurements. The corresponding experimental setup is shown in Fig. 4.8. Its main features are now described as a quasi-identical setup is used for the present work.

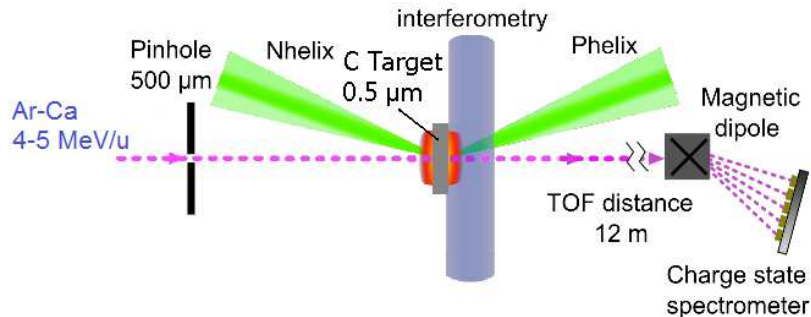


Figure 4.8: Experimental setup of [FBB<sup>+</sup>13]. A hot 200 eV homogeneous and fully ionized carbon plasma is generated by the two-sided irradiation of frequency-doubled laser beams (527 nm for PHELIX and 532 nm for *nhelix*). The projectiles are argon ions at an energy of 4-5 MeV/u, which are detected after a 12 m TOF-distance with a CVD-diamond spectrometer.

In [FBB<sup>+</sup>13], free-standing solid graphite foils with an areal density of  $100 \pm 10 \mu\text{g}/\text{cm}^2$  were heated to the plasma state. Their density of  $1.84 \text{ g}/\text{cm}^3$  corresponds to a thickness close to 500 nm. The target was irradiated from both sides and simultaneously by PHELIX and *nhelix* laser beams. Both beams were frequency-doubled, which resulted in a wavelength of 527 nm for PHELIX and 532 nm for *nhelix*. The PHELIX beam came from the  $10^\circ$  beamline, i.e from the opposite side to the ion beam with a  $9^\circ$  angle in relation to the ion axis. The *nhelix* beam came from the same side as the ion beam with a  $6^\circ$  angle to the ion axis in the horizontal plane. For both beams, an energy close to 30 J and a pulse length of 7 ns FWHM with rectangular shape were employed, resulting in an intensity on the target of  $5 \times 10^{11} \text{ W}/\text{cm}^2$ .

A very important requirement for the energy-loss measurements is the plasma transversal homogeneity in relation to the incoming ion beam, so that all beam ions interact at the same plasma parameters. Therefore, in order to avoid TOF-differences between the different ions of one bunch because of locally different plasma conditions, the laser-beam and ion-beam profiles are tailored in a way that guarantees the maximal possible plasma homogeneity transversally to the ion axis. For this purpose, first, the laser focus-spot profiles are spatially smoothed and set to 1 mm diameters on the target by using frequency-matched lenses and RPP as explained in 4.1.2. In this way, the laser beams feature large uniform top-hat focus profiles. As a result, the plasma features an essentially one-dimensional expansion along the ion axis at early times of the interaction. Its areal density thus stays constant for the first 7 ns after laser irradiation of the target (see also Fig. 4.13).

Second, the ion-beam diameter is cut down to  $500 \mu\text{m}$  through a circular pinhole located a few centimeters before the target foil. Around 30 % of the few thousand ions contained in a bunch are transmitted. In this way, the ion beam only interacts with the central part of the plasma, ensuring that each ion of the beam undergoes the same energy loss and thus the same TOF until it reaches the detector.

In other words, the plasma appears as one-dimensional to the incoming ion beam for a significant duration of the interaction, roughly in the first 10 ns.

The plasma density was experimentally determined with the help of the multi-frame interferometry diagnostic and enabled to validate the RALEF2D simulations predicting the plasma parameter values. The carbon plasma featured  $T_e \leq 200 \text{ eV}$  and  $n_e \leq 10^{21} \text{ cm}^{-3}$ .

In the experiment of [FBB<sup>+</sup>13], the used projectile ion was argon at an energy of 4 MeV/u, corresponding to a  $\frac{v_p}{v_{th}} \approx 4$ .

As this plasma constitutes a well-suited test bed for precise energy-loss investigations, a similar setup can now be employed in order to reach the parameter region of maximum stopping power in plasma. Therefore, keeping the same laser and target parameters, the characteristics of the projectile ions are modified to obtain  $\frac{v_p}{v_{th}} \approx 1$ . Following the discussion of section 3.1, a carbon ion beam at a mean projectile energy of 0.5 MeV/u is thus chosen to probe the plasma.

As explained in section 4.1.1, the minimum ion energy delivered by the UNILAC is 3.6 MeV/u. This is why the carbon beam has to be decelerated before interacting with the plasma. The deceleration process has important consequences on the beam properties, which requires substantial modifications of the previously described setup.

## 4.2 Setup for measurements at stopping maximum

The experimental setup that has been specifically developed for ion energy-loss measurements at  $\frac{v_p}{v_{th}} \approx 1$  is now presented.

In 4.2.1, the deceleration process of the ion beam and the corresponding target design are addressed. In particular, the straggling of the decelerated beam in energy and in angle is evaluated and its consequences on the setup are discussed. In 4.2.2, the development and the construction

of a new CVD-diamond detector system, motivated by the consequences of the beam straggling, are presented. In 4.2.3, the shielding system protecting the detector against electromagnetic radiation, which is a consequence of the small TOF distance of the new setup, is described. Finally, in 4.2.4, the whole experimental setup with the deceleration system, the detector system and the shielding system is summarized and the important experimental parameters are recapitulated.

### 4.2.1 Target design

The decelerating target is aimed at slowing the ion beam from an initial energy of 3.6 MeV/u down to an energy close to 0.5 MeV/u, before it interacts with the plasma target. Under "plasma target" is designated the 0.5  $\mu\text{m}$  thick carbon foil that is irradiated by the laser beams, in order to avoid confusion with the decelerating target. The decelerating target has to feature an adapted thickness and to be positioned properly in relation to the plasma target.

In a first part, the deceleration process and the resulting ion-beam properties are estimated by using simulations carried out with the TRIM and GEANT4 Monte-Carlo codes. Then in a second part, the positioning and the implementation of the decelerating target in the experimental setup are explained. As for the adjustment of the decelerating target during the experiments, this aspect is addressed in section 5.1 in next chapter.

### The deceleration process

For the dimensioning of the experimental setup, the TRIM code (TRansport of Ions in Matter), basing on the SRIM 2011 stopping database (Stopping and Range of Ions in Matter) [sri], as well as the GEANT4 code (GEometry ANd Tracking) [gea] have been employed.

- **TRIM**

To simulate the interaction of projectile ions in matter (solid or gas), TRIM carries out a Monte-Carlo calculation based on a binary-collision approximation (BCA) with a random selection of the impact parameter of the colliding ion. In the BCA frame, it is assumed that the projectile undergoes a sequence of independent binary collisions with the target atoms, and that it travels through a straight path between two collision events. Between two collisions, the projectile undergoes only an electronic stopping power, while the nuclear-recoil stopping power results from the collisions with ions.

As the electronic stopping power is an average fit to a large number of experiments, TRIM consists in a semi-empirical approach. An effective charge state is used on the basis of the Brandt-Kitagawa theory [BK82], as implemented in the Ziegler-Biersack-Littmark model (see section 2.2.1). In addition of considering only binary collisions and thus neglecting the influence of nearby atoms, TRIM also ignores the material structure as well as effects like recombination of atoms with vacancies in the material or the generation of delta electrons during the collision process. It can be used in a wide projectile-energy range from 10 eV to 2 GeV. For more details on the TRIM/SRIM code, the reader is referred to [ZBL85, ZZB10].

- **GEANT4**

While TRIM considers punctual individual projectile ions in a simple geometry, GEANT4 is able to simulate a full ion beam with its spatial and temporal characteristics, as well as complex target geometries. Compared with TRIM, a larger amount of physical processes is considered. The stopping-power model is based on the ICRU-73 stopping database [Sig05] for intermediate projectile energies between 0.025 and 10 MeV/u, which covers a large range of different projectiles and targets.

The ICRU-73 parametrization model is obtained from the PASS code developed by Peter Sigmund and relies on the binary-collision theory of ion stopping [SS02]. To describe the whole projectile-energy range, this model is completed with the Bethe-Bloch model



at high velocity (projectile energy  $> 10$  MeV/u) and with an electron-gas model at low velocity (energy  $< 0.025$  MeV/u). Details about the modeling of electronic stopping power in GEANT4 can be found in [LI08]. The parametrization model has been validated and an accuracy better than 1 % has e.g. been reached in the range of carbon ions in several materials [LIK10].

It has to be noted that the two codes determine the electronic stopping power quite differently: GEANT4 relies on theory, while TRIM is semi-empirical and is thus scaled with experimental data. A comparison of the electronic stopping power used in the two codes is shown in Fig. 4.9 for the case of carbon projectile ions interacting with a graphite target (density of  $1.84$  g/cm<sup>3</sup>). The agreement is very good if small differences mainly around the stopping maximum are disregarded. Comparisons with other programs, data tables and experimental data from the literature can be found in [PS03, Pau06] but may correspond to previous versions of the programs.

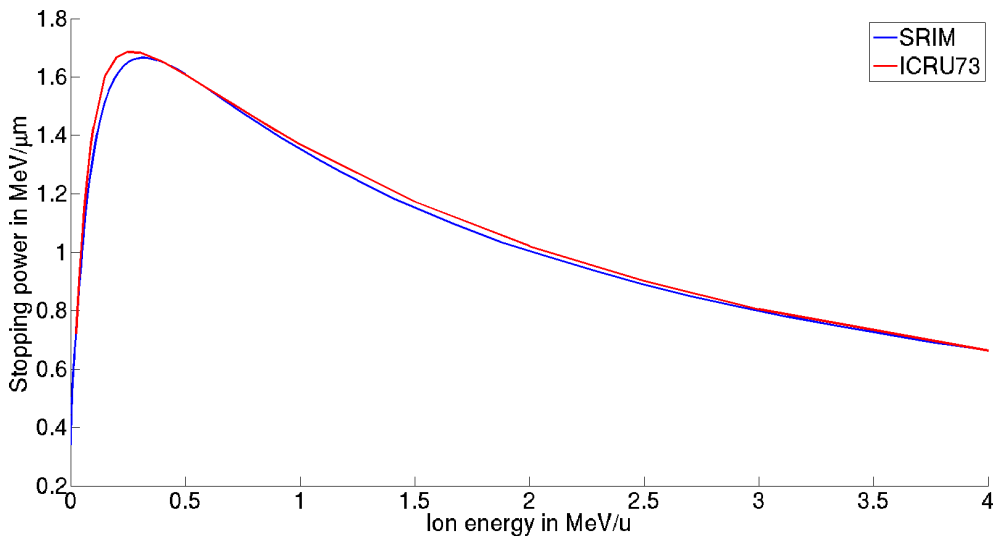


Figure 4.9: Comparison of the semi-empirical stopping power in the TRIM code and of the theoretical ICRU-73 stopping power obtained with the help of the binary-collision theory of P. Sigmund, for carbon projectile ions interacting with a carbon target at a graphite density of  $1.84$  g/cm<sup>3</sup>.

The TRIM and GEANT4 codes are used to evaluate the needed thickness of the decelerating target as well as the resulting energy and angular distributions of the ion beam. These distributions are used on the one hand to optimize the target setup (see next paragraph), and on the other hand for the design of the diamond detector, in the choice of the TOF distance and of the detector surface area (see section 4.2.2). The GEANT4 simulation results have been provided by Commissariat à l'Energie Atomique, Centre d'Etudes Scientifiques et Techniques d'Aquitaine (CEA-CESTA) [Pep].

The decelerating foil, as the plasma target, is made of graphite at a density of  $1.84$  g/cm<sup>3</sup>. In order to determine its required thickness, the interaction of a carbon ion beam at a  $3.6$  MeV/u energy with a graphite foil has been simulated, and the thickness of the foil has been varied in order to reach an ion energy of  $0.5$  MeV/u when exiting the foil. The results are presented in Fig. 4.10 according to TRIM, and show that the decelerating foil has to be about  $46$  μm thick in order for the ion beam to reach a mean output energy of  $0.5$  MeV/u. This is confirmed by the GEANT4 simulation results.

It has to be noted that the thickness of the decelerating foils cannot be characterized better than by 10 % with the usual thickness determination methods. Only an ion TOF measurement in the

experiment enables to access the precise value of the foil thickness. Numerous foil samples thus have to be produced in order to guarantee that the desired thickness is available.

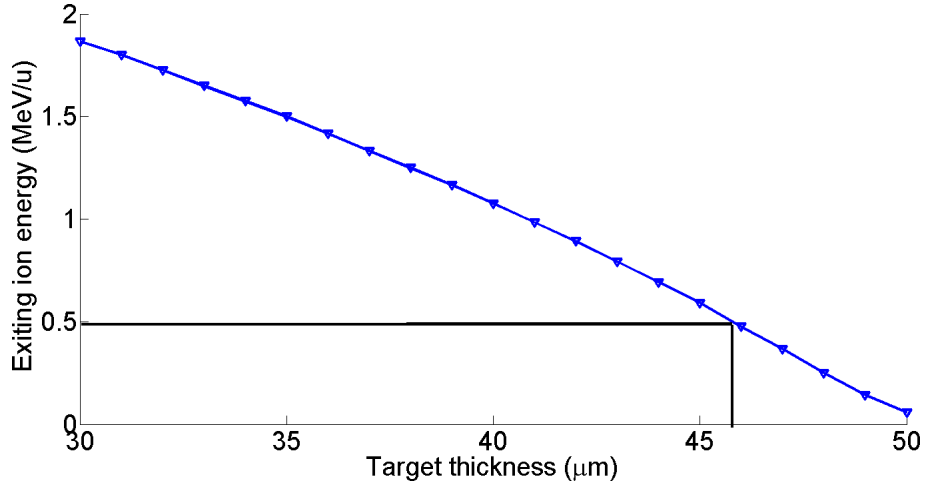


Figure 4.10: Mean energy of projectile ions exiting the graphite decelerating foil as a function of the foil thickness at a density of  $1.84 \text{ g/cm}^3$ . The energy intervals coming from the dispersion are not represented.

However, the beam interaction through the decelerating foil does not only lead to a slowing down of the ions. It also causes a significant longitudinal and transversal straggling of the beam, i.e both an energy dispersion and an angular dispersion. The knowledge of the corresponding distributions is crucial for the dimensioning of the target and the detector system.

A prerequisite for the experiment is the stability of the ion micro-bunch period through the straggling process. The incoming ion bunches in plasma indeed has to feature a very regular temporal pattern for enabling a reliable energy-loss determination. The micro-bunch period has therefore to remain unmodified by the deceleration process.

This was verified in a TRIM simulation of the deceleration of 100000 ions was carried out, representing 100 consecutive UNILAC micro-bunches containing 1000 ions each. The obtained standard deviation of the mean energies of the respective simulated bunches is approximately 11 keV. This corresponds to a 0.2 % fluctuation in the position of the bunch maxima for the total beam energy of 6000 keV. In comparison, the usual dispersion of the bunch maxima of the UNILAC beam is better than 0.1 %. The fluctuation of 11 keV remains small compared to the energy resolution of 100 keV required for the experiment, hence the decelerated bunches are still well-suited for reliable energy-loss measurements.

The energy resolution can however be deteriorated due to the distributions of energy and of angle resulting from the straggling process, as the latter influences the width and the amplitude of the measured ion signals significantly. This influence essentially depends on the TOF distance employed in the experiment. So by choosing a convenient TOF distance, the resolution is not affected by the straggling and depends only on the projectile energy, on the TOF distance and on the temporal resolution of the detector, according to equation 4.1.

The beam distributions have been estimated with the help of TRIM and GEANT4 for a  $46 \text{ μm}$  foil thickness and also for slightly different thicknesses. In this way, not only is the straggling estimated for the desired experimental conditions, but also the dynamics of the process with the output ion energy (i.e the foil thickness) is evaluated. For a  $46 \text{ μm}$  thick foil, corresponding to a  $0.5 \text{ MeV/u}$  output energy, the distributions of energy and angle after the decelerating target are shown in Fig. 4.11 and Fig. 4.12, as obtained from TRIM and GEANT4 calculations.

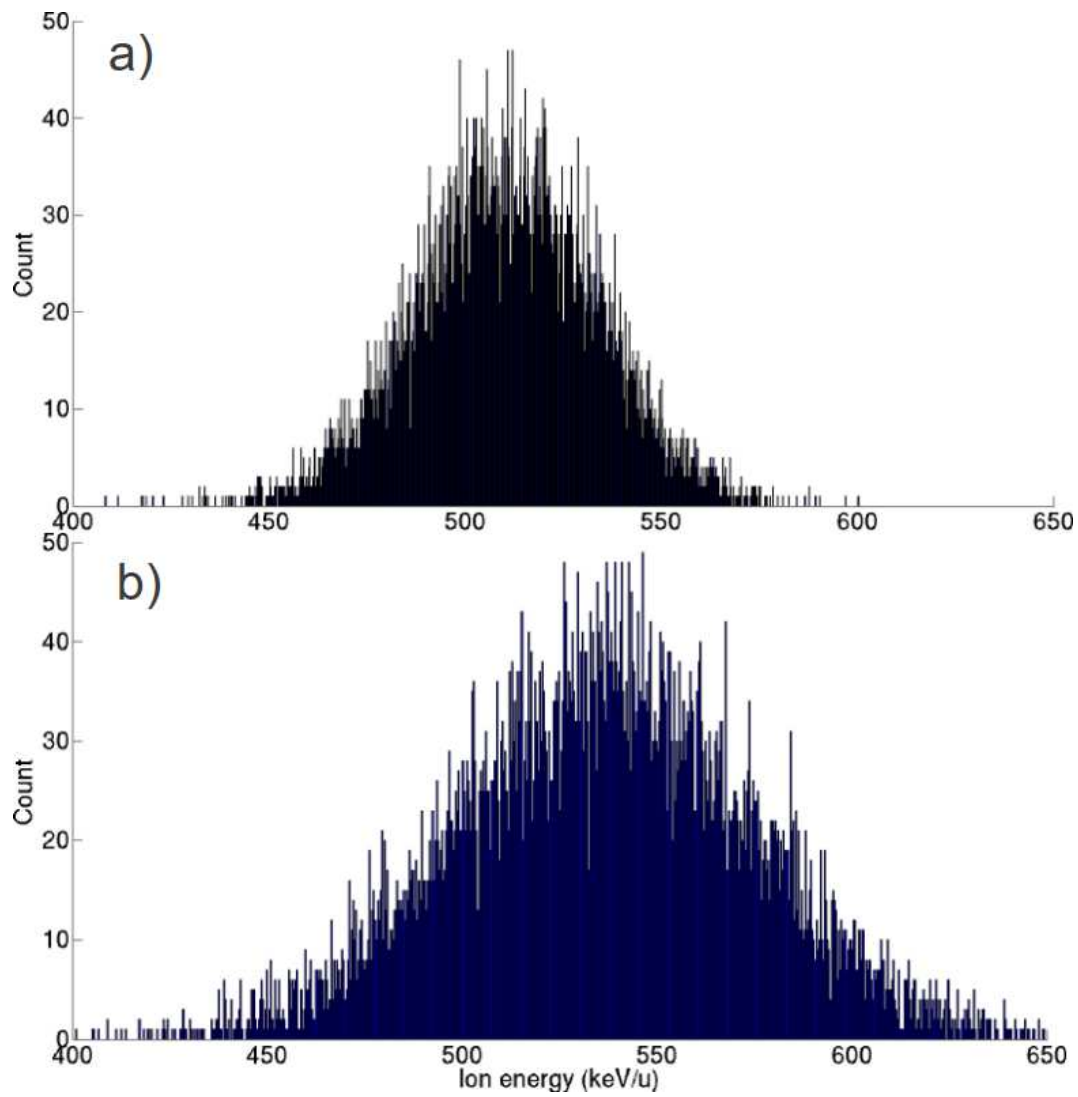


Figure 4.11: Energy distribution of the beam as estimated by TRIM (a)) and GEANT4 (b)), for 0.5 MeV/u energy ions exiting the decelerating foil.

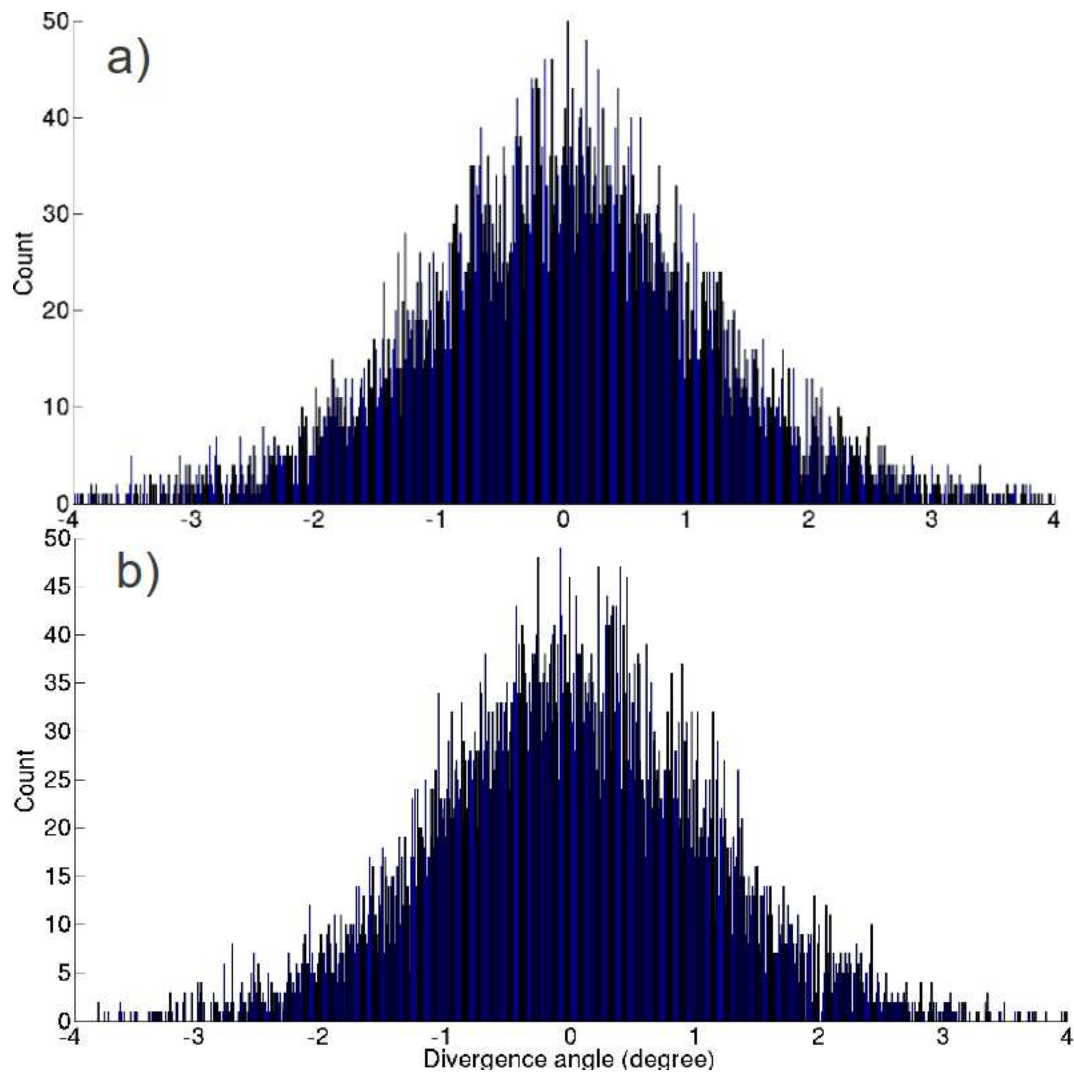


Figure 4.12: Angle distribution of the beam as estimated by TRIM (a)) and GEANT4 (b)), for 0.5 MeV/u ions exiting the decelerating foil.

Fig. 4.11.a) and Fig. 4.11.b) represent the energy distributions before entering the plasma target. As can clearly be recognized, a significant difference appears between the two distributions. The mean ion energy in the GEANT4 case is higher, reaching 0.54 MeV/u instead of 0.51 MeV/u in the TRIM case. Moreover, the distribution is broader according to GEANT4, with a relative width at FWHM of the Gaussian-like distribution reaching more than 17 %, against about 10 % for TRIM. In GEANT4, the beam is therefore slightly less decelerated, but more straggled in energy. This is probably due to the fact that a higher amount of processes are described in the GEANT4 physics package, while TRIM uses a simpler model and more approximations. Yet, the angular distributions (Fig. 4.12.a) and Fig. 4.12.b)) are very similar, featuring an angular width at FWHM of about  $3^\circ$ . Hence, as far as the angular distributions are concerned, the TRIM or the GEANT4 distributions can equivalently be used as they are very similar. However, the GEANT4 distribution of energy is employed if beam properties depending on the energy interval have to be evaluated.

Furthermore, as the ions interact with the plasma target at a relatively low projectile energy (0.5 MeV/u), the straggling through the plasma target is also important. It is evaluated by assuming the plasma target in its solid state throughout the interaction. The beam loses approximately 11 % of its energy in the solid plasma target. This causes an additional energy straggling of a few percent, which according to GEANT4 leads to a total energy interval of up to 26 % at FWHM. As for the angular distribution, it is increased to  $4^\circ$  at FWHM.

By using these simulated distributions for different TOF-distance values, the transverse bunch profile and width as well as its temporal width can be evaluated when entering the plasma target and when impinging on the detector.

The described angular and energy distributions have important consequences on the beam properties and thus on the whole experimental setup. The values of the distribution parameters as well as of the resulting beam characteristics are summarized in a recap table at the end of the chapter (4.2.4).

In the following section, the consequences of the angular distribution of the ion beam on the target setup itself are explained. Indeed, the significant transverse beam broadening along its propagation path sets an important constraint on the positioning of the decelerating foil.

### Design of the target system

An key problematic of the target design is the plasma homogeneity transversally to the ion axis, for which the angular divergence of the ion beam is a critical issue. The initial ion-beam diameter, before the decelerating foil, is  $500\text{ }\mu\text{m}$ , as obtained by a circular pinhole (see 4.1.4). After having been decelerated to 0.5 MeV/u energy through the  $46\text{ }\mu\text{m}$  thick foil, the beam quickly broadens while propagating, reaching a diameter that potentially over-crosses the borders of the homogeneous plasma region.

The RALEF2D code was used to estimate the transverse plasma homogeneity, as shown in Fig. 4.13. The areal-density profile of the plasma is represented in the plasma direction transversal to the ion-beam axis, only in the right half space for symmetry reasons, and for different times after the beginning of plasma creation. Starting from the cold-matter state before the laser irradiation at a value of  $100\text{ }\mu\text{g}/\text{cm}^2$ , the areal density is plotted at each nanosecond time step in a time span of 16 ns. It progressively decreases with the plasma expansion down to a final value of about  $40\text{ }\mu\text{g}/\text{cm}^2$ . For this case, the RALEF2D profiles were extracted from a simulation with a spatially homogeneous laser focus-spot profile. An inhomogeneous profile, though more realistic, indeed causes an additional oscillation of the areal density in the early times of the plasma evolution. The more simple homogeneous case is thus considered here, which does not modify the dynamics of the temporal areal- density evolution.

The curves show that the areal-density profile remains quite homogeneous over  $250\text{ }\mu\text{m}$ , with maximal discrepancies of 10-15 % arising between the ion axis (zero radius) and the plasma zone

at  $250\text{ }\mu\text{m}$  distance from the axis. Therefore, for an ion beam of  $500\text{ }\mu\text{m}$  diameter as in previous experiments, the ions experience maximal differences of 10-15 % in areal density. For larger distances from the ion axis, the areal density further decreases, and discrepancies of 25-30 % appear from a  $400\text{ }\mu\text{m}$  beam radius.

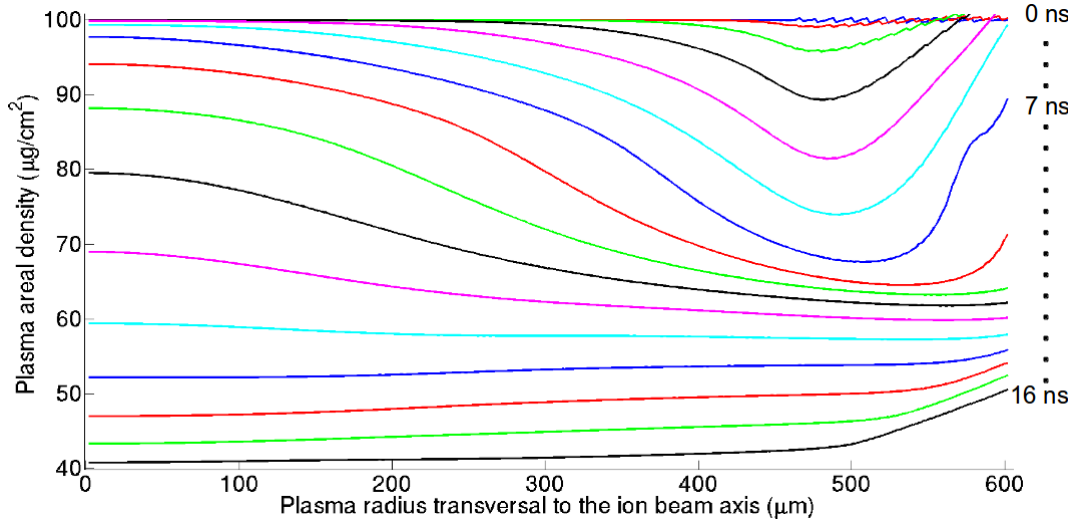


Figure 4.13: Transversal areal-density profile of the plasma in  $\mu\text{g}/\text{cm}^2$ , in one half space over a  $600\text{ }\mu\text{m}$  radius as a function of time, shown in 1 ns steps from 0 to 16 ns after the beginning of the laser irradiation of the target, as obtained from RALEF2D simulations. From an initial uniform value of  $100\text{ }\mu\text{g}/\text{cm}^2$  corresponding to an approximately  $500\text{ nm}$  target thickness, the areal density is progressively reduced due to the plasma expansion, and discrepancies of up to 30 % appear between the ion axis (on the left) and the external side (on the right). The increase in areal density at radius values between  $500$  and  $600\text{ }\mu\text{m}$  comes from the fact that this target part is not heated from the start by the  $1\text{ mm}$  diameter laser pulse.

The ion beam cannot be arbitrarily broad when penetrating the plasma in order to not undergo excessive TOF variations between the most outer ions of the beam and the ions on the axis. The width of the  $0.5\text{ MeV/u}$  carbon beam is calculated by using the angular distribution obtained with the TRIM or the GEANT4 code, assuming that the ion beam incident on the decelerating foil has a  $500\text{ }\mu\text{m}$  diameter. It turns out that even after a short propagation distance of a few millimeters, the ion beam becomes significantly broader and extends partly beyond the nearly transversally homogeneous plasma zone.

A solution could be to reduce the size of the pinhole aperture so that the ion beam has a reduced original diameter. But this option would reduce the number of transmitted ions, which can be critical to obtain exploitable ion signals in the experimental conditions, and the benefit in reduction of the ion beam diameter at plasma position would not be very significant.

This is why it was chosen to position the decelerating target as close as possible to the plasma target to limit the effects of the angular beam divergence. Yet the distance between the two targets cannot be arbitrarily small, as is now explained.

#### • The *nhelix*-beam issue

First, setting the decelerating foil very close to the plasma target is problematic because of the *nhelix* laser beam, which is incident on the plasma target from the same side as the ion beam. The *nhelix* beam is thus likely to heat the decelerating target to the plasma state and to destroy it even before heating the plasma target. Moreover, if a significant part of the laser-beam energy is employed in heating the decelerating foil, the symmetric irradiation of the plasma target by using the *nhelix* and PHELIX lasers simultaneously is not guaranteed anymore. Therefore, the decelerating target has to be positioned at a

sufficient distance from the plasma target, and furthermore its transversal size has to be sufficiently small in order to not lie in the path of the laser beam. A compromise had thus to be found between the ion-beam divergence issue and the laser-beam issue.

The transversal profile of the plasma areal density at  $t = 7$  ns after laser impact, where the inhomogeneities are strongest (see Fig. 4.13), as well as the transversal profile of a propagating ion bunch according to a TRIM simulation are represented in Fig. 4.15. The bunch, when exiting the decelerating foil (in magenta), has a width of  $250 \mu\text{m}$  at FWHM, corresponding to a  $500 \mu\text{m}$  diameter as obtained through the pinhole, and it has acquired an angular distribution that makes it expand rapidly in the transversal direction. Indeed, after a 5 mm propagation distance after the decelerating foil, the bunch has a width of  $390 \mu\text{m}$  (FWHM), and after 10 mm the width has grown to  $670 \mu\text{m}$  at FWHM.

A test experiment was conducted in which a carbon foil, standing for the decelerating target, was positioned at different distances from the plasma target on the ion axis. The *nhelix* laser was used to heat the plasma target in the conditions of the experiment, i.e. with a 532 nm laser beam obtained by frequency doubling, at an energy of 30 J and a pulse length of 7 ns at FWHM and with a 1 mm diameter focus-spot size on the plasma target. For relaxing the constraint of laser heating of the decelerating foil, the *nhelix* incident angle was increased from  $6^\circ$  to  $20^\circ$ . This small angle variation is not expected to lead to noticeable modifications of the plasma characteristics.

Distances of 5-10 mm were tested and it appeared that for a distance larger than 8-9 mm, the decelerating foil is not hit by the laser beam, as indicated by measurements using the multi-frame interferometry diagnostic aimed at monitoring the ablation of the foil surface. The setup as well as examples of interferometric measurements are shown in Fig.4.14 for a distance of 7 mm. A distance of 10 mm thus appears as a suited choice for the experiment.

The TRIM and GEANT4 code then predict an ion-beam spot size on the plasma target of  $670 \mu\text{m}$  at FWHM (see Fig. 4.15). The maximal discrepancy in areal density between the exterior plasma regions and the ion axis thus reaches approximately 30 %. Non-negligible TOF differences can therefore arise between the external part of the incident ion beam and the part on the axis, and this may lead to a poorer quality of the energy-loss measurements. This problem is further discussed in section 4.2.2 in relation to the detector design.

- **The plasma X-ray issue**

Second, the proximity of the decelerating foil to the hot radiating plasma implies its heating by the plasma X-rays, eventually destroying it. The important condition for the energy-loss measurements is the stability of the areal density of the decelerating target during a sufficient time after the laser irradiation of the plasma target of 10-20 ns, so that all ion bunches of interest interact with the plasma at the same initial mean projectile energy.

The influence of X-ray heating on the decelerating target was estimated as follows. In first approximation, the X-ray emission from the hot laser-driven plasma is the bremsstrahlung emission of the free plasma electrons, if plasma line emission is neglected (see 2.1.2). As the plasma parameters are known from the RALEF2D simulations over a 16 ns duration, the plasma thermal bremsstrahlung emissivity per volume unit ( $\text{erg}/\text{cm}^3/\text{s}$ ), integrated over all photon frequencies, can be evaluated over the 16 ns time span by using equation 4.4, as derived e.g in [Hug75]:

$$\frac{dW}{dt dV} = 1.4 \times 10^{-27} T_e^{\frac{1}{2}} Z^2 n_i n_e \bar{g} \quad (4.4)$$

where  $T_e$  is the plasma electron temperature in K,  $Z$  is the atomic number of the target,  $n_i$  and  $n_e$  are the densities of ions and free electrons respectively, and  $\bar{g}$  is the Gaunt factor

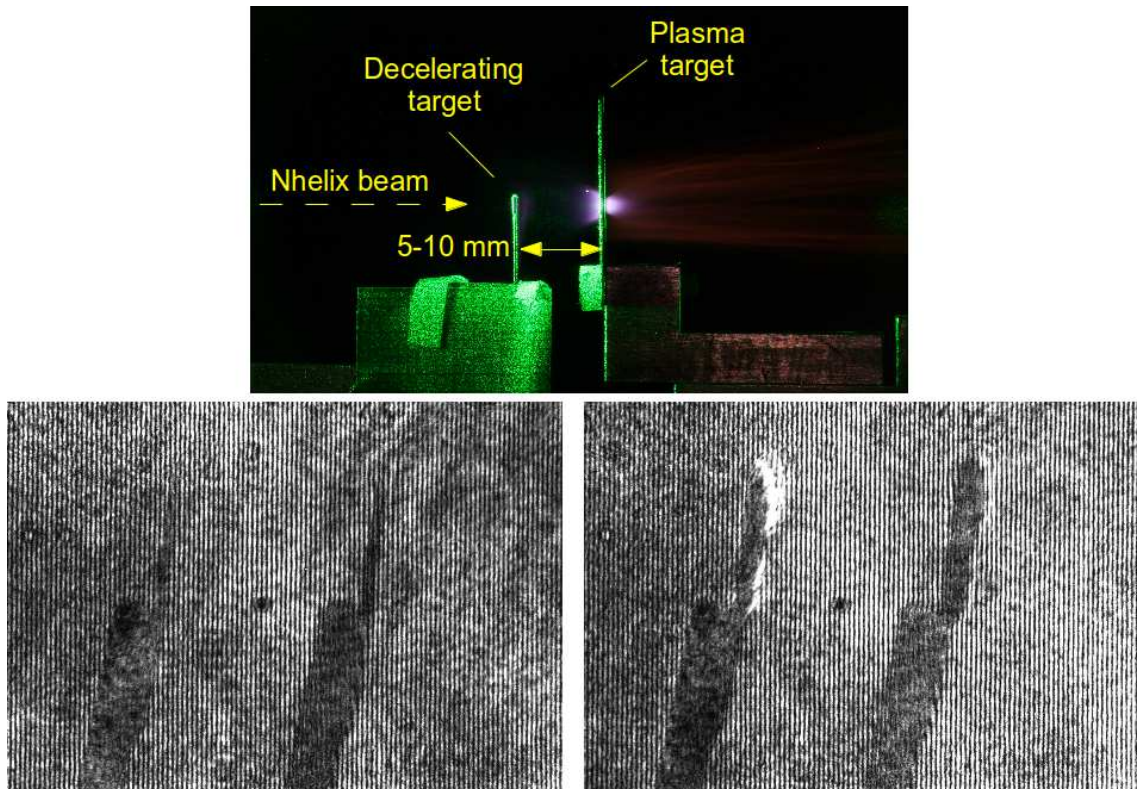


Figure 4.14: Top: Photograph taken with a digital camera showing the experimental setup. Bottom: interferometric measurements of the decelerating foil to monitor the plasma formation, for a distance of 7 mm from the plasma target. The picture on the left is a reference measurement before laser irradiation. The picture on the right, at  $t = 2$  ns after the laser irradiation of the plasma target, shows an ablation of the surface of the decelerating foil.



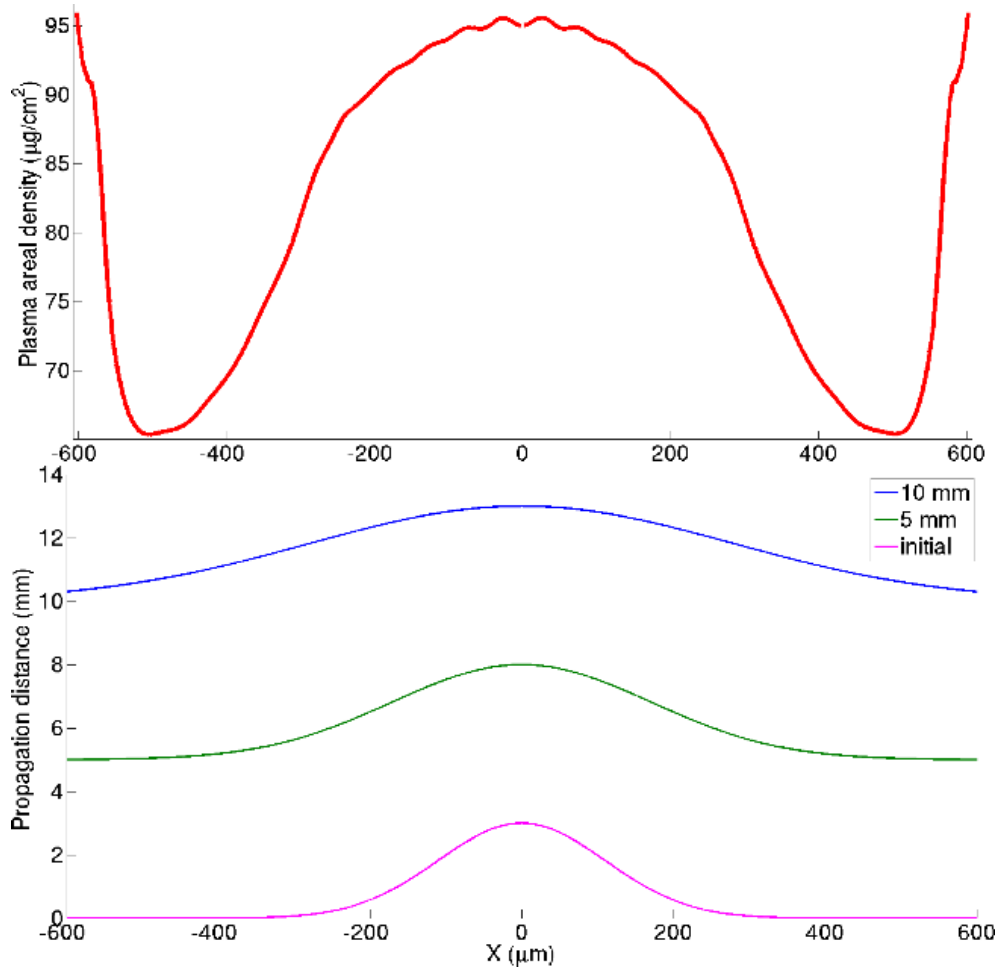


Figure 4.15: Top: transversal areal-density profile of the plasma at a time of 7 ns after the start of the laser irradiation of the target, in the spatial range of  $\pm 600$   $\mu\text{m}$  as simulated by the RALEF2D code. Bottom: transversal ion-beam profile at a distance of 0, 5 and 10 mm after the decelerating target respectively. For the chosen distance of 10 mm in the experiment, due to the beam width, important discrepancies of up to 30 % are thus expected between the areal-density values experienced by the beam ions.

that takes quantum effects into account and whose value is close to unity.

By using the plasma simulation profiles and assuming that the plasma is homogeneous over the laser focus-spot area of 1 mm diameter, the total X-ray energy radiated by the plasma in the form of thermal bremsstrahlung over a duration of 16 ns was estimated as  $2.7 \times 10^6$  erg. The corresponding X-ray flux incident on the decelerating target, located at 10 mm from the plasma target, is  $2.7 \times 10^6$  erg/cm<sup>2</sup>.

The plasma emission spectrum was simulated by the PrismSPECT program [pri]. It is a collisional-radiative code able to simulate spectral and ionization plasma properties for defined plasma conditions [MGW<sup>+</sup>04]. The spectrum is shown in Fig. 4.25a) in section 4.2.3. By using the described flux and spectrum, the heating of the decelerating target was simulated with the help of the one-dimensional ESTHER hydrodynamic code [CCB<sup>+</sup>05]. It turns out that the surface of the decelerating target is heated to at most a few eV. The expansion of the decelerating target is therefore slow and can be considered as one-dimensional for the first tens of nanoseconds after beginning of the laser heating of the plasma target. In comparison, according to the RALEF2D code, the plasma target, that is heated by the laser beams to a temperature of up to 200 eV, has a constant areal density, at least around the ion axis, for approximately 7 ns after beginning of laser irradiation as can be seen in Fig. 4.13. The areal density of the decelerating target can therefore be considered as constant for a time significantly longer than 10 ns. The analysis of the ion signals obtained in the experiment, as explained in section 5.2, confirms this assumption. As a conclusion, a 10 mm distance between the decelerating target and the plasma target is suited for the experiment and this configuration is chosen.

#### • Final design

The decelerating target is designed so that the ion beam penetrates the decelerating foil at a 1 mm distance from the laser-oriented edge. In this way, the risk of interaction of the *nhelix* beam with the foil is further reduced. At the same time, the foil has to uniformly slow down a 500  $\mu$ m diameter ion beam and it has to be mechanically stable.

The decelerating foils were produced at the Target Laboratory of GSI by the process of cold rolling and were characterized by using a chromatic sensor, or alternatively with a taster if the surface quality did not allow a measurement with the sensor [Tar]. The error on the measured thickness was as large as  $\pm 10\%$ . As appeared during the experimental campaign (see section 5.1), the various decelerating foils actually had very similar thicknesses and different foils could be employed while still decelerating the ions to almost the same energy close to 0.5 MeV/u. The foils were glued on a holder that was mounted, together with the plasma target, on an alignment stage, as was designed in collaboration with the Target Laboratory of TUD. A photograph of the alignment stage with both targets as implemented in the experiment is shown in Fig. 4.16. The setup enables, with a micrometric precision, to adjust each axis in translation and in rotation and thus to precisely position both foils in relation to each other, at a distance of 10 mm, parallel to each other and both centered on the ion-beam axis. It was particularly watched that the interferometric (Geola) laser beam, which is incident on the plasma target transversally to the ion axis with a 45° vertical angle, is not blocked by the setup elements.

The next section deals with the design and the construction of the detector that has been developed specifically for the experiment.

### 4.2.2 Detector design

Due to the outstanding properties of CVD diamond as a detector material for charged particles, as described in section 4.1.3, and the important know-how gathered in the field in the past years, particularly at GSI, a CVD-diamond detector was chosen for the ion TOF measurement in the

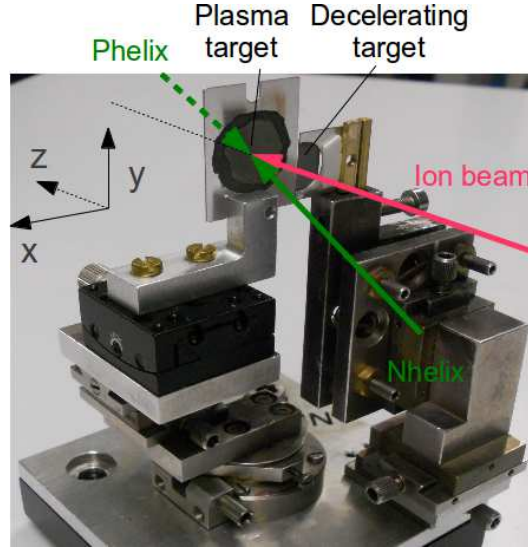


Figure 4.16: Alignment stage employed for the target setup. The decelerating target is on the right hand side, and the plasma target on the left hand side at a 10 mm distance. The ion beam is centered on the z-axis, the *nhelix* beam lies in the (x-z) plane with a  $20^\circ$  angle in relation to the z-axis, and the PHELIX beam comes on the (y-z) plane with a  $9^\circ$  angle in relation to the z-axis. As for the interferometric beam, it is incident on the plasma target in the y-z plane with a  $45^\circ$  angle in relation to the y-axis.

experiment. Because of the ion-beam properties resulting from the deceleration process, a new specific detector had to be conceived and constructed. The longitudinal beam straggling indeed sets a strong constraint on the TOF distance and thus on the resolution of the detector, while the transversal spreading of the beam imposes a sufficiently large detection area. Space-charge effects in diamond (polarization) also have to be considered due to the relatively low projectile energy, causing a non-homogeneous ionization density in the sample.

The work on the detector was carried out in collaboration with the author of [Kne13], where a detailed description of the detector development, construction and characterization can be found. This section is divided as follows. The first part deals with the definition of an optimal TOF distance for the experiment. Second, the polarization issue is discussed and the choice of the diamond thickness is justified. Third, the optimal detector dimensions are determined according to the angular spreading of the ion beam. Finally, the fourth part presents the complete design and the construction of the detector.

### Choice of the time-of-flight distance

The TOF distance has to be defined by considering the influence of the longitudinal straggling of the ion beam, and to a smaller extent, of the transversal beam straggling. The energy resolution, estimated by equation 4.2, has to be sufficiently low, of approximately 100 keV so that 10% discrepancies between the stopping theories can be differentiated in the experiment (see 3.2.4). This implies that the TOF distance has to be sufficiently large (0.3 m at least), yet it cannot be chosen arbitrarily large.

- **Angular spreading**

A first condition on the TOF distance is that no TOF differences arise due to the angular spreading of the beam. Ions traveling along the ion axis and ions featuring an angle of a few degrees in relation to the axis may indeed arrive at quite different times on the detector, if the TOF distance is sufficiently large. If  $\theta$  designates the half angle between the ion

axis and a projectile ion that has been scattered when exiting the decelerating foil and the plasma target (see Fig. 4.17), the TOF difference between the ion with angle  $\theta$  (2) and an ion traveling on the beam axis (1) is given by:

$$\Delta t = \frac{L}{v_p} \left( \frac{1}{\cos\theta} - 1 \right) \quad (4.5)$$

where  $L$  is the TOF distance and  $v_p$  is the projectile velocity. The angular distribution resulting from the interaction through *both* targets was calculated assuming that the plasma target is in its solid state.  $\theta$  was chosen as the corresponding maximum divergence angle, of about  $3^\circ$ , as close to 98 % of the beam ions are contained within  $\pm 3^\circ$ . The TOF difference  $\Delta t$  then reaches 140 ps after a TOF distance of only  $L = 1$  m. This is not negligible in comparison with the typical experimental temporal resolution of CVD-diamond detectors of 200-250 ps. Therefore, in this respect, the TOF distance has to be smaller than 1 meter. In reality, this constraint is relaxed by the fact that the detector does not register the entire ion beam (see also section 4.2.2).

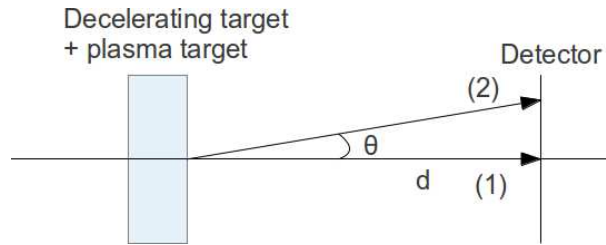


Figure 4.17: Scheme of the effect of the angular ion-beam divergence on the ion TOF: the ion (2) featuring an angle  $\theta = 3^\circ$  flies about 150 ps longer than the ion (1) over a 1 m TOF distance, which is of the same order of magnitude as the temporal resolution of the detector.

- **Energy spreading**

Furthermore, the energy spreading of the beam sets a strong constraint on the TOF distance. As explained in 4.2.1, the longitudinal straggling does influence the micro-bunch period only to a negligible extent.

Yet, another significant issue arises due to the energy interval. Indeed, due to the 26 % energy spread (FWHM) of the ion-beam distribution after passing through the decelerating target and the cold plasma target, the ion bunches become temporally increasingly broader as they propagate. As a consequence, if the propagation path is sufficiently long, two consecutive ion bunches may overlap, i.e the fastest ions of one bunch may overtake the slowest ions of the preceding bunch. As a result, it may become difficult to distinguish between two consecutive ion signals on the detector. Of course, this effect is more critical when the UNILAC ion beam is operated at a bunch frequency of 108 MHz instead of 36 MHz. To avoid this overlapping effect, the TOF distance has to remain sufficiently small. In order to estimate the importance of bunch overlapping as a function of the TOF distance, Monte-Carlo simulations were conducted on the basis of GEANT4 energy distributions obtained after both foils. The initial ion bunches were assumed to have a 3 ns temporal length at FWHM and their Gaussian temporal profiles were simulated by using a random-number generator, considering a realistic number of 1000 ions per bunch. TOF distributions of the ion bunches on the detector were deduced for three different TOF distances of 0.5, 1 and 1.5 m respectively. In this way, the temporal bunch profiles arriving on the detector were estimated. In order to simulate the resulting detector signals, the TOF distributions were convoluted with the detector-response function, which was itself randomly generated with a Monte-Carlo method from existing single-particle data (see [Cay09]). The used data

consisted of signals of single argon ions at 4 MeV/u energy with a 20.5  $\mu\text{m}$  thick diamond detector developed in [Wam06]. Even if this single-ion response is specific to the given projectile and to the time constant of the given detector, it can help to obtain an estimation of what can be expected for signals of carbon ions at 0.5 MeV/u.

$$M(x) = A \cdot \frac{1}{\sqrt{2\pi}} \cdot \exp\left(-\frac{1}{2}(x + \exp(-x))^2\right) \quad (4.6)$$

The single-ion response function can be approximated by a Moyal distribution function  $M$  (equ. 4.6), where  $A$  is a parameter that is randomly generated in the Monte-Carlo simulation. Each randomly generated ion TOF on the detector is thus convoluted with a randomly generated ion-detector response, and the sum of all the convolutions forms the total detector signal. This process was carried out both for a bunch frequency of 36 MHz and of 108 MHz. The results are shown in Fig. 4.18 for three consecutive ion micro-bunches.

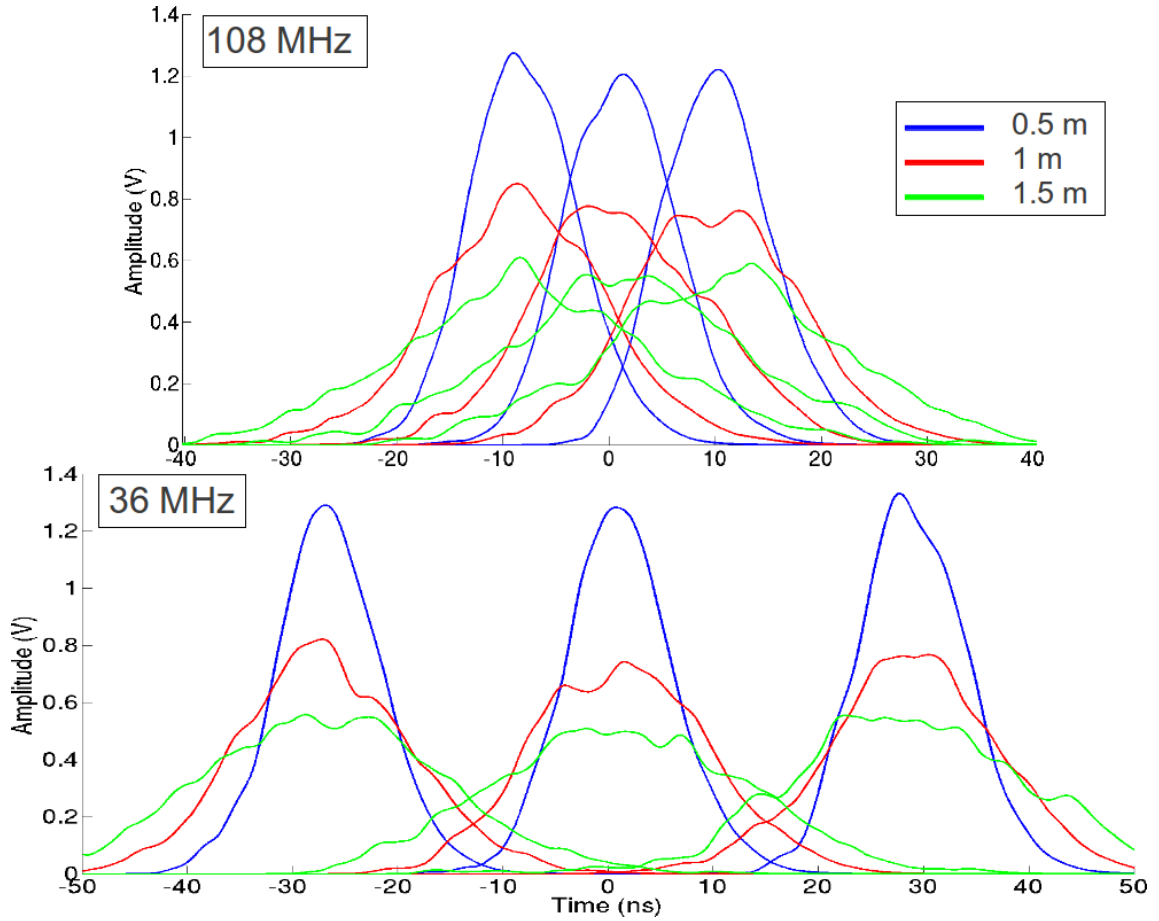


Figure 4.18: Simulation of ion signals on the detector, by using the GEANT4 energy distribution, as obtained by a Monte-Carlo method for TOF distances of 0.5, 1 and 1.5 m respectively, for a 108 MHz and a 36 MHz micro-bunch frequency.

From these simulations, it clearly appears that with an increasing TOF distance, the signals on the detector become significantly broader and of lower amplitude. For a 108 MHz ion-bunch frequency, the bunch signal overlapping happens quickly, being already quite important after a 0.5 m propagation distance. It has to be noted that the bunches themselves do not necessarily overlap during the propagation, but their signals on the detector do overlap, due to the additional convolution with the detector response function. At a 36

MHz frequency, the overlapping starts happening slowly from a 0.5-1 m TOF distance and reaches the half signal amplitude at 1.5 m. The consequence of an excessive overlapping would be an imprecision on the determination of the maxima of the bunches, lowering the resolution of the measurements. For a precise measurement at 36 MHz, a maximum TOF distance of 0.5 m has to be chosen. For a 108 MHz bunch frequency, the overlapping is so important that this case should be avoided.

A test beam time with carbon ions at a 108 MHz frequency, a 0.5 MeV/u energy and a 0.5 m TOF distance was carried out with a 13  $\mu\text{m}$  thick diamond detector. The bunch overlapping was not critical and the signals were mostly exploitable. The smaller detector thickness of 13  $\mu\text{m}$  compared to the simulations (based on single-ion signals registered on a 20.5  $\mu\text{m}$  thick diamond) can explain this. The resulting detector time constant was indeed smaller, accounting for shorter signals and thus relaxing the overlapping issue. As a conclusion, the overlapping may be not critical if the detector thickness is chosen sufficiently small.

In conclusion, a TOF distance of 0.5 m is chosen for the measurements. This value is larger than the minimum 0.3 m distance needed to obtain a 100 keV energy resolution, and remains sufficiently small to avoid a signal deterioration due to both angular and energy straggling. Consequently, an energy resolution around 60 keV is expected, that is better than the required 100 keV.

But a 0.5 m TOF distance also implies that the detector is positioned inside the target chamber. It is therefore particularly exposed to radiation emission resulting from the laser-plasma interaction, which is the topic of section 4.2.3.

It can also be noted that the TOF distance of 0.5 m makes measurements of the charge-state distribution of the projectile ion beam impossible. In the past, such measurements were conducted with the help of a charge-state spectrometer in conjunction with a magnetic dipole, which is compatible exclusively with a 12 m TOF distance as employed in previous experiments in [FBB<sup>+</sup>13] as shown in Fig. 4.8. This is why the charge-state distribution of the ion beam in the experiment is known only from the theoretical calculations of section 3.1.3.

### Choice of the diamond thickness

Another potential problem in the setup is the risk of polarization in the diamond detector. Indeed, in previous experiments the energy of the ion beam was higher than 3.6 MeV/u and the employed diamond detectors had sample thicknesses between 13 and 20  $\mu\text{m}$ . In these conditions, the projectile ions were not stopped inside the sample and created a nearly homogeneous ionization density along their propagation path in the diamond.

However, if for similar diamond thicknesses the projectile energy is reduced down to 0.5 MeV/u, not only are all ions stopped inside the sample, but they also have a short penetration range in diamond. This is illustrated in Fig. 4.19, where the SRIM stopping ranges of 3.6 MeV/u and 0.5 MeV/u carbon ions are represented and compared, assuming a diamond density value of 3.52 g/cm<sup>3</sup>. For a projectile energy of 0.5 MeV/u, the expected range in the diamond is thus only of 1.6  $\mu\text{m}$ . This includes the fact that in the experiment, a 0.5 MeV/u projectile ion incident on the plasma loses an important part of its energy in the plasma, and then again through the filter foil and finally through the metalization layer of the diamond (see below and 4.2.3). The ion energy when impinging on the detector is thus by a factor 2 lower than their energy when entering the plasma (see 4.2.4).

The consequence of this very short range is an inhomogeneous ionization in the diamond, which causes a significant space charge, i.e an internal electric field. This polarization field, oriented in the opposite direction to the external applied bias field, can delay or even prevent the motion of charge carriers in diamond, potentially leading to weak signals with a small amplitude, which might not be exploitable. Preventing polarization would require a very thin diamond sample of

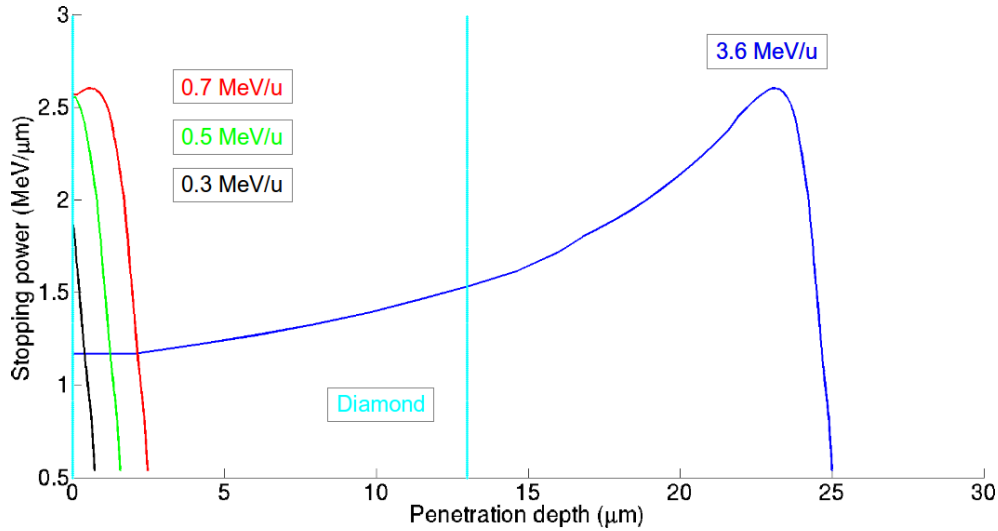


Figure 4.19: Penetration range of projectile ions in diamond for different ion energies, whose values here are those when entering the plasma. The shown penetration range takes the additional energy loss in the plasma target, in the filter foil and in the metalization layer of the diamond into account (see 4.2.4). While the Bragg peak of a 3.6 MeV/u projectile ion lies well outside of the diamond, ions interacting with the plasma at an energy of 0.5 MeV/u have a range of only a few micrometers in the detector.

a few micrometers, which is technically difficult to produce, in particular for a detector surface area of several  $\text{cm}^2$ .

An experimental campaign was conducted in order to test the existing 13  $\mu\text{m}$  thick diamond detector developed in [Wam06], in the new case of a decelerated carbon beam at ion energies around 0.5 MeV/u. No plasma target was used as the focus was directed on the properties of the decelerated beam. The detector, having a surface area of  $8 \times 8 \text{ mm}^2$ , was positioned first at a 0.25 m and then at a 0.5 m distance from the decelerating foil. It could be observed, in this campaign, that in spite of the ion range of a few  $\mu\text{m}$  in diamond, the signals were mostly well-defined and exploitable. The polarization effect thus appeared not to be unacceptable. However, while the signal amplitude was always sufficient when the detector was placed at a 0.25 m distance from the foil, it tended to be significantly weaker and more fluctuating when located 0.5 m away from the foil. This is due to the fact that, because of the angular dispersion, less ions can reach the detector when it is positioned at a larger distance from the decelerating foil.

In conclusion, while the polarization effect appears to remain acceptable for a 13  $\mu\text{m}$  diamond thickness, the number of incident ions and thus the resulting signal amplitude turns out to be more critical due to the angular straggling. As the existing detector proved to register exploitable signals in the test campaign, it was decided to construct a new CVD-diamond detector with the same thickness of 13  $\mu\text{m}$  and the same time constant of 3 ns. As mentioned before, these detector characteristics also preserve the signals from overlapping effects. However, in order to collect a sufficient number of ions for the signal analysis, the surface area of the detector was substantially increased.

### Dimensioning and construction of the detector

The value of the surface area of the detector results from a compromise between the proportion of the detected ions on the one hand and the technical feasibility as well as the price on the other hand. The beam dimensions on the detector were estimated with the help of the angular distributions obtained with TRIM and GEANT4 simulations. In these simulations, the decelerating foil and the solid plasma target were positioned at a distance of 10 mm from each other,

and the beam distributions leaving the plasma target were employed to determine the beam dimensions at a 0.5 m distance away from the plasma target, assuming a  $500\text{ }\mu\text{m}$  broad beam prior to the decelerating target. In Fig. 4.20, the beam focus spot is shown for a bunch of 10000 ions, as obtained with TRIM. Depending on the fact whether the TRIM or the GEANT4 angular distribution is considered, a focus spot width of 35 mm or 30 mm at FWHM is calculated at the detector plane, after a 0.5 m TOF distance.

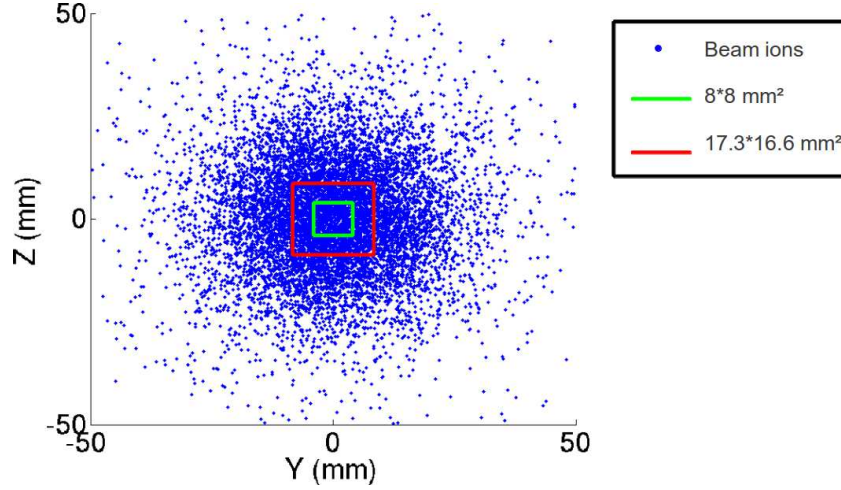


Figure 4.20: Ion bunch at detector position, at a 0.5 m distance after the plasma target, as simulated by using the TRIM angular distribution. The green square represents the limits of the old diamond detector, while the red one stands for the detector developed in the frame of this work. Even if the proportion of the beam focus spot area that is covered by the detector has been increased by a factor 4, the effective detection area has been improved by a factor slightly superior to 2, because of a higher proportion of spacings between the juxtaposed samples composing the new detector.

#### • Optimal detector layout

The larger the detector area, the larger the number of ions that can be detected on the one hand. But on the other hand, the larger the number of detected ions that potentially interacted with plasma conditions different from the ones at the ion axis. And similarly, also the larger the TOF differences between various ions of the beam due to the angular spreading. An excessively large surface area might therefore not be optimal for the energy resolution of the detector, while a too small surface area like the  $8\times 8\text{ mm}^2$  one does not guarantee a sufficient signal amplitude for the subsequent energy-loss analysis. A very large area is also technically more difficult to achieve and is problematic because the large and yet  $13\text{ }\mu\text{m}$  thick diamond sample(s) may not be mechanically stable. A compromise area value of  $287\text{ mm}^2$  was chosen, corresponding to detector dimensions of  $16.6\times 17.3\text{ mm}^2$ . It enables to detect almost 20 % of the beam ions.

A choice had also to be made between using one single large diamond sample and several smaller ones. In order to ensure a metalization of a diamond sample that is free of defects, the metalized part of each sample has to be surrounded by an at least 0.5 mm broad non-metalized border. If two diamond samples are juxtaposed, there is therefore an at least 1 mm broad space between them that cannot be used for ion detection. The more different samples are used and juxtaposed, the larger proportion of effective detection area is thus lost. A single diamond sample enables to avoid this loss of detection area due to spaces between the metalization zones, and is quicker to produce and to metalize than a large amount of them. However, it is quite expensive, mechanically more fragile and the risk of breaking it during the metalization or the subsequent bonding and gluing process



is quite important. Such a risk is not acceptable for the success of the experiment, and consequently it was decided to use several separate smaller diamond samples.

Here again, the possibilities are limited due to the condition on the detector time constant, which has to reach approximately 3 ns. This constrains the area of each sample, and moreover a sample cannot be arbitrarily long due to the mechanical-stability condition. Furthermore, each metalized sample has to be bonded on a surrounding circuit board, and the bonding wires have to be shorter than 5 mm for stability reasons. Finally, too many samples have to be avoided due to their cost, not to mention the resulting loss in detection area. Consequently, as a compromise for all these constraints, 10 samples of  $8.2 \text{ mm} \times 3.3 \text{ mm}$ , corresponding to a  $27.06 \text{ mm}^2$  area each, were employed. The final diamond layout is shown in Fig. 4.21. There, the golden zones represent the metalized diamond areas, each one being  $7.2 \text{ mm} \times 2.3 \text{ mm} = 16.56 \text{ mm}^2$  large. They are all surrounded by a non-metalized border area (in blue). The brown lines, 0.2 mm broad, are the spaces between the different samples. By using this configuration, a detector time constant of 3.21 ns is expected.

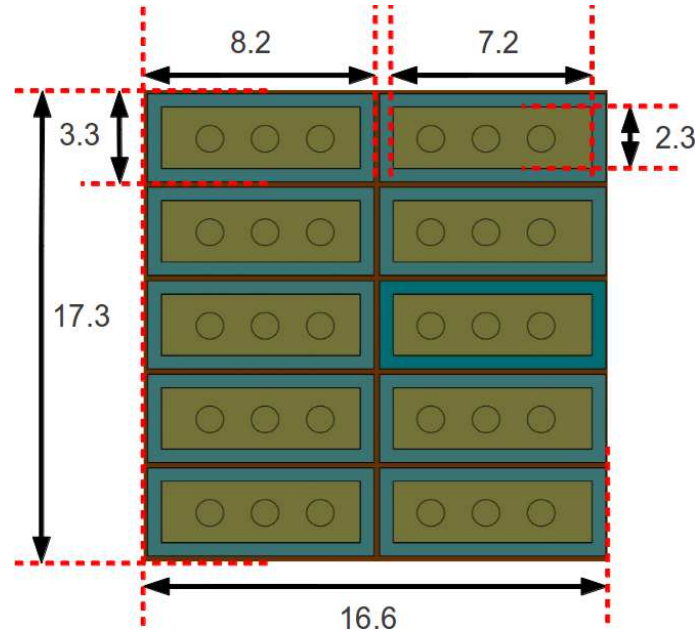


Figure 4.21: Layout of the metalized detector, made of 10 separate high-quality polycrystalline CVD-diamond samples. All dimensions are given in mm and the total detection area is  $166 \text{ mm}^2$ .

It was estimated, by using the ion-beam focus resulting from the TRIM angular distributions, that this detector layout enables to detect close to 17 % of the ions of the decelerated beam at 0.5 MeV/u energy when positioned 0.5 m away from the plasma target. A design using a single diamond sample would result in a 19 % detection capability, thus barely higher than with 10 samples. As the previous  $8 \times 8 \text{ mm}^2$  detector is able to collect only 8 % of the ions, the newly developed detector makes it possible to double the detected ion number and thus to guarantee a sufficiently high ion-signal amplitude.

The detector surface area of  $16.6 \times 17.3 \text{ mm}^2$  being now defined, the issues of ion TOF differences due to angular beam straggling and of ion TOF dispersion due to the transversal areal-density profile of the plasma are now re-examined.

Concerning the first issue, it can be estimated that the ions that reach the detector are those included within a  $\pm 1^\circ$  divergence angle after the plasma. With the TOF distance of 0.5 m, this corresponds, according to formula 4.5, to maximum ion TOF differences of 8 ps. This effect is therefore very small and it can be neglected in the following.

For the second issue, as the detected ions feature a maximum divergence angle of  $1^\circ$  af-

ter the plasma, then assuming a straight propagation in plasma, it can be estimated that these ions are contained within a transversal radius of  $400 \mu\text{m}$  when entering the plasma. Using the areal-density profile of the plasma (Fig. 4.15), a distribution of TOF differences over the  $0.5 \text{ m}$  distance is obtained by assuming that the energy deposited in plasma is proportional to the areal density. According to TRIM, an ion on the axis loses 11 % of its energy. From the areal-density profile at  $t = 7 \text{ ns}$ , where the discrepancies are maximal, the transversal beam profiles of energy and of velocity differences in relation to the ion axis are estimated. Hence, the distribution of TOF differences of the ions leaving plasma is determined, as shown in Fig. 4.22. By averaging this distribution with the Gaussian transversal ion-beam profile at plasma position, the mean TOF variation of the ions because of the plasma transversal areal-density profile is obtained. Its value is approximately  $150 \text{ ps}$  and it contributes to the systematic experimental errors (see 5.2).

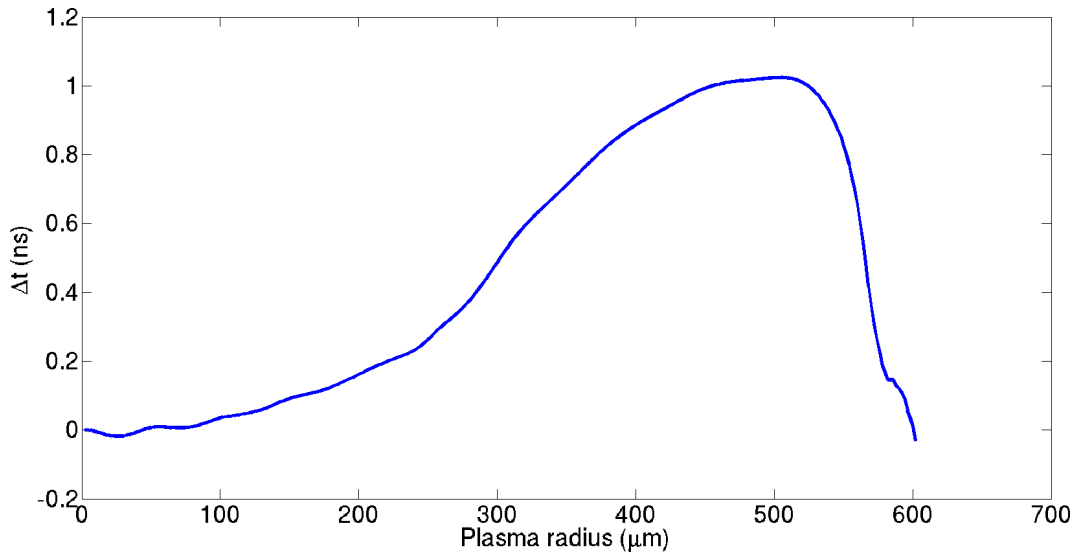


Figure 4.22: Transversal profile of TOF differences of the projectile ions in plasma due to the plasma areal-density profile, in relation to the TOF on the ion axis. Ions at a radius of  $400 \mu\text{m}$  experience a TOF shorter by  $0.9 \text{ ns}$  than ions on the axis. When averaging this distribution with the ion-beam profile of Fig. 4.15 at a  $10 \text{ mm}$  distance after the decelerating target, a mean TOF reduction of  $0.15 \text{ ns}$  is obtained for the ion beam because of the areal-density profile.

In the following paragraph, the construction of the detector is presented.

#### • Detector construction

10 highly-pure polycrystalline CVD-diamond samples were ordered [Dia], and were chemically treated and metalized at GSI with the help of a magnetron-sputtering device [Tar]. The metalization layers are, from inwards to outwards,  $100 \text{ nm}$  Ti,  $30 \text{ nm}$  Pt and  $20 \text{ nm}$  Au. The diamonds were fixed on a circuit board with the help of silver conductive film. Each diamond sample is provided with its own circuit path on the board. The presence of the outer gold metalization layer enabled to apply bonding wires that transmit the signal current from the metalized diamond areas to their corresponding circuit paths.

For the design of the circuit board as well as of the surrounding detector housing, another experimental constraint had to be taken into account. The whole detector system had indeed not to block the PHELIX beam incident on the plasma target with a  $9^\circ$  angle. Therefore the detector design, from the circuit board to the housing, was made as compact as was possible. In the final design, the upper edge of the detector system was estimated to lie  $2 \text{ cm}$  below the lower edge of the PHELIX beam.

The resulting circuit board as well as the aluminum detector housing protecting the board are shown in Fig. 4.23. The signal transmission from the circuit board is operated by SMA connectors and cables, which are located behind the board and not on its sides for compactness reasons. Outside of the target chamber, the signals from the 10 diamonds are individually amplified by means of DBA broadband amplifiers [MBB<sup>+</sup>01] and subsequently added with summers, before being transported up to digital oscilloscopes via coaxial BNC cables.

The detector was tested by means of a radioactive alpha source of  $^{241}\text{Am}$  emitting 115000 Bq at the Target Laboratory of TUD. In this way, single-ion signals were registered. By fitting a simple exponentially decaying function to the falling edges of the measured signals, the time constant of each diamond sample was determined. A mean time constant of 2.84 ns was found by averaging over the ten samples composing the detector, which is in agreement with the expected value of 3.21 ns within a 10 % error interval. This result confirms the high-frequency measurement capability of the detector and validates the predictions.

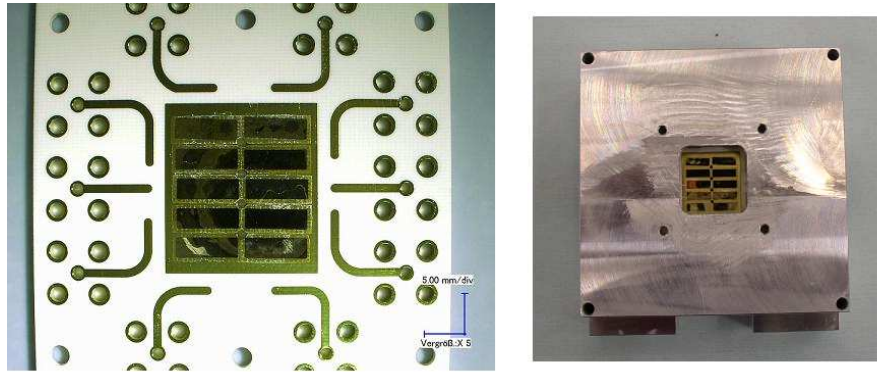


Figure 4.23: Left: metalized detector surface, positioned on the electronic board with the ten circuit paths corresponding to the ten diamond samples. Right: detector in its aluminum housing. This housing is then enclosed in a second housing to ensure a Faraday-cage effect aimed at protecting the detector from electromagnetic pulses (see 4.2.3).

### 4.2.3 Detector screening

Due to the fact that the detector is positioned only 50 cm away from the plasma target, it is likely to undergo strong electromagnetic perturbations because of the plasma generation and of the subsequent emission of radiation in the target chamber. As diamond features a band-gap value of 5.45 eV, any radiation with a wavelength  $\lambda < 235$  nm is able to generate charge carriers and thus to produce parasitic electromagnetic signals that may be superimposed on the ion signals and perturb or prevent the energy-loss analysis. Actually, two distinct kinds of electromagnetic radiation can impinge on the detector.

#### Electromagnetic radiation

- **Plasma X-ray emission**

On the one hand, X-ray radiation is generated from atomic transitions in the hot plasma as well as, chiefly, from the bremsstrahlung-emission process of plasma electrons reach the detector. The resulting X-ray pulse has a relatively short duration of at most 100-150 ns due to the short plasma lifetime. It directly impinges on the detector, traveling straight from the plasma in about 1 ns. The pulse is most intense in the first nanoseconds of the plasma generation, i.e during the laser irradiation time, where most hard X-rays are

produced. It features a pronounced peak after 7 ns, when the plasma becomes fully ionized and reaches its maximum temperature. Afterwards, the pulse amplitude decreases in an exponential way over roughly 100 ns, depending on the experimental parameters.

- **Electromagnetic pulse**

On the other hand, while the *X-ray pulse* starts weakening, an additional phenomenon appears, that is less intense but has a significantly longer duration. Indeed, all conductive elements inside the target chamber, including the target chamber itself, that have been irradiated by the X-rays, radiate in turn. As their atoms have been excited, they de-excite, further emitting X-rays. This is the so-called *electromagnetic pulse* (EMP) that starts being generated shortly after the beginning of the X-ray pulse. The EMP radiation can reach the detector either by directly propagating from the conductive elements onto the diamond, or indirectly, by coupling in any conductive element of the target chamber whose electric ground is connected to the one of the detector.

### Necessity of screening

Both phenomena, the X-ray pulse and the EMP pulse, are likely to cause a saturation of the detector. In Fig. 4.24, examples of signals recorded on a CVD-diamond detector located 50 cm away from a laser-generated plasma are shown in the case of an irradiation of the plasma target with the *nhelix* laser, as carried out in a test experiment. The ion bunches had a frequency of 108 MHz and the laser irradiation occurred at the zero time. Before the time of plasma generation, the ion bunch structure can be recognized. Though shortly after  $t = 0$  ns, due to the laser-plasma interaction, an intense X-ray burst can be seen, that saturates the detector for at least several tens of nanoseconds. If no shielding is applied to the detector, the initial X-ray burst is very intense and is then followed by multiple electromagnetic pulses that extend over several microseconds (not represented here). The signal analysis shows that the ion bunches cannot actually be detected for a time of 10  $\mu$ s. When instead a thin gold foil (450 nm in that case) is mounted as an X-ray filter in front of the detector, the saturation time becomes significantly shorter, of only 80 ns.

For the success of the experiment, it is essential that the detector is not saturated anymore when the first ion bunch that interacted with the plasma reaches it. Indeed, as the plasma dynamics is quick (tens of ns) and the bunch period can be as large as 27.6 ns, for each laser shot there is actually *one* ion bunch interacting with the hot and dense plasma whose conditions are known from the RALEF2D simulations. For a given measurement, it is thus crucial that *the* bunch that interacted with the (dense) plasma is exploitable in spite of the emission of electromagnetic radiation. The TOF of the ions being approximately 50 ns in the experimental conditions, the X-ray pulse has therefore to be shorter than 50 ns so that an analysis of the ion energy loss in plasma is possible. This is why an efficient detector shielding is necessary, basing on the case shown in Fig. 4.24 and further optimized.

It has to be noted that the precise mechanisms of these electromagnetic signals as well as their respective contributions to the saturation of the detector are not well understood, and known only from empirical considerations. The critical phenomenon causing the saturation of the detector is the initial X-ray peak. Even if this peak is expected to result chiefly from the radiative plasma emission, the EMP can also represent a contribution. Therefore, while the blocking of the direct plasma radiation constitutes the most important screening issue, the influence of the subsequent EMP also has to be mitigated in order to minimize the parasitic electromagnetic signals. The shielding of the detector was thus developed in two respects.

### Screening system

- **Shielding against plasma X-ray emission**

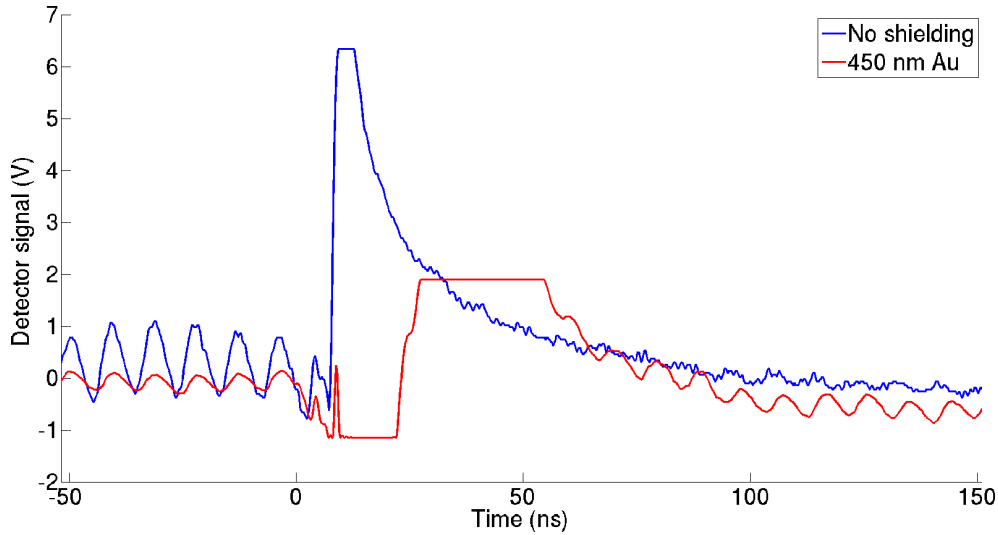


Figure 4.24: 200 ns sequence of detector signals as registered in a test experiment involving a C ion beam at a 108 MHz bunch frequency and the *nhelix* laser. The blue curve represents the signal when no protective shielding is applied, showing a saturation of the detector by the X-ray pulse which prevents the detection of the ion pulses over more than 150 ns. The red curve is the detector signal in the same experimental conditions when an additional 450 nm thick gold foil is positioned in front of the detector aperture, absorbing a part of the plasma radiation. In the latter case, the saturation appears to be significantly shorter and the ion bunches can be detected again after about 70-80 ns after the laser irradiation of the target. The cuts of the upper edges of the X-ray pulses are artefacts due to oscilloscope settings.

On the one hand, as the most important protection, the initial X-ray pulse that is directly incident on the detector has to be mitigated. The spectrum of the X-rays generated from the plasma was estimated with the help of the program PrismSPECT [pri], and is presented in Fig. 4.25.a. It shows that X-ray energies of up to 1 keV are expected, with an important peak between 300 and 400 eV. In order to stop most of the X-rays while still allowing the relatively slow ions to reach the detector, a thin gold foil was mounted in front of the detector aperture, on the ion axis. For a given foil thickness, the X-ray transmission of the foil was estimated with the help of the program *Filter Transmission* [fil], while the resulting ion output energy was determined with TRIM. A 650 nm foil thickness, corresponding to a  $1.3 \text{ mg/cm}^2$  areal density, appeared as a good compromise (see Fig. 4.25.b). Gold foils with a 650 nm thickness and a 30 mm diameter, in order to cover the whole detector aperture, were thus employed. It has to be noted that even if the gold foil induces a substantial additional energy loss of the projectile ions, this does not have any consequence on the energy-loss measurement. Indeed, the gold foil is positioned only a few millimeters before the detector surface, so that the propagation distance between the foil and the detector is not sufficient to induce any perceptible TOF modification.

A proof-of-principle of the shielding system, with the filter foil and the electric isolation, was obtained in an experimental campaign using the PHELIIX laser and the older detector with a smaller gold foil, at a laser intensity higher than the one of the experiment of this work.

Yet, the system calibration during the first experimental (see 5.1) campaign showed that an areal density of  $2.1 \text{ mg/cm}^2$  is more appropriate for the real experimental conditions of this work.

- **Shielding against EMP emission**

On the other hand, all the elements of the detector and of the signal transmission line

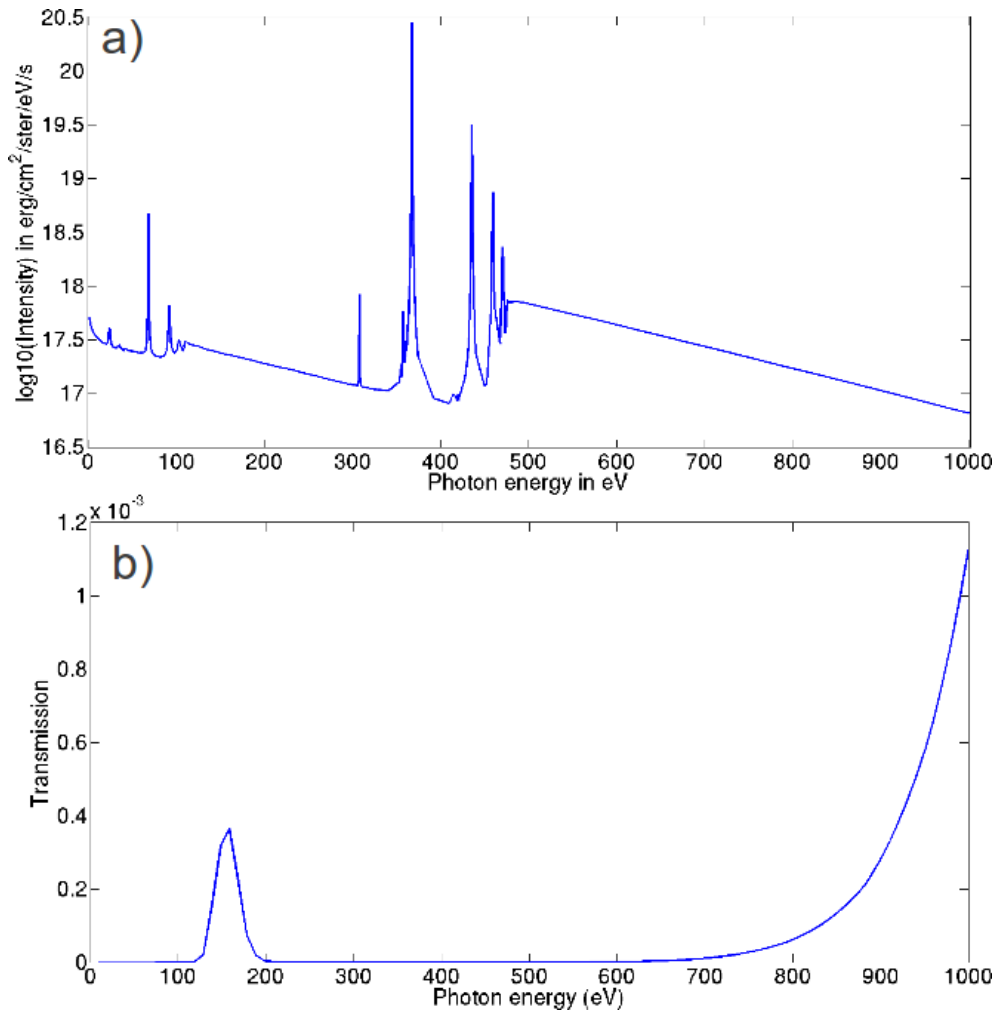


Figure 4.25: a): Plasma emission spectrum as simulated by PrismSPECT, for a logarithmic scale of the intensity in  $\text{erg}/\text{cm}^2/\text{ster}/\text{eV}/\text{s}$  as a function of the photon energy in eV. b): Transmission curve of a 650 nm thick gold foil as calculated with the help of *Filter Transmission*. Both graphs are plotted for a photon energy ranging from 0 to 1000 eV.

up to the exterior of the target chamber were electrically isolated, in order to separate their electric ground from the ground of the target chamber. For this purpose, the detector housing was itself enclosed in another aluminum housing, constituting a protecting Faraday cage. More precisely, the detector in its first housing was fixed on an isolating plastic bloc (hard and well-isolating Trovidur<sup>®</sup> plastic), which was itself fixed inside the second housing as shown in Fig. 4.27. In this way, the external housing had no electric contact with the internal housing and thus with the detector. The external housing was designed in a way that keeps it out of the trajectory of the nearby PHELIX beam. Moreover, it makes it possible to use either the new or the old detector in the experiment.

The housing features an aperture in its rear side in order to leave space for the 10 SMA cables. These cables, extending up to the vacuum flange that leads to the chamber exterior, were enclosed in two protective concentric tubes, one inner plastic tube directly in contact with the SMA cables, and an outer aluminum tube. The tubes were fixed on the rear of the detector and stretched up to the flange, i.e over 60 cm. The flange itself was specially developed for the purpose of this work. It is a CF73 flange in which the 10 SMA vacuum feedthroughs are fixed in a plastic bloc (also Trovidur<sup>®</sup>), shown in Fig. 4.26.

In this way, the electric ground of the detector was disconnected from the one of the chamber. The risk of coupling of EMP signals into the signal transmission line was thus minimized, be it through the detector housing, the SMA cables, the feedthroughs or any other element.



Figure 4.26: CF73 vacuum flange, that contains a 6 mm-thick isolating Trovidur bloc in which the 10 SMA vacuum feedthroughs are fixed. On the vacuum side, the SMA cables are enclosed in a plastic tube which is itself enclosed in an aluminum tube.

#### 4.2.4 Summary

The essential setup elements, namely the decelerating system, the CVD-diamond detector and the shielding system have been presented separately. In this section, the experimental setup is summarized in its globality and its important parameters are recapitulated.

- **Plasma parameters**

The laser beams, both frequency-doubled, feature wavelengths of 527 nm for PHELIX and 532 nm for *nhelix*. The laser energy is 30 J on each side and the laser-pulse length is 7 ns at FWHM. Both laser beams are focused on the plasma target with the help of frequency-matched lenses and are spatially smoothed by using RPP, which results in laser focus-spot diameters of 1 mm. The plasma target is a graphite foil of 0.5  $\mu\text{m}$  thickness and 1.84 g/cm<sup>3</sup> density, i.e around 100  $\mu\text{g}/\text{cm}^2$  areal density. The plasma created by the laser irradiation of this target becomes fully ionized at a time of about 6-7 ns after the beginning of the laser irradiation. It reaches maximal electron densities between  $10^{20}$  and  $10^{21}$  cm<sup>-3</sup> and a maximal electron temperature close to 200 eV, and expands over a few tens nanoseconds

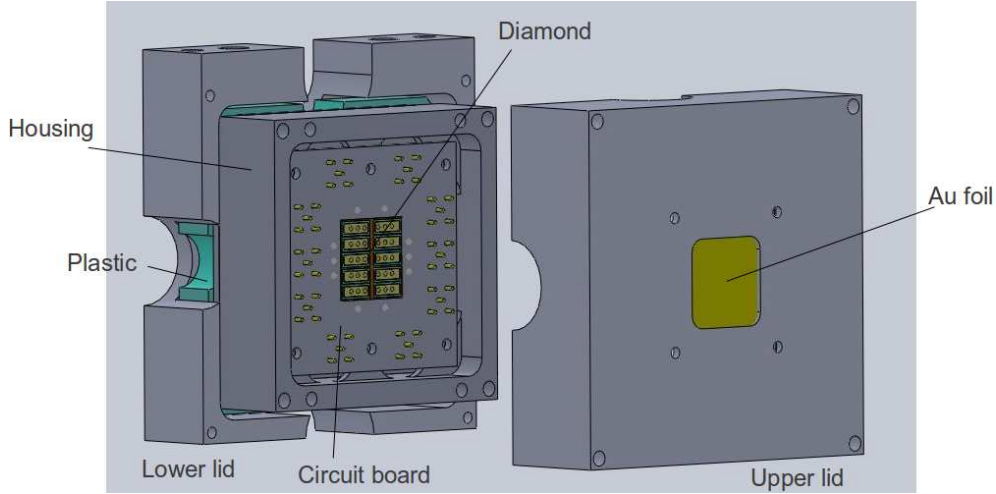


Figure 4.27: View of the detector with its dedicated screening system. The detector housing is positioned on an isolating plastic bloc (in green) which is itself fixed inside a second housing that acts as a Faraday cage. The upper lid of the Faraday cage features an aperture for the ion beam, where the gold filter foil is mounted. The lower lid features an aperture for the transmission of the SMA cables. The lateral apertures of the Faraday cage enable to also use the older detector, whose SMA connectors are located on the side, contrarily to the new detector for which the connectors are on the rear side. These apertures are sealed with aluminum film if the new detector is employed.

duration. The plasma features transversal inhomogeneities in areal density reaching 30 % over a radius of  $600\ \mu\text{m}$ , depending on the interaction time.

The plasma generation and evolution are monitored by the multi-frame interferometry diagnostic at a wavelength of  $355\ \text{nm}$  with a frequency-tripled beam, with a time resolution of  $0.5\ \text{ns}$  and allowing to probe the plasma in  $2\ \text{ns}$  steps in a  $6\ \text{ns}$  time range. The plasma emission produces a broad X-ray spectrum with photon energies of up to  $800\ \text{eV}$ .

#### • Ion-beam parameters

The initial ion beam consists of carbon projectile ions at a bunch frequency of  $36.136\ \text{MHz}$  (one bunch every  $27.673\ \text{ns}$ ), a temporal length of  $3\ \text{ns}$  at FWHM and at an energy of  $3.6\ \text{MeV/u}$ . At a distance of about  $10\ \text{cm}$  before the plasma target, the ion beam, which is originally a few centimeters broad, is filtered through a circular pinhole, which cuts its diameter down to  $500\ \mu\text{m}$ . The decelerating foil is positioned at about  $10\ \text{mm}$  before the plasma target. It is made of graphite with a thickness of  $46\ \mu\text{m}$  and a density of  $1.84\ \text{g/cm}^3$ , corresponding to an areal density close to  $8500\ \mu\text{g/cm}^2$ . The transversal foil extension is of only one millimeter on the side of the *nhelix* beam to avoid its heating by the laser. Through this decelerating foil, the carbon beam is slowed down to a mean energy of  $0.5\ \text{MeV/u}$ , which leads to the formation of an energy interval of 19 % at FWHM and an angle distribution between  $-3$  and  $3^\circ$ . After a  $10\ \text{mm}$  propagation distance, the decelerated beam interacts with the plasma, where due to its own transversal broadening, it is  $670\ \mu\text{m}$  wide at FWHM. The projectile ions thus interact with a plasma that features transversal inhomogeneities in the areal density of up to 30 %. This induces TOF differences of  $150\ \text{ps}$  between the central and the external beam ions. At plasma position, the ion bunches are still  $3\ \text{ns}$  wide at FWHM in spite of the energy straggling, due to the only  $10\ \text{mm}$  propagation distance. Through the plasma target, the ions undergo an energy loss close to 11 %, and after the plasma target the beam features an energy dispersion of 26 % at FWHM and an angular dispersion of up to  $4^\circ$  (estimations for the solid state of the plasma target). The ions propagate over a  $50.5\ \text{cm}$  TOF distance up to a polycrystalline CVD-



diamond detector, that they reach in 53 ns. A few millimeters before the detector surface, the ions pass through the  $0.65\ \mu\text{m}$  thick gold foil, aimed at stopping a major part of the X-rays emitted by the plasma, where they lose an additional fraction of their energy of 40 %. Subsequently, they impinge on the  $0.15\ \mu\text{m}$  thick metalization layer, where they lose again 13 % of their energy. The final ion energy when incoming on the diamond itself is thus  $238\ \text{keV/u}$ , which corresponds to an ion range in the sample of  $1.6\ \mu\text{m}$ . When arriving on the detector, the ion bunches have a 5 ns temporal width at FWHM, which has thus increased by 2 ns in comparison to its initial state.

#### • Detector parameters

The detector is made of the juxtaposition of 10 polycrystalline CVD-diamond samples, each of which features a  $7.2\ \text{mm} \times 2.3\ \text{mm}$  effective detection area. Combined with a  $13\ \mu\text{m}$  diamond thickness, this results in a detector time constant of 3.21 ns when used in conjunction with  $50\ \Omega$  broadband tension amplifiers. Effects of charge polarization and bunch overlapping on the detected signals appeared not to be critical.

The total effective detection surface of  $166\ \text{mm}^2$  is able to register 17 % of the beam ions. The detector has been designed in a compact way in order to keep it out of the trajectory of the nearby PHELIX beam, its upper edge lying 2 cm under the edge of the laser beam. The setup enables a theoretical energy resolution of 60 keV, assuming that the temporal resolution of the detector has a typical value of 200-250 ps.

The plasma targets, the decelerating foils as well as the gold filter foils were produced at the Target Laboratory of GSI. The decelerating setup was designed in collaboration with the Target Laboratory of TUD, and the detector system was developed and constructed at GSI.

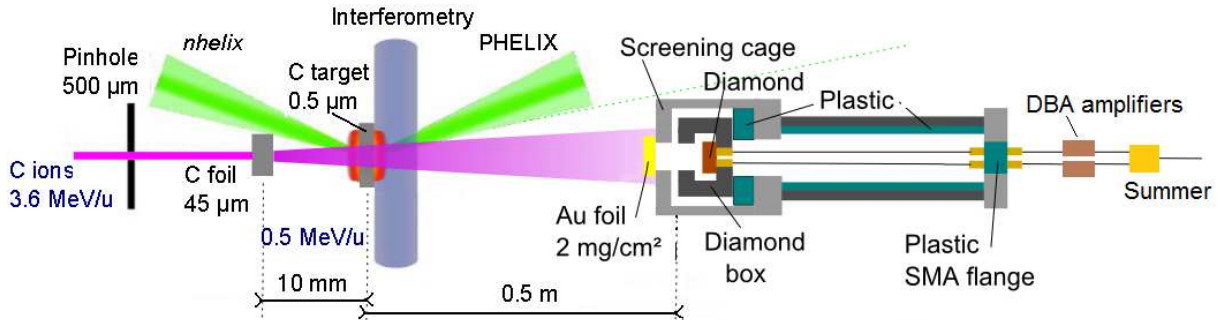


Figure 4.28: Final experimental setup.

#### • Recap table

Finally, the important quantities characterizing the ion beam at  $0.5\ \text{MeV/u}$  mean projectile energy in the experiment are summarized in table 4.2.4. They are also compared with the parameters corresponding to nearby projectile energies of  $0.7\ \text{MeV/u}$  and  $0.3\ \text{MeV/u}$ . This enables to discern the influence of the ion energy and of the associated deceleration process on the beam properties. As before, the GEANT4 distributions have been considered for estimating the beam energy intervals.

Even if measurements at ion energies of  $0.7\ \text{MeV/u}$  and  $0.3\ \text{MeV/u}$  could not be carried out in the frame of this work, they would bring a complementary experimental characterization of the region of the stopping maximum and should be conducted in the future. Measurements at  $0.3\ \text{MeV/u}$  or below would be particularly interesting because they would enable to explore the region below the stopping maximum. At these projectile energies, the perturbation strength on the plasma is possibly even higher (depending on the charge value), and plasma polarization as well as close collisions are expected to play an even more significant role in the stopping process. Moreover, the atomic shell corrections of

the stopping power become relevant in this low energy range. The energy resolution in this energy range would be excellent, reaching values of 25 keV and less, due to the large amount of the projectile energy lost in the plasma, in principle allowing very precise stopping measurements. Yet, the strong energy dispersion as well as the very short penetration range in diamond below 1  $\mu\text{m}$  may be problematic.

Anyway, the experimental setup presented in this chapter can in principle be applied for various projectile energies and also various ion species. Mainly the thicknesses of the decelerating foil and of the filter foil have then to be adapted.

Ion energy	3.6 MeV/u	0.7 MeV/u	0.5 MeV/u	0.3 MeV/u
Thickness of decelerating foil	-	44.1 $\mu\text{m}$	46 $\mu\text{m}$	47.8 $\mu\text{m}$
Energy interval after decelerating foil	0.001 %	10.6 %	17 %	33.4 %
Beam width (FWHM) on PT	0	490 $\mu\text{m}$	670 $\mu\text{m}$	770 $\mu\text{m}$
Energy lost in PT	1 %	7 %	11 %	19 %
Energy interval after PT	0	14.1 %	25.9 %	70.3 %
Energy lost in gold foil	0	27.4 %	38.4 %	50.8 %
Beam width (FWHM) on diamond	6 mm	33 mm	37.2 mm	41.1 mm
Percentage of ions on detector	100 %	29.2 %	22.8 %	19.3 %
Energy lost in metalization	0.8 %	8.5 %	13.1 %	26.1 %
Final ion energy	3430 keV/u	432 keV/u	238 keV/u	75.4 keV/u
Range in diamond	25 $\mu\text{m}$	2.4 $\mu\text{m}$	1.6 $\mu\text{m}$	0.7 $\mu\text{m}$
TOF if 0.5 m distance	17.7 ns	40.1 ns	47.5 ns	61.3 ns
Energy resolution for 0.5 m distance	1210 keV	100.8 keV	60 keV	25.2 keV
Overlapping (FWHM) at 36 MHz	-	6.60 m	3.74 m	1.47 m
Overlapping (FWHM) at 108 MHz	-	1.89 m	1.14 m	0.52 m

All the new aspects of this setup, i.e: the deceleration of the ion beam, the compatibility of the decelerating setup with the *nhelix* target irradiation, the influence of polarization in diamond and of ion signal overlapping, the influence of plasma radiation on the diamond detector and the concept of the shielding system, were tested in several preliminary experimental campaigns, giving proofs-of-principles of the newly developed experimental platform. Yet these aspects could be tested mostly only separately. Therefore the global setup could not be tested until the first experimental campaign, where a system calibration was required.

The next chapter presents the achievements and results of the first and unique experimental campaign carried out with the setup in the frame of this work.



## Chapter 5

# Experimental results

This chapter is devoted to the first experimental campaign that was carried out with the new setup, and is structured as follows.

In 5.1, the *modus operandi* of the campaign is presented, including the adjustment and the calibration of the setup, as well as the encountered issues. Subsequently, in section 5.2, the obtained experimental results are presented. The data-analysis method is explained, and the energy loss in the experiment is determined. Finally, in 5.3, the experimental data are compared with theoretical predictions, and the results are discussed.

### 5.1 First experimental campaign

#### 5.1.1 Adjustment of the experiment

Before each experimental measurement, the target system is prepared on the adjustment stage shown previously in Fig. 4.16. During the calibration phase, the design of the decelerating target was yet modified as shown in Fig. 5.1. The distance between the decelerating target and the plasma target as well as the parallelism between both targets are adjusted by using two CCD cameras, while the axial alignment of both targets is controlled with a laser pointer. The ion beam is to enter the decelerating target at a point located at a distance of 1 mm from its edge on the side of the incident *nhelix* beam. This point is aligned with the center of the plasma target foil.

As soon as the adjustment stage has been positioned in the target chamber center and the chamber has been pumped down to a pressure of  $10^{-5}$  mBar, the stage has to be aligned with the ion and laser beams. This is now explained in relation to Fig. 5.1. The stage is aligned with the ion beam by means of a scintillator fixed on the side of the decelerating foil. The next step is to align the laser beams with the ion beam. This is achieved with the help of a piece of thermal paper fixed on the side of the plasma target and by employing the laser beams in a non-amplified modus. First, the position of the ion beam is marked on the thermal paper and then the PHELIX and *nhelix* beams are overlaid and centered with the ion beam on the thermal-paper surface. When the alignment stage is moved back at its previous position, the three beams are therefore superimposed in the center of the plasma target.

Furthermore, as a pinhole has been added in the design of the decelerating target, the ion beam has to be re-aligned in a finer way a few minutes before each shot. The ion beam has indeed to be guided into the 1 mm pinhole, and this has to be preferably carried out shortly before the measurement, because of the natural fluctuations of the ion-beam position. For this purpose, the diamond detector is directly used to measure the incoming ion signal. The ion transmission is maximized when the beam is centered on the pinhole. The position corresponding to the maximum transmission i.e to the maximum signal amplitude, is thus used for the energy-loss measurement.

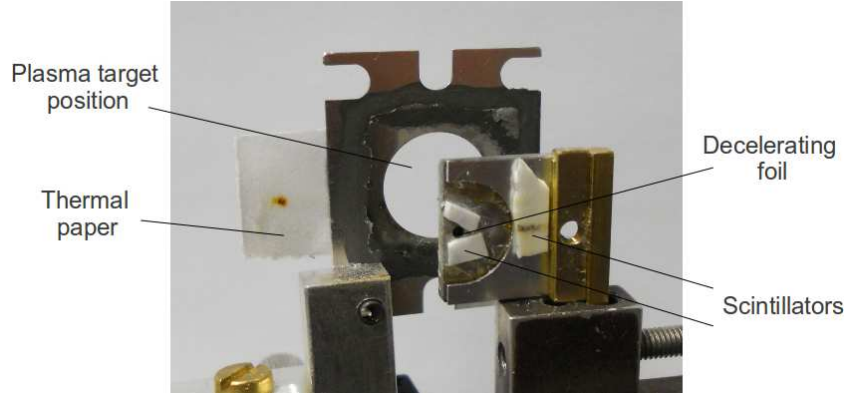


Figure 5.1: New design of the decelerating target implemented in the calibration phase, by fixing the foil over a 1 mm diameter metal pinhole.

Due to the proximity of the decelerating target as well as of the detector system to the regions of laser irradiation and to the resulting hot plasma, several experimental issues appeared due to the laser-plasma interaction. Therefore, the measurements could not be carried out in a systematic way and a calibration of the system was necessary. Along the experimental campaign, the setup was progressively optimized and energy-loss data were finally obtained. Because of the encountered difficulties, only a few data points were obtained and the error bars are relatively important. However, as shown in 5.2, the uncertainties are not critical, and the obtained measurement precision still allows to test the stopping-power theories.

### 5.1.2 Calibration of the experiment

Even if diverse aspects of the experimental setup have been tested separately in several preliminary experiments, the setup could not be tested in the real conditions of the experiment before this first campaign, therefore a calibration had to be carried out. The calibration was necessary both for the decelerating target and for the filter foil.

#### Decelerating target

It appeared that the decelerating foil is systematically destroyed, probably due to the PHELIX beam irradiation, and it has thus to be changed at each shot. This motivated the new setup of the decelerating target of Fig. 5.1. This configuration was implemented to make the decelerating foil less exposed to the incoming PHELIX beam, and to allow a sufficient amount of decelerating foils in the campaign. It consists in fixing a small piece of the decelerating target behind a 1 mm diameter aluminum pinhole. Yet, this still did not prevent the systematic destruction of the target. Therefore various foils with different thicknesses were used, which was likely to cause a substantial change in the energy of the decelerated ions. However, the TOF measurements through both targets (see table 5.2.3) show that the ion energy remains stable. The uncertainty on the thickness of the foils lies therefore more in their characterization, that is particularly difficult for the 40-50  $\mu\text{m}$  thickness range, than in their fabrication process by rolling.

Even if the foils were partly ablated by the plasma-emitted X-rays, it is highly probable that they were mainly damaged by the PHELIX laser beam. This can be seen in Fig. 5.2, on a photograph of the plasma taken with a digital camera.

While symmetric expanding plasmas can be observed on the two surfaces of the plasma target, corresponding to the PHELIX and *nhelix* heated plasma for the energy-loss measurement, another “secondary” plasma can be seen close to the surface of the decelerating foil. A possible explanation is based on the intensity distribution of the focus spot of the PHELIX beam. Due to the structural characteristics of the RPP used to smooth the PHELIX laser beam, an important

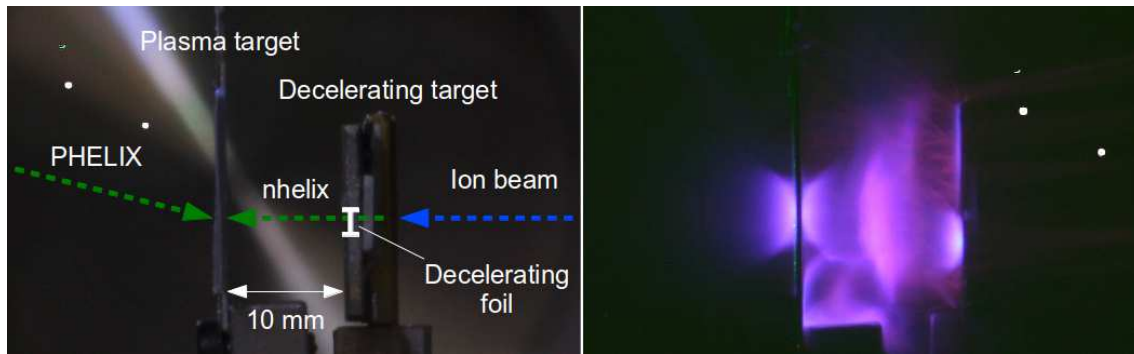


Figure 5.2: Left hand side: decelerating target and plasma target before a shot, with a representation of the incoming beams. Right hand side: plasma during one shot as registered over a 30 s time by means of a digital camera provided with a 532 nm-matched filter.

intensity spike is present in the focus profile, as shown in Fig. 5.3. As soon as the plasma target is sufficiently heated and expanded, the most intense part of the PHELIX beam is able to traverse the generated plasma and to irradiate the vicinity of the foil surface.

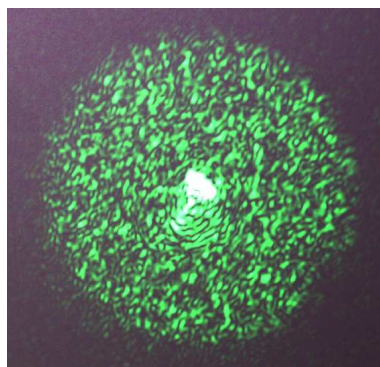


Figure 5.3: Focus-spot profile of the PHELIX laser beam. The presence of a hot spot can be well-recognized in the center, constituting a spike in the laser-focus intensity profile.

Not only did the modified design of the decelerating target probably reduce the ablation of the irradiated decelerating target, but it also allowed, as it requires only small pieces of the foils, to guarantee a sufficient number of samples for the whole campaign. However, because of the pinhole, it led to a reduction of the ion transmission in the experiment and thus to a relatively small ion-signal amplitude. This is why the precise ion-beam adjustment by maximizing the ion-signal amplitude on the CVD-diamond detector was necessary. The small signal amplitude also resulted in enhanced experimental error bars. The used configuration was therefore not optimal and it still can be improved in a next campaign to avoid the foil destruction and/or to obtain larger-amplitude signals.

### Filter foil

As for the gold foil in front of the detector, it appeared to not always efficiently screen the X-rays emitted by the plasma. Hence, most of the shots were not exploitable because of the presence of electromagnetic signals superimposed with the ion signals. The reason is probably the irradiation of the plasma target by the PHELIX laser, which leads to a radiation emission in the direction of the detector, and whose influence could not be tested in previous beam times.

Because of their large area (30 mm diameter) and small thickness ( $0.65 \mu\text{m}$ ), the filter foils are

likely to be damaged due to intense photon absorption or plasma debris. It was observed that the foil was indeed damaged after each shot, which made it inefficient in screening the X-rays in the next shot. Even some foils that did not feature any visible damage proved to be inefficient at their first utilization. Various foils therefore had to be used and eventually combined with each other in order to find a reliable filter configuration.

The success of the screening was very fluctuating throughout the campaign, depending on the laser irradiation parameters and on the foil characteristics, that feature natural fluctuations that are out of the control of the experimental operators. Finally, a 30 mm diameter and 0.65  $\mu\text{m}$  thickness (1.3  $\text{mg}/\text{cm}^2$ ) gold foil and two 200  $\mu\text{g}/\text{cm}^2$  carbon foils of the same diameter worked out as the best filter combination. The threefold-layered filter, featuring a total areal density of 1.7  $\text{mg}/\text{cm}^2$ , was efficient in blocking the X-rays, while still enabling a substantial ion transmission and thus detector signals with a small but mostly sufficient amplitude. A similar configuration will therefore be used in future experiments.

After the calibration phase and chiefly due to the filter optimization, energy-loss measurements were carried out in a more systematic way. In addition of permitting to obtain first energy-loss results, this campaign thus enabled to optimize the setup for future experiments. Basing on the experience gained in this first campaign, the quality and the quantity of the energy-loss measurements in this setup can be significantly improved in a future campaign.

Finally, five experimental shots could be used for an energy-loss analysis. For these shots, the X-ray signals have been sufficiently mitigated to not affect the interesting ion bunch (see 4.2.3). In the most successful case, the duration of the X-ray signal on the detector was reduced down to 20 ns (see Fig. 5.5).

The laser energies corresponding to the five successful shots, measured with calorimeters, are listed in the following table. It shows that the mean values of the PHELIX and *nhelix* energies are very similar, around 31-32 J. However, the energy of the PHELIX beam is more fluctuating. This is one of the reasons why the X-ray signals significantly vary from shot to shot. According to RALEF2D simulations, the hydrodynamic expansion of the carbon plasma and the resulting plasma conditions only significantly vary if the incoming laser energy features a variation of more than 50 %. Therefore the data from the shot 12 have to be considered with care, as the plasma conditions have probably been different there due to the small PHELIX beam energy.

	Phelix	Nhelix
Shot 12	10 J	33 J
Shot 13	32 J	33 J
Shot 16	38 J	31 J
Shot 19	43 J	30 J
Shot 20	33 J	32 J
Mean value	31.86 J	31.43 J
Standard deviation	11.25 J	1.51 J

In next section, the successive steps of the data analysis are described and the experimental results obtained from the five exploitable shots are presented.

## 5.2 Experimental results

### 5.2.1 Principle of the measurements

#### Measured signals

For each energy-loss measurement in plasma, three distinct measurements are conducted. In each of them, an ion macro-bunch is registered with the help of a fast digital oscilloscope. First, the

ion signal is registered after interaction with the decelerating target and the cold plasma target. This reference measurement features a constant ion energy loss, as is expected in cold matter. Second, the ion energy-loss measurement in plasma is carried out. Third, a measurement of the macro-bunch is conducted in vacuum, in order to obtain an absolute reference for the energy loss. A fourth measurement was to be carried out with the decelerating target alone to know the ion energy probing the plasma. However, as the decelerating target was systematically destroyed in the experiment, this measurement registered the same ion signals as in vacuum. Hence, TRIM simulations were used to determine the energy loss in the plasma target and thus to infer the ion energy incident on the plasma target.

By means of a chopper magnet, the duration of the macro-bunch was adjusted to  $30\ \mu\text{s}$ . The data are then sufficiently long to include the part around the laser-trigger point, where the plasma is created and quickly expands, as well as the vacuum region after the projectile ions are not influenced by plasma or by residual gas anymore. In this way, the macro-bunch measurement covers the whole time range of the interaction, from cold matter at the beginning of the macro-bunch, to the plasma state at a defined point within the macro-bunch, and finally to vacuum after the plasma and the residual gas have disappeared. This point is essential for the energy-loss analysis, as is described below. As the micro-bunch frequency in the experiment was 36 MHz, each macro-pulse measurement: in cold matter, with the plasma and in vacuum, contains about 1500 ion micro-bunches. Moreover, a fixed electric signal corresponding to the 36 MHz pulsation of the ion beam in the UNILAC accelerator is also systematically registered as a reference. In this experiment, this 36 MHz signal appeared to be almost in phase with the ion micro-bunches in vacuum, but this was only a coincidence.

In Fig. 5.4, a typical example of registered detector data is shown, where all the signals of one energy-loss measurement have been superimposed for comparison.

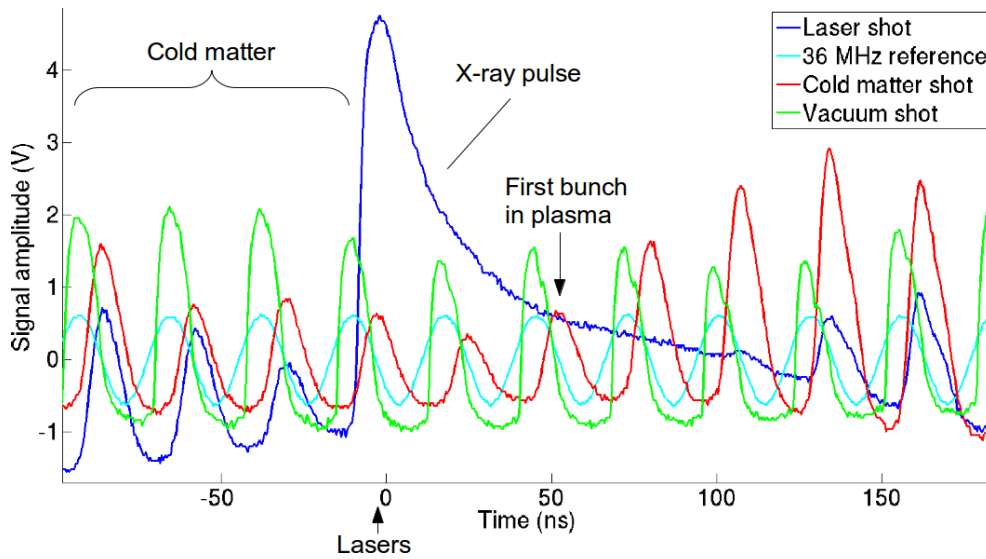


Figure 5.4: Example of detector data registered in the experiment, where the main measurement with plasma, the reference measurement in cold matter, the reference measurement in vacuum and the 36 MHz reference signal are compared. For this shot, the X-ray pulse from the plasma strongly saturated the detector for a time longer than 100 ns, and no data analysis could thus be conducted here as the signal of the relevant ion bunch for the energy-loss determination lies at  $t \approx 50\ \text{ns}$ .

### Qualitative signal analysis

An apparent time shift of 7-8 ns can be observed between the signals in vacuum and the signals in cold matter. The slowing-down process of ions at a projectile energy of 3.6 MeV/u through



both targets results in a time shift close to 35 ns, which is higher than the period of the ion micro-bunches of 27.6 ns. Therefore, the actual time delay that is seen between both signals is  $7 + 27.6$  ns. This corresponds to the expected time shift caused by the ion deceleration down to 0.5 MeV/u, and actually to slightly lower energies because the deceleration through the plasma target is also included. The signals through the cold targets also appear to be slightly broader than the ones of the vacuum measurement, due to the energy straggling caused by the deceleration process. Variations in the amplitudes of both data signals correspond to fluctuations of the ion source in the accelerator.

With the timing adjustment in the experiment, the laser beams heated the target around the zero time. Before the laser irradiation, the maxima of the ion signals are identical to the ones of the reference shot in cold matter because the ions still interact with the cold targets. Then, around the zero time, the laser beams start irradiating the plasma target and the plasma is generated. As can be recognized on the graph, and as was the case in most of the measurements carried out in the experimental campaign, an intense X-ray pulse is generated from the beginning of the laser irradiation of the target. This pulse lasts for about 150 ns, and prevents the detection of the interesting ion bunch for energy-loss measurements. This bunch should be detected at a time of approximately 50 ns that corresponds to the ion TOF, close to the time where the associated bunch in cold matter lies. But in this case, the ion signal is completely absent due to detector saturation, and no energy-loss analysis is possible.

The amplitude and the duration of the X-ray pulse on the detector strongly varies from shot to shot, depending on the exact laser energies, on the precision of the adjustment process and on the quality of the filter foil positioned in front of the detector. In most measurements, the saturation caused by the X-rays was less pronounced than in the case presented here, but often extended over more than 50 ns after laser irradiation, preventing an energy-loss analysis.

At a time of about 100-150 ns after the laser irradiation, the detector is not saturated anymore and the ion bunches can be detected again. Yet at these times, the plasma conditions are unknown and no energy-loss analysis is possible anymore. In particular, the secondary PHELIX plasma is expected to enter the ion path after a few tens nanoseconds if an expansion velocity of  $\approx 100 \mu\text{m/ns}$  is assumed (see equation 2.27). This secondary plasma modifies the areal density experienced by the projectile ions. But as the energy-loss measurements have been carried out in the first 10 ns, they have not been affected by this phenomenon.

The expansion of the secondary PHELIX plasma is also the probable reason for which no clear decrease in the total areal density is to be noted following the expansion of the plasma target. Globally, the areal density indeed remains quite stable for a time of several hundred nanoseconds, as the times of arrival of the ion signals after the heating of the plasma target remain stable in relation to the signals in cold matter for several hundred nanoseconds. This observation suggests that the decelerating target has not been significantly ablated by the plasma-emitted X-rays, as predicted in section 4.2.1. Therefore the expansion of the surface of the decelerating target, heated to a temperature of a few eV at most, does not lead to a noticeable modification of its areal density. This seems to indicate that the decelerating target is neither destroyed by the plasma radiation itself, nor by the PHELIX beam impinging close to its surface, but by the expansion of the nearby plasmas.

In conclusion, even if changes in the global areal density experienced by the projectile ions have occurred, they do not involve the first ten nanoseconds of the beam-plasma interaction where the measurements have been carried out. Neither the projectile energy nor the measured energy loss have therefore been affected.

When considering the final part of the measured macro-bunch, the ion signals of the vacuum measurement (in green) are superimposed with the ion signals of the plasma measurement (in blue), showing that the vacuum has been reached and that no matter lies in the ion path anymore. Therewith, the absolute energy-loss values can be determined.

### 5.2.2 Data analysis

Now, the successive steps of the data-analysis process are presented, from the determination of the bunch maxima to the extraction of the energy-loss values in the plasma target and the evaluation of the experimental errors.

#### Determination of the centers of gravity of the signals

In order to determine the absolute energy-loss values in one given measurement, the centers of gravity of the ion signals are determined and compared with reference values. These references are given by the ion signals at the end of the measured macro-bunch in plasma, corresponding to ions flying through vacuum and experiencing no energy loss. So the centers of gravity of the ion bunches in plasma are compared with the centers of gravity of the ion signals in vacuum, for each measured macro-bunch.

The centers of gravity of the ion signals actually do not correspond to the times of arrival of the ion bunches, because the ion signals that are measured are the convolutions of the actual Gaussian micro-bunch temporal signals and of the response function of the detector [Fra11]. Yet the determination of the absolute arrival times is not necessary, as only the relative time shift between the signals in plasma and the signals in vacuum counts for the energy-loss determination. Therefore the knowledge of the centers of gravity of the respective ion signals is sufficient, provided that these centers of gravity can be correctly determined both in the plasma and in vacuum.

It turned out that for the ion signals registered in this work, no fit function could be found that would well reproduce the signal form in the plasma *and* the signal form in vacuum. The function  $f$  in equ. 5.1 has delivered the best results for the solid and the plasma part of the macro-bunch signals. It is based on an exponentially-modified Gaussian function using the fit parameters  $\lambda$ ,  $\mu$ ,  $\sigma$  and  $a_2$ , where  $erfc$  designates the complementary error function. Because the baseline of the signals does not necessarily correspond to zero Volt and the baseline may fluctuate significantly, in particular when parasitic electromagnetic signals are superimposed on the ion signal, a linear function is added for a more precise fitting process, by using the parameters  $a_0$  and  $a_1$ .

$$f(t) = a_0 + a_1 \cdot t + a_2 \cdot \frac{\lambda}{2} \exp\left(\frac{\lambda}{2}(2\mu + \lambda\sigma^2 - 2t)\right) erfc\left(\frac{\mu + \lambda\sigma^2 - t}{\sqrt{2}\sigma}\right) \quad (5.1)$$

The fitting process produced an important error. Moreover, the function, as any other fit function that was tested, is unable to treat the ion signals in vacuum. The reason for this is the unusual signal shape that is observed especially in the vacuum part, and that was not fully understood yet. Because of the impossibility of signal fitting in the whole measurement span, a more basic method had to be employed for the determination of the signal maxima, while the fit function  $f$  is used for special cases.

The centers of gravity  $t_0$  of all ion bunches were thus determined by integration of the surface of the registered signals by applying formula 5.2, where  $a$  and  $b$  are the time boundaries of a given ion micro-bunch signal  $f(t)$ .

$$t_0 = \frac{\int_a^b t \cdot f(t) dt}{\int_a^b f(t) dt} \quad (5.2)$$

#### Illustrative example of the data-analysis method

The implementation of this integration method is illustrated in Fig. 5.5 on the data from a measurement shot where the X-ray pulse influence has been successfully mitigated. The pulse duration was indeed reduced down to only 20 ns and the energy-loss determination is thus not hindered.

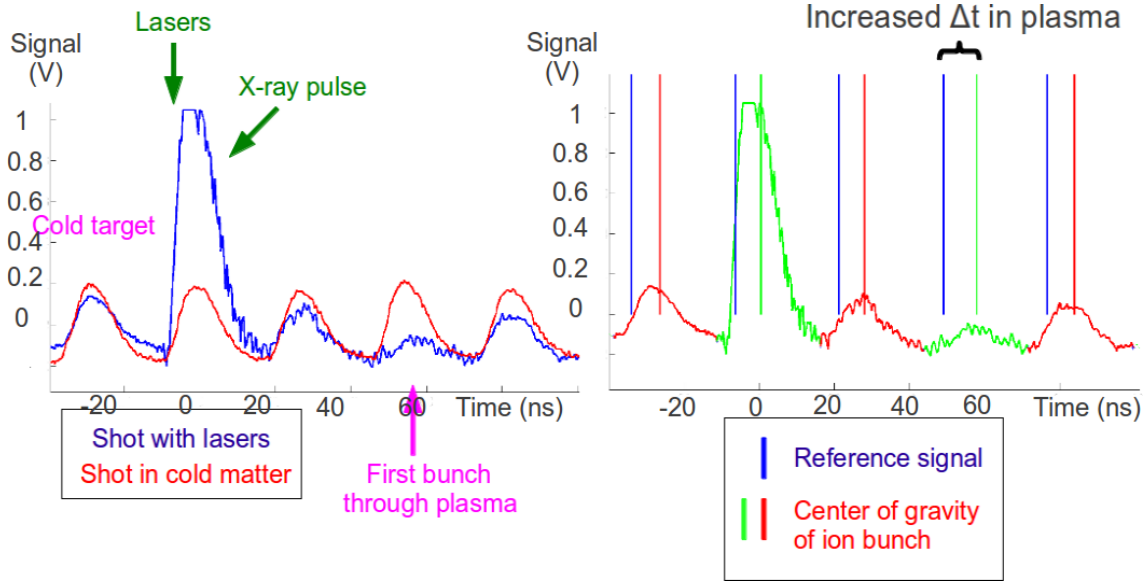


Figure 5.5: Illustration of the data-analysis method with a measurement featuring an efficient X-ray-pulse mitigation. Left hand side: comparison of the signals of the shot in cold matter and with the plasma, where the first ion bunch having interacted with the plasma is indicated. Right hand side: determination of the time shifts of the ion signals by comparing the centers of gravity of these signals (in red and green) with the reference centers of gravity corresponding to the vacuum values (in blue). A significant increase in the time shift and thus in the ion energy loss can be observed for the first ion bunch that interacted with the plasma.

As shown in the right hand side of the figure, the successive ion signals have been identified and for each of them, the center of gravity has been determined by applying equation 5.2, as represented by the red and green vertical bars. The blue vertical bars represent the reference values of the centers of gravity of the ion signals through vacuum. They are obtained by determining the centers of gravity in the vacuum part (e.g the 100 last signals), and by linearly extrapolating them to the whole data by using the 27.6732 ns micro-bunch period. The time shift corresponding to the ion energy loss in one bunch is thus determined by comparing the center of gravity of the given signal (in red or green) with the corresponding reference value (in blue). On the graph, it can clearly be seen that the maximum of the first ion bunch that interacted with the plasma is significantly shifted in respect to its reference value. This increased  $\Delta t$  shows that the ion energy loss in plasma has been enhanced. From the time shifts  $\Delta t$ , the corresponding energy losses can then be determined by using equation 4.1, knowing the TOF distance and the initial ion energy. The time shifts and consequently the energy losses of the 100 last ion signals of the given macro-bunch are considered equal to zero because the corresponding ion bunches interact with vacuum. This gives the absolute reference for the energy-loss determination. The temporal evolution of the energy loss of the ion micro-bunches over the whole duration of the 30  $\mu\text{s}$  macro-bunch is shown in Fig. 5.6.

Before the laser irradiation, the energy loss in the decelerating target and the cold plasma target is constant and approximately equal to 38 MeV. As the initial ion energy before the slowing-down process is 43.2 MeV, the ions thus have an energy of 5.3 MeV = 0.44 MeV/u when leaving the cold plasma target. This is in agreement with a 0.5 MeV/u energy of the ions entering the plasma and losing about 11 % of their energy in it as predicted by the TRIM code. Even if the ions further lose energy in the filter foil and in the metalization layer of the diamond detector, no further TOF difference arises, as explained in 4.2.4. Hence, the time shifts measured on the detector only depend on the energy loss in both targets. From the time of the laser irradiation (at about 0 ns), the energy loss starts varying and progressively decreases, to finally reach the

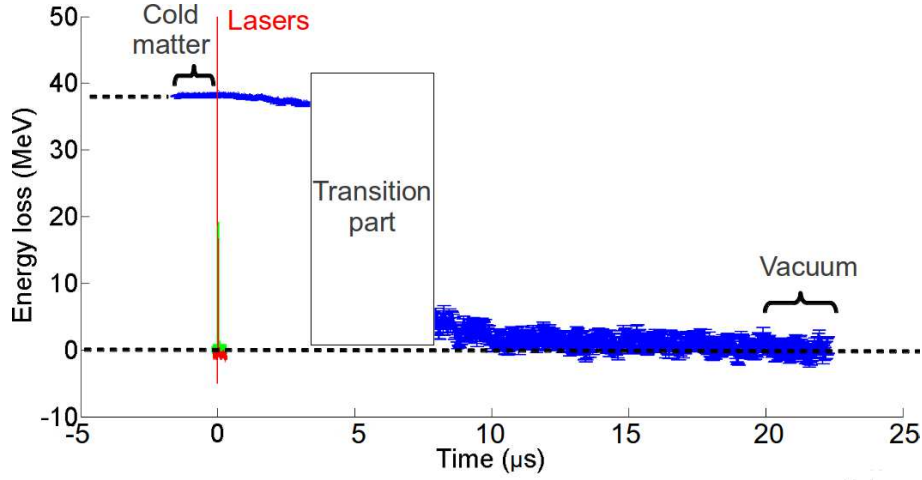


Figure 5.6: Ion energy loss (MeV) as a function of time (ns), over the duration of the whole macro-bunch of 30  $\mu\text{s}$  in one measurement, as experienced by the ions passing through both targets.

zero value after about 20  $\mu\text{s}$ . In the so-called “transition part”, fluctuations in the measured signals prevented a systematic energy- loss determination.

### Laser-ion timing

A crucial point for the interpretation of the ion energy-loss data is the exact timing of the ion bunches in relation to the laser pulses, in order to know which plasma conditions were probed by the ions. For each measurement involving the laser beam heating of the plasma target, the time and the temporal profile of both laser pulses are recorded with photo-diodes. In order to determine the laser-ion delay in each measurement, the different TOF and cable lengths corresponding to the ion and laser signals have to be taken into account. This time shift between the laser signals and the periodic ion signal is given by the difference between the time of the beginning of laser heating of the target ( $t = 0$  ns) and the time at which the decelerated ion beam enters the plasma. The time  $t_{ion}$  at which the first ion bunch that passes through the plasma probes this plasma is thus given by:

$$t_{ion} = t_{ion\_det} - TOF_{ions} + (\Delta t)_{cab} \quad (5.3)$$

where  $t_{ion\_det}$  is the time of the center of gravity of the ion signal registered on the detector,  $TOF_{ions}$  is the TOF of the ions between the plasma and the detector, and  $(\Delta t)_{cab} = t_{cab\_det} - t_{cab\_las}$  is the difference in the signal propagation time between the different transmission cables employed for the detector and for the laser (in the experiment calibration), respectively.

### Energy loss in the plasma target

The total ion energy loss through both targets being determined, what is however of interest for this work is the energy loss in the plasma target alone. So the energy loss in the decelerating target has now to be subtracted. Unfortunately, for time and technical reasons, the energy loss through the decelerating target alone could not be measured, as mentioned previously. Therefore, the TRIM code was employed to determine the ion energy when entering the plasma. As the ion energy after the plasma target is obtained from the experimental TOF measurements and the areal density of the solid plasma target is known with a precision of  $\pm 10\%$ , the projectile energy before entering the plasma can be calculated with a precision of  $\pm 80$  keV, i.e  $\pm 6.7$  keV/u. This consequently brings an additional error source in the experimental energy-loss values. A

complete discussion of the experimental uncertainties and of the error bars is carried out later in this section.

### Signals requiring a special treatment

The uncertainties on the energy-loss values are enhanced in the cases of the measurements shown in Fig. 5.7, and these signals thus require a special treatment. These cases are now emphasized because they represent most of the data obtained in the experimental campaign.

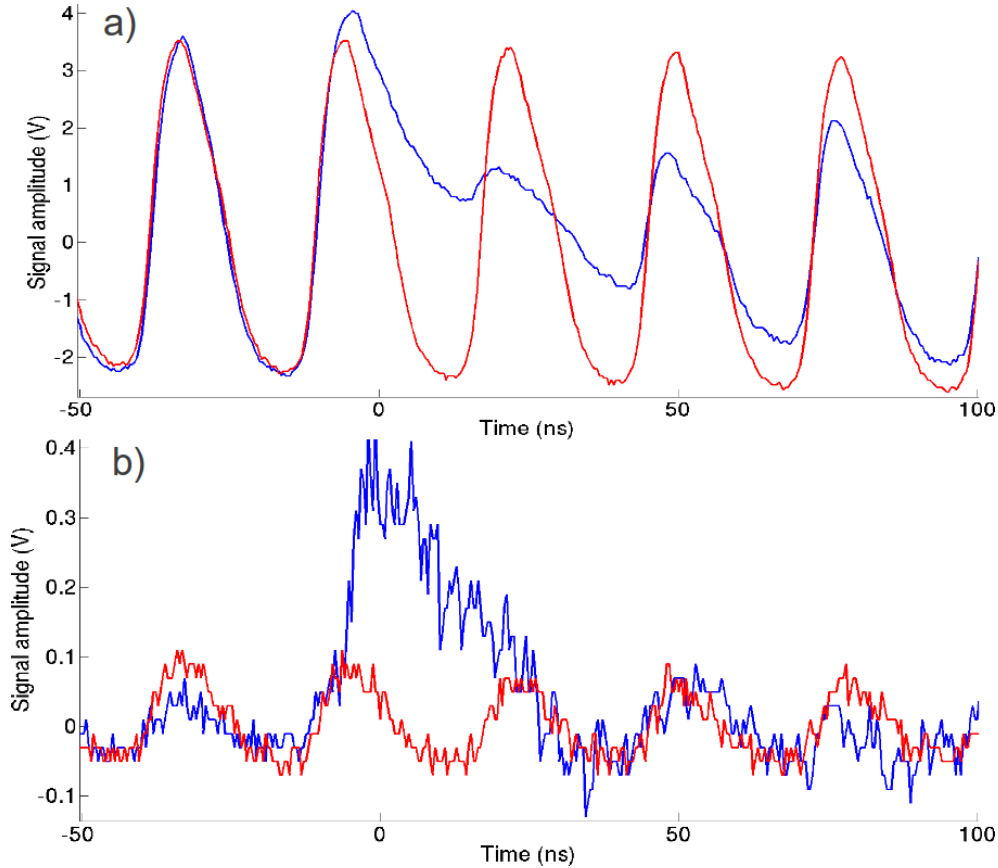


Figure 5.7: a): detector signals featuring a moderate X-ray pulse whose influence on the ion signals has to be taken into account. b): detector signals featuring a particularly weak amplitude of the ion signals.

- **Signals with X-ray pulse**

The detector signals of Fig. 5.7a) are well defined in spite of the presence of the parasitic X-ray signal. However, the position of the maxima of the ion signals may have been shifted because of the variation in the signal baseline caused by the X-ray pulse. In order to take this into account, the following procedure has been applied.

A measurement of the X-ray pulse alone has been carried out with the diamond detector, with the two laser beams and without the ion beam. The corresponding X-ray signal is shown in Fig. 5.8, and it can be fitted with the help of the exponentially modified Gaussian function of equation 5.1. As X-ray signals can vary significantly from shot to shot in duration and in amplitude, but yet feature the same general form, the fit function is used in turn to fit the baseline of the ion signals in Fig. 5.7a). The baseline is then subtracted from the signals, and the original ion signals are deduced. The signals preceding the signal of the first ion bunch that interacted with plasma are then compared with the

corresponding signals of the shot in cold matter. If a good agreement is found between the centers of gravity of the deduced signals of the plasma shot and of the cold matter shot, the X-ray subtraction process is considered as realistic and the associated error is taken as the error in the determination of the maxima of the cold ion signals.

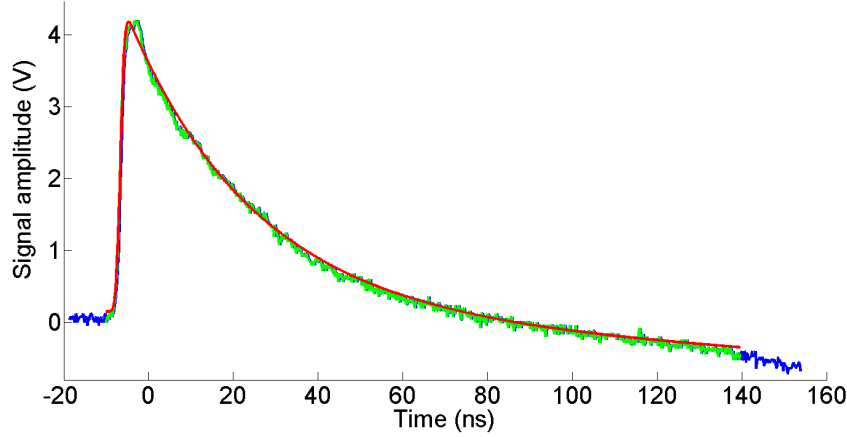


Figure 5.8: Measured X-ray signal generated by the emission of the plasma heated by means of the PHELIX and *nhelix* laser beams, that can be well fitted by means of an exponentially-modified Gaussian function. This function is then employed to fit and subtract the X-ray signal from the ion-signal measurements, where necessary and possible.

- **Signals with small amplitude**

As for the detector signals of Fig. 5.7b), while they are not affected by X-ray signals, the ion signal amplitude is particularly small and an important noise is present. There also, a direct determination of the center of gravity of the signals is difficult and the error on the energy-loss values is consequently enhanced. In order to reduce the noise influence, the small ion signals are first fitted with the exponentially modified Gaussian function 5.1, and the maxima of all ion signals are then determined by the integration method of equation 5.2. The small signals featuring an important noise are simply replaced by their fitted versions. The error given by the fit routine is quite important because of the mentioned signal characteristics.

## Error analysis

The experimental error sources in the determination of the time shift  $\Delta t$  are now discussed and the corresponding error bars are evaluated.

1. Error on vacuum

The uncertainties in the determination of the reference centers of gravity of the ions in vacuum  $\Delta t_{vac}$  can come either from the fluctuations of the maxima of the signals in the vacuum domain, or from the integration method. The error on the integration method, which provides by nature exact results because the signals are sampled, is evaluated as the fluctuation of the signal maxima in the vacuum domain as well. The fluctuation is taken as the standard deviation of the maxima values  $\sigma_{vac}$ .

2. Error on integration

As in the vacuum part, the error on the integration of the signals in the plasma part  $\Delta t_{int}$  is estimated as the fluctuation of the signal maxima in the cold-matter part  $\sigma_{cold}$ .

### 3. Error on energy loss in plasma target

As explained previously, an uncertainty  $\Delta t_{PT}$  of  $\pm 80$  keV and thus of  $\pm 0.4$  ns is present for the mean energy of the projectile ions entering the plasma. This is caused by the absence of an experimental characterization of the energy loss in the decelerating target and by the uncertainty on the initial areal-density value of the plasma target.

### 4. Error on fitting

This error contribution  $\Delta t_{fit}$  occurs when the ion signals are fitted because they feature an excessive noise for a determination of their centers of gravity by integration of the signal surfaces. The error comes from the fit routine and features high values of up to 1 ns.

### 5. Error on baseline

This error  $\Delta t_{bas}$  is present when the baseline corresponding to the X-ray pulse has to be subtracted for the determination of the signal maxima. As the subtraction process relies on the comparison of the obtained ion signals preceding the first bunch signal in plasma with the corresponding signals of the cold-matter shot, the minimum error is the fluctuation of the signal maxima in cold matter  $\sigma_{cold}$ .

### 6. Error on plasma inhomogeneity

As explained in 4.2.1 and 4.2.2, due to the transversal broadening of the ion beam, the ions may experience slightly different plasma conditions in the experiment. By considering a deviation of 30 % in the areal-density profile of the plasma, a 150 ps TOF uncertainty is estimated.

The total experimental uncertainty is estimated with the Gaussian error-propagation formula, assuming that the various error sources are independent from each other:

$$\begin{aligned} \Delta t &= \pm \sqrt{[\Delta t_{vac}^2 + \Delta t_{int}^2 + \Delta t_{PT}^2 + \Delta t_{inh}^2 (\Delta t_{fit}^2 + \Delta t_{bas}^2)]} \\ &= \pm \sqrt{[2 \cdot \sigma_{vac}^2 + \sigma_{cold}^2 + (0.4ns)^2 + (0.15ns)^2 + \Delta t_{fit}^2 + \sigma_{cold}^2]} \end{aligned} \quad (5.4)$$

## Energy resolution

The energy resolution in the experiment is now estimated, to verify whether the measurements can in principle differentiate between the various theoretical stopping-power approaches. The temporal resolution corresponds to the precision with which the centers of gravity of the ion signals can be determined, and it depends essentially on the detector properties. Figure 5.9 shows the method employed to evaluate the temporal resolution. The latter can vary from shot to shot, depending on the ion statistics. The difference  $t_{i+1} - t_i$  between the centers of gravity  $t_i$  and  $t_{i+1}$  of two successive ion signals is first determined for the whole macro-bunch of the measurement in cold matter. The corresponding distribution can be fitted by a Gaussian function as shown on the graph.

Hence the precision  $\sigma_{t_i}$  in the determination of  $t_i$  is given by:

$$\sigma_{t_i} = \frac{\sigma(t_{i+1} - t_i)}{\sqrt{2}} \quad (5.5)$$

where  $\sigma(t_{i+1} - t_i)$  is the standard deviation of the Gaussian distribution of the times of arrival of the micro-bunches. As in similar experiments with CVD-diamond detectors, the time resolution of the detector is found to feature values close to 200 ps. Hence the energy resolution of the experimental setup is approximately 60 keV, as is predicted in 4.2.2. Consequently, the experiment

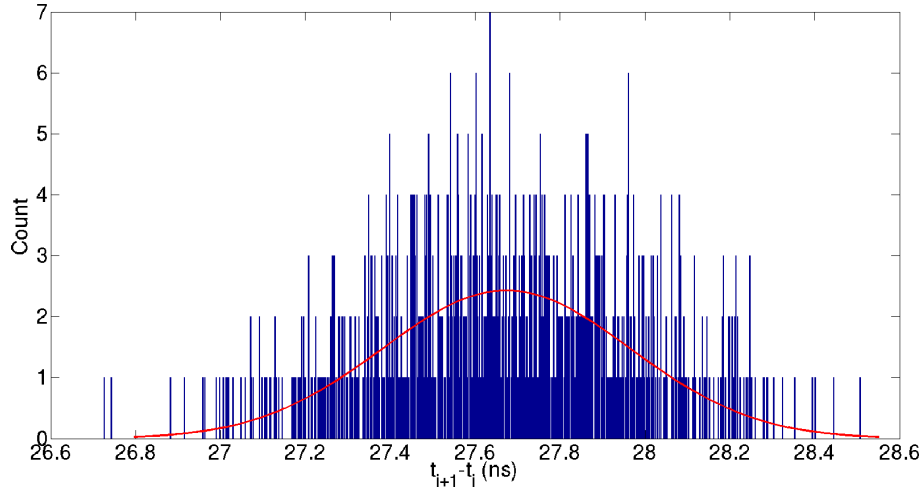


Figure 5.9: Example of distribution of the differences in the times of arrival of two successive ion bunches on the detector  $t_{i+1} - t_i$  for one macro-pulse containing more than 800 micro-bunches. The data are fitted by a Gaussian curve featuring a maximum at 27.67 ns, which enables to determine the time resolution of the detector by using equ. 5.5.

allows a fine energy-loss measurement and makes it in principle possible to differentiate between several stopping theories and to determine which model is best suited for the given physical case. Yet this capability also depends on the experimental error bars.

Finally, the results obtained from all the exploitable measurements are summarized in the following.

### 5.2.3 Energy-loss results

#### Time shift

Figure 5.10 shows the measured time delays  $\Delta t$  of the ions after passing through the plasma target as a function of time. Before the time of the laser irradiation ( $t = 0$  ns), the projectile ions interact with the cold plasma target and  $\Delta t$  is therefore constant, around 3 ns. Shortly after the plasma creation at  $t = 0$  ns, where the measured temporal profiles of the laser pulses are represented, an increase of  $\Delta t$  can be observed, up to values of 4-5 ns. From  $t = 30$  ns after the beginning of plasma generation, the  $\Delta t$  values are difficult to interpret because the plasma conditions and the plasma areal density are unknown. The corresponding data therefore cannot be reliably understood. The energy-loss data are thus limited to the first ion bunches crossing the plasma, which covers a time span from 0.9 ns to 10.3 ns after plasma creation. For these times, the plasma conditions are known from the RALEF2D simulations and no significant expansion of the secondary plasmas has occurred, hence the plasma conditions are well-controlled. The error bars of the measurements span from  $\pm 0.5$  ns to approximately  $\pm 1.5$  ns in the case of small-amplitude signals.

#### Energy loss

Knowing the time differences, the corresponding ion energy losses can be deduced, as shown in Fig. 5.11. The energy loss of the projectile ions through the plasma target stays constant at a value of 0.6-0.7 MeV for the solid state. Following the laser irradiation at  $t = 0$  ns, an increase in the energy loss, to values of up to 1 MeV, can be observed. The subsequent values are not reliable anymore.

The error on the measurements, deduced from the error obtained on the time differences, reaches



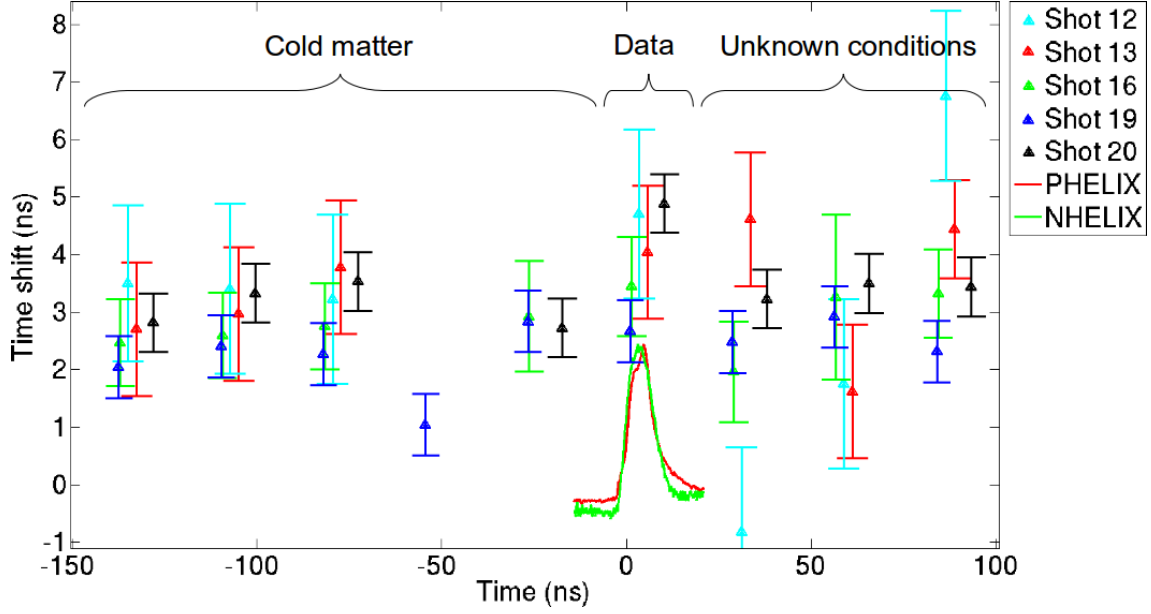


Figure 5.10: Compilation of the five exploitable measurements showing the evolution of the mean time shifts of the projectile ions through the plasma target as a function of time. The laser beams heat the plasma target at  $t = 0$  ns and their temporal profiles are also represented. From  $t \approx 30$  ns, no reliable data analysis can be carried out due to unknown plasma conditions. The data points in cold matter for which the signals could not be analyzed due to the X-ray pulse are not represented.

values from  $\pm 95$  keV to  $\pm 220$  keV depending on the shot. The experimental errors as well as of other significant parameters of each measurement are summarized in the table below.

Yet the most adapted way of comparing the various measurements is to plot them in relation to the solid state. In this way, the influence of the slightly different decelerating targets and plasma targets is eliminated and the relative energy-loss variation, normalized to the solid-state energy loss, is determined. The mean energies of the ion beams when entering the plasma are within the interval 0.51-0.54 MeV/u depending on the shot. According to the calculations of section 3.2.2, the resulting differences in the values of the stopping power are close to 0.5 % and can therefore be neglected.

The results are shown in Fig. 5.12, where only the energy-loss data of the first ion bunch through the plasma are represented. A progressive increase in the energy-loss values as a function of time can be seen. The successive data points feature respective increases of 19, 27, 35, 46 and 53 % in the energy loss in relation to the cold target. The maximum energy-loss value of 153 % is measured at  $t = 10.3$  ns, within the time interval where the plasma is fully ionized. As for this point the plasma areal density is around 70 % of its original value, the increase in energy loss is actually of about 218 %. The error in the measurements spans from 10 % to approximately 25 % depending on the considered shot. This largest error, corresponding to  $\pm 220$  keV, is thus above the 100 keV resolution needed for being able to distinguish between all the theories as mentioned in 3.2.4. However it still allows, in particular, to compare the perturbative first-Born approaches to the nonperturbative T-Matrix approach.

In the recap table below, the main experimental parameters related to the ion energy loss are summarized for the five measurement shots constituting the exploitable data.

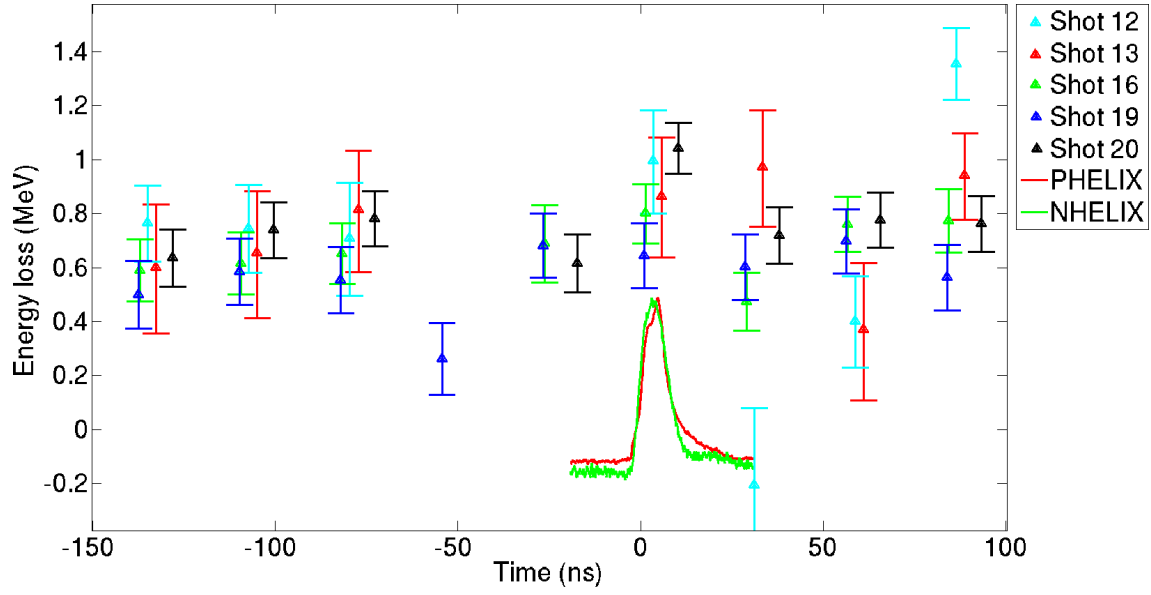


Figure 5.11: Ion energy loss in MeV as a function of time.

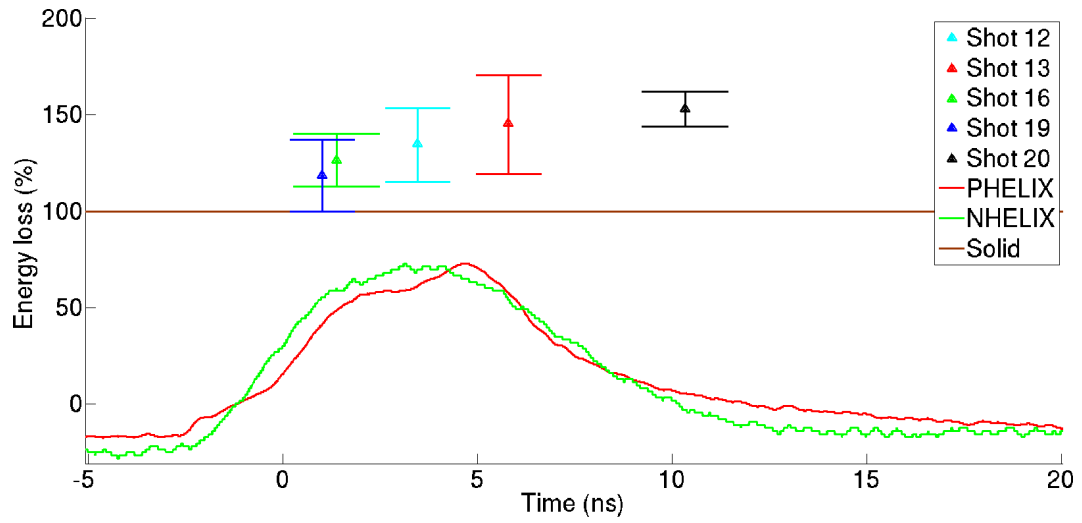


Figure 5.12: Ion energy loss as a function of time, where 100 % represents the energy loss in the solid plasma target.

Shot	DT thickness ( $\mu\text{m}$ )	PT thickness ( $\mu\text{g}/\text{cm}^2$ )	$\Delta t$ cold (ns)	$\Delta E$ cold (MeV)	$\Delta E$ PT (MeV)	TOF (ns)	Time (ns)	Error (keV)
12	47.5	97	35.1	37.8	0.74	54.2	3.5	$\pm 195$
13	47.5	98	34.5	37.7	0.59	53.7	5.8	$\pm 220$
16	43.6	99	33.4	37.8	0.63	52.5	1.4	$\pm 110$
19	43.6	91	33.8	37.7	0.61	51.9	0.9	$\pm 120$
20	43.6	91	34.4	38.0	0.62	53.4	10.3	$\pm 90$

### 5.3 Comparison with theory

Finally, the experimentally determined energy-loss values are compared with the theoretical stopping predictions calculated in section 3.2.4 and shown in Fig. 3.11. An ion beam with a Gaussian time distribution featuring a width of 3 ns at FWHM was assumed, and the energy-loss influence on the actual ion energy was taken into account by using an Euler approximation. An ion energy of 0.53 MeV/u corresponding to the experiment was assumed. The comparison is shown in Fig. 5.13, where all energy-loss values are expressed in percent of the energy loss in the solid plasma target.

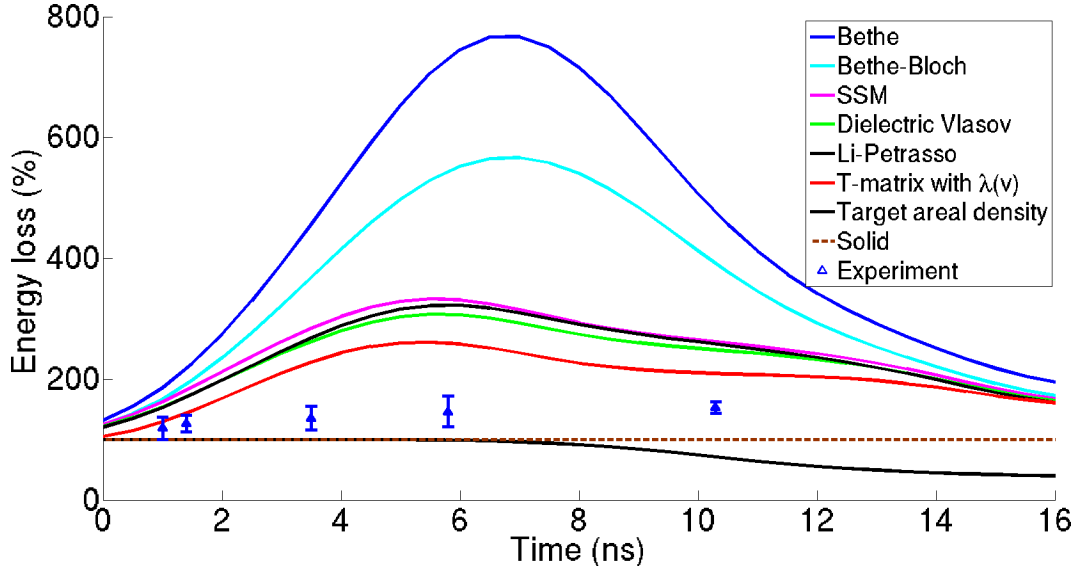


Figure 5.13: Comparison of the measured energy loss with theoretical stopping predictions as a function of time. 100 % represents the energy loss in the solid plasma target.

The obtained energy-loss results agree qualitatively with the theoretical predictions, showing a progressive enhancement of the energy deposited in plasma as a function of time, resulting from an increase in the Coulomb logarithm of the interaction and in the mean projectile charge state. However, quite important discrepancies can be observed between the experimental points and the theoretical values. While the measured data feature values comparable to the theoretical predictions for a time prior to 3.5 ns, the two data points at times  $t = 5.8$  ns and  $t = 10.3$  ns in the hot and highly ionized plasma, i.e. actually within the region of maximum stopping power, lie significantly below all the theoretical energy-loss curves.

All the stopping theories thus seem to over-evaluate the energy deposition in plasma around the maximum stopping power. Even the results of the T-Matrix with  $\lambda(v)$  approach, which predict stopping-power values by a factor 30 % smaller than the theories and models basing on the first-Born approximation and appear to be closest to the experimental points, feature an increase of the energy loss close to 100 % in relation to the cold state, while the experimental values show a maximum increase of 53 %. Therefore, while the perturbative approaches over-estimate the deposited energy by a factor of nearly two, the T-Matrix with  $\lambda(v)$  approach still over-estimates the energy loss by about 0.3-0.4 MeV. This corresponds to a TOF difference close to 2 ns, while the first-Born results over-estimate the TOF by 3.5 ns.

Furthermore, the corresponding stopping power in the experiment is now evaluated for the case of the data point at  $t = 10.3$  ns, by using the simulation results at  $t = 10.5$  ns. It is the point that features the smallest experimental error, namely of  $\pm 90$  keV. The result is shown in Fig. 5.14. The theoretical stopping powers are calculated similarly as in 3.2.2 by using the averaged parameter values of a). The conditions correspond to a fully ionized plasma with  $n_e = 3.7 \times 10^{19}$

$\text{cm}^{-3}$  and  $T_e = 121.4$  eV. The mean projectile energy along its propagation in the target is 0.48 MeV/u, and its mean charge-state value is 5.5. The experimental stopping power is determined in relation to the stopping power in the solid, taking into account the reduction in the plasma areal density close to 30 % for this time of the plasma evolution.

The result of the comparison is shown in c). The estimated experimental stopping power has a value of  $18.5 \pm 1$  keV/( $\mu\text{g}/\text{cm}^2$ ). In comparison, the stopping power according to the T-Matrix approach features 22 keV/( $\mu\text{g}/\text{cm}^2$ ). The obtained stopping power is thus by about 16 % smaller than predicted by the T-Matrix. Yet the T-Matrix calculation implemented here is based on a fit formula, whose precision in respect to the full expression is of 25 %. The experimental result therefore lies within the corresponding error interval. An exact T-Matrix calculation basing on the determination of the scattering cross sections would therefore be of great interest here for a more precise comparison with the data.

Due to the relatively small signal amplitude in the first campaign and to the few obtained data points, these results need to be confirmed with more statistics and a more systematic investigation with an optimized version of the experimental setup. In this way, a larger temporal domain of the plasma evolution can be covered and the error bars can be reduced.

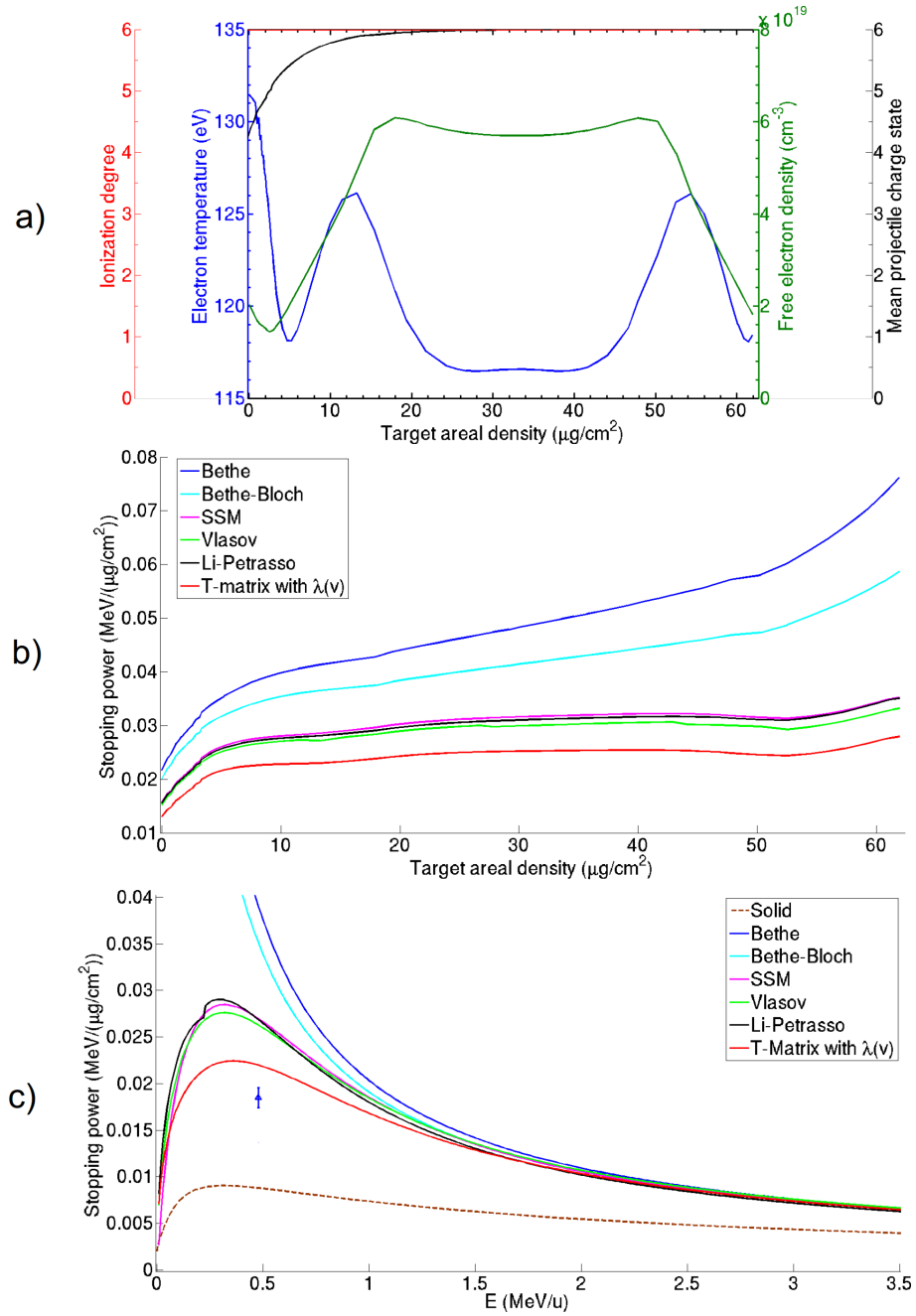


Figure 5.14: Comparison of the theoretical and experimental stopping powers for the data point at  $t = 10.3$  ns, by averaging the plasma and projectile parameters over the target areal-density profile at  $t = 10.5$  ns. a): profiles of plasma and projectile parameters along the plasma areal density. b): corresponding theoretical stopping-power profiles. c): estimation of the experimental stopping power in relation to the theoretical predictions.

## Chapter 6

# Conclusions and perspectives

This work constitutes the first experimental study on ion stopping at maximum stopping power in a laser-generated plasma that enables to reliably test the different stopping theories. While first precise experimental results were obtained and the first comparisons with theory were carried out, there still are improvements to be implemented and questions to be answered, from the experimental as well as from the theoretical point of view. Moreover, further investigations on ion stopping can be considered on the basis of this work. The goal of this conclusion chapter is thus to recall and discuss the results of this work, as well as to suggest next developments to be carried out in the future.

In the first part, the results of this thesis are discussed and the limitations of the present work, notably in relation to the projectile charge-state description, are examined. In particular, possible setup improvements for a next experimental campaign are presented. In the second part, as a further work direction, theoretical as well as experimental investigations on ion stopping in a moderately coupled plasma are outlined, that would make it possible to study the nonlinear regime of the beam-plasma interaction.

Preliminary work on further improvements of the experiment as well as on the investigation of the nonlinear stopping regime has been started in the frame of this thesis and is in progress.

## 6.1 Conclusions of the work

### 6.1.1 Thesis results

Recent developments in the fields of ICF and high-energy-density physics have motivated numerous theoretical investigations on ion-stopping mechanisms in plasmas. Beam-plasma conditions involved in heavy-ion fusion or in alpha-particle stopping in the dense ICF fuel have particularly raised the need for stopping descriptions beyond the standard perturbative approaches basing on a dielectric formalism or on corrected formulas for cold-matter stopping. In this context, non-perturbative ion stopping theories have been developed in the frame of kinetic plasma theory, that notably predict a strongly reduced energy deposition around the stopping-power maximum. In the present work, these important predictions have been put to the test for the first time, for a plasma temperature that is relevant for both heavy-ion fusion and alpha-particle stopping.

This was achieved by carrying out precise stopping measurements in a simplified and fully characterized beam-plasma configuration. The combination of an elaborate laser-heating scheme, of plasma simulations notably including radiative transport, of Monte-Carlo simulations of all charge-transfer processes and of precise time-resolved plasma and ion diagnostics thus enabled to reliably compare the energy-loss results to available stopping theories.

The analysis of the results shows that the nonperturbative theoretical predictions are significantly closer to the experimental energy-loss data. In contrast, the standard perturbative theories over-

evaluate the energy deposition by 50-60 %. However, even the nonperturbative T-Matrix approach, that best fits the data, is shown to over-evaluate the energy loss by around 30 %. When estimating the corresponding stopping powers, a 16 % difference is found with the T-Matrix for the data point with the smallest experimental error bars, while a 30 % discrepancy is found in relation to perturbative results. As the T-Matrix calculation was carried out by means of an approximate fit formula, an exact T-Matrix calculation could potentially reproduce the experimental data and should thus be carried out.

Moreover, stopping-power calculations in the combined scheme are in progress, and further theories as the CKLT approach or the BPS approach can also be put to the test later. Furthermore, numerical PIC or MD simulations would be interesting to provide a complementary stopping-power evaluation.

In any case, the data suggest that most stopping theories tend to over-evaluate the ion stopping power at stopping maximum, implying that this maximum is less pronounced, less “peaked” than usually predicted. These results thus raise the possibility that the energy deposition of alpha particles in the frame of ICF has been over-evaluated in the past studies and that the alpha-particle range in the plasma is thus significantly larger. However, the stopping properties of carbon ions may be not directly transposable to alpha particles. Indeed, in this work the projectile had a charge state by a factor 3 higher than in the case of alpha particles, giving thus rise to a threefold stronger perturbation in the plasma medium. Moreover, the plasma coupling and degeneracy have also to be considered.

For a more complete and a more systematic experimental investigation of the ion energy loss at maximum stopping power, further measurements are necessary. For this purpose, the developed experimental platform can be improved and optimized in several respects, basing on the experience gathered in this work, as explained in the following.

### 6.1.2 Setup optimization for further experiments

Following the acceptance of another experiment proposal at the PHELIX facility, a second experimental campaign has been scheduled at GSI. But due to external reasons, that campaign was postponed beyond the time frame of the thesis. As a consequence, the results of the present work are exclusively based on the first campaign. A large part of the experiment had to be devoted to a calibration of the setup, therefore only few data points were finally obtained. For the second campaign, the measurement platform will be optimized and data will be gathered in a more systematic way.

In the first campaign, only five exploitable energy-loss measurements were obtained. Moreover, the corresponding ion signals featured small amplitudes and mostly a significant noise due to poor ion statistics, leading to relatively important error bars and thus to a loss in the energy resolution. These issues can be solved as explained in the following.

The main issue of the first campaign was the presence of the X-ray pulse at early times of the plasma evolution. It prevented an energy-loss analysis of most measurements. The progressive calibration of the filter foil enabled to suppress the influence of the X-ray pulse, while still allowing acceptable ion-signal amplitudes. The optimum filter configuration has been determined, featuring an areal density of  $1.7 \text{ mg/cm}^2$ , and this will enable to obtain a larger amount of exploitable data in the next campaign.

The poor ion statistics was caused by the non-optimal setup of the decelerating target implemented due to the systematic foil destruction. This can be improved by increasing the distance between the decelerating target and the plasma target to up to 15 mm, to avoid the foil ablation. In this way, the systematic energy-loss measurement through the decelerating target alone will also be possible at each shot. It has however to be systematically determined, by means of TOF measurements, if the areal density of the foil stays approximately stable in spite of plasma X-ray

irradiation, or to what extent it has been ablated. In addition, a fast Dicom camera with a 1 ns time resolution could be employed to diagnose the ablation of the decelerating foil. Furthermore, it has to be evaluated if the TOF discrepancies within the plasma target remain acceptable.

In such a configuration, the signal quality and thus the measurement precision could be enhanced significantly. The errors due to weak ion statistics, to X-ray signals and to the uncertainty on the ion energy probing the plasma would indeed be reduced, while only the error on the TOF dispersion would increase.

As a conclusion, the optimized setup would, on the one hand, enable to obtain a larger amount of data, permitting to corroborate the first results and to extend them by covering a larger temporal span of the ion-plasma interaction. And on the other hand, the measurement precision would be enhanced by a factor 2 at least. In this way, not only could perturbative predictions be distinguished from nonperturbative predictions as was possible in this work, but also different nonperturbative theories could be discriminated. This would thus allow a more precise benchmarking of the stopping theories.

Furthermore, after the ion-plasma interaction at a projectile energy of 0.5 MeV/u has been extensively characterized, measurements at projectile energies slightly above and below the stopping maximum, at 0.7 MeV/u and 0.3 MeV/u respectively, can be considered. This would also be relevant for a more complete characterization of the strongly velocity-dependent stopping curve in that velocity region. The developed experimental setup indeed can be applied for various projectile species and energies by varying the thickness of the decelerating foil, as long as the straggling resulting from the beam deceleration process remains acceptable.

### 6.1.3 Questioning the projectile charge state

In light of the significant discrepancies observed between the experimental results and the theoretical predictions, it is legitimate to question the relevance of the charge-state description in the theoretical part of this work.

#### Nonperturbative charge transfer

In the frame of the described Monte-Carlo code, the charge-transfer cross sections are determined within perturbative methods and might be not adapted to the region of maximum stopping power, where Coulomb coupling is important. Indeed, as explained in [Fra11], the ionization and recombination cross sections in the code are calculated either in a first Born approximation of the projectile-target collision process, or nonperturbative terms are included only in an approximate manner. This is because the code was originally designed for application at higher projectile velocities, as at  $\frac{v_p}{v_{th}} \approx 4$  as in [FBB<sup>+</sup>13]. The cross sections implemented in the code might thus lose their validity for  $\frac{v_p}{v_{th}} \approx 1$  because of the important perturbation exerted by the projectile on the plasma electrons ( $\eta > 1$ ). As mentioned in 3.1.3, the cross sections of the NREC process might notably have been under-evaluated.

In particular, additional nonperturbative processes including multi-electron ionization and recombination events (multiple charge exchange) [WM08], binding effects, polarization of the target atomic shells and strong Coulomb deflections [BBL78] may play a significant role in the charge-state dynamics. Different screening behaviors of the projectile, likely to strongly modify the charge-state dependence of the stopping power, may also play a role, as well as important nonequilibrium charge-transfer phenomena.

To date, the understanding of the charge-state dynamics at high Coulomb coupling remains very incomplete. In any case, given the obtained energy-loss results, the charge-state distribution of the projectile needs to be questioned and put to the test, as it might contribute to the observed discrepancies.



### Classical-trajectory Monte-Carlo simulations

In order to determine the charge-state distribution of the projectile ion beam in a nonperturbative manner, a classical-trajectory Monte-Carlo (CTMC) calculation can be conducted. A CTMC code has been developed recently to determine the stopping power and the charge-state of projectile ions interacting with a solid target self-consistently [GBAS04, GB06].

Hence, unlike in all main stopping theories, the projectile charge state is not taken as a simple input for the stopping-power calculation, but it is determined simultaneously. The code is well-adapted to a nonperturbative beam-target interaction as around the stopping-power maximum, where  $\eta > 1$ . This also means that a classical calculation is possible, hence the designation *classical-trajectory* Monte-Carlo code.

No approximation is needed, and the interaction of a projectile ion carrying  $n$  electrons with  $N$  target electrons is determined by calculating the Coulomb forces and applying the Newtonian motion laws at each calculation time step. The only external parameters are the binding energies of electrons of the projectile and of the target atoms, which are determined by a quantum-mechanical Hartree-Fock calculation. Apart from this, the interaction is thus exclusively determined from first principles, and the multi-body dynamics of the system is thoroughly described, including notably all multiple charge-exchange phenomena.

In the frame of this thesis, work has been started, in collaboration with the developer of the code, in order to extend its domain of applicability to a highly ionized plasma and thus to use it for the studied beam-plasma configuration. Even if this task could not be achieved within the time schedule of the thesis, the work on the code is in progress, by including free electrons in the target description.

### Experimental investigation

A further necessary development for the future is the preparation of experiments aimed at measuring the charge-state distribution of a carbon ion beam at a mean projectile energy of 0.5 MeV/u exiting a laser-generated plasma. At the Z6 experimental area, as a magnetic dipole cannot be implemented inside the target chamber for charge-state separation, a Thomson parabola charge diagnostic has to be used instead. This in turn requires an intense beam of laser-accelerated carbon ions in order to obtain exploitable signals due to the low-transmission characteristics of Thomson parabolas.

With the help of the 100 TW PHELIX beamline (see section 4.1.2), a carbon ion beam can be generated and subsequently probe a carbon plasma heated with the *nhelix* laser system. The ion beam, featuring an exponential energy spectrum, can then be distributed on a detector screen inside the Thomson parabola according to the charge-to-mass ratios of the present ion species. The experimental setup would therefore be similar to the one described in [GCL<sup>+</sup>13]. The analysis of the feasibility of such an experiment is in progress.

Yet, in order to account for the experimental energy-loss data of this work, a charge-state value of roughly 5+ instead of 6+ would be required. It is highly unlikely that the nonperturbative effects lead to such an important discrepancy in the charge state. Therefore, though the latter might contribute, to a moderate extent, in the discrepancies between the measured energy-loss and the theoretical predictions, the major effect is expected to be related to the stopping power itself.

## 6.2 Outlook: nonlinear regime of ion stopping

A further milestone is the investigation of the ion-stopping process in the case of strong beam-plasma correlations, i.e in the nonlinear regime of the beam-plasma interaction, for  $\gamma \geq 0.1$ . This

can occur for projectile ions interacting around the stopping maximum with a dense, strongly coupled plasma, especially if the projectile ions are highly charged.

### 6.2.1 Aiming for the nonlinear regime of ion stopping

#### Ion stopping at strong coupling

The understanding of the beam-plasma interaction is then even more challenging due to the plasma nonideality ( $\Gamma > 0.1$ ). Coupling effects like strong collisions, nonlinear screening or multiple scattering appear. Besides, the plasma degeneracy can play an important role. And as the plasma is then mostly partially ionized, bound states need to be taken into account and the description of the interaction is significantly more involved, in particular concerning the projectile charge-state value. The dependence of the stopping power on the projectile charge state is also expected to be substantially modified due to nonlinear screening phenomena, featuring a  $Z^x$  scaling with  $x \approx 1.5$  instead of the  $Z^2$  scaling that characterizes the linear stopping regime. This has been predicted by nonlinear VP simulations and MD simulations [Boi96, Zwi99, OHK<sup>+</sup>05], and measured for heavy ions decelerated in a cold electron gas in storage rings (see e.g [WBB<sup>+</sup>97]). The understanding of the nonlinear stopping regime is also of high relevance in the frame of ICF and for most applications listed in the introductory part of this thesis.

As highlighted in 2.2.6, important differences between the predictions of various stopping-power theories are expected around the stopping maximum. These discrepancies already appear to be significant for the physical case of this work, for an ideal plasma with  $\Gamma \approx 0.01$ . For an increasing plasma coupling strength, the discrepancies between the perturbative and the nonperturbative stopping theories become even more dramatic.

The present work can therefore be viewed as a preliminary step towards the investigation of the nonlinear regime of ion stopping. It enables to partly benchmark the existing stopping-power theories and simulations, which is also useful for the theoretical description at higher beam-plasma correlations. The deceleration and detection platform developed in the frame of this thesis can also be employed in a future setup for experiments in the nonlinear stopping regime, with a different, nonideal plasma target.

In particular, the stopping power in the nonlinear interaction regime in a hydrogen or a deuterium plasma is of great interest. First, ion stopping in a strongly coupled hydrogen plasma is an important issue especially for the energy deposition of alpha particles in the initial phase of the thermonuclear fusion burn. As highlighted in 3.3, alpha-particle stopping in the early phase of the ignition of an ICF pellet is poorly understood notably because of degeneracy and strong-coupling effects. Furthermore, as a hydrogen atom features only one electron, a fully-ionized hydrogen plasma is relatively simple to obtain, even if it is relatively cold and strongly coupled. Therefore the interpretation of the results is facilitated, making it a case in hand to understand the fundamental interaction mechanisms.

#### Ion-stopping experiments in strongly coupled hydrogen plasmas

Hence, a long-term goal of the ion-stopping studies is the preparation of experiments investigating the ion energy loss in a strongly coupled hydrogen plasma. This goal is pursued conjointly by CELIA and TU-Darmstadt in collaboration with GSI, and is notably stimulated by the recent development of cryogenic hydrogen targets at TUD.

A cryogenic setup was constructed at TUD in order to produce thin planar solid hydrogen or deuterium target foils [Men10, BBS<sup>+</sup>12]. In this way, starting from an initial density significantly higher than in the gaseous state, a dense and strongly coupled hydrogen plasma can be generated. Deuterium is preferred to basic hydrogen because its cryogenic density, reaching  $0.2 \text{ g/cm}^3$ , is about twice higher than the one of hydrogen. Moreover, its cryogenic temperature is at the same time slightly higher than the one of hydrogen, thus requiring less cooling.

In order to pave the way towards ion-stopping experiments in a strongly-coupled deuterium

plasma, a preliminary parametric analysis has been started at CELIA. Hydrodynamic simulations have been conducted with the purpose of defining the best-suited plasma parameters that can be reached and thus the best-adapted target-heating scheme. The plasma has to be as dense and strongly coupled as well as transversally homogeneous as possible over the longest possible duration, in order to be able to carry out high-quality ion-stopping measurements as in this work. Both  $\Gamma$  and  $\gamma$  should be  $\geq 0.1$  in order to reach the nonlinear regime of beam-plasma interaction. Another point to be taken into consideration is that the colder the plasma (which increases the value of  $\Gamma$ ), the smaller is the value of the thermal electron velocity  $v_{th}$ . Therefore, for a very cold plasma, the projectile ions need to have a very low velocity in order to reach  $\frac{v_p}{v_{th}} \approx 1$ . This in turn requires a strong beam deceleration if the same setup as in this work is employed, which might not be feasible because of the important beam straggling at low velocities. For increasingly warm plasmas, the stopping maximum is progressively shifted to higher values of  $\frac{v_p}{v_{th}}$ , and a compromise temperature value thus has to be found.

### 6.2.2 Preliminary work

#### Hydrodynamic simulations of the plasma heating

At CELIA, in order to simulate the heating and the expansion of a solid deuterium target into a dense plasma state, the hydrodynamic code ESTHER (Effets Thermomécaniques et Hydrodynamiques engendrés par un Rayonnement) [CCB<sup>+</sup>05] has been used. Three heating methods have been considered for the generation of a dense and nonideal deuterium plasma, sufficiently homogeneous and whose lifetime is at least comparable to the 3 ns ion-bunch duration.

ESTHER is a one-dimensional Lagrangian hydrodynamic code making it possible to simulate the interaction between different kinds of radiation and matter. It can efficiently model the energy deposition of laser beams, ions or X-rays in a plane target and its subsequent evolution from the solid state to a plasma. ESTHER is especially well-suited for a low-fluence interaction and is able to describe phase transitions precisely.

To describe the target material and its properties, a large set of thermodynamic material data is required, such as multiphase equations of state, transport coefficients (ionization degree, electric and thermal conductivities) ranging from the cold matter case to the hot plasma state. The SESAME equation of state for deuterium [SES], the transport coefficients of deuterium and the stopping powers of protons in deuterium provided by the SCAALP code [FBCR10, Sca] developed at CEA, as well as the hydrogen opacities from the ESTHER database, either cold opacities measured by Henke [HGD93] or warm opacities obtained with the NOHEL code [BDF<sup>+</sup>03] are used for the calculations. A particular challenge comes from the fact that the properties of deuterium have to be described over a very wide span of density and temperature, when possible from the solid cryogenic state up to the hot plasma.

In a first phase, two-sided direct laser-beam compression has been simulated, both at the fundamental frequency and at the doubled frequency of the available laser systems. Then, isochoric heating by means of laser-generated TNSA protons has been studied. Finally, volumetric heating with soft laser-induced X-rays has been considered.

#### Experimental implementation

The heating of the D<sub>2</sub> target by using soft X-rays appears to be the most efficient alternative to obtain the best-suited plasma density and temperature profiles as well as homogeneity characteristics over a sufficient duration. This can be implemented experimentally in the so-called *indirect laser heating scheme*, in opposition to the *direct laser heating scheme* employed in this work.

In the indirect heating scheme, the target is heated by soft X-rays generated by the irradiation of the PHELIX laser beam in a gold hohlraum cavity. The latter is composed of a "primary" hohlraum i.e a converter part where the laser light is converted into thermal X-rays, as well as

a "secondary" hohlraum where a solid foil target is heated by the X-rays to the plasma state and where the ion beam can interact with the resulting warm and dense plasma. Typically, a PHELIX laser beam at an energy of 150 J, a pulse length of 1.5 ns (FWHM) and at a wavelength of 527 nm (frequency-doubled) interacts with the gold walls of the primary hohlraum and its energy is converted into thermalized Planckian X-ray radiation. These X-rays are transported to the secondary hohlraum where they volumetrically heat the thin carbon foils that are positioned at both ends of the hohlraum. In this way, a dense plasma, homogeneous in space over a long time span, is generated, with  $n_e \leq 10^{22} \text{ cm}^{-3}$  and  $T_e \approx 20 \text{ eV}$ . A plasma coupling parameter  $\Gamma \approx 0.25$  can thus be reached, corresponding to the case of a weakly nonideal plasma. The obtained plasma conditions are therefore very different from the ones obtained by using a direct laser heating.

The experimental work on the indirect heating scheme is also backed up by hydrodynamic simulations obtained with the RALEF2D code. More details about this experimental scheme and the corresponding results are presented in [Sch11]. Stopping experiments on swift ions in this scheme are in progress [SBB<sup>+</sup>12, OBB<sup>+</sup>13].

### First estimations

For the ESTHER simulations, a temporal profile of the radiative temperature in a hohlraum as measured in [Sch11] has been taken as input data. Simulations have been conducted for different maximum radiation temperatures but for the same temporal profile, and for different target thicknesses. It turns out that an X-ray irradiation of 1-10  $\mu\text{m}$  thick  $\text{D}_2$  target leads to temperature and  $\Gamma$  profiles that are well-adapted for stopping-power measurements in the nonlinear regime [CBF<sup>+</sup>12].

The importance of plasma correlations (nonideality) and beam-plasma correlations (nonlinearity) in the interaction as well as their influence on the stopping process have been evaluated for various ion species at different projectile energies (corresponding to different thicknesses of the deceleration foil). Estimations are in progress to determine the technical feasibility and the physical relevance of such experiments, that would be of considerable interest for fusion research.



# Bibliography

- [AB84] N. R. Arista and W. Brandt. Dielectric response of quantum plasmas in thermal equilibrium. *Physical Review A*, 29:1471–1480, March 1984.
- [AMtV04] S. Atzeni and J. Meyer-ter Vehn. *The Physics of Inertial Fusion : Beam-Plasma Interaction, Hydrodynamics, Hot Dense Matter*. International Series of Monographs on Physics. Clarendon Press, 2004.
- [Azi04] A. Azima. Design und Aufbau eines Hochenergielasersystems (Diploma thesis, Technische Universität Darmstadt), 2004.
- [B10] M. Börner. Aufbau eines Nomarski-Multiframe-Interferometers zur Bestimmung der freien Elektronendichte in lasererzeugten Plasmen (Master thesis, Technische Universität Darmstadt), November 2010.
- [BAB<sup>+</sup>10] V. Bagnoud, B. Aurand, A. Blazevic, S. Borneis, C. Bruske, B. Ecker, U. Eisenbarth, J. Fils, A. Frank, E. Gaul, S. Goette, C. Haefner, T. Hahn, K. Harres, H.-M. Heuck, D. Hochhaus, D. H. H. Hoffmann, D. Javorková, H.-J. Kluge, T. Kuehl, S. Kunzer, M. Kreutz, T. Merz-Mantwill, P. Neumayer, E. Onkels, D. Reemts, O. Rosmej, M. Roth, T. Stoehlker, A. Tauschwitz, B. Zielbauer, D. Zimmer, and K. Witte. Commissioning and early experiments of the PHELIX facility. *Applied Physics B: Lasers and Optics*, 100:137–150, July 2010.
- [Bal60] R. Balescu. Irreversible Processes in Ionized Gases. *Physics of Fluids*, 3:52–63, January 1960.
- [Bar10] M. D. Barriga-Carrasco. Full conserving dielectric function for plasmas at any degeneracy. *Laser and Particle Beams*, 28:307–311, June 2010.
- [Bas] M. M. Basko, <http://www.basko.net/mm/ralef/ralef.html>.
- [BBL78] George Basbas, Werner Brandt, and Roman Laubert. Universal cross sections for K-shell ionization by heavy charged particles. II. Intermediate particle velocities. *Phys. Rev. A*, 17:1655–1674, May 1978.
- [BBS<sup>+</sup>12] S. Bedacht, A. Blazevic, G. Schaumann, M. Roth, and D. H. H. Hoffmann. *Cryogenic Targets for Laser and Particle Beams*, volume 2012-1 of *GSI Report*. GSI Helmholtzzentrum für Schwerionenforschung, Darmstadt, 2012.
- [BBv02] A. Blazevic, H. G. Bohlen, and W. von Oertzen. Stopping power of swift neon ions in dependence on the charge state in the non-equilibrium regime. *Nuclear Instruments and Methods in Physics Research B*, 190:64–68, May 2002.
- [BDF<sup>+</sup>03] C. Bowen, A. Decoster, C. J. Fontes, K. B. Fournier, O. Peyrusse, and Y. V. Ralchenko. Review of the NLTE emissivities code comparison virtual workshop. *Journal of Quantitative Spectroscopy & Radiative Transfer*, 81:71–84, September 2003.

- [BDH63] W. H. Barkas, J. N. Dyer, and H. H. Heckman. Resolution of the  $\Sigma^-$ -Mass Anomaly. *Physical Review Letters*, 11:26–28, July 1963.
- [Bet30] H. Bethe. Zur Theorie des Durchgangs schneller Korpuskularstrahlen durch Materie. *Annalen der Physik*, 397:325–400, 1930.
- [Bet32] H. Bethe. Bremsformel für Elektronen relativistischer Geschwindigkeit. *Zeitschrift für Physik*, 76:293–299, May 1932.
- [Bet83] H. D. Betz. Heavy Ion Charge States. In S. Datz, editor, *Applied Atomic Collision Physics, Volume 4: Condensed Matter*, volume 4, pages 2–+, 1983.
- [BFF<sup>+</sup>12] M. Börner, J. Fils, A. Frank, A. Blažević, T. Hessling, A. Pelka, G. Schaumann, A. Schökel, D. Schumacher, M. M. Basko, J. Maruhn, A. Tauschwitz, and M. Roth. Development of a Nomarski-type multi-frame interferometer as a time and space resolving diagnostics for the free electron density of laser-generated plasma. *Review of Scientific Instruments*, 83(4):043501, April 2012.
- [BK82] W. Brandt and M. Kitagawa. Effective stopping-power charges of swift ions in condensed matter. *Physical Review B*, 25:5631–5637, May 1982.
- [Blo33] F. Bloch. Zur Bremsung rasch bewegter Teilchen beim Durchgang durch Materie. *Annalen der Physik*, 408:285–320, 1933.
- [BMT09] M. M. Basko, J. Maruhn, and A. Tauschwitz. An efficient cell-centered diffusion scheme for quadrilateral grids. *Journal of Computational Physics*, 228:2175–2193, April 2009.
- [Boh13] N. Bohr. On the Theory of the Decrease of Velocity of Moving Electrified Particles on Passing through Matter. *Phil. Mag.*, 25(6):10–31, 1913.
- [Boh41] N. Bohr. Velocity-Range Relation for Fission Fragments. *Physical Review*, 59:270–275, February 1941.
- [Boi96] O. Boine-Frankenheim. Nonlinear stopping power of ions in plasmas. *Physics of Plasmas*, 3:1585–1590, May 1996.
- [BPS05] L. S. Brown, D. L. Preston, and R. L. Singleton, Jr. Charged particle motion in a highly ionized plasma. *Phys. reports*, 410:237–333, May 2005.
- [BRH06] A. Blazevic, B. Rethfeld, and D.H.H. Hoffmann. High energy density matter generated by heavy-ion beams, and application to fusion science. *Matematisk-fysiske Meddelelser*, 52, 2006.
- [BSM<sup>+</sup>12] M. M. Basko, P. V. Sasorov, M. Murakami, V. G. Novikov, and A. S. Grushin. One-dimensional study of the radiation-dominated implosion of a cylindrical tungsten plasma column. *Plasma Physics and Controlled Fusion*, 54(5):055003, May 2012.
- [cas] <http://www.casp-program.org/>.
- [Cay09] W. Cayzac. Ein CVD-Diamant Spektrometer für die Messung der Ladungszustände von Schwerionen im lasererzeugtem Plasma (Master thesis, Technische Universität Darmstadt), November 2009.
- [CBF<sup>+</sup>12] W. Cayzac, A. Blazevic, A. Frank, L. Hallo, G. Malka, A. Ortner, G. Schaumann, T. Schlegel, and M. Roth. *First steps into the nonlinear regime of ion stopping in plasma*, volume 2012-1 of *GSI Report*. GSI Helmholtzzentrum für Schwerionenforschung, Darmstadt, 2012.

- [CCB<sup>+</sup>05] J. P. Colombier, P. Combis, F. Bonneau, R. Le Harzic, and E. Audouard. Hydrodynamic simulations of metal ablation by femtosecond laser irradiation. *Physical Review B*, 71(16):165406, April 2005.
- [CDN<sup>+</sup>94] C. Couillaud, R. Deicas, P. Nardin, M. A. Beuve, J. M. Guihaumé, M. Renaud, M. Cukier, C. Deutsch, and G. Maynard. Ionization and stopping of heavy ions in dense laser-ablated plasmas. *Physical Review E*, 49:1545–1562, February 1994.
- [CFS<sup>+</sup>13] W. Cayzac, A. Frank, D. Schumacher, M. Roth, A. Blažević, F. Wamers, M. Träger, E. Berdermann, B. Voss, and T. Hessling. A spectrometer on chemical vapour deposition-diamond basis for the measurement of the charge-state distribution of heavy ions in a laser-generated plasma. *Review of Scientific Instruments*, 84(4):043301, April 2013.
- [Cha43] S. Chandrasekhar. Stochastic Problems in Physics and Astronomy. *Reviews of Modern Physics*, 15:1–89, January 1943.
- [Cha60] S. Chandrasekhar. *Principles of stellar dynamics*. New York: Dover, 1960, Enlarged ed., 1960.
- [CT99] D. A. Callahan-Miller and M. Tabak. Increasing the coupling efficiency in a heavy ion, inertial confinement fusion target. *Nuclear Fusion*, 39:1547–1556, November 1999.
- [DHB<sup>+</sup>92] K.-G. Dietrich, D. H. H. Hoffmann, E. Boggasch, J. Jacoby, H. Wahl, M. Elfers, C. R. Haas, V. P. Dubenkov, and A. A. Golubev. Charge state of fast heavy ions in a hydrogen plasma. *Physical Review Letters*, 69:3623–3626, December 1992.
- [DHL98] J. D’Avanzo, I. Hofmann, and M. Lontano. Charge dependence of nonlinear stopping power. *Nuclear Instruments and Methods in Physics Research Section A: Accelerators, Spectrometers, Detectors and Associated Equipment*, 415(3):632 – 636, 1998.
- [DHW<sup>+</sup>90] K.-G. Dietrich, D. H. H. Hoffmann, H. Wahl, C. R. Haas, H. Kunze, W. Brandenburg, and R. Noll. Energy loss of heavy ions in a dense hydrogen plasma. *Zeitschrift fur Physik D Atoms Molecules Clusters*, 16:229–230, December 1990.
- [Dia] Diamond Materials GmbH, Hans-Bunte-Str. 19, 79108 Freiburg, Germany - <http://www.diamond-materials.com/EN/index.htm>.
- [DLTB95] J. D’Avanzo, M. Lontano, E. Tome’, and P. F. Bortignon. LETTER: Alpha particle stopping in a dense burning plasma. *Nuclear Fusion*, 35:210–214, February 1995.
- [DMC<sup>+</sup>] C. Deutsch, G. Maynard, M. Chabot, M. Gardes, S. Della-Negra, R. Bimbot, M. F. Rivet, C. Fleurier, C. Couillaud, D. H. H. Hoffmann, H. Wahl, K. Weyrich, O. N. Rosmej, N. A. Tahir, J. Jacoby, M. Ogawa, Y. Oguri, J. Hasegawa, B. Y. Sharkov, A. A. Golubev, A. Fertman, V. E. Fortov, and V. Mintsev. Ion stopping in dense plasma target for high energy density physics. *The open plasma physics journal*, 3:88 – 115.
- [DPM11] J. Davis, G. M. Petrov, and T. A. Mehlhorn. Generation of laser-driven light ions suitable for fast ignition of fusion targets. *Plasma Physics and Controlled Fusion*, 53(4):045013, April 2011.
- [Eli02] S. Eliezer. *The Interaction of High-Power Lasers with Plasmas*. Series in Plasma Physics. Taylor & Francis, 2002.



- [FBB<sup>+</sup>13] A. Frank, A. Blažević, V. Bagnoud, M. M. Basko, M. Börner, W. Cayzac, D. Kraus, T. Heßling, D. H. H. Hoffmann, A. Ortner, A. Otten, A. Pelka, D. Pepler, D. Schumacher, A. Tauschwitz, and M. Roth. Energy Loss and Charge Transfer of Argon in a Laser-Generated Carbon Plasma. *Physical Review Letters*, 110(11):115001, March 2013.
- [FBCR10] G. Faussurier, C. Blancard, P. Cossé, and P. Renaudin. Equation of state, transport coefficients, and stopping power of dense plasmas from the average-atom model self-consistent approach for astrophysical and laboratory plasmas. *Physics of Plasmas*, 17(5):052707, May 2010.
- [FBG<sup>+</sup>10] A. Frank, A. Blažević, P. L. Grande, K. Harres, T. Heßling, D. H. H. Hoffmann, R. Knobloch-Maas, P. G. Kuznetsov, F. Nürnberg, A. Pelka, G. Schaumann, G. Schiwietz, A. Schökel, M. Schollmeier, D. Schumacher, J. Schütrumpf, V. V. Vatulín, O. A. Vinokurov, and M. Roth. Energy loss of argon in a laser-generated carbon plasma. *Physical Review E*, 81(2):026401–+, February 2010.
- [Fer98] A. Ferrari. Modeling Extragalactic Jets. *Annual Review of Astronomy and Astrophysics*, 36:539–598, 1998.
- [FHA<sup>+</sup>09] J. C. Fernández, J. J. Honrubia, B. J. Albright, K. A. Flippo, D. C. Gautier, B. M. Hegelich, M. J. Schmitt, M. Temporal, and L. Yin. Progress and prospects of ion-driven fast ignition. *Nuclear Fusion*, 49(6):065004–+, June 2009.
- [fil] [http://henke.lbl.gov/optical\\_constants/filter2.html](http://henke.lbl.gov/optical_constants/filter2.html).
- [Fra11] A. Frank. *Energieverlust und Umladung von schweren Ionen in lasererzeugten Plasmen*. PhD thesis, Technische Universität Darmstadt, October 2011.
- [GB06] F. Grüner and F. Bell. First-principles-simulation of both charge state and stopping power of swift heavy ions in solids. *Nuclear Instruments and Methods in Physics Research B*, 245:15–18, April 2006.
- [GBAS04] F. Grüner, F. Bell, W. Assmann, and M. Schubert. Integrated Approach to the Electronic Interaction of Swift Heavy Ions with Solids and Gases. *Physical Review Letters*, 93(21):213201, November 2004.
- [GBF<sup>+</sup>98] A. Golubev, M. Basko, A. Fertman, A. Kozodaev, N. Mesheryakov, B. Sharkov, A. Vishnevskiy, V. Fortov, M. Kulish, V. Gryaznov, V. Mintsev, E. Golubev, A. Pukhov, V. Smirnov, U. Funk, S. Stoewe, M. Stetter, H.-P. Flierl, D. H. Hoffmann, J. Jacoby, and I. Iosilevski. Dense plasma diagnostics by fast proton beams. *Physical Review E*, 57:3363–3367, March 1998.
- [GCL<sup>+</sup>13] M. Gauthier, S. N. Chen, A. Levy, P. Audebert, C. Blancard, T. Ceccotti, M. Cerchez, D. Doria, V. Floquet, E. Lamour, C. Peth, L. Romagnani, J.-P. Rozet, M. Scheinder, R. Shepherd, T. Toncian, D. Vernhet, O. Willi, M. Borghesi, G. Faussurier, and J. Fuchs. Charge Equilibrium of a Laser-Generated Carbon-Ion Beam in Warm Dense Matter. *Physical Review Letters*, 110(13):135003, March 2013.
- [GD67] H. A. Gould and H. E. Dewitt. Convergent Kinetic Equation for a Classical Plasma. *Physical Review*, 155:68–74, March 1967.
- [gea] <http://geant4.cern.ch/>.
- [Ger02a] D. O. Gericke. Stopping power for strong beam-plasma coupling. *Laser and Particle Beams*, 20:471–474, July 2002.

- [Ger02b] D. O. Gericke. Stopping power for strong beam-plasma coupling (erratum). *Laser and Particle Beams*, 20:643–643, October 2002.
- [GS99] D. O. Gericke and M. Schlanges. Beam-plasma coupling effects on the stopping power of dense plasmas. *Physical Review E*, 60:904–910, July 1999.
- [GS02] P. L. Grande and G. Schiwietz. The unitary convolution approximation for heavy ions. *Nuclear Instruments and Methods in Physics Research B*, 195:55–63, October 2002.
- [GS03] D. O. Gericke and M. Schlanges. Energy deposition of heavy ions in the regime of strong beam-plasma correlations. *Physical Review E*, 67(3):037401, March 2003.
- [GSB02] D. O. Gericke, M. Schlanges, and T. Bornath. Stopping power of nonideal, partially ionized plasmas. *Physical Review E*, 65(3):036406, March 2002.
- [HBF<sup>+</sup>00] D. H. H. Hoffmann, R. Bock, A. Y. Faenov, U. Funk, M. Geissel, U. Neuner, T. A. Pikuz, F. Rosmej, M. Roth, W. Süß, N. Tahir, and A. Tauschwitz. Plasma physics with intense laser and ion beams. *Nuclear Instruments and Methods in Physics Research B*, 161:9–18, March 2000.
- [HFT<sup>+</sup>09] J. J. Honrubia, J. C. Fernández, M. Temporal, B. M. Hegelich, and J. Meyer-Ter-Vehn. Fast ignition of inertial fusion targets by laser-driven carbon beams. *Physics of Plasmas*, 16(10):102701, October 2009.
- [HFT<sup>+</sup>10] J. J. Honrubia, J. C. Fernández, M. Temporal, B. M. Hegelich, and J. Meyer-ter-Vehn. Fast ignition by laser-driven carbon beams. *Journal of Physics Conference Series*, 244(2):022038, August 2010.
- [HGD93] B. L. Henke, E. M. Gullikson, and J. C. Davis. X-Ray Interactions: Photoabsorption, Scattering, Transmission, and Reflection at  $E = 50\text{--}30,000$  eV,  $Z = 1\text{--}92$ . *Atomic Data and Nuclear Data Tables*, 54:181–342, July 1993.
- [HHT95] D. D.-M. Ho, J. A. Harte, and M. Tabak. Configurations of radiation driven targets for heavy ion fusion. *Nuclear Fusion*, 35:1125–1132, September 1995.
- [HL01] N. M. Hoffman and C. L. Lee. Application to ICF ignition of a charged-particle energy-loss model valid for all projectile velocities. In *APS Meeting Abstracts*, page 2012, October 2001.
- [HLS<sup>+</sup>00] D. G. Hicks, C. K. Li, F. H. Séguin, A. K. Ram, J. A. Frenje, R. D. Petrasso, J. M. Soures, V. Y. Glebov, D. D. Meyerhofer, S. Roberts, C. Sorce, C. Stöckl, T. C. Sangster, and T. W. Phillips. Charged-particle acceleration and energy loss in laser-produced plasmas. *Physics of Plasmas*, 7:5106–5117, December 2000.
- [Hug75] T.P. Hughes. *Plasmas and laser light*. Halsted Press book. John Wiley & Sons, Incorporated, 1975.
- [HWW<sup>+</sup>90] D. H. H. Hoffmann, K. Weyrich, H. Wahl, D. Gardés, R. Bimbot, and C. Fleurier. Energy loss of heavy ions in a plasma target. *Physical Review A*, 42:2313–2321, August 1990.
- [JBF<sup>+</sup>96] J. Jacoby, C. Bickes, H.-P. Flierl, D. H. H. Hoffmann, M. Dornick, K. Weyrich, H. Wetzler, and C. Stöckl. Interaction of heavy ions with plasmas. *Nuclear Instruments and Methods in Physics Research B*, 115:7–13, July 1996.

- [JHL<sup>+</sup>95] J. Jacoby, D. H. H. Hoffmann, W. Laux, R. W. Müller, H. Wahl, K. Weyrich, E. Boggasch, B. Heimrich, C. Stöckl, H. Wetzler, and S. Miyamoto. Stopping of Heavy Ions in a Hydrogen Plasma. *Physical Review Letters*, 74:1550–1553, February 1995.
- [Kne13] A. Knetsch. Entwicklung eines pcCVD Diamant Detektors zur Messung von Ionen-Energieverlust bei maximalem Bremsvermögen (Master thesis, Technische Universität Darmstadt), October 2013.
- [Kra79] M. O. Krause. Atomic radiative and radiationless yields for K and L shells. *Journal of Physical and Chemical Reference Data*, 8:307–327, April 1979.
- [Kru88] W.L. Kruer. *The physics of laser plasma interactions*. Frontiers in physics. Addison-Wesley, 1988.
- [KSB85] D. Kremp, M. Schlanges, and T. Bornath. Nonequilibrium real time Green’s functions and the condition of weakening of initial correlation. *Journal of Statistical Physics*, 41:661–670, November 1985.
- [Lan36] L. Landau. Kinetic equation for the Coulomb effect. *Phys. Z. Sowjetunion*, 1936.
- [LEMP01] P. T. León, S. Eliezer, J. M. Martínez-Val, and M. Piera. Fusion burning waves in degenerate plasmas. *Physics Letters A*, 289:135–140, October 2001.
- [Len60] A. Lenard. On Bogoliubov’s kinetic equation for a spatially homogeneous plasma. *Annals of Physics*, 10:390–400, July 1960.
- [LHK<sup>+</sup>02] B. Lommel, W. Hartmann, B. Kindler, J. Klemm, and J. Steiner. Preparation of self-supporting carbon thin films. *Nuclear Instruments and Methods in Physics Research A*, 480:199–203, March 2002.
- [Li93] C. Li. *Conceptual study of moderately coupled plasmas and experimental comparison of laboratory X-ray sources*. PhD thesis, Massachusetts Institute of Technology, 1993.
- [LI08] A. Lechner and V. N. Ivanchenko. Recent developments of electronic stopping models for heavy ions in GEANT4. *IEEE Nuclear Science Symposium Conference Record*, October 2008.
- [LIK10] A. Lechner, V. N. Ivanchenko, and J. Knobloch. Validation of recent Geant4 physics models for application in carbon ion therapy. *Nuclear Instruments and Methods in Physics Research B*, 268:2343–2354, July 2010.
- [Lin54a] J. Lindhard. On the properties of a gas of charged particles. *Dan. Vidensk. Selsk. Mat. Fys. Medd.*, 28(8):1–57, 1954.
- [Lin54b] J. Lindhard. *On the Properties of a Gas of Charged Particles*, by J. Lindhard. E. Munksgaard, 1954.
- [LP93a] C.-K. Li and R. D. Petrasso. Charged-particle stopping powers in inertial confinement fusion plasmas. *Physical Review Letters*, 70:3059–3062, May 1993.
- [LP93b] C.-K. Li and R. D. Petrasso. Fokker-Planck equation for moderately coupled plasmas. *Physical Review Letters*, 70:3063–3066, May 1993.
- [LP95] C. Li and R. D. Petrasso. Effects of scattering upon energetic ion energy loss in plasmas. *Physics of Plasmas*, 2:2460–2464, June 1995.

- [LPB08] B. G. Logan, L. J. Perkins, and J. J. Barnard. Direct drive heavy-ion-beam inertial fusion at high coupling efficiency. *Physics of Plasmas*, 15(7):072701, July 2008.
- [LS61] J. Lindhard and M. Scharff. Energy Dissipation by Ions in the key Region. *Physical Review*, 124:128–130, October 1961.
- [LS96] J. Lindhard and A. H. Sørensen. Relativistic theory of stopping for heavy ions. *Physical Review A*, 53:2443–2456, April 1996.
- [MBB<sup>+</sup>01] P. Moritz, E. Berdermann, K. Blasche, H. Stelzer, and B. Voss. Broadband electronics for CVD-diamond detectors. *Diamond and Related Materials*, 10:1765–1769, September 2001.
- [MCG00] G. Maynard, M. Chabot, and D. Gardès. Density effect and charge dependent stopping theories for heavy ions in the intermediate velocity regime. *Nuclear Instruments and Methods in Physics Research B*, 164:139–146, April 2000.
- [MD85] G. Maynard and C. Deutsch. Born random phase approximation for ion stopping in an arbitrarily degenerate electron fluid. *J. Physique*, 46:1113–1122, July 1985.
- [MDD<sup>+</sup>02] G. Maynard, C. Deutsch, K. Dimitriou, K. Katsonis, and M. Sarrazin. Evaluation of the energy deposition profile for swift heavy ions in dense plasmas. *Nuclear Instruments and Methods in Physics Research B*, 195:188–215, October 2002.
- [Men10] J. Menzel. *Aufbau und Inbetriebnahme einer Kryoanlage zur Targeterzeugung für Experimente mit Hochenergielasern und Schwerionenstrahlen*. PhD thesis, Technische Universität Darmstadt, February 2010.
- [MGW<sup>+</sup>04] J. J. MacFarlane, I. E. Golovkin, P. R. Woodruff, D. R. Welch, B. V. Oliver, T. A. Mehlhorn, and R. B. Campbell. Simulation of the Ionization Dynamics of Aluminum Irradiated by Intense Short-Pulse Lasers. *Proc. Inertial Fusion and Sciences Applications 2003*, page 457, 2004.
- [MR96] K. Morawetz and G. Röpke. Stopping power in nonideal and strongly coupled plasmas. *Physical Review E*, 54:4134–4146, October 1996.
- [MSB<sup>+</sup>88] P. Maine, D. Strickland, P. Bado, M. Pessot, and G. Mourou. Generation of ultra-high peak power pulses by chirped pulse amplification. *IEEE Journal of Quantum Electronics*, 24:398–403, February 1988.
- [MZDK01] G. Maynard, G. Zwicknagel, C. Deutsch, and K. Katsonis. Diffusion-transport cross section and stopping power of swift heavy ions. *Physical Review A*, 63(5):052903, May 2001.
- [NMH09] E. Nardi, Y. Maron, and D. H. H. Hoffmann. Dynamic screening and charge state of fast ions in plasma and solids. *Laser and Particle Beams*, 27:355, April 2009.
- [Nor63] L. C. Northcliffe. Passage of Heavy Ions Through Matter. *Annual Review of Nuclear and Particle Science*, 13:67–102, 1963.
- [NZ82] E. Nardi and Z. Zinamon. Charge State and Slowing of Fast Ions in a Plasma. *Physical Review Letters*, 49:1251–1254, October 1982.
- [OAM96] A. M. Oparin, S. I. Anisimov, and J. Meyer-Ter-Vehn. Kinetic simulation of DT ignition and burn in ICF targets. *Nuclear Fusion*, 36:443–452, April 1996.

- [OBB<sup>+</sup>13] A. Ortner, A. Blazevic, M. Basko, S. Bedacht, W. Cayzac, A. Frank, S. Faik, D. Kraus, T. Rienecker, G. Schaumann, D. Schumacher, An. Tauschwitz, F. Wagner, and M. Roth. *Interaction of heavy ions with warm dense plasma using hohlraum targets (combined experiment with PHELIX and UNILAC)*, volume 2013-1 of *GSI Report*. GSI Helmholtzzentrum für Schwerionenforschung, Darmstadt, 2013.
- [OHK<sup>+</sup>05] Y. Oguri, J. Hasegawa, J. Kaneko, M. Ogawa, and K. Horioka. Stopping of low-energy highly charged ions in dense plasmas. *Nuclear Instruments and Methods in Physics Research A*, 544:76–83, May 2005.
- [PAM86] T. Peter, R. Arnold, and J. Meyer-Ter-Vehn. Influence of dielectronic recombination on fast heavy-ion charge states in plasma. *Physical Review Letters*, 57:1859–1862, October 1986.
- [Pau] H. Paul, <http://www.exphys.uni-linz.ac.at/stopping/>.
- [Pau06] H. Paul. A comparison of recent stopping power tables for light and medium-heavy ions with experimental data, and applications to radiotherapy dosimetry. *Nuclear Instruments and Methods in Physics Research B*, 247:166–172, June 2006.
- [PDB<sup>+</sup>93] D. A. Pepler, C. N. Danson, R. Bann, I. N. Ross, R. M. Stevenson, M. J. Norman, M. Desselberger, and O. Willi. Focal spot smoothing and tailoring for high-power laser applications. In H. T. Powell and T. J. Kessler, editors, *Society of Photo-Optical Instrumentation Engineers (SPIE) Conference Series*, volume 1870 of *Society of Photo-Optical Instrumentation Engineers (SPIE) Conference Series*, pages 76–87, May 1993.
- [Pep] Kévin Pépitone and Ludovic Hallo, CEA CESTA, private communication, 2012.
- [Pet85] T. Peter. Zur effektiven Ladung schneller Ionen in heißen dichten Plasmen, November 1985.
- [Phe] [https://www.gsi.de/en/start/research/forschungsgebiete\\_und\\_experimente/appa\\_pni\\_gesundheit/plasma\\_physicsphelix/phelix.htm](https://www.gsi.de/en/start/research/forschungsgebiete_und_experimente/appa_pni_gesundheit/plasma_physicsphelix/phelix.htm).
- [PM91a] T. Peter and J. Meyer-Ter-Vehn. Energy loss of heavy ions in dense plasma. I - Linear and nonlinear Vlasov theory for the stopping power. *Physical Review A*, 43:1998–2030, February 1991.
- [PM91b] T. Peter and J. Meyer-Ter-Vehn. II. Nonequilibrium charge states and stopping powers. *Physical Review A*, 43:2015–2030, February 1991.
- [Pot90] H. Poth. Electron cooling: Theory, experiment, application. *Physical reports*, 196:135–297, November 1990.
- [PREZ93] J. M. Pitarke, R. H. Ritchie, P. M. Echenique, and E. Zaremba. The  $Z^3_1$  correction to the Bethe-Bloch energy loss formula. *EPL (Europhysics Letters)*, 24:613, December 1993.
- [pri] <http://www.prism-cs.com/Software/PrismSpect/PrismSPECT.htm>.
- [PS03] H. Paul and A. Schinner. Judging the reliability of stopping power tables and programs for heavy ions. *Nuclear Instruments and Methods in Physics Research B*, 209:252–258, August 2003.

- [RCK<sup>+</sup>01] M. Roth, T. E. Cowan, M. H. Key, S. P. Hatchett, C. Brown, W. Fountain, J. Johnson, D. M. Pennington, R. A. Snavely, S. C. Wilks, K. Yasuike, H. Ruhl, F. Pegoraro, S. V. Bulanov, E. M. Campbell, M. D. Perry, and H. Powell. Fast Ignition by Intense Laser-Accelerated Proton Beams. *Physical Review Letters*, 86:436–439, January 2001.
- [Rot97] M. Roth. *Experimentelle Bestimmung des Energieverlustes schwerer Ionen in lasererzeugten Plasmen*. PhD thesis, Technische Universität Darmstadt, 1997.
- [RSS<sup>+</sup>00] M. Roth, C. Stöckl, W. Süß, O. Iwase, D. O. Gericke, R. Bock, D. H. H. Hoffmann, M. Geissel, and W. Seelig. Energy loss of heavy ions in laser-produced plasmas. *Europhysics Letters*, 50:28–34, April 2000.
- [RVS96] J. P. Rozet, D. Vernhet, and C. Stéphan. ETACHA: A program for calculating charge states at GANIL energies. *Nuclear Instruments and Methods in Physics Research B*, 107:67–70, February 1996.
- [SBB<sup>+</sup>12] D. Schumacher, S. Bedacht, A. Blazevic, S. Busold, A. Frank, G. Schaumann, and M. Roth. *Indirectly plasma heating and energy loss experiments with PHELIX*, volume 2012-1 of *GSI Report*. GSI Helmholtzzentrum für Schwerionenforschung, Darmstadt, 2012.
- [Sca] G. Faussurier and C. Blancard, private communication, 2011.
- [Sch07] D. Schumacher. *Spektrale Charakterisierung thermischer Plasmastrahlung* (Diploma thesis, Technische Universität Darmstadt), December 2007.
- [Sch11] D. Schumacher. *Untersuchung laserinduzierter Hohlraumstrahlung und Energieverlust von Schwerionen in indirekt geheizten Plasmen*. PhD thesis, Technische Universität Darmstadt, October 2011.
- [SES] [http://t1web.lanl.gov/doc/SESAME\\_3Ddatabase\\_1992.html](http://t1web.lanl.gov/doc/SESAME_3Ddatabase_1992.html).
- [SG01] G. Schiwietz and P. L. Grande. Improved charge-state formulas. *Nuclear Instruments and Methods in Physics Research B*, 175:125–131, April 2001.
- [SH53] L. Spitzer and R. Härm. Transport Phenomena in a Completely Ionized Gas. *Physical Review*, 89:977–981, March 1953.
- [Sig05] P. Sigmund. *Stopping of ions heavier than helium*, volume 73. Journal of the ICRU - Oxford University Press, jun 2005.
- [Sin08] R. L. Singleton, Jr. Calculating the charged particle stopping power exactly to leading and next-to-leading order. *Journal of Physics Conference Series*, 112(2):022034, May 2008.
- [SK06] H. Suno and T. Kato. Cross section database for carbon atoms and ions: Electron-impact ionization, excitation, and charge exchange in collisions with hydrogen atoms. *Atomic Data and Nuclear Data Tables*, 92:407–455, July 2006.
- [SK08] Y. Sentoku and A. J. Kemp. Numerical methods for particle simulations at extreme densities and temperatures: Weighted particles, relativistic collisions and reduced currents. *Journal of Computational Physics*, 227:6846–6861, July 2008.
- [Sla30] J. C. Slater. Atomic shielding constants. *Phys. Rev.*, 36:57–64, Jul 1930.
- [SM85] D. Strickland and G. Mourou. Compression of amplified chirped optical pulses. *Optics Communications*, 56:219–221, December 1985.

- [Spi56] L. Spitzer. *Physics of fully ionized gases; 1st ed.* Internat. Sci. Tracts Phys. Astron. Interscience, New York, NY, 1956.
- [sri] <http://www.srim.org/>.
- [SS00] P. Sigmund and A. Schinner. Binary stopping theory for swift heavy ions. *European Physical Journal D*, 12:425–434, November 2000.
- [SS02] P. Sigmund and A. Schinner. Binary theory of electronic stopping. *Nuclear Instruments and Methods in Physics Research B*, 195:64–90, October 2002.
- [SS03] P. Sigmund and A. Schinner. Anatomy of the Barkas effect. *Nuclear Instruments and Methods in Physics Research B*, 212:110–117, December 2003.
- [SS06] P. Sigmund and A. Schinner. Shell correction in stopping theory. *Nuclear Instruments and Methods in Physics Research B*, 243:457–460, February 2006.
- [SSR<sup>+</sup>05] G. Schaumann, M. S. Schollmeier, G. Rodriguez-Prieto, A. Blazevic, E. Brambrink, M. Geissel, S. Korostiy, P. Pirzadeh, M. Roth, F. B. Rosmej, A. Y. Faenov, T. A. Pikuz, K. Tsigutkin, Y. Maron, N. A. Tahir, and D. H. H. Hoffmann. High energy heavy ion jets emerging from laser plasma generated by long pulse laser beams from the NHELIX laser system at GSI. *Laser and Particle Beams*, 23:503–512, October 2005.
- [Sug81] H. Sugiyama. Electronic stopping power formula for intermediate energies. *Radiation Effects*, 56(3-4):205–211, 1981.
- [Tab] <https://www.llnl.gov/str/November01/Tabak.html>.
- [Tar] [https://www.gsi.de/en/work/fairgsi/common\\_systems/target\\_laboratory.htm](https://www.gsi.de/en/work/fairgsi/common_systems/target_laboratory.htm).
- [TBF<sup>+</sup>13] A. Tauschwitz, M Basko, A. Frank, V. Novikov, A. Grushin, A. Blazevic, M. Roth, and J. A. Maruhn. 2D radiation-hydrodynamics modeling of laser-plasma targets for ion stopping measurements. *High Energy Density Physics*, 9:158–166, March 2013.
- [Tem06] M. Temporal. Fast ignition of a compressed inertial confinement fusion hemispherical capsule by two proton beams. *Physics of Plasmas*, 13(12):122704–+, December 2006.
- [THG<sup>+</sup>94] M. Tabak, J. Hammer, M. E. Glinsky, W. L. Kruer, S. C. Wilks, J. Woodworth, E. M. Campbell, M. D. Perry, and R. J. Mason. Ignition and high gain with ultrapowerful lasers. *Physics of Plasmas*, 1:1626–1634, May 1994.
- [THK<sup>+</sup>01] N. A. Tahir, D. H. Hoffmann, A. Kozyreva, A. Tauschwitz, A. Shutov, J. A. Maruhn, P. Spiller, U. Neuner, J. Jacoby, M. Roth, R. Bock, H. Juranek, and R. Redmer. Metallization of hydrogen using heavy-ion-beam implosion of multilayered cylindrical targets. *Physical Review E*, 63(1):016402, January 2001.
- [TSR<sup>+</sup>10] V. T. Tikhonchuk, T. Schlegel, C. Regan, M. Temporal, J.-L. Feugeas, P. Nicolaï, and X. Ribeyre. Fast ion ignition with ultra-intense laser pulses. *Nuclear Fusion*, 50(4):045003, April 2010.
- [TSS<sup>+</sup>12] N. A. Tahir, J. B. Sancho, A. Shutov, R. Schmidt, and A. R. Piriz. Impact of high energy high intensity proton beams on targets: Case studies for Super Proton Synchrotron and Large Hadron Collider. *Physical Review Special Topics Accelerators and Beams*, 15(5):051003, May 2012.

- [Uni] [https://www.gsi.de/en/work/fairgsi/linac\\_and\\_operations/linac.htm](https://www.gsi.de/en/work/fairgsi/linac_and_operations/linac.htm).
- [Wam06] F. Wamers. Entwicklung eines Detektors für gepulste Schwerionenstrahlen (Diploma thesis, Technische Universität Darmstadt), May 2006.
- [WBB<sup>+</sup>97] T. Winkler, K. Beckert, F. Bosch, H. Eickhoff, B. Franzke, F. Nolden, H. Reich, B. Schlitt, and M. Steck. Electron cooling of highly charged ions in the ESR. *Nuclear Physics A*, 626:485–489, February 1997.
- [WM08] L. Wu and G. H. Miley. Multi-electron ionization and charge exchange in heavy ion fusion. *Journal of Physics Conference Series*, 112(3):032030, May 2008.
- [WSS<sup>+</sup>97] H. Wetzler, W. Süss, C. Stöckl, A. Tauschwitz, and D. H. H. Hoffmann. Density Diagnostics of an Argon Plasma by Heavy Ion Beams and Spectroscopy. *Laser and Particle Beams*, 15:449, 1997.
- [Z6] [https://www.gsi.de/en/start/research/forschungsgebiete\\_und\\_experimente/appa\\_pni\\_gesundheit/plasma\\_physicsphelix/anlagen\\_in\\_der\\_experimenthalle\\_z6.htm](https://www.gsi.de/en/start/research/forschungsgebiete_und_experimente/appa_pni_gesundheit/plasma_physicsphelix/anlagen_in_der_experimenthalle_z6.htm).
- [ZBD00] M. R. Zaghoul, M. A. Bourham, and J. M. Doster. A simple formulation and solution strategy of the Saha equation for ideal and nonideal plasmas. *Journal of Physics D Applied Physics*, 33:977–984, April 2000.
- [ZBL85] J.F. Ziegler, J.P. Biersack, and U. Littmark. *The stopping and Range of Ions in Matter*, volume 1. 1985.
- [Zie99] J. F. Ziegler. Stopping of energetic light ions in elemental matter. *Journal of Applied Physics*, 85:1249–1272, February 1999.
- [Zwi99] G. Zwicknagel. Stopping of heavy ions in plasmas at strong coupling. *Physical reports*, 309:117–208, February 1999.
- [Zwi02] G. Zwicknagel. Nonlinear energy loss of heavy ions in plasma. *Nuclear Instruments and Methods in Physics Research B*, 197:22–38, November 2002.
- [ZZB10] J. F. Ziegler, M. D. Ziegler, and J. P. Biersack. SRIM - The stopping and range of ions in matter (2010). *Nuclear Instruments and Methods in Physics Research B*, 268:1818–1823, June 2010.



## List of publications and communications

### Publications

- \* W. Cayzac, E. Berdermann, A. Blazevic, A. Frank, T. Hessling, D. Schumacher, M. Träger, B. Voss, F. Wamers and M. Roth. *A spectrometer on chemical vapour deposition-basis for the measurement of the charge-state distribution of heavy ions in a laser-generated plasma*, Rev. Sci. Instr., **84**, 043301 (2013)
- \* A. Frank, A. Blazevic, V. Bagnoud, M.M. Basko, M. Börner, W. Cayzac, D. Kraus, T. Hessling, D.H.H. Hoffmann, A. Ortner, A. Otten, A. Pelka, D. Pepler, D. Schumacher, An. Tauschwitz and M. Roth. *Energy loss and charge transfer of argon in a laser-generated carbon plasma*, Phys. Rev. Lett. **110**, 115001 (2013)
- \* D. Kraus, J. Vorberger, D.O. Gericke, V. Bagnoud, A. Blazevic, W. Cayzac, A. Frank, G. Gregori, A. Ortner, A. Otten, F. Roth, G. Schaumann, D. Schumacher, K. Siegenthaler, F. Wagner, K. Wünsch and M. Roth. *Probing the complex ion structure in liquid carbon*, accepted for publication in Phys. Rev. Lett.
- \* W. Cayzac, V. Bagnoud, M.M. Basko, S. Bedacht, A. Blazevic, O. Deppert, A. Frank, D.O. Gericke, A. Knetsch, L. Hallo, D. Kraus, G. Malka, A. Ortner, K. Pépitone, G. Schaumann, T. Schlegel, D. Schumacher, An. Tauschwitz, J. Vorberger, F. Wagner and M. Roth. *A setup for ion energy-loss measurements at maximum stopping power in a laser-induced plasma*, submitted to J. of Physics, Conf. Ser. (IFSA 2013 proceedings)
- \* A. Ortner, D. Schumacher, A. Frank, W. Cayzac, M.M. Basko, S. Bedacht, A. Blazevic, S. Faik, D. Kraus, T. Rienecker, G. Schaumann, An. Tauschwitz, F. Wagner and M. Roth. *A novel experimental setup for energy loss and charge state measurements in dense weakly coupled plasma using laser-heated hohlraum targets*, submitted to J. of Physics, Conf. Ser. (IFSA 2013 proceedings)
- \* W. Cayzac, V. Bagnoud, M.M. Basko, S. Bedacht, A. Blazevic, O. Deppert, A. Frank, D.O. Gericke, A. Knetsch, L. Hallo, D. Kraus, G. Malka, A. Ortner, K. Pépitone, G. Schaumann, T. Schlegel, D. Schumacher, An. Tauschwitz, J. Vorberger, F. Wagner and M. Roth. *Energy loss of carbon ions at maximum stopping power in a laser-generated plasma*, in preparation

### Communications

- Talks
- \* Guest talk at CEA-DIF, Bruyères-le-Châtel, France, Mar. 2011. *Investigation of the energy loss of ions in a strongly coupled H (D) plasma*
- \* 3rd Workshop 'CARAT - advanced diamond detectors' at Helmholtzzentrum für Schwerionenforschung, Darmstadt, Germany, Dec. 2011. *Applications of polycrystalline CVD diamond in plasma physics experiments*
- \* 1st ISTC-GSI Summer School on high intensity light science and technologies, Darmstadt, Germany, Oct. 2011. *Investigation of the ion energy loss in a deuterium plasma in the nonlinear regime* (best presentation award)

- \* 33rd International Workshop on Physics of High Energy Density in Matter, Hirschegg, Austria, Jan. 2013. *Ion energy loss at maximum stopping power in a laser-generated plasma*
- \* 22nd General Congress of the French Physical Society, Marseille, France, Jul. 2013. *Ion energy loss in a laser plasma*
- \* 8th International Conference on Inertial Fusion Science and Applications (IFSA 2013), Nara, Japan, Sep. 2013. *Ion energy loss at maximum stopping power in a laser-generated plasma*
- Contributions to poster sessions
- \* 31st International Workshop on Physics of High Energy Density in Matter, Hirschegg, Austria, Feb. 2011. *Investigation of the ion energy loss in a strongly coupled hydrogen plasma*
- \* 4th EMMI Workshop on Plasma Physics with Intense Heavy-Ion and Laser Beams, Darmstadt, Germany, May 2011. *Investigation of the ion energy loss in a strongly coupled hydrogen plasma*
- \* 68th Scottish Universities Summer School in Physics, Glasgow, United Kingdom, Aug. 2011. *Investigation of the ion energy loss in a strongly coupled deuterium plasma*
- \* 7th International Conference on Inertial Fusion Science and Applications (IFSA 2011), Bordeaux, France, Sep. 2011. *Investigation of the ion energy loss in a strongly coupled deuterium plasma*
- \* 1st ISTC-GSI Summer School on high intensity light science and technologies, Darmstadt, Germany, Oct. 2011. *Investigation of the ion energy loss in a deuterium plasma in the nonlinear regime*
- \* 32nd International Workshop on Physics of High Energy Density in Matter, Hirschegg, Austria, Feb. 2012. *First steps into the nonlinear regime of ion stopping in plasma*
- \* Summer school 'Applications of Electronics in Plasma Physics', Rethymno, Greece, Jul. 2012. *Stopping power of C ions in a hot C plasma in the Bragg-peak region*
- \* 5th Conference on Laser-plasma interaction (Forum ILP 2012), Ile de Ré, France, Sep. 2012. *Stopping power of C ions in a hot C plasma in the Bragg-peak region*

## Curriculum

### Personal data

CAYZAC, Witold  
700 chemin de Bellevue  
34820 ASSAS, FRANCE

Tel: +33 6 42 66 78 00

E-mail: `cayzac@celia.u-bordeaux1.fr` ; `w.cayzac@gsi.de`

Born on July 11th 1985, in Wrocław, Poland

Citizenship: French

### Education

\* 12/2010 - 12/2013

International joint PhD student at Université Bordeaux 1 / Centre Lasers Intenses et Applications (CELIA), Talence, France, supervised by G. Malka and L. Hallo, and at Technische Universität Darmstadt (TUD), Darmstadt, Germany, supervised by M. Roth

\* Since 06/2010

Member of the Helmholtz Graduate School for Hadron and Ion research (HGS-HIRE) at GSI Helmholtzzentrum für Schwerionenforschung (GSI), Darmstadt, Germany

\* 02/2010

Master degree 'Master of Science in Engineering Physics' of TUD, and Engineer degree of Ecole Centrale de Lyon

\* 10/2007 - 02/2010

Double degree (Master of engineering physics) at TUD, Master Thesis internship at TUD and GSI, on '*Development of a CVD-diamond spectrometer for the measurement of the charge states of heavy ions in a laser-generated plasma*'

\* 2005 - 2010

Student at the engineering school 'Ecole Centrale de Lyon', Ecully, France

**Declaration of authorship**

I hereby declare that the thesis submitted is my own unaided work. All direct or indirect sources used are acknowledged as references. This paper was not previously presented to another examination board and has not been published.

Bordeaux, 02.12.13

.....